GRADUATE SCHOOL APPROVAL RECORD

NORTHEASTERN UNIVERSITY
Graduate School of Arts and Sciences

Dissertation Title:	Measurement of the Top Quark Mass in Lepton+Jets Events with Secondary-Vertex Tagging
Author:	Robert D. Harrington
Department:	Graduate School of Arts and Sciences

Approved for Dissertation Requirements of the Doctor of Philosophy Degree

Dissertation Committee

Emanuela Barberis, Advisor	Date
Pran Nath	Date
George Alverson	Date

Head of Department

	Date

Graduate School Notified of Acceptance

Director of the Graduate School	Date

Copy Deposited in Library

Signed	Date

DEPARTMENTAL APPROVAL RECORD

NORTHEASTERN UNIVERSITY
Graduate School of Arts and Sciences

Dissertation Title:	Measurement of the Top Quark Mass in Lepton+Jets Events with Secondary-Vertex Tagging
Author:	Robert D. Harrington
Department:	Graduate School of Arts and Sciences

Approved for Dissertation Requirements of the Doctor of Philosophy Degree

Dissertation Committee

Emanuela Barberis, Advisor	Date
Pran Nath	Date
George Alverson	Date

Head of Department

	Date

Graduate School Notified of Acceptance

Director of the Graduate School	Date

MEASUREMENT OF THE TOP QUARK MASS IN LEPTON+JETS EVENTS WITH SECONDARY-VERTEX TAGGING

A dissertation presented

by

Robert D. Harrington

to
The Graduate School of Arts and Sciences

In partial fulfillment of the requirements for the degree of
Doctor of Philosophy

in the field of

Physics

Northeastern University
Boston, Massachusetts
February 2007

MEASUREMENT OF THE TOP QUARK MASS IN LEPTON+JETS EVENTS WITH SECONDARY-VERTEX TAGGING

by

Robert D. Harrington

ABSTRACT OF DISSERTATION

Submitted in partial fulfillment of the requirements
for the degree of Doctor of Philosophy in Physics
in the Graduate School of Arts and Sciences of
Northeastern University, February 2007

ABSTRACT

A measurement of the top quark mass with the matrix element method in the lepton + jets final state in DØ Run II is presented. Events with single isolated energetic charged lepton (electron or muon), exactly four calorimeter jets, and significant missing transverse energy are selected. Probabilities used to discriminate between signal and background are assumed to be proportional to differential cross-sections, calculated using event kinematics and folding in object resolutions and parton distribution functions. The event likelihoods constructed using these probabilities are varied with the top quark mass, m_t, and the jet energy scale, *JES*, to give the smallest possible combined statistical + JES uncertainty. The results using 425 pb^{-1} of DØ Run II data are:

$$\begin{aligned} l\text{+jets} &: m_{top} = 169.2\ ^{+3.4}_{-9.2}(stat + JES)\ ^{+1.8}_{-1.7}(syst) \\ l\text{+jets (with } b-\text{tagging)} &: m_{top} = 172.2\ ^{+3.2}_{-4.6}(stat + JES)\ \pm 1.6(syst) \end{aligned}$$

Also presented is an overview of the installation of several scintillation detectors in the DØ muon system, and a comprehensive calibration of the muon scintillation system.

ACKNOWLEDGMENTS

I would like to thank my advisor, Emanuela Barberis, for all her patience and the attention she gave me, and my committee members, George Alverson and Pran Nath, for a careful reading of my thesis. I would also like to thank Stephen Reucroft, John Swain, and other in the High Energy group at Northeastern for the many beers that helped me to keep my sanity.

In addition, I am particularly grateful to Aurelio Juste for his help in the earliest stages of this analysis, and for assistance and encouragement later on when I ran into difficulties. I greatly value the advice and support of Arnulf Quadt through the early months of the analysis as well.

I benefited from the work of many others in the top group, especially Philip Schieferdecker and Frank Fiedler, whose work on the untagged version of the analysis laid the foundation for my analysis. I give thanks to Jonas Strandberg for his patience and support with the b-tagging, and to Sara for always answering my questions.

I had countless discussions with Michael Begel, Michele Weber, and Martijn Mulders that were helpful in so many ways, I would not be done even now without their remarkable insight and patience to understand the subtleties of this analysis.

Thanks to all my friends and family that are too numerous to mention. Your support was very important to me. Most importantly, I appreciate my wife, Ioana Vladescu, for being here, for making me move back to Boston, for listening to my incredibly boring explanations about my analysis, and for giving me a reason to continue through the hard times.

TABLE OF CONTENTS

Page

Page

Page

Page

Page

Page

Page

LIST OF FIGURES

Figure Page

Figure Page

Figure Page

Figure Page

Figure Page

Figure Page

LIST OF TABLES

1. INTRODUCTION

The Standard Model is a theoretical framework that describes fundamental particles and their interactions. The first ingredient is the Glashow-Salam-Weinberg (GSM) model, developed in the early 1960s, which unifies the electromagnetic and weak forces. [1] This model was extended between 1970 and 1973 to include the strong force, [2] giving rise to the Standard Model.

The Standard Model has been a great success since its inception. Several new particles were predicted and discovered in the early years of its development. In the 1970s, the charm quark (1974), the τ lepton (1975), and the bottom quark (1977) were discovered. Most impressively, the W and Z bosons were predicted by the GSM model, and then subsequently discovered in 1983 after a twenty year search at the *Organisation Européenne pour la Recherche Nucléaire* (known as *CERN* for historical reasons) located in the environs of Geneva, Switzerland. More recently in 1995, the top quark was observed at the Tevatron collider at the Fermi National Accelerator Laboratory in Batavia, Illinois (Fermilab). Finally, in 2000, the τ neutrino was observed at Fermilab. Only the Higgs boson remains to be observed of all the fundamental particles of the Standard Model. At all energies within our reach, to all levels of precision so far measured, the Standard Model has held up.

The Standard Model must, however, eventually fail. This is primarily because the Standard Model does not describe gravitational interactions. As particle accelerators reach higher and higher energies, they probe physics at increasingly shorter length scales. The Planck scale, the energy at which all four fundamental forces are expected to unify, and quantum gravity is

expected to be important, is given by: $M_{Planck} = \sqrt{\hbar c/G} \approx 1.2 \times 10^{16}$ TeV. This corresponds to a length of 1.6×10^{-35}m.

In addition to problems with high energy due to gravitational effects, there are other concerns regarding the Standard Model and reasons to believe that it may be incomplete. Some of these are enumerated below:

1. 19 independent free parameters (29 if one includes massive neutrinos to explain neutrino oscillations) which must be determined empirically,
2. three generations of leptons and hadrons instead of just one, and mixing between generations,
3. the preponderance of matter over anti-matter in the universe,
4. "dark" matter, and
5. cosmic inflation.

Discrepancies in the Standard Model will be found through precision measurements of electroweak parameters, discovery of new particles such as supersymmetric partners of existing particles, or failure to observe expected particles such as the Higgs boson.

These are all still possible at the Tevatron. The Tevatron, currently operating at 2 TeV, has only collected a small fraction of its total expected luminosity. The Tevatron has delivered more than 2 fb^{-1} already, and is expected to deliver roughly three times this luminosity in the remaining operation of Run II. [3] The Tevatron has already successfully provided the first precision measurements of many observables related to the top quark, and these measurements are expected to become more precise as the more data is collected. Single top production has recently been observed, and it is not unthinkable that the Higgs boson will be observed using the full luminosity of Run II if its mass is within reach of the Tevatron.

The Large Hadron Collider (LHC), currently under construction at CERN, is expected to operate at ∼14 TeV. This is far below the Planck scale, but an order of magnitude above the center of mass energy available at the Tevatron. The higher energies of the LHC extend the reach of searches for new particles, while higher luminosities make it possible to also perform precision measurements providing stringent tests of the Standard Model.

The top quark mass is a particularly important electroweak precision observable for a number of reasons. Firstly, within the Standard Model radiative corrections depend quadratically on the top quark mass. This immediately impacts the ability to test the Standard Model. Secondly, models both within and beyond the Standard Model predict Higgs boson masses which depend very strongly on the top quark mass. Thirdly, the top quark is massive enough that, if non-Standard Model particles do indeed exist, it is possible that they could be top decay daughters. Beyond these considerations, the top quark mass is one of the 19 free parameters of the Standard Model, so it is an important quantity in its own right.

This thesis describes a measurement of the top quark mass done using a matrix element method on data collected at the DØ experiment at Fermilab. Proton-antiproton ($p\overline{p}$) collisions produce top quarks in top-antitop ($t\overline{t}$) pairs at the Tevatron (at $\sqrt{s} = 1.96$ TeV in Run II). The channel in which one top quark decays to a b-quark and a W boson, which then decays to a lepton (e, μ, τ) and a neutrino, and the other top quark decays to a b-quark and a hadronically-decaying W boson, is called the *lepton + jets* channel. Approximately 425 pb^{-1} of data in the e+jets and μ+jets channels (τ+jets events with leptonically-decaying τs are included) were used in the analysis presented here.

A brief overview of top quark physics is given in Chapter 2. Chapter 3 describes the accelerator complex and DØ detector. The reconstruction of physics events detected in the DØ detector, as well as the method of selecting events for the top mass analysis, are described in Chapter 4. The matrix element method and calibration of the method, as well as final results,

are described in Chapters 5 and 6. Finally, conclusions and prospects for future improvements in the matrix element method are given in Chapter 7.

2. THEORETICAL OVERVIEW

Firstly, a brief overview of the Standard Model is given. Next, the production and decay channels of $t\bar{t}$ pairs are described. Then the importance of measuring the top quark mass is discussed. Lastly, since the top quark mass can be defined many ways, a brief explanation of the quantity that is actually being measured is given.

2.1 The Standard Model

The Standard Model is a theory of interacting quantum fields, the excitations of which appear as particles within the theory. There are two classes of particles contained in the Standard Model: *fermions* and *bosons*. Fermions have half-integer spins and obey the Pauli exclusion principle, which states that no two fermions can occupy the same state. Bosons, on the other hand, are characterized by zero or whole-integer spins and do not obey the Pauli exclusion principle.

All matter is made up of fermions, and, in the Standard Model, all forces are mediated by bosons. Fermions interact with bosons, changing their momenta in such a way that overall momentum is conserved. This is essentially equivalent to the action of forces on fermions.

There is a different type of boson, called a *gauge boson*, corresponding to each of the fundamental forces. The *photon* mediates the electromagnetic force, W and Z bosons mediate the weak force, and *gluons* mediate the strong force. Gravity is not included in the Standard Model, but it is hypothesized to be carried by a spin-2 boson called a *graviton*.

There are two types of fermions, *leptons* and *quarks*, and 3 generations of each. The leptons are characterized by neutral or integer charge, while quarks have fractional charges of $+1/3$ or $-2/3$ the charge of an electron. The charge and weak isospin structure (explained later) of

fermions are summarized in Table 1. Each charged fermion also has an oppositely-charged anti-matter partner. In addition, fermions can have either left- or right-handed chirality (indicated by subscript L or R in Table 1) with the exception of neutrinos for which right-handed chirality has not been observed.

isospin multiplet			T	T_z	Q
$\binom{\nu_e}{e}_L$	$\binom{\nu_\mu}{\mu}_L$	$\binom{\nu_\tau}{\tau}_L$	1/2	$\binom{+1/2}{-1/2}$	$\binom{0}{-1}$
ν_{eR}	$\nu_{\mu R}$	$\nu_{\tau R}$	0	0	0
e_R	μ_R	τ_R	0	0	-1
$\binom{u}{d}_L$	$\binom{c}{s}_L$	$\binom{t}{b}_L$	1/2	$\binom{+1/2}{-1/2}$	$\binom{+2/3}{-1/3}$
u_R	c_R	t_R	0	0	+2/3
d_R	s_R	b_R	0	0	-1/3

Table 1
The weak-isospin structure of the fermions in the Standard Model. T is the weak isospin, T_z is the z-component of the weak isospin, and Q is the electric charge.

Below is a brief explanation of the Standard Model, including gauge symmetries, spontaneous symmetry breaking, and the generation of mass for fermions and the massive gauge bosons.

2.1.1 Lagrangians and Gauge Transformations

Lagrangians are constructed in the Standard Model consisting of terms corresponding to quantum fields and their interactions. As will be seen below, Lagrangians are constructed in such a way that they are invariant under various gauge transformations. The particular types of gauge transformations arise from empirical observation, and the observations that particular attributes of groups of particles such as charge, isospin, lepton number, etc., are conserved in particular types of interactions. Conserved quantities are seen to arise naturally from symmetries in the transformations.

2.1.2 Quantum Electrodynamics

The following is based on material in Ref. [4], [5], and [6]. The gauge transformation corresponding to the electromagnetic force is U(1), the single-parameter unitary group transformation. This is simply a phase factor $e^{-i\alpha(x)}$, so the U(1) transformation may be written as

$$\psi \rightarrow \psi' = e^{-i\alpha(x)}\psi \tag{2.1}$$

To each gauge transformation corresponds a distinct gauge field, in this case a massless photon. With the electromagnetic energy tensor, $F_{\mu\nu}$, defined as

$$F_{\mu\nu} = \partial_\mu A_\nu - \partial_\nu A_\mu, \tag{2.2}$$

A_μ, the gauge field, can undergo the following U(1) gauge transformation:

$$A_\mu(x) \rightarrow A'_\mu(x) = A_\mu(x) + \frac{1}{e}\partial_\mu \alpha(x). \tag{2.3}$$

with no change to the physical $F_{\mu\nu}$. The constant e is the electric charge, a free parameter of the Standard Model that must be fixed empirically. The gauge field A_ν represents the electromagnetic field. Since the electromagnetic field possesses only 2 independent components, the gauge freedom manifest in Eqn. 2.3 is a reflection of A_μ having two components more than needed to describe the electromagnetic field.

In the absence of matter, the Lagrangian may be written as

$$\mathcal{L}^{EM}_{gauge} = -\frac{1}{4}F_{\mu\nu}F^{\mu\nu}. \tag{2.4}$$

With the covariant derivative defined as

$$D_\mu \psi = (\partial_\mu + \mathrm{i}eA_\mu)\psi, \tag{2.5}$$

the QED Lagrangian with massless fermions may be written as

$$\mathcal{L}^{EM} = \overline{\psi}\mathrm{i}\gamma^\mu D_\mu \psi - \frac{1}{4}F_{\mu\nu}F^{\mu\nu}. \tag{2.6}$$

2.1.3 Lepton Interactions

Requiring invariance of the Lagrangian under local SU(2) gauge transformations gives rise to the weak force. The SU(2) transformation may be written as

$$\mathbf{U} = \exp(-\frac{\mathrm{i}}{2}\boldsymbol{\tau}\cdot\boldsymbol{\alpha}(x)) \tag{2.7}$$

where $\boldsymbol{\alpha}$(x) is a vector function and $\boldsymbol{\tau}$ are the 3 Pauli spin matrices, the generators of SU(2). SU(2) acts on the lepton SU(2) doublet:

$$\mathbf{L} = \begin{pmatrix} \nu_e \\ e_L \end{pmatrix},$$
$$\mathbf{L} \rightarrow \exp(-(\mathrm{i}/2)\boldsymbol{\tau}\cdot\boldsymbol{\alpha}(x))\ \mathbf{L}, \tag{2.8}$$

while right-chiral leptons, e_R, are singlets and unaffected by SU(2) transformations:

$$\mathbf{R} = e_R, \tag{2.9}$$

$$\mathbf{R} \rightarrow \mathbf{R}, \tag{2.10}$$

Note that two other generations of leptons exist, μ and τ leptons. They are omitted here to simplify the explanation.

U(1) acts on both the isospin doublet and singlet, so it can be written as:

$$\begin{pmatrix} L \\ R \end{pmatrix} = \begin{pmatrix} \nu_e \\ e_{\mathrm{L}} \\ e_{\mathrm{R}} \end{pmatrix} \rightarrow \begin{pmatrix} e^{-i\beta(x)/2} & 0 & 0 \\ 0 & e^{-i\beta(x)/2} & 0 \\ 0 & 0 & e^{-i\beta(x)} \end{pmatrix} \begin{pmatrix} \nu_e \\ e_{\mathrm{L}} \\ e_{\mathrm{R}} \end{pmatrix}. \tag{2.11}$$

The combined SU(2)×U(1) transformations for right- and left-handed leptons are then

$$\begin{aligned} \mathbf{L} \rightarrow \mathbf{L}' &= e^{-\mathrm{i}\beta(x)/2}\mathbf{U}(x)\mathbf{L}, \\ e_R \rightarrow e'_R &= e^{-\mathrm{i}\beta(x)}e_R. \end{aligned} \tag{2.12}$$

The combination of SU(2)×U(1) gives electroweak interactions. The Lagrangian for electroweak interactions is similar to that of the pure QED Lagrangian, but there are now 3 additional gauge fields corresponding to each of the three Pauli spin matrices. These are W_μ^i ($i = 1, 2, 3$). The single gauge field corresponding to the U(1) group (A_μ before) is now B_μ. The Lagrangian for electroweak interactions with leptons will be described first, then electroweak interactions with quarks.

Electroweak Interactions with Leptons

SU(2) only acts on the left-handed doublet, so the covariant derivative has different definitions for left- and right-handed leptons:

$$D_\mu \mathbf{L} = \left(\partial_\mu - \frac{\mathrm{i}g}{2}\tau \cdot W_\mu + \frac{\mathrm{i}g'}{2}B_\mu\right)\mathbf{L}, \tag{2.13}$$

$$D_\mu \mathbf{R} = (\partial_\mu + \mathrm{i}g' B_\mu)\,\mathbf{R}. \tag{2.14}$$

An extra term arises in the transformation of the gauge field (compare with Eqn. 2.3) due to the non-Abelian nature of the SU(2) symmetry,

$$W^i_\mu(x) \rightarrow W^{i'}_\mu(x) = W^i_\mu(x) - \frac{1}{g}\partial_\mu \theta^i(x) - \varepsilon^{ijk}\theta^j W^k_\mu. \tag{2.15}$$

The SU(2) and U(1) gauge-field tensors, $F^i_{\mu\nu}$ and $G_{\mu\nu}$, respectively, are defined as

$$F^i_{\mu\nu} = \partial_\mu W^i_\nu - \partial_\nu W^i_\mu + g\varepsilon^{ijk} W^j_\mu W^k_\nu, \tag{2.16}$$

$$G_{\mu\nu} = \partial_\mu B_\nu - \partial_\nu B_\mu. \tag{2.17}$$

With these definitions, the electroweak Lagrangian with massless leptons

$$\mathcal{L}^{EW} = \mathrm{i}\overline{\psi}\gamma^\mu D_\mu \psi - \frac{1}{4}(F^i_{\mu\nu}F^{i,\mu\nu} + G_{\mu\nu}G^{\mu\nu}). \tag{2.18}$$

is invariant under SU(2) $\times$ U(1).

The charged $W^\pm$ bosons arise solely from SU(2) and are defined as follows:

$$W^\pm_\mu = \frac{1}{\sqrt{2}}(W^1_\mu \mp \mathrm{i}W^2_\mu) \tag{2.19}$$

The Z boson and normal electromagnetic gauge boson, A^{EM}_μ, are linear combinations of W^3_μ and B_μ:

$$Z_\mu = \cos\theta_W W^3_\mu - \sin\theta_W B_\mu \tag{2.20}$$

$$A^{EM}_\mu = \sin\theta_W W^3_\mu - \cos\theta_W B_\mu \tag{2.21}$$

The Weinberg angle, θ_W, is a new parameter of the Standard Model that is fixed empirically. It is defined as

$$\tan\theta_W = \frac{g'}{g}. \tag{2.22}$$

Thus, there are 2 free parameters of the Standard Model corresponding to the electroweak force for massless fermions: the electroweak lepton coupling constants, g and g'.

Quark interactions

SU(2) acts on the quark SU(2) doublet,

$$\mathbf{L_q} = \begin{pmatrix} u_L \\ d_L \end{pmatrix}. \tag{2.23}$$

SU(2) singlets are right-handed quarks, u_R and d_R.

The transformations for quarks under SU(2)×U(1) are

$$\begin{aligned} \mathbf{L_q} \rightarrow \mathbf{L'_q} &= e^{-\mathrm{i}\beta(x)/3}\mathbf{U}(x)\mathbf{L_q}, \\ u_R \rightarrow u'_R &= e^{-4\mathrm{i}\beta(x)/3}u_R, \\ d_R \rightarrow d'_R &= e^{2\mathrm{i}\beta(x)/3}d_R, \end{aligned} \tag{2.24}$$

and the covariant derivatives are

$$
\begin{aligned}
D_\mu u_L &= \left(\partial_\mu + \frac{\mathrm{i}g}{2}\tau\cdot W_\mu + \frac{\mathrm{i}g'}{6}B_\mu\right)u_L,\\
D_\mu d_L &= \left(\partial_\mu + \frac{\mathrm{i}g}{2}\tau\cdot W_\mu + \frac{\mathrm{i}g'}{6}B_\mu\right)d_L,\\
D_\mu u_R &= \left(\partial_\mu + \frac{2\mathrm{i}g'}{3}B_\mu\right)u_R,\\
D_\mu d_R &= \left(\partial_\mu - \frac{\mathrm{i}g'}{3}B_\mu\right)d_R.
\end{aligned}
\tag{2.25}
$$

Now the electroweak Lagrangian with massless quarks is:

$$
\mathcal{L}^{EW} = \mathrm{i}\overline{u}\gamma^\mu D_\mu u + \mathrm{i}\overline{d}\gamma^\mu D_\mu d - \frac{1}{4}(F^i_{\mu\nu}F^{i,\mu\nu} + G_{\mu\nu}G^{\mu\nu}). \tag{2.26}
$$

In addition to forming isospin SU(2) doublets, quarks possess *color* as well. SU(3) is the symmetry underlying quantum chromodynamics (QCD), and acts on SU(3) triplets with 3 colors for each quark:

$$
\boldsymbol{q} = \begin{pmatrix} q_R \\ q_G \\ q_B \end{pmatrix}. \tag{2.27}
$$

The QCD Lagrangian can be found in most quantum field theory textbooks:

$$
\mathcal{L}^{QCD} = -\frac{1}{2}\mathrm{Tr}\left[G_{\mu\nu}G^{\mu\nu}\right] + \mathrm{i}\Sigma_{k=1}^{n_f}\overline{q}_k\gamma^\mu D_\mu q_k, \tag{2.28}
$$

where

$$
\begin{aligned}
G_{\mu\nu} &= \partial_\mu G_\nu - \partial_\nu G_\mu - \mathrm{i}g_s\left[G_\mu, G_\nu\right] \\
D_\mu q_k &= (\partial_\mu + \mathrm{i}g_s G_\mu) q_k \\
G_\mu &= \sum_{a=1}^{8} G_\mu^a \lambda^a/2,
\end{aligned}
\tag{2.29}
$$

and n_f is the total number of quark flavors.

The 8 λ^as are the Gell-Mann matrices of SU(3), similar to the Pauli spin matrices of SU(2). G_μ^a are gluons which mediate the strong force. Note that the Lagrangian being used contains massless particles. Masses will be introduced through the Higgs mechanism (Sect. 2.1.5). Including massless quarks adds a single parameter to the Standard Model, the strong coupling constant g_s.

2.1.4 Cabibbo-Kobayashi-Maskawa matrix

There are also 3 generations of quarks, so there are 3 SU(2) quark doublets

$$
\begin{aligned}
\mathbf{L_{q_1}} &= \begin{pmatrix} u_L \\ d_L \end{pmatrix} \\
\mathbf{L_{q_2}} &= \begin{pmatrix} c_L \\ s_L \end{pmatrix} \\
\mathbf{L_{q_3}} &= \begin{pmatrix} t_L \\ b_L \end{pmatrix}
\end{aligned}
\tag{2.30}
$$

and 6 SU(2) quark singlets for the right-handed quarks, u_R, d_R, c_R, s_R, t_R, and b_R. Weak decays between quarks are flavor changing, and the strengths of the couplings between flavors can be determined experimentally. A 3×3 matrix called the Cabibbo-Kobayashi-Maskawa (CKM)

matrix, $\mathbf{V_{CKM}}$, contains this information. The element $V_{qq'}$ is the probability for transition from quark q to another quark q'.

$$\begin{pmatrix} V_{ud} & V_{us} & V_{ub} \\ V_{cd} & V_{cs} & V_{cb} \\ V_{td} & V_{ts} & V_{tb} \end{pmatrix} \tag{2.31}$$

The condition of unitarity reduces the number of independent parameters from $2N^2$ to $N^2 = 3^2 = 9$ parameters. Three of the nine parameters of the CKM matrix are phases which are absorbed into the gluon fields. A fourth parameter is unobservable. This leaves four parameters in the Standard Model associated with the CKM matrix.

2.1.5 The Higgs mechanism

Mass is generated for 3 of the 4 gauge bosons associated with SU(2)×U(1) through the introduction of a complex scalar Higgs doublet:

$$\mathbf{\Phi} = \frac{1}{\sqrt{2}} \begin{pmatrix} \phi^+ \\ \phi^0 \end{pmatrix} = \begin{pmatrix} \phi_3 + i\phi_4 \\ \phi_1 + i\phi_2 \end{pmatrix}$$

where $\phi_1, \ldots, \phi_4$ are real. This doublet behaves under covariant differentiation in the same way as the SU(2) doublet,

$$D_\mu \mathbf{\Phi} = \left(\partial_\mu - \frac{\mathrm{i}g}{2} \boldsymbol{\tau} \cdot \boldsymbol{W_{\mu\nu}} - \frac{\mathrm{i}g'}{2} B_\mu \right) \mathbf{\Phi}, \tag{2.32}$$

giving the following Lagrangrian:

$$\mathcal{L} = (D_\mu \mathbf{\Phi})^\dagger (D_\mu \mathbf{\Phi}) + m^2 \mathbf{\Phi}^\dagger \mathbf{\Phi} - \lambda (\mathbf{\Phi}^\dagger \mathbf{\Phi})^2 - G_e (\overline{\mathbf{L}} \mathbf{\Phi} \mathbf{R} + \overline{\mathbf{R}} \Phi^\dagger \mathbf{L}). \tag{2.33}$$

The last term contains interactions between the scalar field and fermions. It can be written as

$$\mathcal{L}^{Higgs}_{\text{coupling}} = y_e \overline{\mathbf{L}} \mathbf{\Phi} e_R + y_u \overline{\mathbf{L}}_{\mathbf{q}} i\tau_2 \mathbf{\Phi}^* u_R + y_d \overline{\mathbf{L}}_{\mathbf{q}} \mathbf{\Phi} d_R + h.c., \tag{2.34}$$

where h.c. denotes all Hermitian conjugate terms. y_e, y_u, and y_d are the Yukawa coupling constants.

The first three terms can be written as

$$\mathcal{L}^{Higgs}_{\mathbf{\Phi}} = (D_\mu \mathbf{\Phi})^\dagger (D^\mu \mathbf{\Phi}) - V(\mathbf{\Phi}), \tag{2.35}$$

with the potential energy defined as

$$V(\mathbf{\Phi}) = \frac{m^2}{2\phi_0^2} [\mathbf{\Phi}^\dagger \mathbf{\Phi} - \phi_0^2]^2, \tag{2.36}$$

and

$$\phi_0 = \frac{m}{\sqrt{2\lambda}}. \tag{2.37}$$

For a normal scalar field, with $m^2 > 0$, the lowest energy state corresponds to $\phi = 0$. If, instead, $m^2 < 0$, the lowest energy state is at

$$(\mathbf{\Phi}^\dagger \mathbf{\Phi})_0 = -\frac{m^2}{\lambda}, \tag{2.38}$$

then the ground state is degenerate in the four-dimensional space of the scalar fields. Choosing a gauge breaks the symmetry. For convenience, a gauge is chosen for which $\phi^+ = 0$ and ϕ is real, giving

$$\mathbf{\Phi}_{\text{ground}} = \begin{pmatrix} 0 \\ \phi_0 \end{pmatrix}. \tag{2.39}$$

The vacuum expectation value (VEV) of the Higgs field is the value of the scalar field at which the minimum in $V(\mathbf{\Phi}^\dagger \mathbf{\Phi})$ occurs,

$$\langle 0|\mathbf{\Phi}|0\rangle = \frac{1}{\sqrt{2}}\begin{pmatrix} 0 \\ \upsilon \end{pmatrix}, \tag{2.40}$$

with $\upsilon = \sqrt{m^2/\lambda}$.

Physical Higgs fields are perturbations about $|\mathbf{\Phi}| = \upsilon/\sqrt{2}$. The reparametrized Higgs field is then

$$\Phi' = U(\zeta)\mathbf{\Phi} = \frac{1}{\sqrt{2}}\begin{pmatrix} 0 \\ \upsilon + \eta(x) \end{pmatrix}, \tag{2.41}$$

and $\mathcal{L}^{Higgs}_{\text{coupling}}$ can now be written as

$$\begin{aligned} \mathcal{L}^{Higgs}_{\text{coupling}} &= \frac{\eta(x)}{\sqrt{2}}[y_e \overline{e}'_L e'_R + y_u \overline{u}'_L u'_R + y_d \overline{d}'_L d'_R] \\ &+ \frac{\upsilon}{\sqrt{2}}[y_e \overline{e}'_L e'_R + y_u \overline{u}'_L u'_R + y_d \overline{d}'_L d'_R] + h.c. \end{aligned} \tag{2.42}$$

The first set of terms is due to interactions between the fermions and the shifted Higgs field which has acquired a mass. The latter terms proportional to $\upsilon/\sqrt{2}$, the Higgs VEV, correspond to massive fermions (e.g. $m_e = y_e \upsilon/\sqrt{2}$). Thus the introduction of the Higgs field has given mass to the previously massless fermions.

The $W^{\pm}$ and Z bosons also acquire mass through the Higgs mechanism. The $(D_\mu \mathbf{\Phi}')$ term in $\mathcal{L}_{\mathbf{\Phi}}^{Higgs}$ gives two new terms corresponding to massive vector mesons

$$\mathcal{L}_{VMM} = M_W^2 W_\mu^+ W^{-\mu} + \frac{1}{2} M_Z^2 Z_\mu Z^\mu, \tag{2.43}$$

where the $W^{\pm}$ and Z are as defined in Eqns. 2.19 and 2.21.

M_W^2 and M_Z^2 are given by

$$M_W^2 = g^2 \upsilon^2/4 \tag{2.44}$$

$$M_Z^2 = (g^2 + g'^2)\upsilon^2/4 \tag{2.45}$$

thus allowing a prediction of the ratio M_W/M_Z expected to arise from the Higgs mechanism. This introduces a single parameter to the Standard Model, either M_W or M_Z. There are also 10 parameters corresponding to 3 lepton masses, 6 quark masses, and the Higgs mass, M_H. This brings the total number of parameters for the Standard Model to 18. The 19th parameter is a CP-violating parameter associated with strong interactions.

2.2 Top Quark Production and Decay

Production rates

At the Tevatron, the top quark is produced by $p\overline{p}$ collisions predominantly in pairs through the QCD processes $q\overline{q} \rightarrow t\overline{t}$ and $g\overline{g} \rightarrow t\overline{t}$ (see Figures 2.1 and 2.2). A large fraction of the partons' momenta is needed for $t\overline{t}$ production – threshold production of $t\overline{t}$ pairs requires ~18% of the total center of mass energy at $\sqrt{s} = 1.96$ TeV. For this reason, about 85% of the $t\overline{t}$ pairs produced at the Tevatron are produced through the first process, $q\overline{q} \rightarrow t\overline{t}$. [13]

A technique called *resummation* is used to apply corrections to the leading order (LO) cross-section calculation for soft gluon emission. These corrections take the form of logarithms, $[\ln^l(x_{th})/x_{th}]_+$, where x_{th} is a kinematic variable that indicates the distance from threshold, and $l \leq 2n-1$ for the order α_s^l correction. The calculations done in Ref. [14] have NNLO corrections done to next-to-next-to-leading logarithm (NNLL) accuracy, and include some additional NNNLL corrections. These results, along with earlier NLO calculations, are shown in Table 2. The NNLO-NNNLL cross-section for $m_t = 175$ GeV/c^2, $\sqrt{s} = 1.96$ TeV is:

$$\sigma(p\overline{p} \rightarrow t\overline{t}) = 6.77 \pm 0.42 \text{ pb} \tag{2.46}$$

These are calculated using the CTEQ6M PDF set. (PDFs, or *parton distribution functions*, are used to describe the probability to find particular partons within a hadron.)

The large systematic uncertainty is due primarily to choice of kinematic variables used in calculations. The kinematic calculations are constrained by energy and momentum conservation, so, in addition to the momenta of the incoming partons, only one 4-momenta in the final state (containing a top and anti-top quark) is required to calculate all kinematic variables. One can use the momentum of one of the top quarks (single particle inclusive, or *1PI*, kinematics), or alternately the momentum of the $t\overline{t}$ pair (invariant mass, or *PIM*, kinematics). Clearly, the cross-section should not depend on the choice of kinematics, so it is expected that the results for all kinematics choices would be identical if all NNNLL corrections were applied.

Top quarks are also generated singly, mediated by virtual s-channel and t-channel W-bosons. The combined cross-section for single-top production is only 3 pb at 1.96 TeV [15], however. It is also somewhat difficult to distinguish the single-top signal from a larger background.

Order	σ (pb)		
	$\mu = m_t/2$	$\mu = m_t$	$\mu = 2m_t$
NLO	6.79	6.54	5.85
NNLO-NNNLL + ζ 1PI	7.01	7.21	7.04
NNLO-NNNLL + ζ PIM	6.08	6.33	6.29

Table 2
The $\overline{\text{MS}}$ top quark production cross-section in $p\overline{p}$ collisions at the Tevatron for $m_t = 175$ GeV/c^2 with different choices of renormalization scales.

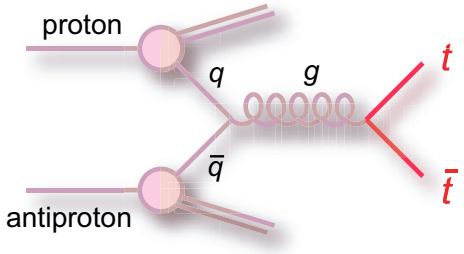

Fig. 2.1. Feynman diagram for $p\overline{p} \to q\overline{q} \to t\overline{t}$

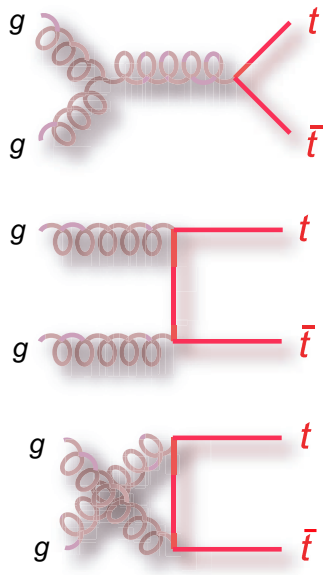

Fig. 2.2. Feynman diagrams for $gg \to t\overline{t}$

Top quark decay channels

Top quarks decay to Wb, Ws, and Wd final states. The decay to the latter two final states is expected to be suppressed relative to $t \to Wb$ because $|V_{ts}|^2$ and $|V_{td}|^2$ are small compared to $|V_{tb}|^2$ [16]. If V_{tb} is fixed to 1, lattice QCD calculations give $|V_{td}| = .0074 \pm .0008$, and the ratio $|V_{td}/V_{ts}| = .208^{+.008}_{-.006}$. Independent measurements of relative branching fractions $R = \mathcal{B}(t \to Wb)/\mathcal{B}(t \to Wq)$ give $|V_{tb}| > 0.78$ [17], [18]. An earlier result which constrains $|V_{tb}|$ from electroweak data allowing V_{tb} to float freely gives $V_{tb} = 0.77^{+.18}_{-.24}$ [19].

The two W bosons from the t and $\bar{t}$ decays then decay either leptonically or hadronically. The branching ratio for W decay to a lepton and neutrino is $\mathcal{B}(W \to l\nu_l) = 1/3$, with equal probabilities for $l = e, \mu, \tau$. Hadronically, W decays to a quark-antiquark pair with $\mathcal{B}(W \to q_1\overline{q}_2) = 2/3$. The top quark and subsequent W decay are shown diagrammatically in Figure 2.3.

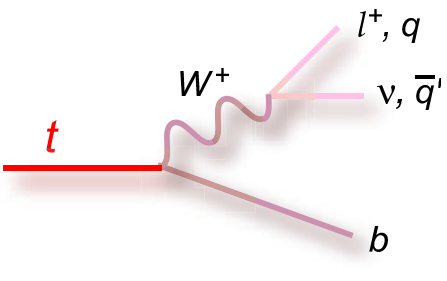

Fig. 2.3. Feynman diagrams for top quark decay to final state particles

Since W-bosons can decay either leptonically or hadronically, the $t\bar{t}$ decay channels are classified according the W-decay. The three channels are *dilepton*, *lepton+jets*, and *all-jets*.

Dilepton channel The decay channel in which both W bosons decay leptonically is known as the dilepton (ll) channel. The branching ratio for $t\bar{t} \to b\bar{b}l_1l_2\nu_{l_1}\nu_{l_2}$, where $l = e, \mu$, is

$2/9 \times 2/9 = 4/81 \approx 4.9\%$. τ leptons decay leptonically with a branching ratio of approximately $9/25$, so the total dilepton branching ratio is

$$\left[\frac{2}{9} + \left(\frac{1}{9}\right) \cdot \left(\frac{9}{25}\right)\right]^2 \approx 6.9\%. \tag{2.47}$$

The dilepton channel has less hadronic activity, since there are only 2 b-quarks in the final state. This reduces somewhat the systematic uncertainty due to uncertainties in the jet energy scale. This advantage is offset, however, by the presence of two neutrinos in the final state for which momenta can not be directly measured, and also by the poor statistics relative to the other two decay channels.

All-jets/all-hadronic channel The branching ratio for W-bosons to decay hadronically is $2/3$. Thus, the total branching ratio for $t\bar{t} \to b\bar{b}q_1\overline{q}_2q_3\overline{q}_4$ is $2/3 \times 2/3 = 4/9 \approx 44.4\%$. τ leptons decay hadronically with a branching ratio of $\sim$16/25, so the total all-jets branching ratio is

$$\left[\frac{2}{3} + \left(\frac{1}{9}\right) \cdot \left(\frac{16}{25}\right)\right]^2 \approx 54.4\%. \tag{2.48}$$

This is clearly the best channel with respect to statistics, and all particles in the final state can be detected as jets in the detector. This channel suffers the most, however, from uncertainties in jet energy scale, and also a very large background.

Lepton+jets channel Lepton+jets events provide the best compromise between the various factors of statistics, signal-to-background ratio, and resolution of measurements for final-state particles. The branching ratio for $t\bar{t} \to b\bar{b}l\nu_l q_1\overline{q}_2$, $l = e, \mu$, without contribution from τ decays, is $2/9 \times 2/3 = 4/27 \approx 14.8\%$. Including τ lepton decays, the total branching ratio is

$$2 \times \left[\frac{2}{9} + \left(\frac{1}{9}\right) \cdot \left(\frac{9}{25}\right)\right] \times \left[\frac{2}{3} + \left(\frac{1}{9}\right) \cdot \left(\frac{16}{25}\right)\right] \approx 38.6\%. \tag{2.49}$$

Branching ratios are shown graphically in Figure 2.4.

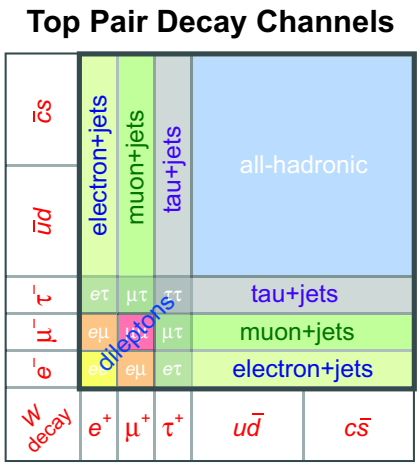

Fig. 2.4. Branching ratios for various decay channels of $t\bar{t}$ pairs

2.3 Importance of Top Quark Mass

The importance of having a precise measurement of the top quark mass for electroweak precision calculations, as well as an input to models beyond the Standard Model, are explained in the following sections.

2.3.1 Electroweak precision physics

As described in Sections 2.1.2 through 2.1.5, there are 19 SM parameters. 16 of these are from fermion masses and mixings, and 1 is the Higgs boson mass. This leaves 3 parameters. The set of observables commonly used for the remaining 3 parameters is: [16]

1. α, the *fine structure constant*, determined from the $e^{\pm}$ anomalous magnetic moment, the quantum Hall effect, and other measurements,

2. G_F, the *Fermi constant*, determined from muon lifetime measurements, and

3. M_Z, the Z boson mass, measured directly at LEP and at the Tevatron.

From these three observables, with known values of the observables m_t and M_H, $\sin^2\theta_W$ and M_W can be calculated. Since M_H is not yet known, values of $\sin^2\theta_W$ extracted from Z-pole observables and neutral-current processes are used to constrain M_H. But the value of $\sin^2\theta_W$ and constraints on M_H depend upon the renormalization scheme used. (See Section 2.4 for a discussion about renormalization schemes.)

The top quark mass enters into the renormalization scheme through loop corrections. The particular scheme described here is the on-shell renormalization scheme, motivated by its use in QED and extended to the non-Abelian SU(2)×U(1) by Sirlin [9] in 1980. The summary given here follows from the review by Hollick [11].

The on-shell scheme redefines M_W^2 so that it is corresponds to the on-shell value actually measured in experiment. This can be seen as a modification to the bare mass, M_{W0}. M_{W0} is obtained in terms of G_F using the tree-level diagram for muon decay, shown in Figure 2.5.

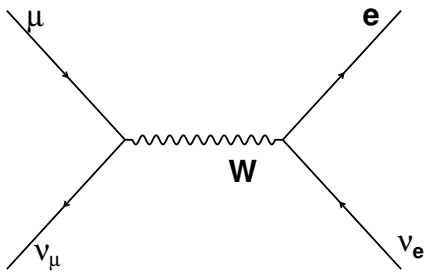

Fig. 2.5. μ decay tree-level diagram

The tree-level muon decay process gives for the μ lifetime:

$$\tau_\mu^{-1} = \frac{\alpha^2}{384\pi} m_\mu^5 \left(1 - \frac{8m_e^2}{m_\mu^2}\right) \frac{1}{M_W^2 \sin^2\theta_W}. \tag{2.50}$$

Comparison with the low-energy Fermi model result

$$\tau_\mu^{-1} = \frac{G_F^2}{192\pi^3} m_\mu^5 \left(1 - \frac{8m_e^2}{m_\mu^2}\right) \tag{2.51}$$

gives the tree-level definition of M_W^2 in terms of G_F:

$$M_W^2 \sin^2\theta_W = \frac{\pi\alpha}{\sqrt{2}G_F}. \tag{2.52}$$

The on-shell renormalization scheme redefines M_W^2 to be

$$M_W^2 \sin^2\theta_W = \frac{\pi\alpha}{\sqrt{2}G_F}\frac{1}{1-\Delta r}, \tag{2.53}$$

where Δr contains all the radiative corrections, and α and G_F are obtained from experiment. The quantity $\sin^2\theta_W$ remains as defined,

$$\sin^2\theta_W = 1 - \frac{M_W^2}{M_Z^2}. \tag{2.54}$$

Δr can be shown to be [16]

$$\Delta r = \frac{\hat{\Sigma}^W(0)}{M_W^2} + \frac{\alpha}{4\pi\sin^2\theta_W}\left(6 + \frac{7 - 4\sin^2\theta_W}{2\sin^2\theta_W}\log(\cos^2\theta_W)\right). \tag{2.55}$$

The first term is the renormalized self-energy of the W boson, which contains loop corrections from all the particles of the model. $\sin^2\theta_W$ is itself a function of Δr:

$$\sin^2\theta_W = 1 - \frac{M_W^2}{M_Z^2} = \frac{1}{2}\left(1 - \sqrt{1 - \frac{4\alpha\pi}{\sqrt{2}G_F M_Z^2(1-\Delta r)}}\right), \tag{2.56}$$

so Δr must be solved by iteration. The leading term arising from the W boson self-energy can be shown to be

$$\frac{\hat{\Sigma}^W_{ferm}(0)}{M_W^2} = (\Delta r)_{f\neq t} + (\Delta r)_{top} \tag{2.57}$$

$$(\Delta r)_{top} \approx -\frac{\alpha}{4\pi}\frac{3\cos^2\theta_W}{4\sin^2\theta_W}\frac{m_t^2}{M_W^2}. \tag{2.58}$$

The $(\Delta r)_{f\neq t}$ term contains only $\log(m_f)$ dependencies. So it is seen that the top quark mass enters into radiative corrections with a quadratic dependence, making it a very important parameter indeed for precision electroweak physics.

Note that the calculation of $\sin^2\theta_W$ and M_W depends upon the Higgs mass, M_H. Since this is not known, and $\sin^2\theta_W$ is known only approximately, Z-pole observables are used to calculate M_H. Due the logarithmic dependence on M_H, the value is only known approximately. The top quark mass is second only to the W boson mass as a source of errors in these calculations. The LEP Electroweak Working Group [12] gives the following for a fit of M_H using Run II Tevatron and LEP-II data:

$$M_H = 85^{+39}_{-28}\ \mathrm{GeV}/c^2. \tag{2.59}$$

2.3.2 The Top Quark and the Minimal Supersymmetric Standard Model

The Minimal Supersymmetric Standard Model (MSSM) is the minimal extension of the Standard Model, which predicts sypersymmetric partners of Standard Model particles. Within MSSM, there are two doublets of complex fields, leading to three Higgs particles. [20] The mass of

the lightest SM-like Higgs boson, m_h, is set by the quartic Higgs coupling, λ (see Section 2.1.5). At tree level, m_h is limited to be less than the Z mass,

$$m_h^2 \leq m_Z^2 \cos^2 2\beta, \tag{2.60}$$

where the angle β is a parameter of the two-Higgs-doublet model and characterizes the relative strengths of the couplings of the two Higgs to the b- and t-quarks. Radiative corrections to the quartic couplings give an increase in the SM-like Higgs boson mass [21]

$$m_h^2 \leq m_Z^2 \cos^2 2\beta + \frac{3}{\pi^2}\frac{m_t^4 \sin^4 \beta}{\upsilon^2} \log \frac{m_{\tilde{t}}}{m_t}, \tag{2.61}$$

which depends on the top quark mass, m_t, and the mass of the top squark, $m_{\tilde{t}}$, the supersymmetric partner of the top quark. (υ is the same Higgs expectation value defined in Sect. 2.1.5.) The very strong dependence on the top quark mass makes it a very important parameter in MSSM models.

2.4 Definition of Top Quark Mass

The effective strong coupling constant, $\alpha_s = g_s/4\pi$, depends on the renormalization scale, μ, in the following way: [16]

$$\begin{aligned}\alpha_s(\mu) = \frac{4\pi}{\beta_0 \ln(\mu^2/\Lambda^2)} \Bigg[1 - \frac{2\beta_1}{\beta_0^2} \frac{\ln[\ln(\mu^2/\Lambda^2)]}{\ln(\mu^2/\Lambda^2)} + \frac{4\beta_1^2}{\beta_0^4 \ln^2(\mu^2/\Lambda^2)} \\ \times \left(\left(\ln\left[\ln(\mu^2/\Lambda^2)\right] - \frac{1}{2} \right)^2 + \frac{\beta_2 \beta_0}{8\beta_1^2} - \frac{5}{4} \right) \Bigg],\end{aligned} \tag{2.62}$$

where the parameters $\beta_0 \cdots \beta_2$ depend on the numbers of quarks with mass less than the renormalization scale μ. Since the top quark mass is calculated with a running coupling constant,

the top quark mass also has a dependence on the renormalization scale. In addition, the top mass is calculated using perturbation theory:

$$m_t = A_1\alpha_s + A_2\alpha_s^2 + \cdots . \tag{2.63}$$

Divergences arise in the calculations of Feynman diagrams beyond leading order, and these must be regulated with a particular renormalization scheme. The modified minimal subtraction ($\overline{\text{MS}}$) scheme is the one most commonly used. Note that β_2 also depends on the renormalization scheme.

The actual physical mass is given by the pole in the quark propagator, and it is the pole mass that is measured and referred to for the remainder of this dissertation. The relation between the pole mass, m_t, and the $\overline{\text{MS}}$ mass, $\widehat{m_t}$, is: [16]

$$\widehat{m_t}(\mu = \widehat{m_t}) = m_t[1 - \frac{4}{3}\frac{\alpha_s}{\pi} + \mathcal{O}(\alpha_s^2)].$$

3. EXPERIMENTAL APPARATUS

The experimental apparatus includes the following:

1. the accelerator,
2. the DØ detector, and
3. triggering and data acquisition system.

3.1 Accelerator

The accelerator is described in detail in Ref. [43] and summarized briefly here. It consists of the *pre-accelerator*, the linear accelerator (*linac*), the *booster*, the *antiproton source*, the *main injector*, and the *Tevatron*. An overview of the accelerator complex is shown in Figure 3.1.

3.1.1 Pre-accelerator

The pre-accelerator produces negatively-charged hydrogen ions (H^-) and boosts them to an energy of 750 keV for insertion into the linac. H^- ions are easily produced with a surface plasma H^- source (SPS). Typical SPS devices [44] produce H^- ions through the interaction of plasmas, consisting of protons, ionized hydrogen molecules, or heavier positive ions, with cathode surfaces contained absorbed hydrogen atoms. H^- ions are pulled through the plasma from the cathode to the anode for collection. The magnetron source used at the Tevatron is a particular type of SPS.

The Tevatron's 50 mA magnetron source, shown in Figure 3.2, consists of a central oval molybdenum cathode surrounded by a small ($\sim$1 mm) anode-cathode gap. The apparatus is

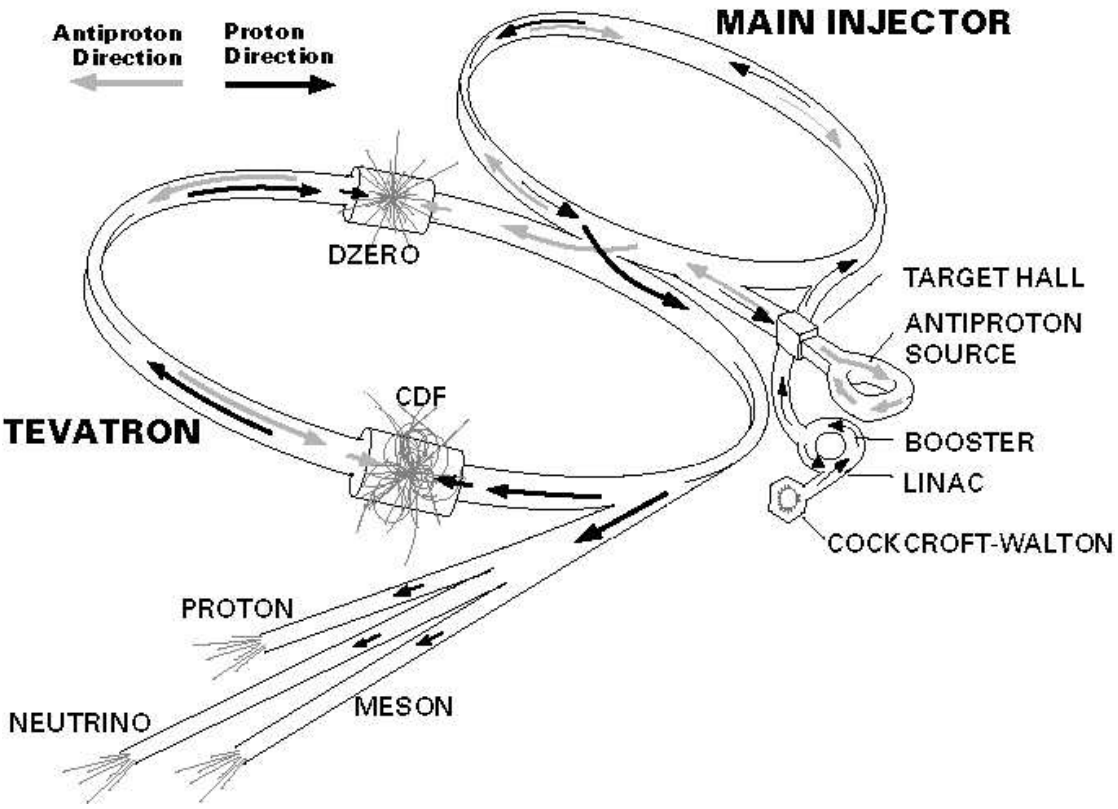

Fig. 3.1. Overview of Fermilab accelerator complex

immersed in a constant magnetic field, aligned to confine the plasma to circulate around the cathode. Some of the H^- ions are removed through the anode aperture. These are accelerated to 18 keV through the extractor plate. A supply of hydrogen gas is provided at one end of the magnetron at a pressure of a few hundred millitorr. The gas supply, plasma discharge, and H^- extraction voltage are all pulsed at 15 Hz to match the linac cycle frequency. Cesium is used to lower the work function of the cathode, thus raising the efficiency of the H^- extraction process. [42]

Prior to insertion into the linac, H^- ions are accelerated to 750 keV with a generator of a Cockcroft-Walton design, designated a "Haefely" after its Swiss manufacturer. This is a device which charges capacitors in parallel using an AC voltage source, and then discharges them in

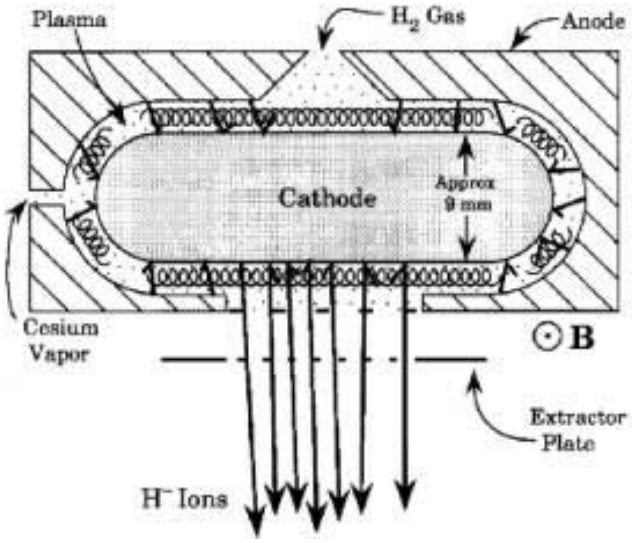

Fig. 3.2. Schematic view of typical H^- magnetron source

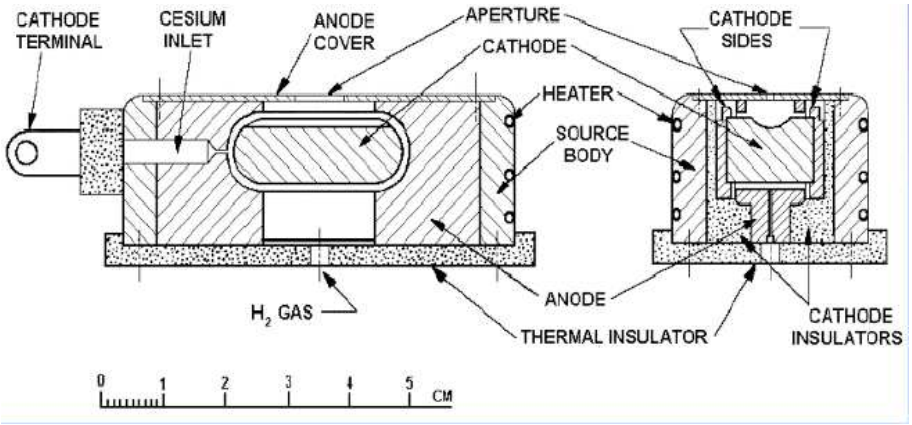

Fig. 3.3. Schematic view of Fermilab's H^- magnetron source

series through the use of diodes. A simple 3-stage diode voltage multiplier is shown in Figure 3.4. The Haefely generators used in Fermilab's pre-accelerators use 5 stages, giving a factor of 10 increase in voltage to 750 kV. [45]

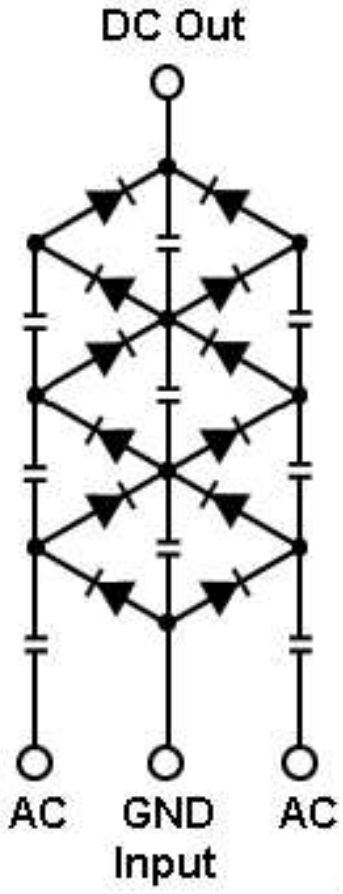

Fig. 3.4. Schematic diagram for a simple dual leg three-stage diode voltage multiplier. The second leg (mirror image of left-hand side on right-hand side) is used to obtain the same output voltage with less ripple.

3.1.2 Linac

The linac [45], [42] consists of five sections of Alvarez drift-tubes and a series of single side-coupled RF cavities. The Alvarez drift tubes are RF cavities made of steel and clad with copper. The side-coupled cavities are the same in principle as the Alvarez drift tubes, but have a different resonant frequency and an improved cavity design. In addition, a chopper and buncher serve to shape the beam to improve efficiency.

Alvarez drift-tube

Each of the first 5 RF tanks has a resonant frequency of 201.24 MHz, tuned by precisely varying the cavity volume and maintaining tank temperatures within a tenth of a degree Fahrenheit. Tanks are driven by 5 MW power amplifiers which operate in 400 μs pulses phase-locked to the booster (and pre-accelerator) cycle of 15 Hz. Within each steel tank is a series of drift tubes separated from each other by gaps. The lengths of drift tubes and gaps are such that particles are accelerated by the electric field while traversing the gaps, and shielded from the reverse electric field while traveling through the drift tube. The 5 tanks total approximately 70 m in length, with the lengths increasing from 6 to 27 cm to accommodate longer lengths traveled by the particles between gaps. Particles leave the last RF cavity with energies of $\sim$116 MeV.

The 750 keV chopper and buncher

Particles arriving too late will be accelerated less than desired, and will arrive at the next gap even later. These particles are eventually lost. Particles arriving early are slowed as desired, but particles arriving too early can be slowed too much and will also be lost. In the end, only about 105°/360°, or 25-30%, of protons would end up being accelerated if injected as a continuous beam. To improve transport efficiency, beams coming out of the pre-accelerator are first "chopped" by the *chopper* into lengths from 10 to 57 μs (2000-11000 RF cycles). This is done using a pair of conducting plates to periodically energize an electric field transverse to the beam direction, causing a deflection of the beam into a carbon disk. Particles are then bunched together in the *buncher* to get as many particles as possible within the 105 degree ($\sim$1.45 ns) window. The buncher is a single-gap RF cavity operating at the same frequency as the rest of the linac, with a phase chosen so that particles arriving early are decelerated, while particles arriving late are accelerated. This is illustrated in Figure 3.5.

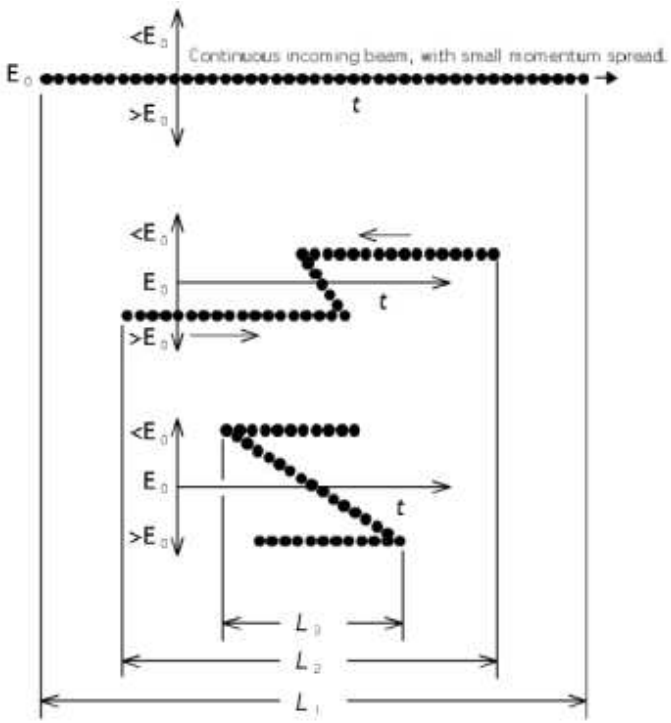

Figure 4.30

Fig. 3.5. Bunching particles into 105° bunches. Particles arriving late are accelerated by the positive electric field (shown as $> E_0$), while particles arriving early are decelerated ($< E_0$), resulting in a smaller bunch of particles.

Side-coupled RF cavities

The original linac had nine Alvarez drift tubes and no side-coupled RF cavities. In 1993, an upgrade increased the linac output energy from 200 to 400 MeV. This was done within the same linac enclosure by replacing the last four Alvarez drift tubes with seven newly-designed RF cavities. These cavities operate at a larger RF frequency and have external cavities coupled to the main RF cavity, resulting in a higher concentration of electric field lines in the gap (see Figure 3.6) and a three-fold increase in accelerating gradient to 7.5 MV/m. This allows an acceleration from 116 MeV to 400 MeV in the same linear space as before.

Each of the seven modules uses a 12 MW 805 MHz klystron power supply to drive four sections of 16 cells each with a 125 μs pulse. The klystron pulses repeat at a 15 Hz rate, synchronized with the booster and pre-accelerator. Since the RF frequency is four times larger, only every fourth RF cycle ("bucket") contains bunched particles. These tanks are known as "klystron tanks".

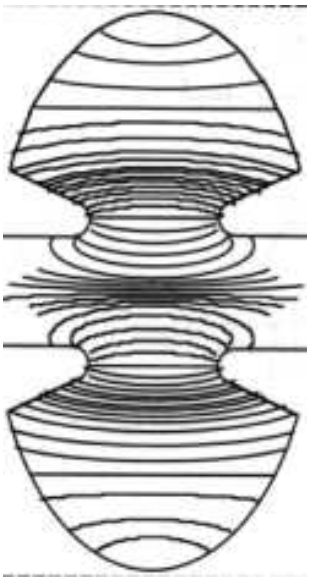

Fig. 3.6. Increase in axial electric field due to side-coupled cavity.

3.1.3 Booster

After passing through the linac, 400 MeV H^- ions are transferred to the booster. [49] The booster is the first synchrotron, consisting of a sequence of dipole and quadrupole magnets and 17 RF cavities in a 151 m circle that accelerate particles from 400 MeV to 8 GeV.

After leaving the linac, H^- ions are first sent through the 400 MeV chopper, a device similar to the 750 MeV chopper that is used to control the beam intensity. Next, H^- ions pass through the phase matching section. This is necessary to remove the 805 MHz RF structure from

the linac, and to reduce the momentum spread. The phase-matching section uses quadrupole magnets and RF manipulation to shape the beam and give it the proper phase characteristics. H^- ions are then merged with protons circulating in the booster using dipole magnets. Finally, the combined beam is passed through carbon foil to strip electrons.

The RF cavities are used to form bunches and to accelerate the beam. Bunches occur naturally as the RF fields are brought into phase. During injection, the RF fields are phased in the various cavities such that there is no net acceleration. Once the beam in the booster is filled, the RF cavities are brought into phase over the next 100-200 μs. The RF frequency is maintained at the 84^{th} harmonic of the booster beam revolution frequency. As the RF fields are brought into phase, 84 discrete bunches of protons are formed around the ring, each bunch occupying a discrete RF "bucket".

As protons are accelerated, it is necessary to increase the RF frequency so that protons continue to experience the maximum electric field when crossing the RF cavity gaps. The RF frequency is increased from 37.86 MHz at injection to 52.81 MHz at extraction. The beam is continuously steered and focused as it traverses the ring. This is done with the dipole and quadrupole magnets, which use sinusoidal electrical current from a solid-state power supply system for excitation. Magnetic strengths vary from 740 gauss at injection to 7000 gauss at extraction.

The beam has a cycle frequency of 15 Hz, synchronized with the pre-accelerator and linac. Beam injection lasts for the first 2 ms of the cycle. Acceleration lasts $\sim$29 ms, and extraction takes place over the final $\sim$2.5 ms. Since the cycle period is 66.7 ms, the booster functions for approximately one-half of the cycle.

3.1.4 Main injector

The second synchrotron is the main injector [50], a roughly elliptical ring of several kilometers circumference containing 20 RF cavities for particle acceleration and a series of dipole and quadrupole magnets for beam focusing and steering. The main injector does the following:

1. accelerates protons from the booster (or antiprotons from the antiproton source) from 8 GeV to 150 GeV for injection into the Tevatron, and

2. accelerates protons to 120 GeV for use by the antiproton source in creating 8 GeV antiprotons.

The main injector also has uses for neutrino experiments, but these will not be discussed here.

The main injector is very similar in principle to the booster. The RF frequency ranges from 52.8 MHz at injection to 53.1 MHz at extraction. [53] Each of the 20 RF cavities is powered by two 150 kW tetrode amplifiers, and each cavity delivers 288 kW RF power to the beam for a total of 5.76 MW. [54]

For normal collider operations, the main injector is first filled with protons from the booster. Seven of the 84 8 GeV bunches of the booster are transferred in a single batch to the main injector, accelerated to 150 GeV, and then coalesced into a single superbunch. This superbunch is transferred to the Tevatron. The process is repeated until 36 proton bunches have been transferred to the Tevatron.

Then 8 GeV antiprotons are transferred from the antiproton source to the main injector. Four groups of antiprotons are transferred at a time, each group containing several bunches. These groups are coalesced into 4 bunches, accelerated to 150 GeV, and transferred to the Tevatron. This is done 9 times for a total of 36 antiproton bunches.

3.1.5 Antiproton Source

For antiproton production, a full batch of protons is accelerated to 120 GeV in the main injector. This beam is diverted to a nickel target, producing a shower of secondary particles. A dipole magnet acts on the resulting particles, bending the negative particles which have energies of 8 GeV into another line. This beam is sent to the debuncher.

Debuncher

When the debuncher receives antiprotons, the momentum spread is large. It is necessary to reduce this momentum spread prior to injection into the Tevatron. This is done through bunch rotation and adiabatic debunching.

There are eight RF cavities in the debuncher – the first six for bunch rotation, and the last two for debunching. Bunch rotation rotates the phases of bunches, giving a reduction in the momentum spread. After this is accomplished, the RF voltage on the first six cavities is dropped very quickly, while the voltage on the last two cavities is lowered over 60 ms to achieve debunching.

The debuncher has a larger circumference than the accumulator, and has 90 RF buckets while the accumulator has 84. A second RF system is used to maintain a suitable gap in the beam so that the entire beam can be transferred to the smaller accumulator. This system uses a 2.36 MHz RF wave to create a "bucket barrier" that excludes particles from occupying a 200 ns gap.

Accumulator

Unbunched 8 GeV antiprotons are extracted from the debuncher and injected into the accumulator. These antiprotons are placed in an orbit which is $\sim$80 mm outside the orbit of

antiprotons that may already exist in the accumulator. A 53 MHz RF system is used to capture the particles in 84 bunches. Then the beam is decelerated ∼60 MeV, moved to the end of the stack that already exists (still in a larger orbit), and the RF frequency is reduced to zero. A process of stochastic cooling is then used to slow individual groups of particles within the bunches until all bunches are in the same orbit as the original stack. This removes an additional ∼150 MeV from the beam. This process, which takes approximately 30 minutes, is repeated for hours or days until the desired stack of antiprotons in the accumulator is achieved.

3.1.6 *The Recycler*

The recycler [47] receives antiprotons from the antiproton source and acts as a storage ring. It is located along the ceiling of the tunnel of the main injector. The recycler uses stochastic cooling, similar to the accumulator, until the intensity reaches 200×10^{10} antiprotons in the recycler. At this point, stochastic cooling is inefficient and electron cooling is used to further cool the antiprotons. This works by transferring momentum from the antiprotons to relatively "cooler" electrons, which are driven at the same energy as the antiprotons and injected in a very concentrated beam on top of the antiprotons. The antiprotons transfer momentum to the electrons, giving cooled antiproton bunches. The electron beam is removed to recover the charge when cooling is complete. The recycler stores antiprotons until needed for injection into the Tevatron.

3.1.7 The Tevatron

The Tevatron [52] is a 1 km radius synchrotron that accelerates particles from 150 to 980 GeV. It uses RF frequencies from 53.103 to 53.104 MHz with 8 accelerating cavities. It is a superconducting magnet synchrotron, with all dipole and quadrupole magnets cooled to 4.6 K with liquid helium.

The Tevatron has 6 sectors, labeled A through F, each of which has 5 sections. The first section of each sector is straight. Two of these, BØ and DØ are the locations of proton-antiproton collisions and house the CDF (the Collider Detector at Fermilab) and DØ detectors respectively.

The Tevatron has 1113 RF buckets. When the protons are injected into the Tevatron, they are spaced 21 RF buckets (396 ns) apart. There are 3 trains of 12 bunches each, and there is a 139 bucket gap (2.617 μs) between each of them. Antiprotons have the same spacing, and occupy the same bucket at BØ and DØ where the CDF and DØ collision halls are located.

Devices called *separators* are used to create stable orbits for the protons and antiprotons so that they do not collide outside the two collision halls. Separators create electric fields, either horizontally or vertically aligned, at locations around the ring so that helical orbits are created. The protons and antiprotons are pulled apart as they pass through the separator. This is undone just prior to the beams entering the collision halls.

3.1.8 Shot Setup

There are 5 major steps to injecting protons and antiprotons into the Tevatron and preparing for a store. This is called the shot setup. The five steps are:

1. Proton/antiproton injection tune up.
2. Proton and antiproton injection.
3. Acceleration to 980 GeV.
4. Low β squeeze and begin colliding.
5. Scrape away beam halo.

During shot setup, a series of operation sequences are executed and signaled to the CDF and DØ control rooms. These sequences are described in the following shot setup steps:

Proton/Antiproton Injection Tune Up

Before injecting protons and antiprotons into the Tevatron, the injection lines must be tuned up to prevent excessive losses and to maintain bunch integrity. This is done first with protons, as beam is brought into the main injector, accelerated to 150 GeV, and transferred to the Tevatron through the normal sequence. The beam is aborted, and the quadrupole and dipole magnets are tuned to achieve the proper injection orbit. This is the *proton injection tune up*. Then, rather than using antiprotons to tune up the antiproton line, protons are injected into the Tevatron with the separator polarities reversed so that the protons are in the antiproton helical orbit. The protons are sent through the line normally used for antiproton injection in the reverse direction, and a tune up of the antiproton injection line is done. This is the *reverse injection tune up*.

Proton/Antiproton Injection

36 coalesced proton bunches are injection into the Tevatron, one bunch at a time, spaced 21 RF buckets apart. Three trains of 12 bunches each are injected with an abort gap of 139 buckets (see Section 3.1.7). This is the *inject final protons* sequence.

Then the sequence *setup pbar injection* takes place. This injects antiprotons with a 21 ns bucket spacing in 4 trains of 9 bunches each to the main injector, where they are accelerated to 150 GeV to match the protons in the Tevatron. Then they are coalesced and injected into the Tevatron. Each group of four coalesced bunches are placed in 4 RF buckets using the scheme described above. This is done until 36 bunches are injected into the Tevatron.

Acceleration to 980 GeV

The sequence *prepare to ramp* takes the injection lines out of injection mode. The sequence *accelerate* accelerates the beam to 980 GeV by ramping dipole and quadrupole magnets simultaneously.

Low β squeeze

Once the beam has been accelerated to 980 GeV, *goto low beta* reduces the amplitude of the beam oscillations to bring the protons and antiprotons closer to each other at the interaction region of both detectors. Finally, *initiate collisions* removes the electric fields from the separators near the collision halls, allowing collisions to occur.

Scrape Away Beam Halo

As the beams are brought into collision, the beam halo must be reduced to avoid damage to detectors near the beam and also to reduce background. This is done with scrapers, which are simply steel blocks placed very near the beam to remove halo particles through interaction. A second block is used, slightly farther away from the beam, to block particles that are created through interaction of beam halo with the first block. This process is the *remove halo* sequence. When this is done, the final sequence is *HEP store*. Luminosity monitoring begins as does the physics store.

3.2 Overview of the DØ Detector

The DØ detector [33] is a multipurpose collider detector designed to detect the particles arising from the proton-antiproton collisions occurring at the DØ section of the Tevatron. It consists of 3 major systems:

1. a central tracker immersed in a 2 T magnetic field

2. a sampling calorimeter

3. a muon spectrometer

Figure 3.7 gives an overview of the detector. The three systems are described in more detail in the following subsections.

3.2.1 Coordinate System

The Cartesian coordinate system is used to describe the four-momenta of particles arising from $p\overline{p}$ collisions. The z-axis is aligned along the beam axis, with the positive z-direction along the proton beam. The y-axis points vertically upward, and the x-axis points horizontally toward the center of the Tevatron ring. The ϕ and θ angles describe, respectively, the azimuthal and polar angles, with θ=0 along the beam pipe. When polar coordinates are used, r is the transverse distance, defined as

$$r = \sqrt{x^2 + y^2}. \tag{3.1}$$

A useful parameter for physics analyses is the pseudorapidity, η, defined as

$$\eta = -\ln\ tan\frac{\theta}{2}. \tag{3.2}$$

This is a convenient parameter for hadron colliders because the multiplicity of high energy particles is approximately constant in rapidity. Rapidity distributions are also invariant under Lorentz boosts in the z-direction.

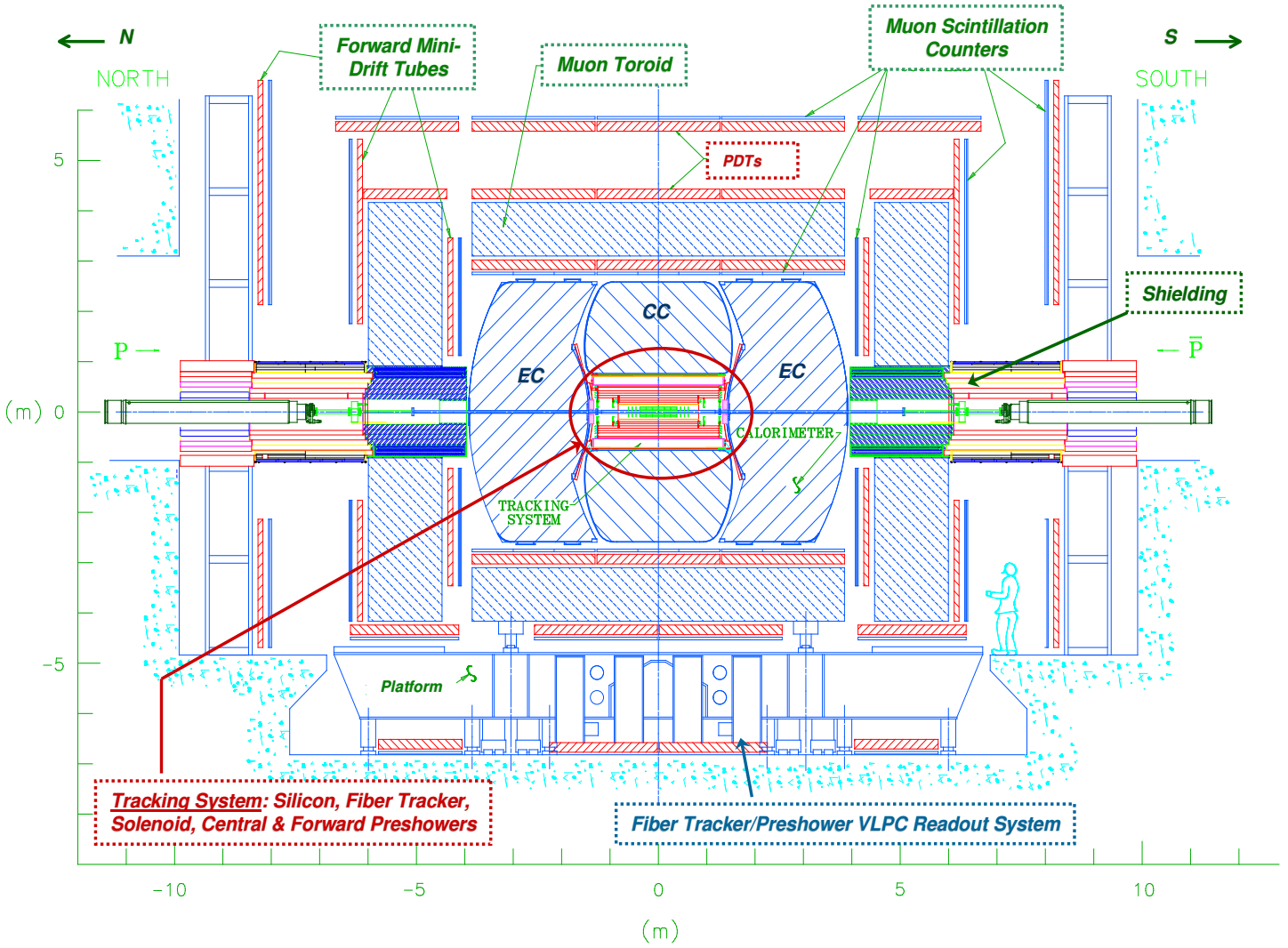

Fig. 3.7. Cross-section of the DØ Detector.

In $p\overline{p}$ collisions, an individual parton's longitudinal momentum is not known. For this reason, analyses usually work with transverse momenta. Transverse momentum is defined to be

$$p_T = p \sin\theta. \tag{3.3}$$

Similarly, transverse energy is defined as

$$E_T = E \sin\theta. \tag{3.4}$$

It is assumed that the transverse momentum of the $p\overline{p}$ system is essentially zero.

The beam bunch length is about 30 cm in z, so collisions do not necessarily occur at the center of the detector. It is therefore necessary to distinguish between "detector η", which is measured assuming a particle trajectory from the center of the detector, and "physics η", measured with respect to the point along the z-axis where the collision occurred. Unless otherwise noted, all η values should be taken to be detector η.

3.2.2 Luminosity System

The luminosity monitor (LM) [55] is used to accurately determine the luminosity of the Tevatron collider at the DØ interaction region. The LM detectors consist of scintillation detectors mounted on the endcap cryostats which house the end calorimeters (see Section 3.2.4) at $z = \pm 140cm$. The scintillators within each detector are arranged in a vertical plane, perpendicular to the beam direction, and are arranged in wedges segmented in ϕ as shown in Figure 3.8. There are 24 wedges in either of the two LM detectors. The detectors are 15 cm long and cover the pseudorapidity range $2.7 < |\eta| < 4.4$.

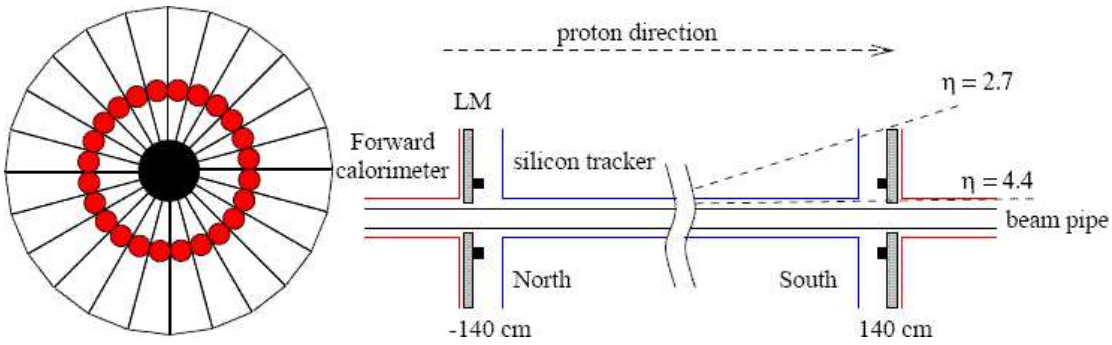

Fig. 3.8. Luminosity detector with photomultiplier tubes.

The luminosity is calculated using the following:

$$\mathcal{L} = \frac{R}{\epsilon A \sigma_{inel}},$$

where R is the event rate. ϵ is related to the *emittance*, which describes the beam quality. A is related to the amplitude function, which is related to the focusing of the beam. The inelastic cross-section, σ_{inel}, is obtained by measuring directly σ_{total} and $\sigma_{elastic}$, and taking the difference

$$\sigma_{inel} = \sigma_{total} - \sigma_{elastic}.$$

The total cross-section can be obtained from event rates. The optical theorem can be used to obtain

$$\sigma_{total} = \frac{16\pi}{1+\rho^2} \frac{1}{R_{el} + R_{inel}} \left(\frac{\mathrm{d}R_{el}}{\mathrm{d}t} \right)_{t=0},$$

where $\rho = \frac{\mathrm{Re}F(0)}{\mathrm{Im}F_0}$ is the ratio of the real to the imaginary part of the forward scattering amplitude, and R_{el} and R_{inel} are the elastic and inelastic event rates, respectively. The variable t is the Mandelstam variable, $t = -2k^2(1 - \cos\theta)$. The elastic cross-section is also determined experimentally.

3.2.3 Central Tracking System

The central tracking system measures the momentum, direction, and the sign of the electric charge for charged particles produced in a collision. A solenoid provides a nearly uniform 2 T magnetic field parallel to the beam axis. Charged particles leave a pattern of "hits" in the layers of the tracking detectors, and these hits are used to reconstruct a curved trajectory in 3-dimensional space. The curvature of the track gives the momentum and the sign of electric charge. The components of the central tracking system are:

1. the silicon microstrip tracker,

2. the central fiber tracker,

3. the solenoid, and

4. the forward and central pre-showers.

A cross-section of the central tracking region is shown in Figure 3.9.

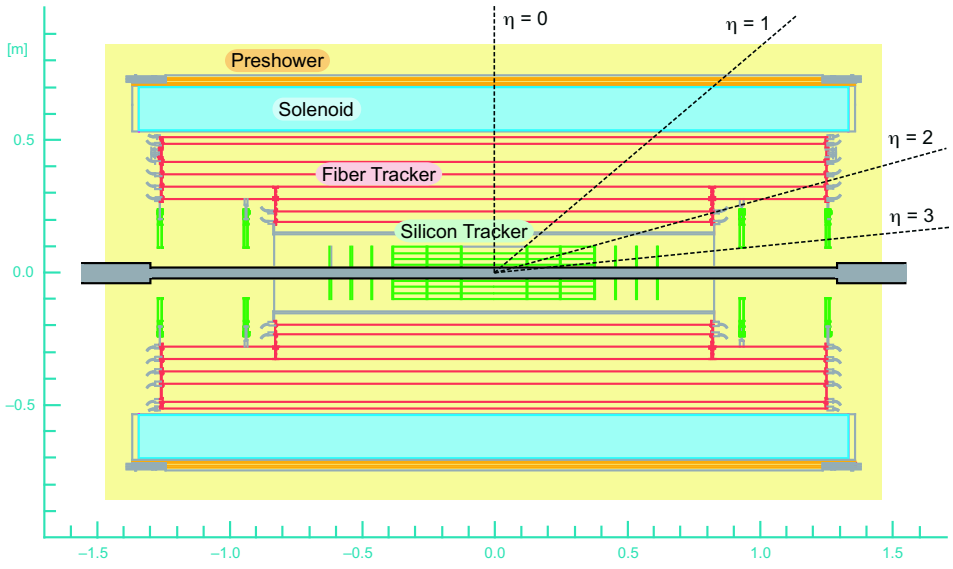

Fig. 3.9. Cross-section of the central tracking region at DØ.

Silicon Microstrip Tracker

The silicon microstrip tracker (SMT) [56] is a silicon detector which uses reverse-biased p-n junctions for charged particles detection. When a particle passes through the semiconductor material, electrons and holes are created which can be used to signal the incidence of the particle.

The SMT consists of three modules: six barrels instrumenting the central detector along the z-axis, twelve "F-disks" inserted vertically along the barrels, and four "H-disks" covering the

forward ($|\eta| \geq 2$) regions. A 3-dimensional representation is shown in Figure 3.10. A cross-section is shown in Figure 3.11. Barrels are used to measure the $r - \phi$ coordinate, while disks are used for $r - z$ and $r - \phi$.

Barrels and disks have 300 μm n-type silicon wafers onto which narrow p-type strips are mounted. Some wafers have n^+-type strips on the reverse side, stereoscopically aligned at 90° or 2° relative to the p-type strips to give measurement precision along the z-axis of 35 μm and 450 μm, respectively. For this reason, some double-sided barrels also allow $r - z$ measurements. The inner four barrels each have four double-sided layers, while the outer two barrels have 2 double-sided layers and 2 single-sided layers. The layers are spaced to achieve an axial position resolution of 10 microns. F-disks are made of twelve double-sided wedge detectors with strips aligned at stereo angles of ±15°. H-disks are made of 24 single-sided wedge detectors glued back-to-back with strips aligned with stereo angles at ±7.5°.

The length of the barrel region is 76 cm, chosen because the beam bunches are distributed along the beam axis with a Gaussian distribution centered at the detector center with $\sigma_z = 30$ cm. The H disks provide coverage out to $|\eta| < 3$. There are almost 800,000 readout channels in all.

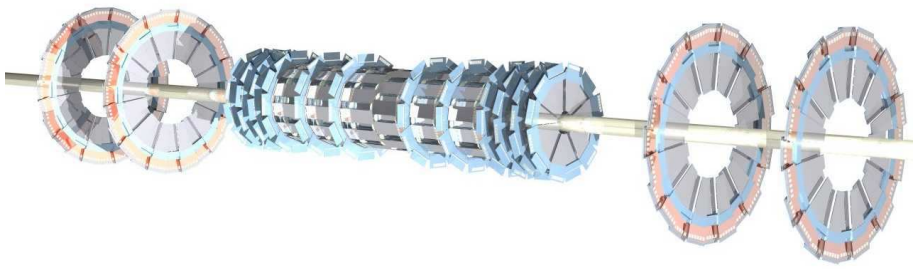

Fig. 3.10. 3D representation of the silicon microstrip tracker.

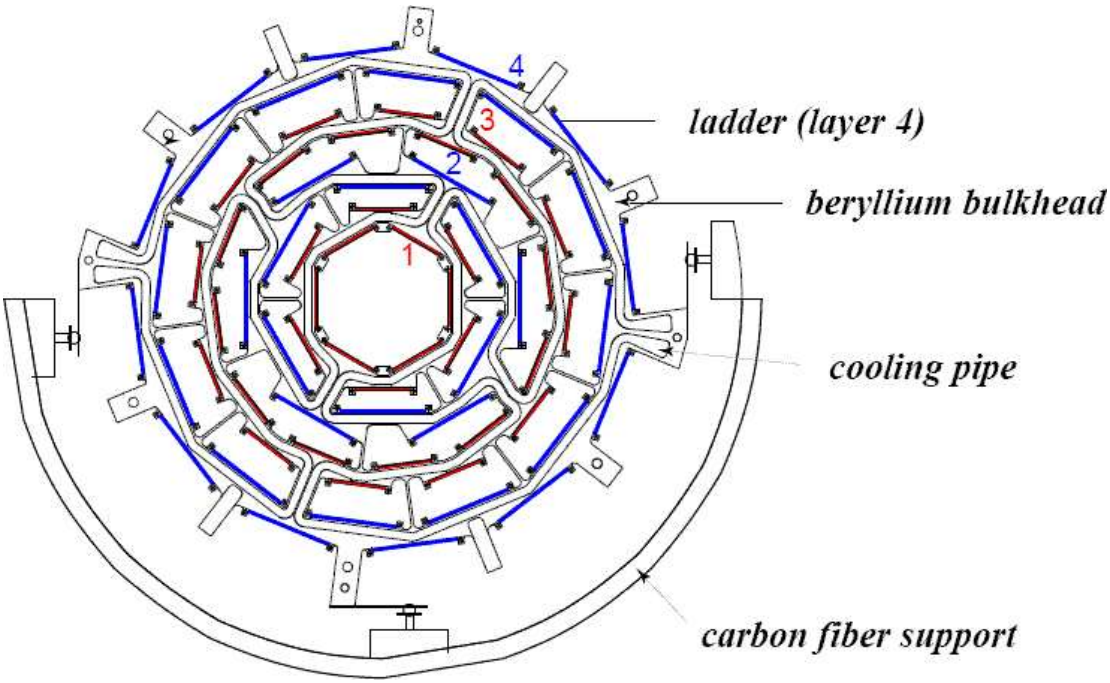

Fig. 3.11. Cross-section of a typical SMT barrel assembly.

Central Fiber Tracker

The central fiber tracker (CFT) [57] uses 835 μm scintillating fibers arranged in eight concentric cylinders occupying the radial space from 20 to 52 cm from the center of the beam pipe. The two innermost cylinders are 1.66 m long, while the outer six cylinders are 2.52 m long, giving coverage up to $|\eta| < 1.7$. The CFT has 77,000 readout channels.

The fibers are arranged in overlapping layers of doublets of fibers. The doublets consist of two layers each which overlap by half a fiber width. This gives a track cluster resolution of 100 μm per doublet layer. Each of the 8 cylinders has two doublet layers, with the outer doublet aligned at a stereo angle of $\pm 3^\circ$.

Charged particles passing through scintillating fibers cause the emission of light at 340 nm through rapid fluorescence decay. To increase the mean free path length of the resulting photons, fibers contain wave-shifting dye which absorb light at 340 nm and re-emit light at 530 nm. This

increases the propagation length to 4 m, which is more than enough to travel to the end of the scintillating fiber. One end of the fiber is optically connected to a clear fiber waveguide, which carries the light to visible light photon counters (VLPCs) where photons are converted to electronic pulses. The other end of the scintillating fiber is coated with aluminum to reflect the light to the other end of the fiber. The VLPCs are in a liquid Helium cryostat located directly beneath the DØ detector and operate at a temperature of 9 K.

Solenoid magnet

Momentum and charge sign measurements improved significantly in Run II with the addition of a highly uniform 2 T axial magnetic field. This is maintained with a superconducting solenoid surrounding the tracking region, fitting inside the central bore of the calorimeter. The solenoid is 2.73 m in length and 1.42 m in diameter. [60]

This magnetic field is maintained with a rather large 4825 A current. The solenoid must be superconducting to maintain such a large current. The solenoid is constructed of two types of superconducting high-purity aluminum stabilized multifilamentary Cu-NbTi Rutherford cable maintained at 4.7 K in a cryostat.

Preshower detectors

The addition of the 2 T solenoidal magnetic field for Run II introduced a significant amount of absorbing material in the core of the calorimeter. The extra material causes more energy loss, degrading electromagnetic energy resolution and particle identification. To offset this, additional scintillation detectors have been placed between the solenoid and calorimeter. These detectors consist of scintillating fibers similar to the CFT, except that fibers have triangular cross-sections to minimize the gaps between fibers. The detectors also contain lead absorbers of varying thickness to make the radiation length uniform for all particle trajectories.

The central pre-shower (CPS) [59] covers the range $|\eta| < 1.2$ and is mounted on the solenoid. It consists of three layers of fibers, with one layer parallel to the beam axis and the other two arranged at stereo angles of $\pm 20°$. The triangular cross-sections have 9 mm bases and 4.5 mm heights. The forward pre-shower (FPS) [58] covers the range $1.4 < |\eta| < 2.5$ and is mounted on the inner surface of the end calorimeter cryostat. It has two layers of scintillators at opposing stereo angles of 22°, a layer of lead with a thickness equivalent to 2 radiation lengths, and another two layers of scintillators with the same stereo angles.

3.2.4 Calorimeter

The calorimeter [61] measures the energy primarily of electrons, photons, taus, and hadronic particles. The calorimeter can also detect muons as minimum ionizing particles. [34] Particles entering the calorimeter are detected by the showers of electromagnetic energy which are deposited in and measured by the calorimeter.

The calorimeter is divided into a central calorimeter (CC), which covers up to $|\eta| < 1$, and two end calorimeters (EC) extending to $|\eta| \sim 4$. The section of the calorimeter closest to the interaction region, known as the electromagnetic (EM) section, is designed to measure electromagnetic particles. The outer two sections are the fine hadronic (FH) and coarse hadronic (CH) sections. Figure 3.12 shows one quadrant of the DØ calorimeter. [33]

The calorimeter consists of alternating layers of absorber plates and readout cells, with liquid argon in the gaps between them. To achieve the same energy response in each section of the calorimeter, different materials are used for absorber plates. The EM section uses 3-4 mm thick depleted uranium plates. The FH section uses 6 mm thick plates made of a uranium-niobium alloy. The CH section uses 46.5 mm copper plates in the the CC and stainless steel plates of the same size in the EC. The calorimeter is located within a cryostat that maintains the temperature at 80 K.

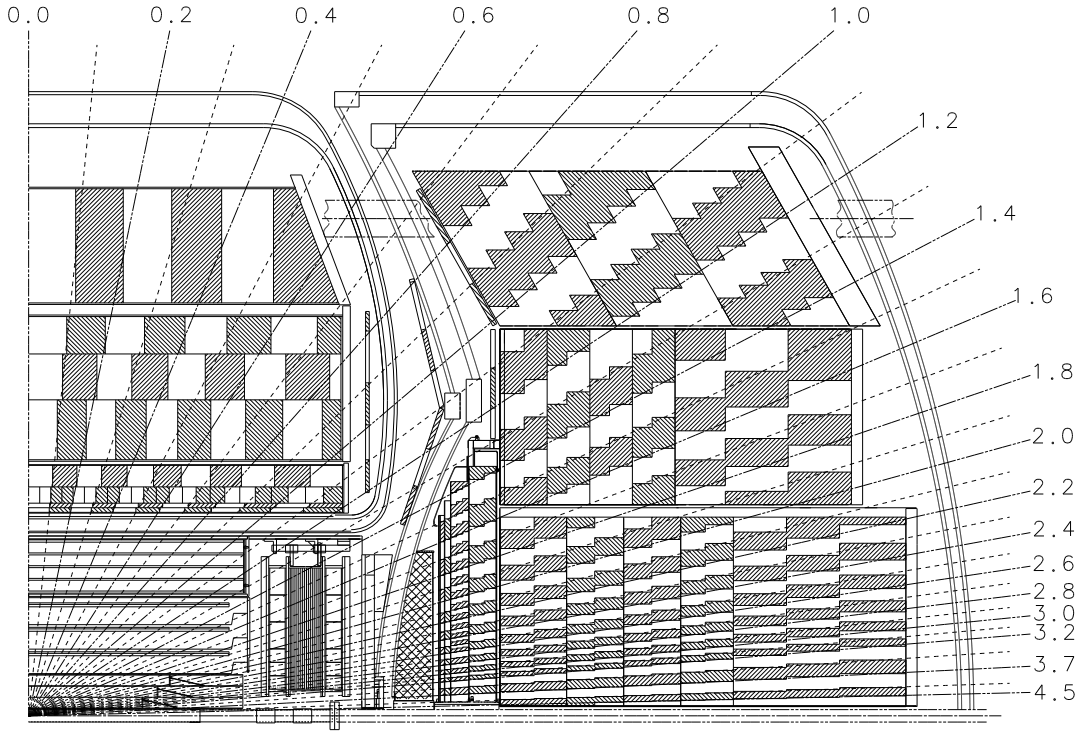

Fig. 3.12. Cross-section of a quarter of the calorimeter.

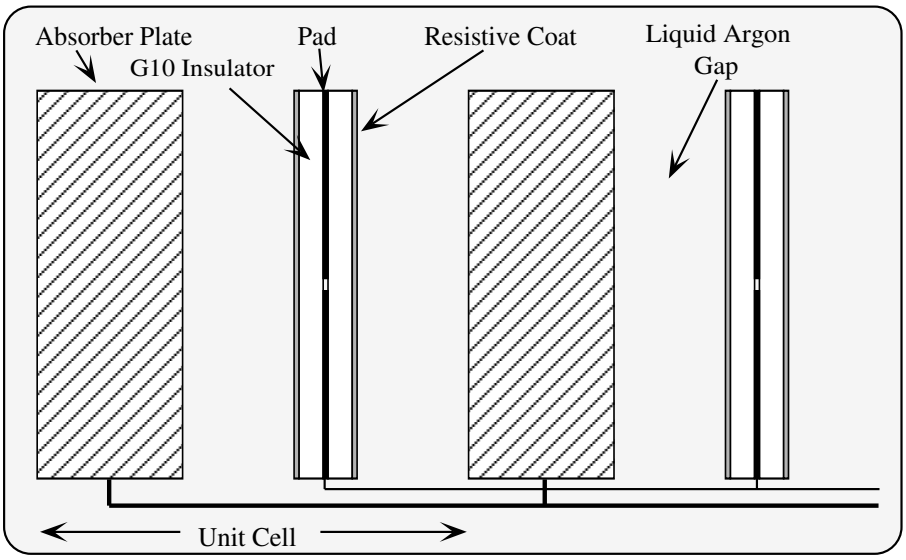

Fig. 3.13. Schematic view of a calorimeter cell.

When charged and neutral particles pass through metal plates in the calorimeter, they interact producing electromagnetic particles of smaller energy. These in turn interact in the metal plates, producing even more particles. The charged particles create ionization as they pass through the liquid argon, and this charge is detected by the readout cells. Figure 3.13 shows a typical readout cell.

Readout cells consist of copper readout pads mounted on insulating G10 and covered in a resistive epoxy. An electric field is created between the absorber plate and the readout pad by holding the absorber plate at ground and holding the resistive surface of the pad at $\sim$1.6 keV. The gap between absorber and readout is 2.3 mm, and the time for electrons to drift across this gap is approximately 450 ns. Thus the calorimeter readout is slow compared to other detectors.

The CC has 4 EM layers with 32 ϕ modules, and 4 FH layers and 1 CH layer with 16 ϕ modules each. This gives a coverage for readout cells of roughly $\Delta\eta \times \Delta\phi = 0.1 \times 0.1$, except for the third layer of the EM section. The third layer is where the shower maximum is expected

to occur and has a coverage area of 0.05×0.05 to improve precision. Jets typically have cone sizes of $\Delta R = \sqrt{\Delta\eta^2 + \Delta\phi^2} \approx 0.5$.

The pseudorapidity region $0.8 < |\eta| < 1.4$ is not well covered due to gaps between the EC and CC sections of the calorimeter. To improve the energy resolution in this region, a single-layered scintillation detector is installed in the gap between the EC and CC cryostats. This detector is called the inter-cryostat detector (ICD). The segmentation is the same as in the liquid argon calorimeter, $\Delta\eta \times \Delta\phi = 0.1 \times 0.1$

3.2.5 Muon System

Muons deposit very little energy in the calorimeter, making them difficult to detect and identify. A dedicated muon system is used, therefore, to identify muons, provide approximate locations, momenta, and charges of these muons, and allow for fast triggers based on the presence of high energy muons likely to have come from the interaction region. The muon system [62] is placed outside the calorimeter because all particles other than muons (and neutrinos, of course, which aren't detected in the detector at all) are typically absorbed in the DØ calorimeter. Since muons have larger masses than the other particles traversing the calorimeter, they interact primarily through ionization rather than *bremsstrahlung*. This is true for muons having energies up to a few hundred GeV, as shown in Figure 3.14 for muons in copper.

The muon system was designed to detect the ionization of muons as they pass through the detector. It is a spectrometer consisting of drift tubes, scintillators, and iron toroidal magnets. The central region covers up to $|\eta| < 1$, while the forward region covers $1 < |\eta| < 2$. Both regions have an A-layer of drift tubes and scintillators placed outside the calorimeter and inside the muon system toroids. Both regions also have B- and C-layer drift tubes and scintillators located outside the toroids. The drift tubes in the central region are housed in proportional drift tube (PDT) chambers, while those in the forward regions have Mini Drift Tube (MDT)

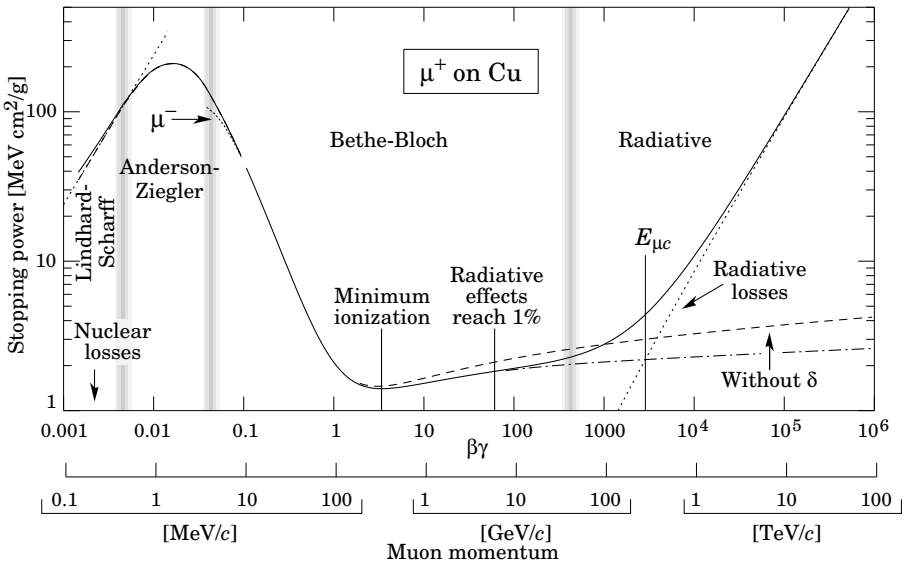

Fig. 3.14. -$\left\langle \frac{dE}{dx} \right\rangle$ as a function of muon momentum in copper.

chambers. These will be described in more detail in the following subsections. The muon system can be seen in Figure 3.7.

Toroid magnets

The central and forward regions each have dedicated 1.9 T toroidal magnets, as shown in Figure 3.15. The central region has a central iron (Fe) magnet known as the CF magnet, shown in Figure 3.16. It consists of a a steel yoke with 20 coils having 10 turns each. The forward regions each have an end iron (EF) magnet consisting of a single steel yoke with eight coils of eight turns each. The coils are all connected in series and powered by a 200 V power supply, which provides 1500 A in either direction for reversal of the magnetic field. The three magnets are mounted directly on the detector platform.

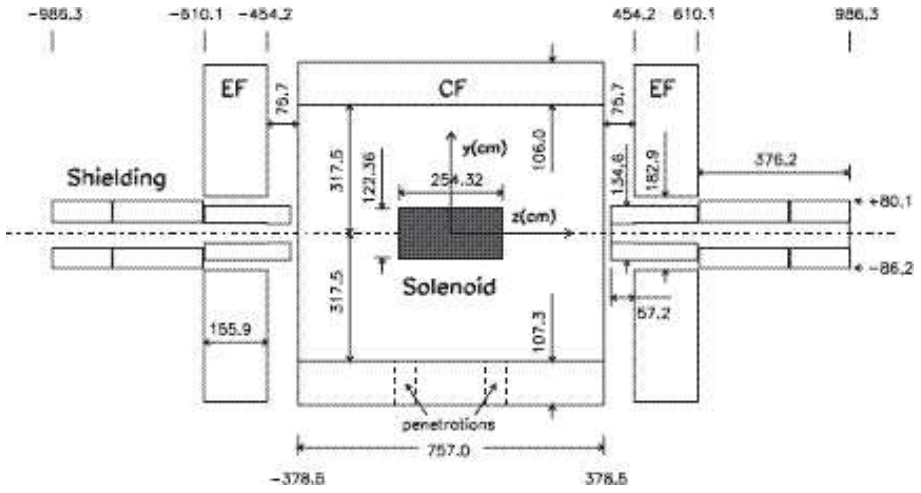

Fig. 3.15. Cross-sectional view of the magnet system.

The magnetic fields existing inside the toroids are shown in Figures 3.17 and 3.18. The magnetic field lines from the central solenoid magnet inside the calorimeter are returned by iron in the toroids and shielding assemblies as shown in Figure 3.19.

Scintillation Detectors

The central region $|\eta| < 1.0$ of the detector has multiple layers of scintillation detectors. The inner A-layer detectors are mounted on the A-layer PDT chambers (see Section 3.2.5). A C-layer exists where space permits outside the muon toroid, and coverage is very good everywhere except for the bottom of the detector in the central region where detector supports interfere with muon coverage. To help compensate for the decreased coverage, a B-layer was added in the bottom part of the DØ detector. This installation is described briefly in Appendix F. The forward regions have three layers of scintillation detectors. The scintillation detector layout can be seen in Figure F.1.

The scintillation detectors are made of 12.7 mm-thick BICRON 404A scintillator sheets. As in the CFT and pre-shower, scintillating materials emit photons as charged particles pass

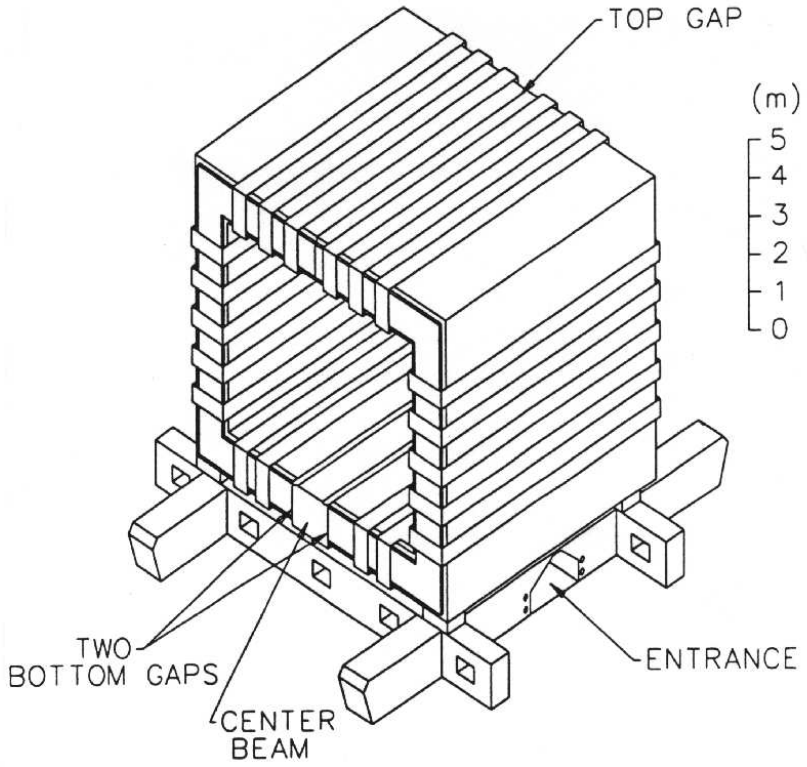

Fig. 3.16. 3-dimensional view of the muon toroid.

through. The photons are carried by wavelength-shifting (WLS) materials to photomultiplier tubes (PMTs) for detection. The scintillation detectors are sized to provide a ϕ segmentation of $\sim$4.5° for both central and forward regions. Central detectors are rectangular in shape, while forward are trapezoidal. The scintillators have a 420 nm emission peak, a 2.0 ns decay time, and a 1.7 m attenuation length.

Because of the different shapes and sizes, different types of WLS materials are used. Central scintillation detectors have WLS fibers embedded in grooves machined 4.5 cm apart and 6 mm deep, running lengthwise along the detector. The WLS fibers are BICRON BCF 92, with

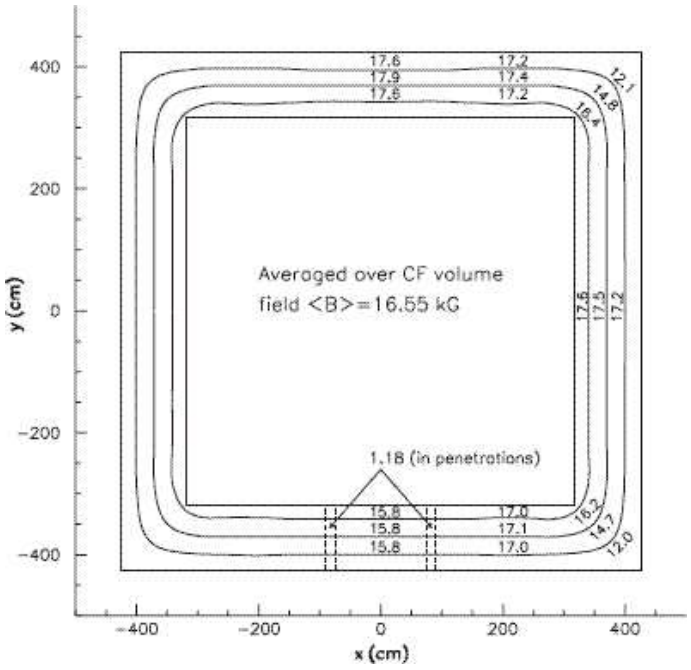

Fig. 3.17. Magnetic field in the $x - y$ plane of the central toroid magnet (in kG).

absorption peaks matching the scintillator emission peak, a 480 nm emission peak, and a 2.7 ns decay time. The attenuation length is more than sufficient for photons to travel the length of the fiber. Fibers run from the edge of the counter, 6 fibers per groove, to the center, where they are bundled together and optically connected to 1 or 2 PMTs. (B- and C- layer detectors are larger and need 2 PMTs due to the larger number of fibers.) Figure 3.20 shows a typical A-layer (single PMT) scintillation detector.

The forward scintillation detectors, known as *pixels*, have Kumarin 30 type WLS bars instead for the same purpose. Kumarin 30 has the same characteristics as BICRON BCF 92. WLS bars are placed along two edges of the trapezoidal scintillator sheets. The ends of the bars deliver light to the single PMT. Due to space considerations, approximately 150 of the over 4000 pixel counters have WLS fibers similar to those of the central scintillation detectors mounted to the edges of the scintillator sheets instead of WLS rods.

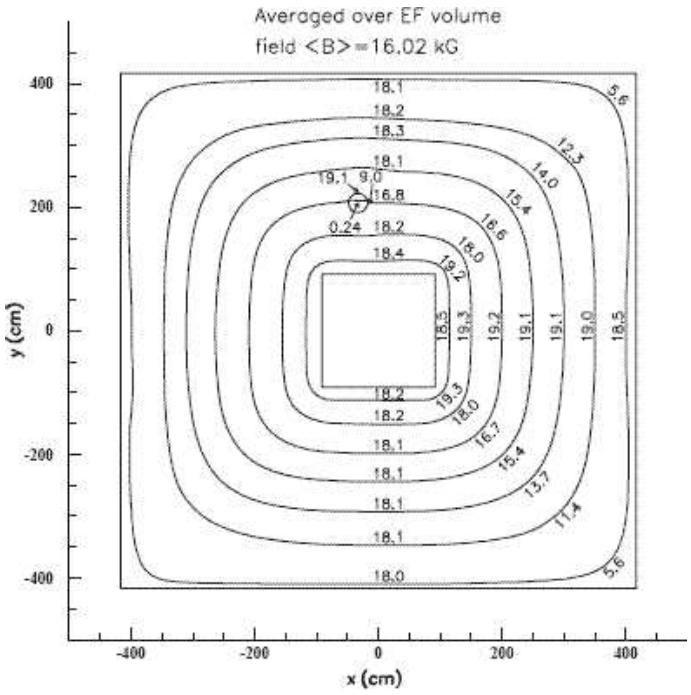

Fig. 3.18. Magnetic field in the $x - y$ plane of the end toroid magnet (in kG).

All PMTs are MELZ 115M phototubes having an average quantum efficiency of 15% at 500 nm with a maximum gain of 10^6. PMTs are 25 mm wide, except for B-layer detectors on the side of the DØ detector which have 38 mm PMTs. [64] The PMTs convert light pulses to electrical pulses for further use by the muon readout system. The pulse is sent from the PMT to a muon scintillator front-end (SFE) board, located in SFE crates within the body of the detector, where it is used to determine the time in nanoseconds that the muon passed through the scintillation detector. Calibration constants are added prior to the signal being sent to the muon readout crate so that, on average, muons coming from physics events from $p\overline{p}$ collisions in the interaction region will be registered at 0 ns. (The calibration of this system is described in some detail in Appendix G.) Muon times occurring more than a few nanoseconds away from zero are considered to be muons from external sources.

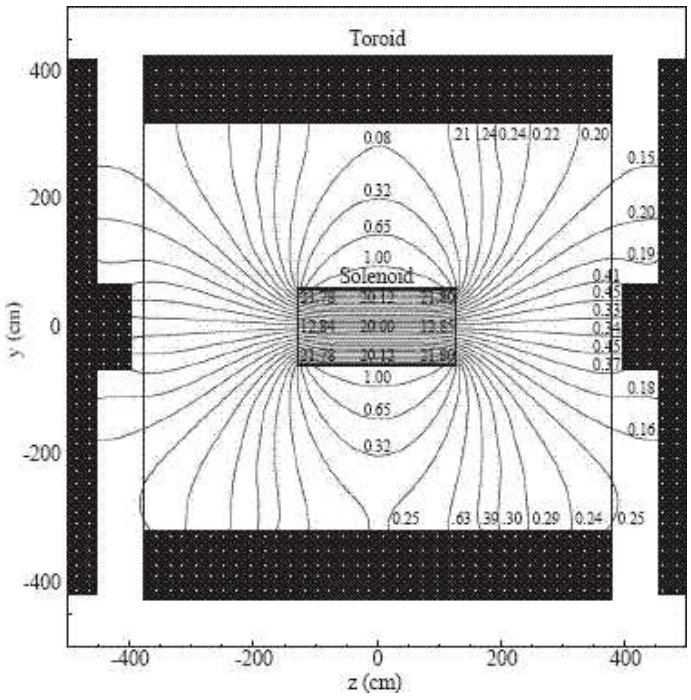

Fig. 3.19. Solenoid magnetic field in the $y - z$ plane of the detector (in kG, 10 kG = 1 T).

PMTs are powered by negative high-voltage power supplies rated at 3.5 kV with a maximum current of 3 mA. Typical currents for phototubes are 145 μA at 1.85 kV, but power supplies provide power to 10-15 PMTs each so the total current per power supply is approximately 2 mA.

Drift Tubes

Drift tubes [63] are used in the muon system to provide muon tracking information. Each drift tube has a wire running lengthwise down the center, held at a positive voltage with respect to the drift tube walls. Multiple drift tubes are arranged in larger chambers, with chambers containing 1 or more layers of drift tubes arranged side-by-side. The chamber contains a gas which is free to circulate within the drift tubes. As muons pass through the gas, electrons are

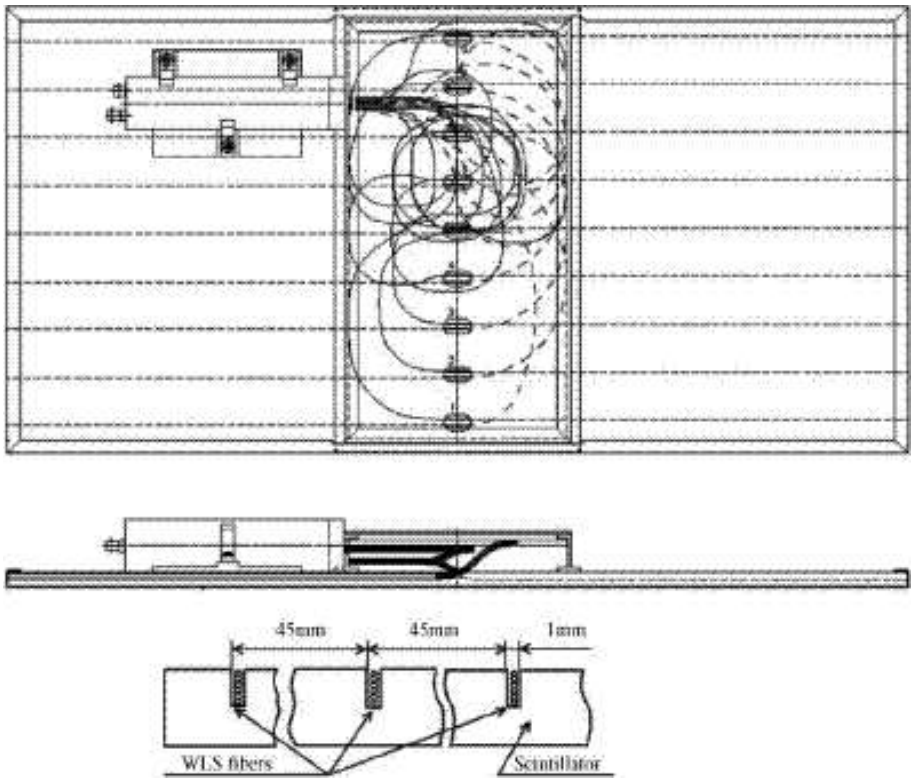

Fig. 3.20. Top and side view and cross-section of a central A-layer scintillation detector.

formed through ionization. These electrons move toward the sensing wires in the drift tubes, causing further ionizations. The resulting avalanche of electrons is detected by the sensing wire.

Drift tube chambers in the central region are known as proportional drift tube (PDT) chambers. PDT chambers contain 3 or 4 decks of drift tubes, and each drift tube has a 10.1 cm width. There are two cathode pads above and below the wires made of thin copper-clad Glasteel (B- or C-layer) or G10 (A-layer) strips with etched copper vernier pads which give charge detection with a resolution of 5 mm. These are only completely instrumented in the central A-layer to assist in matching tracks inside the muon toroid with tracks in the SMT and CFT. In the central B- and C-layers, approximately 10% of the vernier pads are instrumented to monitor the PDT

voltage gains. Anode wires are operated at 4.7 kV, and cathode pads are at 2.3 kV. The PDT end views and vernier pads are shown in Figures 3.22 and 3.23.

Drift tube chambers are known as Mini Drift Tube (MDT) chambers in the forward region. MDT cells are 9.8×9.8 mm^2, and each MDT chamber has a single layer of 8 cells. There are no vernier pads, and the anode wire is held at ground while the operating voltage of the cathode is -3.2 kV.

Drift chambers provide the following for each muon hit:

- drift time, T, to the anode wire,
- difference, ΔT, in the arrival time of the hit between a hit cell and the neighboring cell, and
- for central PDTs only, charge deposition on inner and outer vernier pads.

The drift time, T, gives the axial distance of the muon hit from the wire, while ΔT gives the approximate lengthwise position on the wire. A series of hits in several drift tubes can then be used to reconstruct a muon track. Single cell resolution is about 1 mm. The layout of PDTs and MDTs is shown in Figure 3.21. The design parameters are summarized in Table 1.

Parameter	PDT (Central)	MDT (Forward)
Wire Step	130 mm	10 mm
Wire Thickness	0.6 mm	0.6 mm
Cathode Material	Extruded Al	Al, Stainless Steel
Wire Material	Gold-plated Tungsten	Gold-plated Tungsten
Wire Diameter	50 μm	50 μm
Gas Material	CH_4-CF_4 (90%,10%)	Ar-CH_4-CF_4 (80%,10%,10%)
Gas Gain	1.1×10^5	1.1×10^5
Cathode Potential	2500 V	3100 V
Maximum Drift Time	500 ns	60 ns

Table 1
Parameters of muon drift tubes.

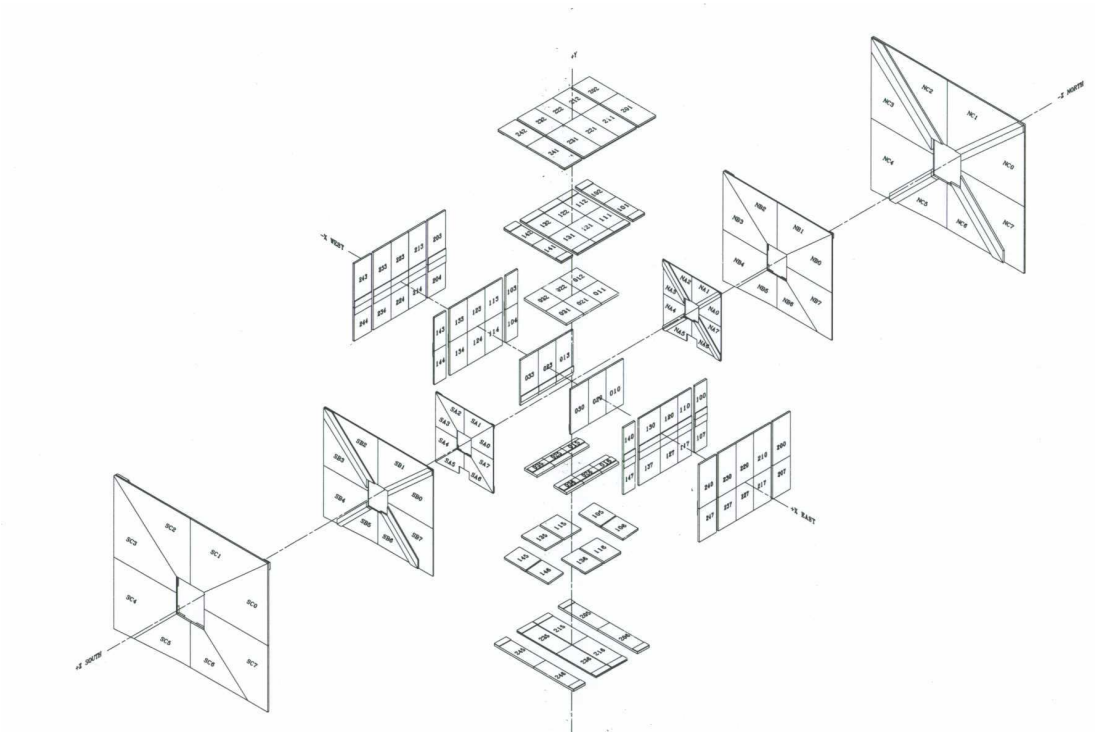

Fig. 3.21. 3-dimensional layout of the muon tracking system.

3.3 Triggering

At the DØ interaction region of the Tevatron, $p\overline{p}$ collisions occur at a rate of 2.5 MHz. Most of these are inelastic collisions. The most interesting events occur at much smaller rates, however. CPU resources limit the ability to process recorded events to approximately 50 Hz, so it is necessary to have a means of deciding for each event whether it gets discarded or recorded. This is the trigger system.

The DØ trigger system reduces the rate in three stages. Each successive level of the trigger system takes events which passed the previous level and examines the information available from the detector components in more detail to determine whether the event passes or not. The three levels are Level 1, 2, and 3.

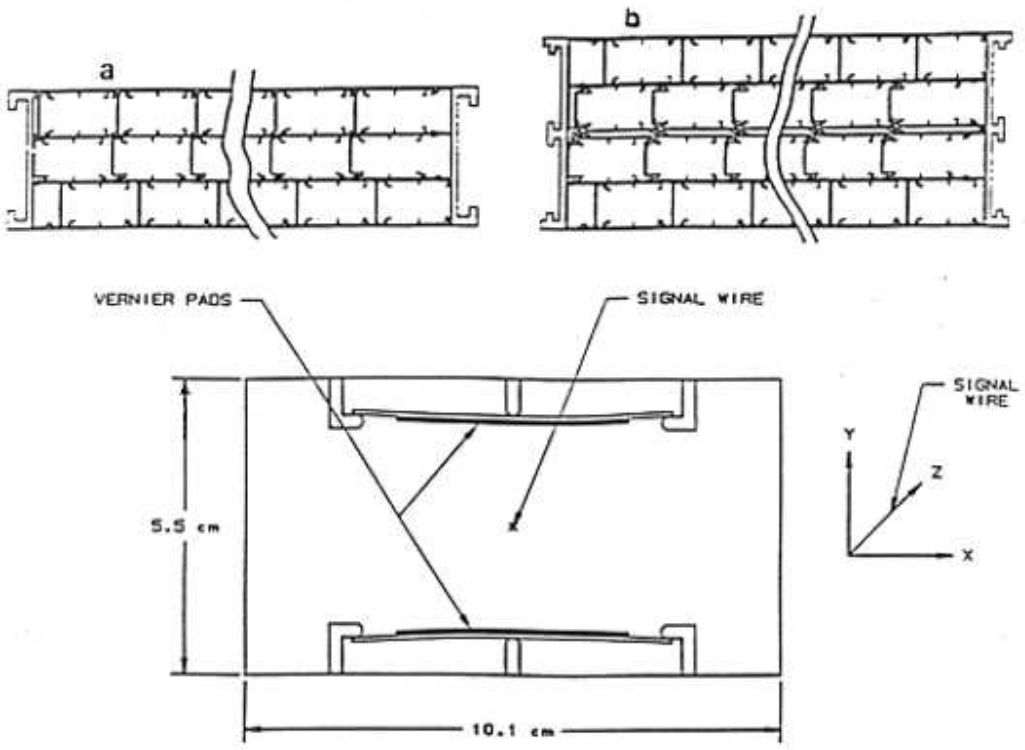

Fig. 3.22. (a) and (b): end views of the 3- and 4-deck PDT chambers. (c): end view of a single cell including vernier pads.

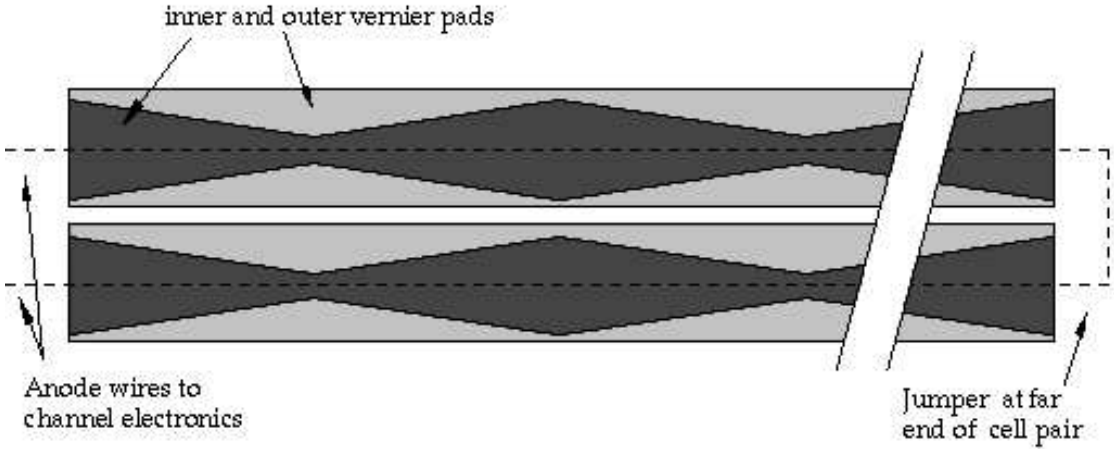

Fig. 3.23. Top view of central PDT vernier pads.

3.3.1 Level 1 Trigger

The Level 1 (L1) trigger is hardware-based. For every beam crossing, it takes information from the calorimeter, muon, and central tracking subsystems in the form of L1 terms, which are either 1 or 0 depending on whether certain conditions are met for the detector. L1 terms are combined to determine whether the event is passed to Level 2. The design output rate of L1 is 10 kHz. Events are stored in a buffer while the L1 decision is being made, and the required size of this buffer is determined primarily by the L1 decision time, so the L1 trigger system has a 3.3 μs decision time.

Level 1 Calorimeter Trigger

Calorimeter towers are combined to form $0.2 \times 0.2\eta - \phi$ trigger towers. EM trigger towers are used to form CEM(n,x) trigger terms, while EM + hadronic trigger towers are used to form CJT(n,x) terms. The triggers require n towers above a threshold E_T of x GeV/c^2.

Level 1 Central Track Trigger

The L1 central track trigger (L1CTT) [65] uses hits from the CFT/CPS axial fibers and the FPS to form tracks in 4.5° sectors in the transverse plane. CFT hits are compared to approximately 20,000 track equations for four p_T thresholds.

The six highest p_T tracks are identified for each sector. Numbers of tracks for various p_T thresholds, sector occupancy, and total p_T are used to determine L1CTT trigger terms. In addition, the tracks from each sector are sent to the L1 muon trigger where tracks are matched to hits in the muon detector.

Level 1 Muon

The Level 1 muon (L1Mu) system takes input from L1CTT and the readout crates of the PDTs, MDTs, and muon scintillation detectors. Triggers at L1 are formed from combinations of drift tube hits, scintillator hits, and CTT tracks. L1Mu triggers all have the following format: muNptTRSWx, where:

- N is the number of muons,
- T is the p_T threshold of the CTT track, or x if no track is required,
- R is the region of the detector:
  - a = all regions
  - c = central
  - b = forward
  - w = wide
- S is the scintillator trigger requirement:
  - t = tight trigger (A+C layers in central region, A+B in forward region)
  - l = loose trigger (A-layer only except bottom of detector, where any layer fires trigger)
- W is the PDT trigger, t or l (same requirement as for scintillators)

The tracks from L1CTT are used as seeds for tracks in L1Mu, and high p_T tracks are also required to have times in scintillation counters consistent with muons coming from $p\overline{p}$ collisions rather than cosmic rays or other sources.

An schematic diagram of flow of information from detector components to Levels 1 and 2 is shown in Figure 3.24

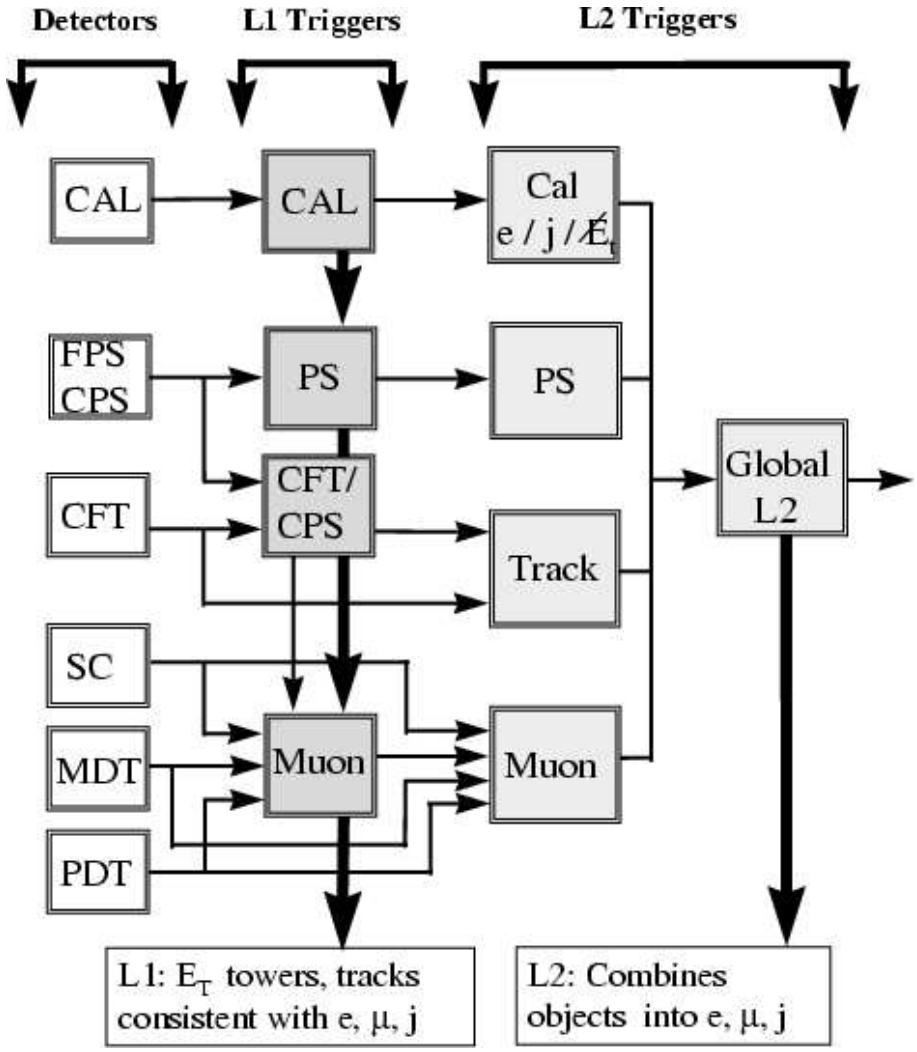

Fig. 3.24. Flow of information through L1 and L2 trigger elements.

3.3.2 Level 2 Trigger

The Level 2 trigger [68] is designed to take events that pass Level 1 and reduce the rate by a factor of 10 to 1 kHz. This is the first level of triggers that has the ability to combine information from all components of the detector. Each subsystem analyzes the data in greater detail and passes the processed information to a global processor, which determines whether to issue a L2 accept to allow the event to be sent to Level 3. The decision is made within 100 μs.

L2 Calorimeter

The L2 calorimeter [67] uses algorithms to do simplified identification of electromagnetic (EM) objects (electrons or photons), jets, and missing transverse energy ($\not\!\!E_T$) using the precision calorimeter readout. The L1 towers can be used as seeds to select the towers for the L2 trigger. The L2 jet triggers are based on 5×5 towers centered on the L1 seed towers. The sum of E_T in all towers in the L2 jet is used as the trigger. The sum of E_T in all jets in the event can also be used as a trigger. EM objects are constructed using the most energetic of the 4 towers nearest to the L1 seed tower. These are used to calculate a total E_T in EM towers and the total E_T in all towers. The cluster E_T is also found using 3×3 towers centered on the seed tower. These can all be used to trigger on electrons and/or photons in the event. The $\not\!\!E_T$ algorithm calculates the vector sum of all E_T in the calorimeter for use in $\not\!\!E_T$ triggers.

L2 Tracks and Vertices

The Level 2 central tracking trigger (L2CTT) [69] takes an input from the Level 2 silicon tracking trigger (L2STT), which gets an input from L1CTT. L2CTT takes the tracks from L2STT, removes duplicate tracks, and sorts tracks by p_T and by track impact parameter into two separate lists. These sorted track lists are then used in making L2 global trigger decisions.

L2 Muon

Level 2 Muon (L2Mu) [70] repeats the L1 calculations using more precise information from muon drift tube chambers and scintillation detectors. Rather than using raw hits from the PDTs to determine rough tracks, actual drift times and wire ϕ values are used to calculate more precise tracks. MDTs and scintillators also send more precise hit information directly to L2Mu. Track finding is 3-dimensional in L2, whereas wide 2D algorithms are used by L1Mu. Tracks are determined in A- and BC-layers separately, then combined according to track quality to determine final muon candidates. The final muon candidates are used for the final L2 global decision.

3.3.3 Level 3 Trigger

The Level 3 trigger uses a farm of Linux PCs which reconstruct the events to create physics objects such as electrons, muons, and jets. This is done using a modified version of the same reconstruction software that is used offline. The time allowed for processing events is 100 ms. When a L2 global accept is received, a L3 farm node is chosen to process the event. The event builder is the first program to run. The event builder is told from which detector subsystems to receive information. If it does not receive information from any expected subsystem, the event is rejected. The second program is the event filter. This program runs the reconstruction software, and determines whether the event meets the requirements of the L3 trigger. If the event is accepted, all detector information is written to tape for permanent storage. The final rate of writing events to tape is approximately 50 Hz.

The particular triggers used for the analysis presented here are summarized in Tables 2 and 3.

	v8-v11	v12-v13
	EM15_2JT15	E1_SHT15_2J20
L1	CEM(1,10)CJT(2,5)_ncu 1 EM tower, $E_T > 10$ GeV; 2 JET towers, $E_T > 5$ GeV.	CEM(1,11)_ncu 1 EM object, $E_T > 11$ GeV.
L2	EM(.85,10.)_2JET(10.) 1 EM candidate, $E_T > 10$ GeV ($f_{EM} > .85$); 2 jets, $E_T > 10$ GeV.	none
L3	ELE_LOOSE_SHT(1,15)_JET(2,15) 1 electron, $E_T > 15$ GeV; 2 jets, $E_T > 15$ GeV.	ELE_NLV_SHT(1,15)_JET(2,20) 1 electron, $E_T > 15$ GeV, tight shower shape; 2 jets, $E_T > 20$ GeV.

Table 2
$e+$ jets triggers used in the matrix element top mass analysis for different trigger lists, corresponding to different data-taking periods.

	v8-v12	v13.0-13.1	v13.2-13.3
	MU_JT20_L2M0	MUJ2_JT25	MUJ2_JT25_LM3
L1	mu1ptxatxx_CJT(1,3) 1 μ, scint; 1 JET tower, $E_T > 3$ GeV.	mu1ptxatlx_CJT(1,5) 1 μ, scint & loose wires; 1 JET tower, $E_T > 5$ GeV.	mu1ptxatlx_CJT(2,3) 1 μ trigger, scint & loose wires; 2 JET towers, $E_T > 3$ GeV.
L2	MUON(1,med)_JET(1,10) 1 MEDIUM muon; 1 jet with $E_T > 10$ GeV.	MUON(1,med)_JET(1,8) 1 MEDIUM muon; 1 jet with $E_T > 8$ GeV.	
L3	Jet(1,15) 1 JET with $E_T > 15$ GeV.	Jet(1,25) 1 jet, $E_T > 25$ GeV & $\|\eta\| < 3.6$.	Jet(1,25)_Muon(1,3,loose) 1 jet, $E_T > 25$ GeV & $\|\eta\| < 3.6$; 1 loose muon, $p_T > 3$ GeV.

Table 3
$\mu+$ jets triggers used in the matrix element top mass analysis for different trigger lists, corresponding to different data-taking periods.

4. EVENT RECONSTRUCTION AND DATA SELECTION

A very large amount of information is recorded for every event that passes the final level of the DØ triggering system. Each subsystem of the DØ detector records data in hundreds or thousands of channels, and all channels containing data must be analyzed to reconstruct the momenta and identity of particles that pass through the detector. Complex algorithms are used at the reconstruction level to combine information from the multiple layers of detectors. Tracks and primary vertices are reconstructed using data obtained from the central tracking system (combined with other detectors, if possible). The data obtained from the calorimeter is used to reconstruct hadronic *jets*, or showers of particles arising from hadrons in the calorimeter. The calorimeter data is also used to reconstruct missing transverse energy ($\not\!\!E_T$), as well as particles likely to be electrons. The muon system is used to reconstruct muon tracks and to identify good muons from physics (i.e. not cosmic) events. The reconstruction of these physics objects is described in this chapter.

The top quark mass analysis uses $t\bar{t}$ events in which one of the W bosons arising from top quark decay decays leptonically to a lepton and the corresponding neutrino, and the other W boson from the other top quark decay decays hadronically to two quarks. All four quarks hadronize and form four jets in the detector, so event selection requires four energetic jets. The lepton can be a muon, electron, or a tau lepton which decays either to a muon or an electron. To cover all these scenarios, events are selected with a single energetic lepton (muon or electron) and missing transverse energy. Event selection is discussed in more detail below.

4.1 Central Track Reconstruction

Reconstruction of tracks using information from the Central Fiber Tracker (CFT) and Silicon Microstrip Tracker (SMT) is done by fitting clusters of hits into tracks. Clusters are formed differently in the SMT and CFT. For hits in the SMT, clusters consist of neighboring strips that have electric charge deposition above a minimum noise threshold. The positions of clusters are determined by the average positions of individual strips, weighted by the deposition of charge on each strip. [71] In the CFT, clusters are formed from one or two fibers. If two fibers are used, the position is taken to be the average of the two fibers. If more than two neighboring fibers have hits, multiple clusters are used for each pair of neighbors. [72] Two different methods are combined to find tracks: the Alternate Algorithm (AA) and Histogram Track Finding (HTF).

The AA method [71] starts from three clusters in the SMT barrels or disks, chosen to be consistent with a charged particle having: 1) a transverse momentum of at least 180 MeV, 2) an impact parameter with respect to the beam spot less than 2.5 cm, and 3) the χ^2 of the resulting track hypothesis less than 16. Clusters are then added for each successive layer, working outward toward the CFT, adding only those clusters that are within an expected region based on the trajectory formed from previous hits. At the end, track candidates are required to have at least 4 layers of hits in the SMT and/or CFT, in addition to further requirements on the number of missed layers allowed.

The HTF algorithm [74] takes 2D hits and uses them to find the most likely values of curvature and trajectory angles for track candidates. For each hit, the algorithm calculates a value of the curvature, ρ, and the direction of the track at the point of closest approach to the beam spot, ϕ, for a track constrained to pass through the beam spot. The curvature is calculated with

$$\rho = \frac{qB}{p_T}, \tag{4.1}$$

where q is the electric charge and B is the magnetic field. A 2D histogram is constructed with ρ on one axis and ϕ on the other, and the bin corresponding to the calculated (ρ, ϕ) coordinate is incremented. This is done for all hits in the event. Hits belonging to the same track will contribute to the same peak, and hits belonging to different tracks will give a randomly distributed background. The Hough transform improves the fit by taking errors in measured values into account, giving ranges of ϕ for each hypothetical ρ value considered for each hit. This is described in detail in Ref. [74]. The result is a series of lines that intersect at a particular (ρ, ϕ) value. The histogram bins with too few hits are discarded, as are bins for which all hits are contained in neighboring bins. The bins that remain are used to form candidate tracks.

For either algorithm, Kalman filtering [75] is used to clean the tracks and also to perform a more refined fit. Then track candidates from both algorithms are combined to give a final set of track candidates.

4.2 Primary Vertex Reconstruction

The point in space at which the proton and antiproton collision occur is referred to as the "primary vertex" (PV). PV reconstruction is done using a two-pass algorithm. The first pass uses a loose track selection to determine the position of the beam spot center and a set of possible primary vertices. The second pass uses the first-pass vertices to recalculate track parameters, and applies tighter cuts to ensure that only tracks coming from the primary vertex are used to determine the PV position. Then the primary vertex is selected from the list of primary vertex candidates.

Two different algorithms are used for track selection and vertex finding: **d0reco** and **d0root**. The **d0reco** PV is used to reconstruct calorimeter objects (jets, electromagnetic objects, and $\not\!\!E_T$). The **d0root** PV is used for tracking-related quantities, such as electron and muon impact parameters and secondary vertices for b-tagging (see Sect. 5.3.3).

Track selection, vertex finding, and final vertex selection are described below. Further details can be found in Ref. [77].

4.2.1 Track Selection/Primary Vertex Finding

The **d0root** algorithm first uses a clustering algorithm to cluster tracks within 2.0 cm of each other in the z-direction. The **d0reco** algorithm uses non-clustered tracks. For either method, a list of primary vertices is first generated to approximate the position of the beam spot. To do this, tracks (or clusters of tracks for **d0root**) are selected that have a loose track selection, which means the impact parameter significance (dca/σ), calculated with respect to the position $(x, y) = (0, 0)$ in the transverse plane, is less than 100. These tracks are used to find a list of first-pass vertices.

Next, a tight dca/σ cut (calculated with respect to the the first-pass vertices) is used to select tracks. Tracks having: 1) 2 SMT hits (unless Monte Carlo-simulated events for the **d0reco** algorithm), 2) $p_T > 0.5$ GeV/c, and 3) dca/$\sigma < 5.0$ (**d0reco**) or dca/$\sigma < 3.0$ (**d0root**) are used to calculate the final list of PV candidates.

4.2.2 Primary Vertex Fitting

It is necessary to distinguish tracks coming from the hard-scattering process and other tracks. The proton and antiproton that collided to create the hard scatter event are accompanied by a large number of other protons and antiprotons due to the high luminosities. It is likely that these will collide also. These collisions, known as *minimum bias* events, usually have much smaller transverse momenta. The $\log_{10} p_T$ distribution of minimum bias processes is thus used to create a probability for a track to come from a minimum bias vertex. For each PV candidate in an event, the minimum bias probability is constructed from the product of each track's minimum

bias probability divided by the total number of tracks. The PV candidate with the lowest minimum bias probability is chosen as the primary vertex of the event.

For the top quark mass analysis, the following event selection cuts are used to ensure a high reconstruction quality:

- $z_{PV} \leq 60$ cm,
- at least three tracks fitted to the PV, and
- $\mathrm{PV_{d0reco}}$ and $\mathrm{PV_{d0root}}$ must agree to within 5 cm in the z-direction.

4.3 Calorimeter

Prior to identifying calorimeter objects such as electrons, jets, and $\not\!\!E_T$, it is necessary to apply algorithms to remove undesired cells. The first of these is the NADA algorithm [78], [79], which removes "hot cells". Hot cells are cells which contain spurious or excessive energies due to detector problems such as hardware failure, electronic noise, uranium noise, or argon contamination, or physics processes such as cosmic ray showers or backscattering of beam particles interacting outside the interaction region. The NADA algorithm removes cells with high p_T if neighboring cells have energy below a threshold p_T.

A T42 algorithm [80] is also used to reduce calorimeter noise. Calorimeter noise, somewhat more subtle than hot cells, is caused by readout fluctuations and energy deposition from previous beam crossings (known as *pile-up*). The T42 algorithm uses thresholds which are multiples of the RMS of the noise distribution, σ, to determine whether to keep or reject calorimeter cells. Cells with energy greater than 2.5 σ are kept if neighboring cells have energies expected to be from signal rather than noise. Cells are believed to have energies from signal if above +4 σ.

4.3.1 Electrons

An electron deposits energy in the electromagnetic portion of the calorimeter with a characteristically narrow shape. It is also expected that a track in the central tracker will be matched to the calorimeter shower. Electromagnetic objects without central tracks are called *photon candidates*, and are not used in the top quark mass analysis.

Electron Identification

To identify electrons, a cluster is formed in the calorimeter using a simple cone algorithm which clusters calorimeter cells in groups of calorimeter towers in a cone with $\Delta R = \sqrt{\Delta\eta^2 + \Delta\phi^2} < 0.2$ centered on the cell containing the highest energy. For this cluster, several parameters are calculated to help in identifying true electrons: [81]

EM Fraction A true EM object is expected to deposit most of its energy in the first few EM layers of the calorimeter. So it is expected to have a large EM fraction, $f_{EM} = E_{EM}/E_{tot}$, where E_{EM} is the energy deposited in the EM layers and E_{tot} is the total energy of the cluster.

H-Matrix8 The shape of the shower is compared to the expected shape of an electron, and 8 parameters are used to create a covariance matrix. The inverse of the covariance matrix is used to construct a χ^2 value, with low values of χ^2 corresponding to more electron-like EM objects.

Isolation An electron should have most of its energy in a tight cone, with little energy in a halo outside this cone. The isolation fraction,

$$f_{iso} = \frac{E_{tot}(R < 0.4) - E_{EM}(R < 0.2)}{E_{EM}(R < 0.2)}, \tag{4.2}$$

is expected to be smaller for genuine electrons.

Track Match χ^2 Global tracks, i.e. tracks containing both SMT and CFT hits, are matched to EM objects. A global track is considered to be matched to the EM cluster if it is within 0.05 in ϕ and η. The quality of the track match is given by

$$\chi^2 = \left(\frac{\Delta\phi}{\sigma_\phi}\right)^2 + \left(\frac{\Delta z}{\sigma_z}\right)^2. \tag{4.3}$$

The values of ϕ and z are given by the extrapolation of the global track to the third EM layer for the matched EM object. The σ_ϕ and σ_z values are the measured RMS resolutions of ϕ and z.

Electron Likelihood Six parameters are combined into a single electron likelihood. Three of them are H-Matrix8, f_{EM}, and track match χ^2 (described above). The following are also incorporated into the electron likelihood discriminant:

E_T/p_T Real electrons should have values of E_T/p_T close to 1.

DCA The distance of closest approach (dca) of the track to the line passing through the primary vertex parallel to the z-axis.

***N_trks* ($R < 0.05$)** The number of tracks in a $\Delta R < 0.05$ cone is used to eliminate π^0 conversions to real electrons, where a neutral pion first decays into photons which subsequently create e^+e^- pairs. These are expected to have more than one track, whereas real electrons should have only one track.

total track *p_T* ($R < 0.4$) The sum of the p_T of all tracks within a $\Delta R < 0.4$ cone around the associated track. This removes π^0s produced in association with charged hadrons from QCD multijet processes.

CPSstripmax The number of hits in CPS fibers in the 3D cluster within 20 cm of the EM object containing the largest number of single strips in its single layer. This variable is used in the CC only.

Event Selection

Cuts on these variables for electrons used in the top quark mass analysis are shown in Table 1. In addition, events are selected with $|\eta| < 1.1$ to reject events in the ICR and EC regions of the calorimeter where electron misidentification is higher. A p_T requirement is imposed to reduce the physics background. In addition, events with more than one electron are rejected to maintain orthogonality with the dilepton top quark mass analysis.

The EM-Likelihood variable is used as an isolation variable. Events passing the EM-Likelihood cut are referred to as *tight* electrons. If electrons pass all other cuts, they are called *loose* electrons.

electron selection	
f_{EM}	> 0.9
f_{iso}	< 0.15
χ^2	< 50
associated track	required
p_T	> 20 GeV/c
$\|\eta\|$	< 1.1
$\Delta z(e, \mathrm{PV})$	< 1 cm
Second Electron Veto	required
EM-Likelihood (tight electrons)	> 0.85

Table 1
Electron selection for the e+jets sample.

4.3.2 Jets

Jet Reconstruction

Before jets are reconstructed, calorimeter towers are first used to form preclusters. [82] These will be used as seeds to form jets. Preclustering is done to reduce computation time, since several hundred towers would have to be used if used as seeds individually.

Geometrical towers are approximately 0.1×0.1 in (η, ϕ) for $|\eta| < 3.2$. For each tower, a precluster is made of all cells containing at least 2.5 σ (σ is the RMS value of the calorimeter noise, as used in the T42 algorithm), either positive or negative energy. This is done after NADA and T42 cell removal (see Sect. 4.3). The energy and momenta are constructed by adding the energy and momenta of individual cells. Towers having more than one cell can acquire mass if the momenta of cells are not collinear, as is usually the case since towers are projective with respect to the geometric center of the detector. Towers also acquire mass if two or more cells have measured energies with opposite signs. Towers with excessively negative squared masses are rejected.

Preclustering starts with a list of towers ordered by p_T. The highest p_T tower is used as a seed, and other towers are added to the precluster (and removed from the list) if they are within a cone with $\Delta R = 0.3$ and the p_T of the tower is above 1 MeV. This is repeated until there are no towers with $p_T > 0.5$ GeV remaining to use as seed towers. When this is done, preclusters with $p_T < 1$ GeV and/or having only one tower are removed from the list of preclusters.

These preclusters are then used as the initial seeds in an iterative process which first builds a cone with $\Delta R = 0.5$ around the highest-p_T precluster, evaluates the 4-momenta of the cone, and uses the centroid of the cone as the new seed. This is repeated until a stable cone is achieved, and the precluster is removed from the list. The process is repeated for all preclusters that are more than half a cone size away from other stable clusters. In addition to preclusters, midpoints between preclusters are also used as seeds to reduce the sensitivity to soft gluon radiation.

Finally, an algorithm is used to merge jets that share towers if the shared towers contain more than 50% of the total p_T of the jets combined. If the shared towers contain less than 50% of the total p_T, the shared towers are assigned to the neighbor and the jet quantities are recalculated.

At the end, only jets with $p_T > 8$ GeV/c are considered to be "good" jets. The following quality requirements must also be met:

- $\mathbf{0.05 < f_{EM} < 0.95}$ (see Sect. 4.3.1), used to reject electromagnetic particles.
- $\boldsymbol{f_{EM} < 0.4}$, where $f_{CH} = E_{CH}/E_{tot}$ is the fraction of energy deposited in the coarse hadronic (CH) section of the calorimeter. Jets consisting mostly of cells from this noisy region are assumed to be noise.
- **L1 Confirmation.** Coherent noise in the precision readout system creates fake jets which pass all other quality cuts at the reconstruction level. If the event does not have the expected jet characteristics in the L1 trigger information, the event is rejected.

Two additional cuts on $n90$ and f_{hot} are used to remove jets clustered around hot cells, but these cuts are largely unnecessary due to the NADA and T42 algorithms.

In $t\bar{t} \rightarrow l\nu_l b\bar{b}qq'$ events, two jets are expected to arise from the decay of the hadronically-decaying W boson, and one jet is expected from each of the two top quark decays. Due to technical limitations of the matrix element method, extra jets arising from gluon radiation or splitting can not be considered in evaluating event probabilities, so events are chosen with exactly 4 jets. Jets are required to have $p_T > 20$ GeV/c with $|\eta| < 2.5$. The η cut preferentially selects $t\bar{t}$ events, which typically have smaller pseudorapidities.

Jet Energy Scale

Several mechanisms affect the measured energy of partons interacting to form jets in the calorimeter. One of these is differences in calorimeter response to the many types of particles interacting with the calorimeter. Another is additional energy deposition (described in Sect. 4.3). It is also possible that not all particles within a jet will deposit their energy within the cone used in the cone algorithm. For all these reasons, the jet energy will be distorted and corrections must be applied. [82]

The actual particle energy is given by

$$E_{jet}^{particle} = \frac{E_{jet}^{meas} - E_0(\eta, \mathcal{L})}{R_{jet}(E_{jet}^{meas}, \eta) \times R_{cone}(E_{jet}^{meas}, \eta)}, \tag{4.4}$$

where $E_0(\eta, \mathcal{L})$ is the offset energy, $R_{jet}(E_{jet}^{meas}, \eta)$ is the calorimeter response to the hadronic jet, and $R_{cone}(E_{jet}^{meas}, \eta)$ is the fraction of the particle jet energy contained within the algorithm cone. These are all described below.

Offset Energy Energy not due to the hard scattering process is present in the calorimeter. This is the offset energy, $E_0(\eta, \mathcal{L})$. Offset energy can be from underlying events, multiple interactions, energy pile-up, noise from decay of uranium in the absorber plates, and/or electronic noise. It is determined using randomly recorded data events that have no trigger requirement (minimum bias events).

Calorimeter Response The calorimeter response is measured using γ+jet events where the photon is back-to-back with the jet. The calorimeter response to photons is well known from high-precision measurements using $Z \rightarrow ee$ events. The p_T imbalance in the γ+jets events can therefore be used to determine the calorimeter response to jets. The response is measured in bins of jet energy.

Showering Correction Particles created either outside or inside the region bounded by the algorithm cone may deposit only a fraction of energy inside the cone as the shower develops. The shower can also be bent by the magnetic field. Both of these are instrumental effects and can be corrected using jet energy profiles from dijet data and MC samples. There will also be out-of-cone (OOC) showering due to physics processes, namely gluon emission and fragmentation at the particle level. Since the showering correction should only correct for instrumental effects, the physics OOC showering is estimated using MC and the effect is removed from the total showering correction.

Total jet energy scales for data and MC, binned in jet energy and η, are shown in Figures 4.1 and 4.2.

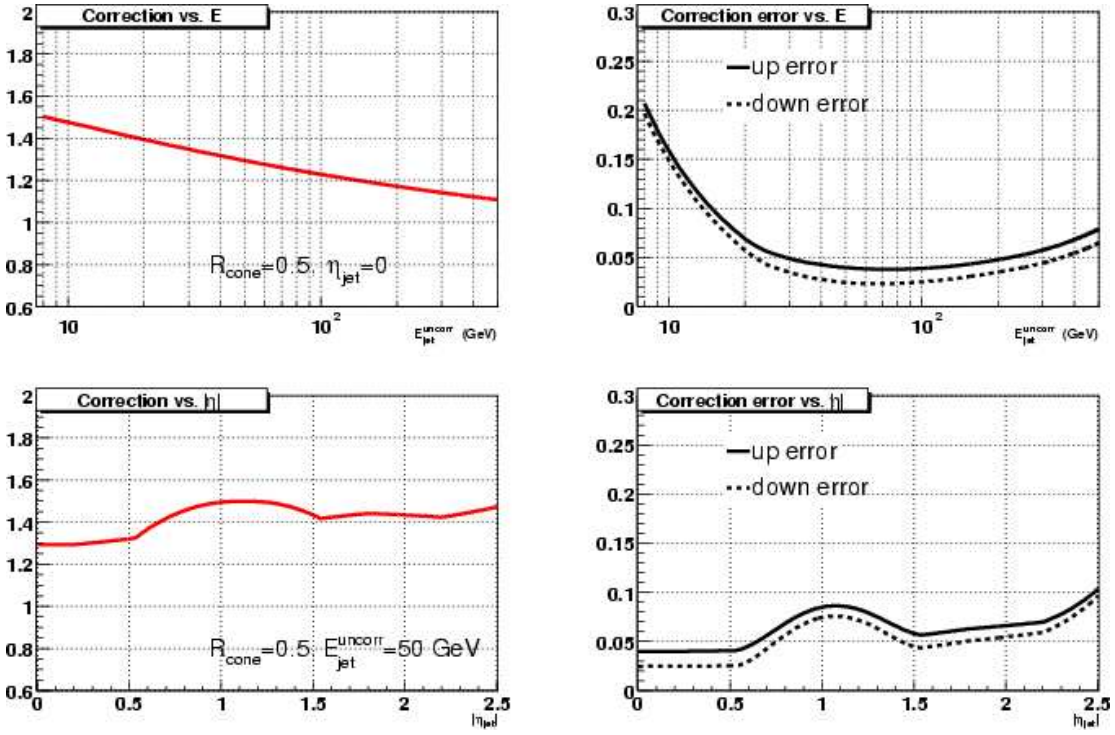

Fig. 4.1. Jet energy scale and uncertainties for jets in data as functions of jet energy and jet $|\eta|$.

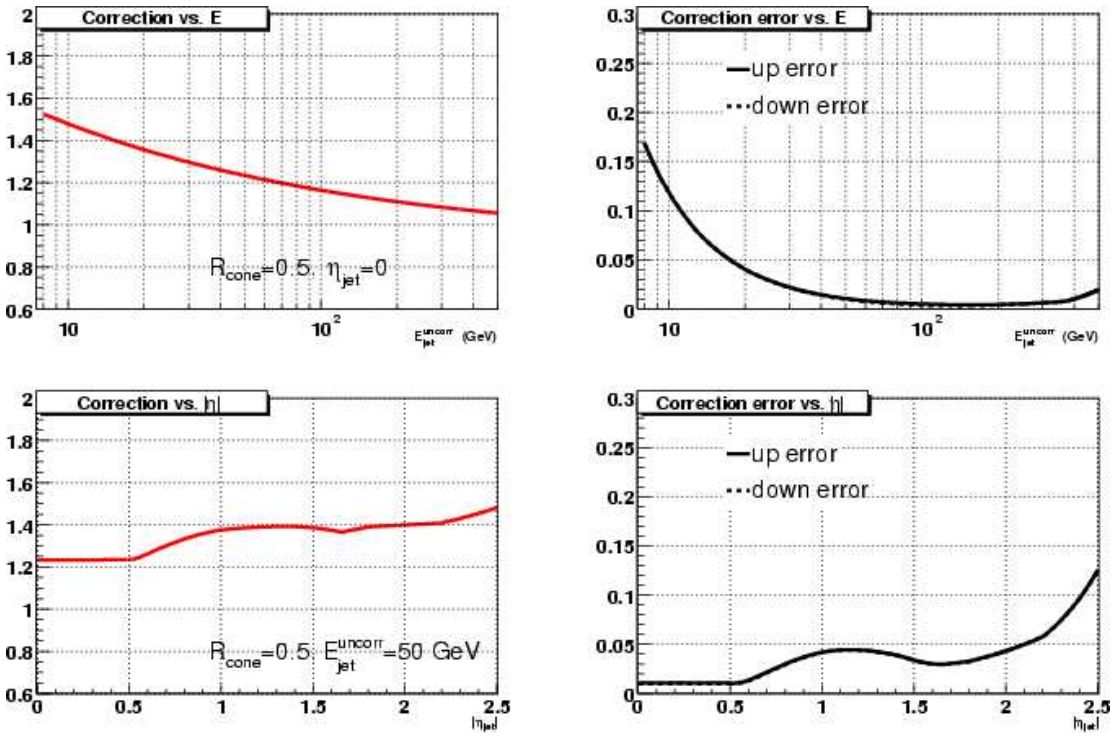

Fig. 4.2. Jet energy scale and uncertainties for jets in MC as functions of jet energy and jet η.

η-dependent Corrections The previous jet energy scale corrections are applied to a γ+jet sample, and the variable

$$\Delta S = \frac{p_T^{jet} - p_T^{\gamma}}{p_T^{\gamma}} \tag{4.5}$$

for the sample is binned in η to get more subtle corrections to the jet energy scale with respect to pseudorapidity. [83] These corrections are shown in Figure 4.3.

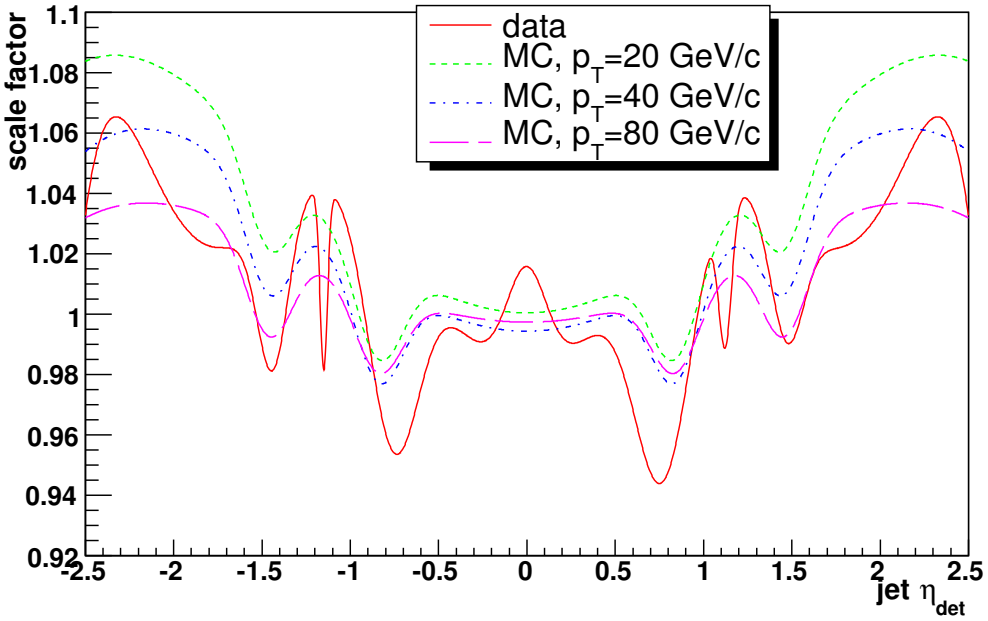

Fig. 4.3. η-dependent jet energy corrections after jet energy scale correction for data and MC jets.

Jet Energy Resolution

The top quark mass measurement uses jet energy resolutions directly, and the precision of the measurement is directly related to the jet energy resolution. The resolutions are determined

separately for jets above and below 50 GeV. [84] For $p_T > 50$ GeV/c, a dijet sample is used and the width of the asymmetry variable

$$\mathcal{A} = \frac{|p_T^1 - p_T^2|}{p_T^1 + p_T^2} \tag{4.6}$$

is determined using p_T^1 and p_T^2, the transverse momenta of the two jets. The jet energy resolution is given by

$$\frac{\sigma_{p_T}^{jet}}{p_T^{jet}} = \sqrt{2}\sigma_{\mathcal{A}}. \tag{4.7}$$

For jet energies below 50 GeV, a γ+jet sample is used. The asymmetry variable used is

$$\mathcal{A}_{pj} = \frac{p_T^{jet} - p_T^{\gamma}}{p_T^{\gamma}}, \tag{4.8}$$

and

$$\frac{\sigma_{p_T}^{jet}}{p_T^{rel}} = \sigma_{\mathcal{A}_{pj}} \times R_{pj}, \tag{4.9}$$

where $R_{pj} = p_T^{\gamma}/p_T^{jet}$ corrects for imbalance between average jet and photon p_T.

The results for the two samples are combined to get a single parametrization of jet energy resolution as a function of jet p_T. The resolutions are shown in Figures 4.5 and 4.4. Since the resolutions in MC are found to be underestimated, MC jets are smeared accordingly.

4.3.3 Missing Transverse Energy

Neutrinos are not detected at all in the DØ detector, so their presence must be inferred from energy missing in the transverse plane. The missing transverse energy, $\not\!\!E_T$, is determined by taking the vector sum of all calorimeter cells passing the T42 algorithm, except for cells in the

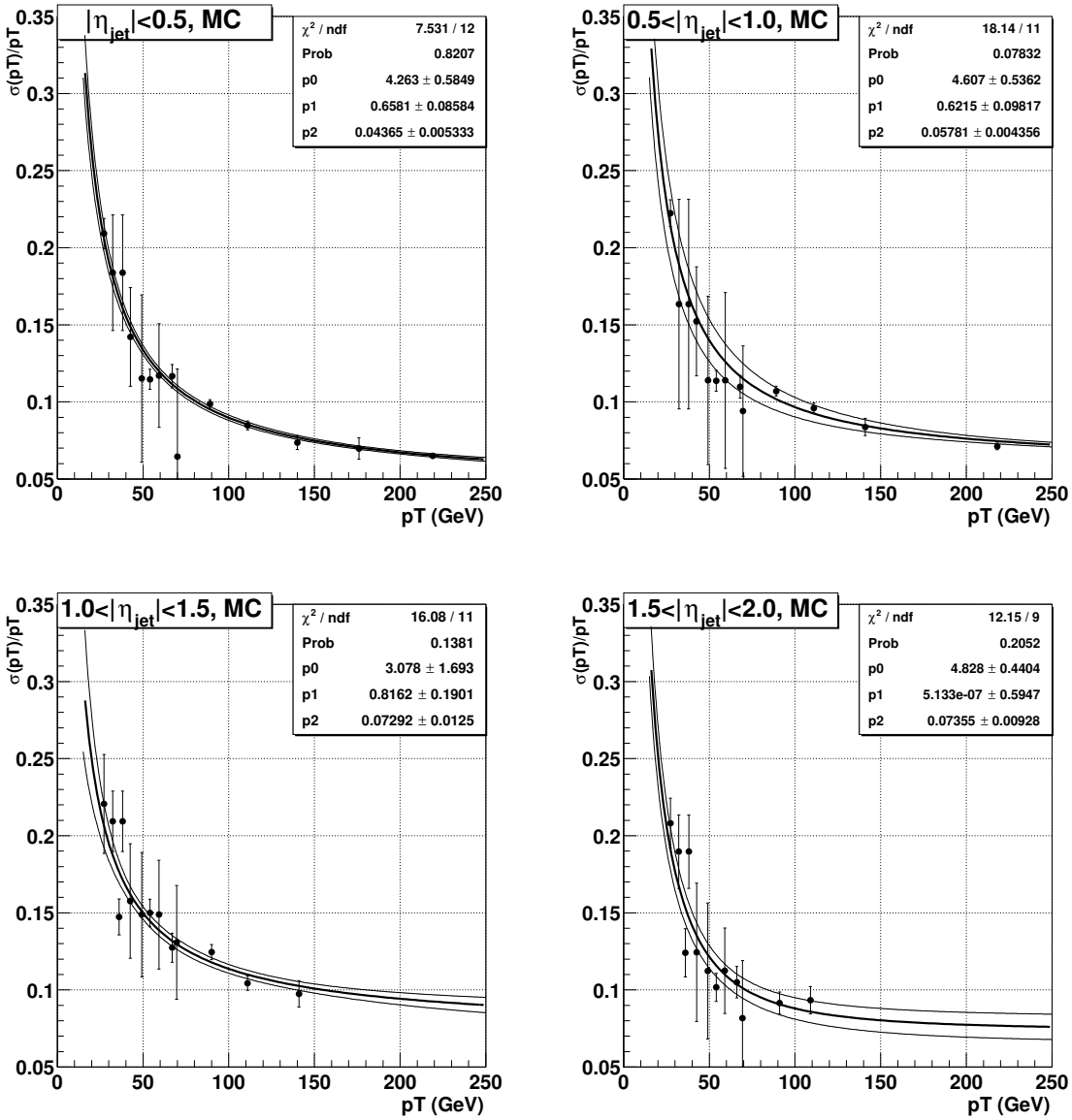

Fig. 4.4. Jet p_T resolutions for different η_{det} regions in MC. The points below $\sim$50 GeV are obtained using photon+jet events, whereas for p_T >50 GeV resolutions are measured using dijet data. Bands of $\pm 1\sigma$ statistical error are also shown.

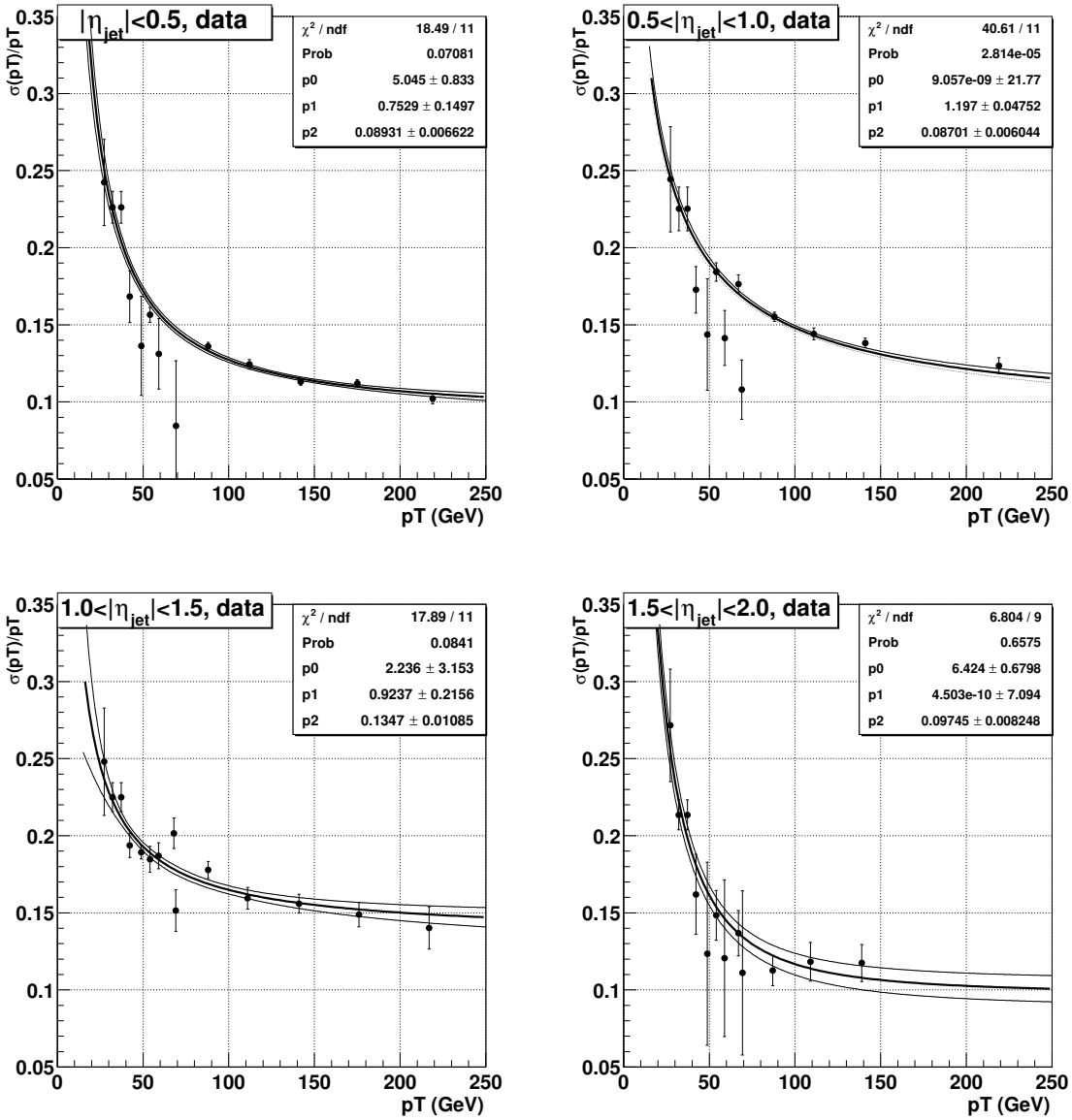

Fig. 4.5. Jet p_T resolutions for different η_{det} regions in data. The points below ∼50 GeV are obtained using photon+jet events, whereas for p_T >50 GeV resolutions are measured using dijet data. Bands of $\pm 1\sigma$ statistical error are also shown.

coarse hadronic section of the calorimeter. For this section, which is somewhat noisy compared to other sections, cells are only used if they are clustered into a reconstructed jet. The $\not\!\!E_T$ vector is that vector which balances the calorimeter vector sum.

Calorimeter response corrections to EM objects and jets are propagated to the calculated $\not\!\!E_T$ vector. Muons detected in the muon system are also used to correct the $\not\!\!E_T$, both for the presence of a muon and for the energy deposited in the calorimeter as a minimum ionizing particle.

The top mass analysis uses $\not\!\!E_T$ only as an event selection cut. $t\bar{t}$ events are expected to have a single energetic neutrino from the decay of the leptonically-decaying W boson, so lepton + jets are events are required to have $\not\!\!E_T > 20$ GeV.

4.4 Muons

Reconstruction of muons uses information from both the muon system and the central tracking system. [85] Muons identified by the muon detector are referred to as *local muons*. Local muons that are matched to tracks in the central tracking system are called *central track-matched muons*.

The *type* of muon is indicated by the *nseg* parameter. Central track-matched muons have positive values of *nseg*, while negative *nseg* values indicate no central track match. Values of $|nseg|$ =1, 2, or 3 indicate, respectively, A-layer only hits, BC-layer only hits, and A- and BC-layer hits combined.

Matching to central tracks is done by extending the muon tracks to the point of closest approach to the beam. The track parameters are compared with tracks within 1 radian in η and ϕ, and the track with the best fit of the muon track parameters (i.e., the highest χ^2 probability) is chosen as the matched track. The χ^2 value must be greater than zero to be matched.

4.4.1 Muon Quality

The *quality* of muon can be "Loose", "Medium", or "Tight". The quality criteria vary with the muon type. Muons in events selected for the top mass analysis are required to be Medium $nseg = +3$ muons, so only Medium and Tight $|nseg| = 3$ classifications are described here. Further details about the various classifications can be found in Ref. [85].

A muon of type $|nseg| = 3$ is considered Medium if it has the following:

- at least two A-layer wire hits,
- at least one A-layer scintillator hit,
- at least two BC-layer wire hits, and
- at least one BC-scintillator hit. (Central muons with less than four BC wire hits are not required to have a BC scintillator hit.)

If $|nseg| = 3$ muons pass the Medium criteria, have an additional BC-layer wire hit, and a converging local track fit (which would mean $nseg = +3$), they are considered to be Tight.

CFT-only Tracks

Roughly 18% of central tracks have no hits in the SMT, causing a degradation in the momentum resolution. This can be improved by fitting the tracks for these muons to $(0, 0, z)$, where z is the z-component of the primary vertex. [86] The corrected value of charge over transverse momentum is given by

$$\left(\frac{q}{p_T}\right)' = \frac{q}{p_T} - dca \times \frac{\sigma_{dca,q/p_T}}{\sigma_{q/p_T,q/p_T}}. \tag{4.10}$$

Here $\sigma_{i,j}$ is the (i, j) element of the track error matrix, and dca is the distance of closest approach to $(0, 0, z)$.

Muon Momentum Resolution

$Z \rightarrow \mu\mu$ samples are used to compare muon reconstruction in data and MC. [84] Dimuon invariant masses are reconstructed in these samples. The width of the Z mass peak gives the muon momentum resolution. The location of the Z mass peak can be used to correct the momentum scale. Momentum resolution is better in MC than data, so MC muon transverse momenta are rescaled and smeared with the following:

$$\frac{1}{p_T'} = \frac{1}{\alpha p_T} + \xi, \tag{4.11}$$

where α is a scale factor, and ξ is a random Gaussian correction. The width of the Gaussian is chosen so that the Z width in MC matches the observed width in data.

Muon Isolation

Muons from the decay of W bosons are expected to be isolated from jets, while muons from semileptonic decays of hadrons will be non-isolated. Muon isolation is therefore used in the top quark mass analysis to remove the otherwise large QCD multijet background.

A loose isolation cut requires that muons be separated from jets with $\Delta R(\mu, \text{jet}) > 0.5$. In addition, the following two variables are used for tight muon isolation: [84]

$$\text{Rat11} = \text{Halo}(0.1, 0.4)/p_T^{\text{muon}} < 0.08 \tag{4.12}$$

$$\text{Rattrk} = \text{TrkCone}(0.5)/p_T^{\text{muon}} < 0.06 \tag{4.13}$$

Halo(0.1,0.4) is the sum of the E_T of calorimeter clusters in a hollow cone between $\Delta R = 0.1$ and $\Delta R = 0.4$ away from the muon. Clusters in the coarse hadronic calorimeter are not used

muon selection	
Muon quality	medium, nseg=+3
track match	required
Cosmic veto	required
p_T	$\geq 20\text{GeV}/c$
$\lvert\eta\rvert$	≤ 2.0
Isolation	tight isolation
DCA significance	3
$\Delta z(\mu, \text{PV})$	$\leq 1\text{cm}$
Second Muon Veto	required

Table 2
Muon selection for the μ+jets sample.

due to the larger noise. TrkCone(0.5) is the sum of the p_T of all tracks (except for the muon's track) within a cone of radius $\Delta R = 0.5$ around the muon.

Event Selection

All event selection criteria pertaining to muons are summarized in Table 2. The cosmic cut is a cut on the timing of hits in the muon scintillation detectors (see Sect. 3.2.5). The $|\eta|$ cut is used to ensure that the muon is within the full coverage of the muon system. The veto on events with more than one muon is to ensure orthogonality with the dilepton top quark mass analysis.

4.5 Secondary Vertex Tagger

Since $t\bar{t}$ events are expected to have two b-quarks from the decays of the two top quarks, the ability to identify jets likely to have arisen from b-quarks provides a powerful discrimination between signal and background. The b-quark has a relatively long lifetime (1.6 ps), and typical b-quarks from top quark decays have decay lengths of about 3 mm (assuming a momentum of $\sim$40 GeV/c). b-quarks form b-hadrons, which travel a few millimeters away from the primary

vertex before decaying. This creates a *secondary vertex*. If a jet can be associated with a secondary vertex, it is likely to have come from the hadronization of a b-quark. This is the basis behind the secondary vertex tagging (SVT) algorithm. [87]

The SVT algorithm has the following three steps:

- primary vertex reconstruction,
- track-jet reconstruction, and
- secondary vertex reconstruction.

The first step, primary vertex reconstruction, is done using the same **d0root** algorithm described in Ref. 4.2. The remaining two steps are described below.

4.5.1 Track-jet Reconstruction

Track-jets are jets formed out of tracks rather than calorimeter towers. First tracks are preclustered according to the distance of closest approach to the primary vertex in the z-direction. Tracks are added to pre-clusters, starting with the highest p_T track, if the z position is within 2 cm of the centroid of the precluster. Tracks must have: 1) $p_T > 0.5$ GeV/c, 2) at least 2 SMT clusters, 3) a transverse $dca < 0.15$cm, and 4) a dca in the z-direction < 0.40 cm with respect to the primary vertex. The preclusters are used to form jets using the same algorithm used for calorimeter jets (described in Section 4.3.2).

4.5.2 Secondary Vertex Reconstruction

Tracks within reconstructed track-jets having large transverse impact parameter significance ($dca/\sigma > 3.0$) are selected. These tracks are used to form 2-seed tracks, where pairs of tracks within track-jets are fit to common vertices and kept as seeds if the fit χ^2 is less than a threshold. Additional tracks are fit to the seeds if their χ^2 values are below the threshold.

Preliminary vertices are selected with the following requirements:

- opening angles smaller than 0.1,
- at least 1 track with $p_T > 2$ GeV/c (track multiplicity = 2) or > 1.5 GeV/c (track multiplicity > 2),
- transverse decay length < 2.5 cm, and
- longitudinal decay length < 3 cm.

The final vertex selection is done through an iterative process that removes multiple vertices sharing the same tracks. The vertices are ordered by opening angle. The vertex with the smallest opening angle is selected, and then all vertices are selected that share at least one track with the selected vertex. Then the next-best vertex is selected, and the process is repeated until no vertices remain.

A calorimeter jet is considered to be b-tagged if it has at least one secondary vertex with ΔR(SV,jet) < 0.5, with a decay length significance greater than 5.0. The Tight version of SVT was used for the top mass analysis b-tagging. The Tight criteria, chosen to maximize the b-tagging efficiency and minimize the mistag rate for light-flavor jets, are:

- track $p_T > 1.0$ GeV/c
- track impact parameter significance > 3.5
- track $\chi^2 < 3.0$
- vertex $\chi^2 < 100$
- vertex decay length < 2.6 cm
- decay length significance > 7.0

5. THE MATRIX ELEMENT METHOD

5.1 Method Overview

The top quark mass is measured using a maximum likelihood estimation (MLE) technique. With maximum likelihood estimation, a likelihood is constructed for the data sample that contains the parameter to be measured. For an unbinned likelihood, the total likelihood is the product of likelihoods for each individual event. Maximizing the likelihood with respect to the parameter to be measured gives the most likely value of the parameter.

The dependence of the likelihood on a parameter to be measured, α, depends on whether the event is a signal or background event. It is shown in Appendix B that

$$\mathcal{L}(D|n_s, n_b, \alpha) = q(N, n_s + n_b) \prod_{i=1}^{N} \frac{n_s p(y_i, \alpha|\text{sgn}) + n_b p(y_i, \alpha|\text{bkg})}{(n_s + n_b)}, \tag{5.1}$$

where $p(y_i, \alpha|\text{sgn})$ is the likelihood for the i^{th} event, calculated under the assumption that the event is a signal event, and $p(y_i, \alpha|\text{bkg})$ is the likelihood for the same event with the assumption that it is background. The set of kinematic variables measured for the i^{th} event is indicated by y_i. The numbers of signal and background events are, respectively, n_s and n_b. The term $q(N, n_s + n_b)$ allows for Poisson fluctuations of n_s and n_b for a fixed value of N, the total number of events.

The likelihood, $p(y_i, \alpha)$, depends on the likelihood of detecting the event, $Acc(y_i)$, the likelihood of the event firing a trigger, $\eta_{trigger}$, and, if b-tagging information is to be used, the likelihood of the event being b-tagged with one or more b-jets, η_{btag}. The first two clearly do not depend on whether the event is signal or background, since detector acceptance and trigger

efficiencies depend only on the measured kinematics. The estimation of b-tagging efficiencies do, however, depend on the type of event, since different flavors of jets have different likelihoods of being b-tagged. The Poisson term $q(N, n_s + n_b)$ can be dropped because it contributes a multiplicative term to the likelihood only. The final likelihood can then be written as

$$\mathcal{L}(f_{sgn}, m_t, JES) = \prod_{i=1}^{N} \frac{\mathrm{Acc}(y_i)\eta_{trigg}(y_i)}{p(y_i)} \times \left(f_{sgn}\eta_{tag}(y_i|\mathrm{sgn})P^i_{sgn}(m_t, JES) + (1 - f_{sgn})\eta_{tag}(y_i|\mathrm{bkg})P^i_{bkg} \right), \tag{5.2}$$

where f_{sgn}, the signal fraction, has replaced $n_s/n_s + n_b$. P_{sgn} and P_{bkg} are referred to as *signal* and *background probabilities*, respectively. P_{sgn} and P_{bkg} calculations are summarized briefly here, and described in more detail (including integration techniques) in App. C.

The matrix element method makes the assumption that the event likelihoods are proportional to differential cross-sections, calculated according to Fermi's Golden Rule. The differential cross-section $\mathrm{d}^n\sigma_{hs}$ for a hard-scatter interaction between two partons with four-momenta q_1 and q_2 and masses m_1 and m_2 into a final state with n particles with momenta $p_1, \cdots, p_n$, is given by

$$\mathrm{d}^n\sigma_{hs} = \frac{(2\pi)^4|\mathcal{M}|^2}{4\sqrt{(q_1 \cdot q_2)^2 - m_1^2 m_2^2}}\, \mathrm{d}\Phi_n(q_1, q_2; p_1, \cdots, p_n). \tag{5.3}$$

The scattering amplitude, $|\mathcal{M}|^2$, is calculated using the Feynman diagrams for the event, which depend on whether the event is assumed to be signal or background. For the top quark mass analysis, the signal process is assumed to be $q\overline{q} \to t\overline{t} \to l\nu b\overline{b}qq'$. The main sources of background are $W(\to l\nu)$ + jets and QCD multijet events. The QCD background is expected to be small, and the topology is expected to be similar to W + jets, so P_{bkg} is calculated using W + jets matrix elements only.

Since the incoming parton momenta are not known, Eqn. 5.3 is convoluted with parton distribution functions (PDF) to allow for all combinations of quark flavors and momenta. It

is assumed that the x- and y-components of the incoming parton momenta are zero, with the z-direction aligned along the beam axis, so the differential cross section for $p\overline{p}$ collisions can be written as

$$\mathrm{d}^n\sigma = \sum_{flavors} \int_{q_1} \int_{q_2} \mathrm{d}^n\sigma_{hs}\ \mathrm{d}q_1\ \mathrm{d}q_2 f(q_1) f(q_2). \tag{5.4}$$

The final state momenta are also not known exactly, so it is necessary to take this into account in the calculation of the event probabilities. It is assumed that the angles of reconstructed particles (i.e. jets and leptons) are precisely measured, so angles of reconstructed particles are used directly for the parton angles. Eqn. 5.4 is convoluted with a resolution function, $W(x, y)$, for each pairing of a reconstructed particle with a parton. The resolution function, also called a *transfer function*, gives the probability density of a parton state x to be reconstructed as y. Transfer functions are described in more detail in Sec. 5.2.

The parameter to be measured is the top quark mass, m_t. It is assumed that the dependence of the W+jets differential cross sections on m_t is negligible, so background probabilities do not depend on m_t. Thus the entire dependence of the total event likelihood comes from P_{sgn}.

The leading uncertainty in the top quark mass measurement arises from uncertainties in the overall jet energy scale, *JES* (see Sect. 4.3.2). The JES parameter is a global parameter used to rescale the energies of all jets in the event. By varying the likelihood with respect to JES in addition to m_t, the resulting fit gives an error which contains contributions from statistics and the JES systematic error. This method gives a smaller combined statistical + JES error. The primary dependence of the likelihood on JES comes from P_{sgn}, since signal events contain a hadronically-decaying W boson and the Bred-Wigner shape of the W decay gives tighter constraints on jet energies than for background events. So P_{bkg} is calculated with JES fixed at 1.0.

5.2 Transfer functions

The *transfer function*, $W(y,x)$, is used to estimate the initial state parton momenta from the final state momenta. The following assumptions are made in the construction of the transfer function:

- Parton angles are the same as reconstructed particle angles for the lepton and all four jets.
- For quarks, parton momentum can be approximated by a double Gaussian centered on the measured particle momentum for jets, with widths determined by Monte Carlo (MC).
- For electrons, the resolution is good enough that reconstructed momentum can be used for parton momentum.
- For muons, parton momenta is determined similarly to quark momenta, except a single Gaussian is used.

Of course, none of these assumptions are absolutely correct. They are expected to be reasonable, however, given the current precision of the measurement.

The final form of $W(y,x)$ is given by:

$$\begin{aligned} W(y,x) = & \frac{\delta^2(\Omega_{lep}^{meas} - \Omega_{lep})}{|\vec{p}_{lep}^{meas}|^2} W_{lep}(|\vec{p}_{lep}^{meas}|, |\vec{p}_{lep}|) \\ & \times \prod_{i=1}^{4} \frac{\delta^2(\Omega_{jet_i} - \Omega_{q_i})}{|\vec{p}_{jet}|^2} W_{jet}(|\vec{p}_{jet_i}|, |\vec{p}_{q_i}|), \end{aligned} \tag{5.5}$$

where W_{jet} is a double Gaussian,

$$\begin{aligned} W_{jet}(p_{jet}, p_q) = & \frac{1}{\sqrt{2\pi}(p_2 + p_3 p_5)} \\ & \left(\exp\left(\frac{-(p_q - p_{jet} - p_1)^2}{2p_2^2} \right) + p_3 \exp\left(\frac{-(p_q - p_{jet} - p_4)^2}{2p_5^2} \right) \right), \end{aligned} \tag{5.6}$$

and W_{lep} is a single Gaussian,

$$W_{lep}(p_{lep}^{meas}, p_{lep}) = \frac{1}{\sqrt{2\pi}\sigma_{lep}} \exp\left(\frac{-(1/p_{lep} - 1/p_{lep}^{meas})^2}{2\sigma_{lep}^2}\right). \quad (5.7)$$

Note that $W_{jet}(p_{q_i}, p_{jet_i})$ and $W_{lep}(p_{lep}, p_{meas})$ are normalized by construction. $W_{lep}(p_{lep}, p_{meas})$ is replaced by $\delta(\vec{p}_{lep}^{meas} - \vec{p}_{lep})$ for the e+jets channel. The parameters p_1, p_2, p_4, and p_5 have the same dimensions as p_q and p_{jet}. The parameter p_3 is dimensionless.

5.2.1 Jet Transfer Function Derivation

The derivation of jet transfer functions, discussed in detail in Ref. [22], is only briefly summarized here. The p_i parameters in Eqn. 5.5 are parametrized as linear functions of parton energies,

$$p_i = a_i + E_p b_i, \quad (5.8)$$

where E_p is the parton energy (in GeV). Each transfer function has five p_i parameters, so there are 10 parameters (a_i and b_i) to be fit for each transfer function. A different set of parameters is derived for each of four $|\eta|$ regions: $|\eta| < 0.5$, $0.5 < |\eta| < 1.0$, $1.0 < |\eta| < 1.5$, and $1.5 < |\eta| < 2.5$. Jet transfer functions are parametrized separately for light- and heavy-flavor jets, so there are 80 parameters in all to completely characterize the transfer functions for all jets. (Forty additional parameters, described in Ref. [22], are used for soft-muon tagged b-jets, but these are not used for the top mass analysis described in this dissertation.)

Transfer functions are determined with $t\bar{t}$ Monte Carlo samples. Samples are available with m_t values ranging from 160 to 190 GeV/c^2 in 5 GeV/c^2 increments, and also 150 GeV/c^2, and 200 GeV/c^2. All events are combined into a large sample to determine transfer functions. Events from the sample are selected in which one top quark decays to a b quark and a W boson which

- q_1, q_2 are incoming parton momenta, described by *parton distribution functions*: $f_{PDF}(q)$

- $\mathcal{F}$, the flux factor, is given by:

$$\mathcal{F} = \frac{(2\pi)^4}{4\sqrt{(q_1 \cdot q_2)^2 - m_1^2 m_2^2}} \tag{5.11}$$

- $|\mathcal{M}|^2$ is the squared matrix element for the process

- $\mathrm{d}\Phi_6$ is the phase space factor for a process giving 6 particles in the final state

- $W(y,x)$, the *transfer function*, is described in Sec. 5.2.

5.3.1 P_{sgn}

The signal process is assumed to be:

- $qq \to t\bar{t} \to l + \text{jets}$.

Since approximately 85% of the $t\bar{t}$ events come from $q\overline{q}$ collisions, this is a reasonable assumption. The other 15% of the events come from gluon fusion and are ignored. The matrix element, $|\mathcal{M}|^2$, was calculated directly using [88]

$$|\mathcal{M}|^2 = \frac{g_s^4}{9} F\overline{F}(2 - \beta^2 \sin^2\theta_{qt}). \tag{5.12}$$

Here $g_s^2/(4\pi) = \alpha_s$ is the strong coupling constant. The parameters β and θ_{qt}, the velocity of the top quarks and the angle between the incoming partons (the z-axis) and the outgoing top quarks, are evaluated in the $t\bar{t}$ rest frame. F and $\overline{F}$ are given by

$$\begin{aligned} F = \frac{g_w^4}{4} &\left(\frac{m_{bl\nu}^2 - m_{l\nu}^2}{(m_{bl\nu}^2 - m_t^2)^2 + (m_t\Gamma_t)^2} \right) \\ &\times \left(\frac{m_{bl\nu}^2(1 - \cos^2\theta_{bl}) + m_{l\nu}^2(1 + \cos^2\theta_{bl})^2}{(m_{l\nu}^2 - m_W^2)^2 + (m_W\Gamma_W)^2} \right), \end{aligned} \tag{5.13}$$

$$\begin{aligned} \overline{F} = \frac{g_w^4}{4} &\left(\frac{m_{\overline{b}d\overline{u}}^2 - m_{d\overline{u}}^2}{(m_{\overline{b}d\overline{u}}^2 - m_t^2)^2 + (m_t\Gamma_t)^2} \right) \\ &\times \left(\frac{m_{\overline{b}d\overline{u}}^2(1 - \cos^2\theta_{\overline{b}d}) + m_{l\nu}^2(1 + \cos^2\theta_{\overline{b}d})^2}{(m_{d\overline{u}}^2 - m_W^2)^2 + (m_W\Gamma_W)^2} \right). \end{aligned} \tag{5.14}$$

Here g_w is the weak charge, $g_w^2 = 8m_W^2 G_F\sqrt{2}$, m_W is the W boson mass, Γ_t and Γ_W are the widths of the top quark and W boson masses. The squared masses of the top quarks and W bosons within the event are denoted by m_{xyz}^2 and m_{xy}^2, respectively, where x,y, and z are the decay products. The angles $\theta_{l\nu}$ and $\theta_{d\overline{u}}$ are evaluated in the W rest frame. The symbols d and $\overline{u}$ denote all possible hadronic W decay products.

5.3.2 P_{bkg}

The background process is assumed to be either of the following:

- $qq \rightarrow W + gggg$
- $qq \rightarrow W + bbgg$

The code for calculating the matrix element was downloaded from the MadGraph website (see Ref. [29]) and used directly. To reduce the time required to compute the probabilities, only the positive helicity solutions were calculated. The final result for $|\mathcal{M}|^2$ was doubled to account for two helicity states. MadGraph was used for two reasons:

- it allows calculating the background probability normalizations directly, and
- it allows an easier introduction of Wbbjj (and additional) matrix elements.

The background probability integration has divergences arising from small angles between neighboring quarks. To eliminate these divergences, cuts are imposed on the angles between quarks. The parton-level cuts used for the background probability integration are:

- $|\eta_{quark}| \leq 3$
- $\Delta R(q_1, q_2) \geq 0.4$

The two probabilities, P_{Wgggg} and P_{Wbbgg}, are combined according to their expected contribution to the total background. This is calculated using the normalizations, which represent the

total cross-section for each process after acceptance is considered (with no b-tagging applied). With the following definitions:

$$f_{Wgggg} = \frac{\sigma_{Wgggg}}{\sigma_{Wgggg} + \sigma_{Wbbgg}}$$
$$f_{Wbbgg} = \frac{\sigma_{Wbbgg}}{\sigma_{Wgggg} + \sigma_{Wbbgg}}$$

The b-tagging efficiency weighted P_{bkg} becomes:

$$\eta^{bkg}_{Wgggg} P_{bkg} = f_{Wgggg}\eta^{tag}_{Wgggg} P_{Wgggg} + f_{Wbbgg}\eta^{tag}_{Wbbgg} P_{Wbbgg}. \tag{5.15}$$

5.3.3 Normalizations

The normalizations for signal and background event probabilities come from integrating Eqn. 5.10 over all available reco-level phase space. Since the event probability is itself an integration over all available parton-level phase space, the resulting integral is a 21-dimensional integration (20-dimensional for the e+jets channel, which has a δ-function for the leptonic transfer function).

The integral performed for the normalization is

$$\begin{aligned}\sigma_{norm} = &\int \mathrm{d}q_1 \mathrm{d}q_2 f_{PDF}(q_1) f_{PDF}(q_2) \frac{(2\pi)^4 \mathrm{Acc}_x(x) |\mathcal{M}|^2}{8|\vec{q}_1||\vec{q}_2|} \mathrm{d}x \\ &\times W_{lep}(p^{meas}_{lep}, p_{lep})\ \mathrm{d}|\vec{p}^{meas}_{lep}| \left(\prod_{i=1}^{4} W_{jet}(p_{jet_i}, p_{q_i})\ \mathrm{d}|\vec{p}_{jet_i}| \right) \\ &\times \mathrm{Acc}_y(y)\, \eta_{trigger}(y)\, \eta_{btag}(y) \mathrm{d}y. \end{aligned} \tag{5.16}$$

$\mathrm{Acc}_y(y)$ accounts for the detector acceptance. This has a value of zero for the following:

- if any reco-level jet fails the kinematic jet cut (20 GeV)
- if the reco-level lepton fails the kinematic lepton cuts (20 GeV)

- if the missing E_T (calculated as the negative of the vector sum of all reco-level particles in the event) fails the missing E_T cut (20 GeV)

$\mathrm{Acc}_x(x)$ places limits on parton-level variables. The cuts are the same used for the event probability integrations. The trigger efficiency, $\eta_{trigger}(y)$, accounts for trigger selection. It is computed using dedicated tools developed within the DØ top group. [26]

To account for the b-tagging selection, η_{tag} weights the integral by the b-tagging probability. The b-tagging efficiencies are parametrized in both jet p_T and jet $|\eta|$, as described in Ref. [23]. To simulate the jet p_T, parton energies in the integration are "smeared" using transfer functions to simulate the conversion of partons to jets in the detector. These smeared jet energies are then used for the calculation of b-tagging efficiencies.

Normalizations are calculated with and without the use of b-tagging efficiencies. The 0, 1, and $\geq$2 tag normalizations are used in the matrix element method. Further details can be found in App. C.

Signal Normalization

The untagged normalization is parametrized as a function of JES and m_t, 1st order in JES and 3rd order in m_t. The equation used for the fit is

$$\begin{aligned}\sigma_{norm}^{untagged} &= p_0 + p_1 JES + (p_2 + p_3 JES)m_t + (p_4 + p_5 JES)m_t^2 \\ &\quad + (p_6 + p_7 JES)m_t^3. \end{aligned} \tag{5.17}$$

The values of p_0 through p_7 found for the untagged samples are tabulated in Table 3. The fits are shown in Fig. 5.1.

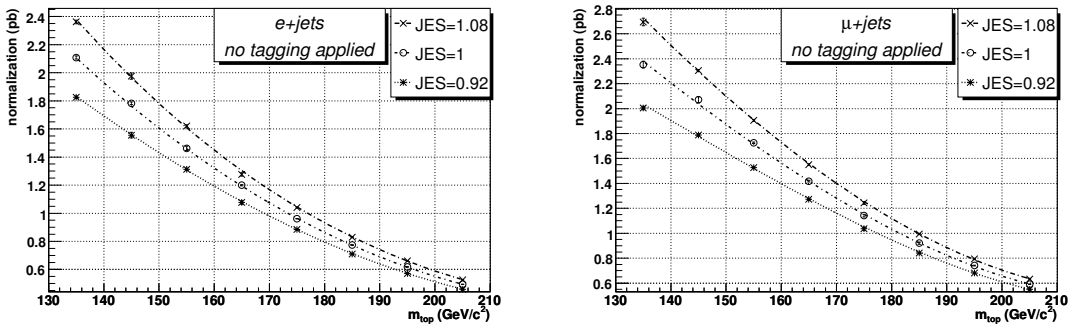

Fig. 5.1. Normalization constants vs. mass hypotheses with no tagging requirements.

	e+jets	μ+jets
p_0	-40.2994	-53.1806
p_1	48.6478	65.8293
p_2	5.9998×10^{-1}	7.9708×10^{-1}
p_3	-6.6026×10^{-1}	-9.0843×10^{-1}
p_4	-2.9921×10^{-3}	-3.9921×10^{-3}
p_5	3.0679×10^{-3}	4.2802×10^{-3}
p_6	5.0018×10^{-6}	6.6827×10^{-6}
p_7	-4.8535×10^{-6}	-6.8410×10^{-6}

Table 3
$t\bar{t} \rightarrow l + jets$ normalization parameters for ≥ 0 b-tags (untagged). (see Eqn. 5.17)

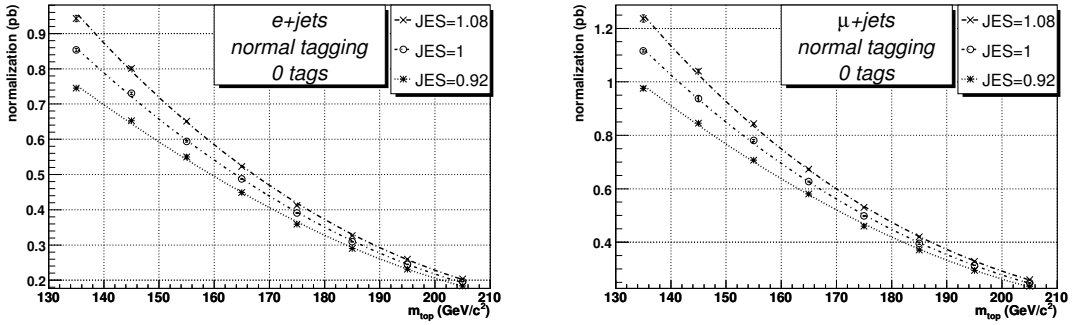

Fig. 5.2. Normalization constants vs. mass hypotheses for 0 tags.

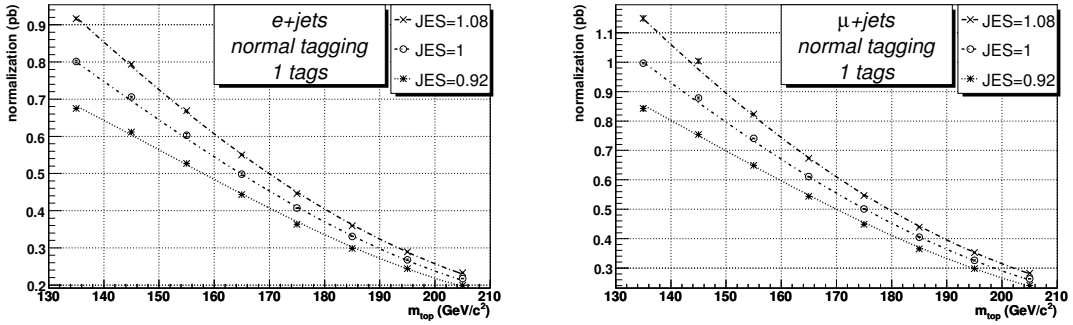

Fig. 5.3. Normalization constants vs. mass hypotheses for 1 tag.

The tagged normalizations use a scale factor multiplied by the untagged normalization. The scale factor is parametrized as a function of JES and m_t using the following equation:

$$\sigma_{norm}^{tag} = \left(q_0 + q_1 \left(\frac{m_t - 175}{m_t} \right) + q_2 (JES - 1) \right) \sigma_{norm}^{untagged}. \tag{5.18}$$

The values of q_0, q_1, and q_2 for the tagged normalizations are tabulated in Table 4.

Figures 5.2 through 5.4 show the normalizations for the 0-tagged (no b-tagged jets), single-tagged (1 b-tagged jet), and double-tagged (2 or more b-tagged jets) event probabilities.

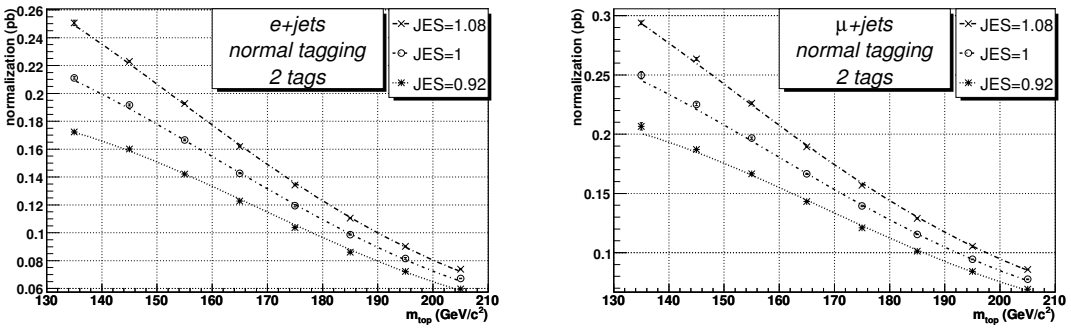

Fig. 5.4. Normalization constants vs. mass hypotheses for $\geq$2 tags.

# tags	q_n	e+jets	μ+jets
0 tags	q_0	0.4287 ± 0.0003	0.4427 ± 0.0003
	q_1	-0.0344 ± 0.0020	-0.0372 ± 0.0028
	q_2	-0.1257 ± 0.0038	-0.1336 ± 0.0051
1 tag	q_0	0.4473 ± 0.0003	0.4422 ± 0.0002
	q_1	0.1305 ± 0.0019	0.1291 ± 0.0018
	q_2	0.0339 ± 0.0038	0.0302 ± 0.0034
$\geq$2 tags	q_0	0.13122± 0.00008	0.12360± 0.00008
	q_1	0.0821 ± 0.0005	0.0830 ± 0.0007
	q_2	0.0553 ± 0.0010	0.0596 ± 0.0013

Table 4
$t\bar{t} \rightarrow l + jets$ normalization parameters for 0, 1, and $\geq$2 b-tags. (see Eqn. 5.18)

	0 tag	1 tag	$\geq$ 2 tag	$\geq$ 0 tags
e +jets	0.644±0.017	(7.69±0.10)×10^{-3}	(3.60±0.06)×10^{-5}	0.645±0.014
μ+jets	0.918±0.021	(1.10±0.01)×10^{-2}	(5.05±0.07)×10^{-5}	0.956±0.023

Table 5
$Wgggg$ normalization constants for 0, 1, $\geq$2, and $\geq$0 b-tags (in pb).

	0 tag	1 tag	$\geq$ 2 tag	$\geq$ 0 tags
e +jets	0.040±0.001	0.044±0.002	(1.02±0.02)×10^{-2}	0.095±0.002
μ+jets	0.062±0.002	0.060±0.002	(1.38±0.04)×10^{-2}	0.140±0.004

Table 6
$Wbbgg$ normalization constants for 0, 1, $\geq$2, and $\geq$0 b-tags (in pb).

Background Normalization

Normalizations for background probabilities are calculated similarly to calculations for signal probabilities. The MadGraph matrix element is used to calculate $|\mathcal{M}^+|^2$, and the following integral is performed:

$$\begin{aligned}\sigma_{norm}^{bkg} = & \int \mathrm{d}x_1 \mathrm{d}x_2 f'(x_1) f'(x_2) \frac{(2\pi)^4 2\mathrm{Acc}(x)|\mathcal{M}^+|^2}{8|\vec{q}_1||\vec{q}_2|}\ \mathrm{d}x \\ & \times W_{lep}(p_{lep}^{meas}, p_{lep})\ \mathrm{d}|\vec{p}_{lep}^{meas}| \left(\prod_{i=1}^{4} W_{jet}(p_{q_i}, p_{jet_i})\ \mathrm{d}|\vec{p}_{jet_i}|\right) \\ & \times\ \mathrm{Acc}(y)\, \eta_{trigger}(y)\, \eta_{btag}(y)\ \mathrm{d}y. \end{aligned} \tag{5.19}$$

It is not necessary to vary m_t or JES in determining the background normalization, since these are not varied in calculating background probabilities (see Sect. 5.1. The values obtained from integrations are shown in Table C.5.3.

Jet-parton combinations

For each event, there are 4!=24 ways to match 4 jets in the final state to 4 final state partons. For signal events, the number of combinations is reduced to 12 by taking a mean value of the two combinations with the quarks from the hadronic-W decay interchanged. For P_{Wgggg}, all 4 gluons can be interchanged without affecting the matrix element. Thus only one combination needs to be calculated. For P_{Wbbgg}, all 24 combinations are calculated explicitly.

Each combination has a unique tagging probability, η^{tag}, since the per-jet tagging probability depends on the flavor of the jet. An average is calculated using the probabilities for all jet-parton combinations, weighting each probability by its tagging probability. Thus the total b-tag weighted probability is given by:

$$\eta_{sgn} P_{sgn} = \frac{1}{12} \sum_{icomb=1}^{12} \prod_{j=1}^{4} w_j^{icomb} P_{sgn}^{icomb}$$

$$\eta_{bkg} P_{bkg} = \left(\prod_{j=1}^{4} w_j P_{Wgggg} \right) + \left(\frac{1}{24} \sum_{icomb=1}^{24} \prod_{j=1}^{4} w_j^{icomb} P_{Wbbgg}^{icomb} \right),$$

If the jet is tagged, w_j^{icomb} is equal to η^{tag}. This is calculated using the parametrizations described in Section 5.3.3, which vary with jet p_T and η, and depend on the jet flavor. If the jet is not tagged, w_j^{icomb} is equal to (1 - η^{tag}).

***b*-tagging**

The secondary vertex b-tagging algorithm (SVT) identifies jets likely to have arisen from b-quark hadronization. This is done by reconstructing the decay vertex of the relatively long-lived B hadron within the jet. The details of the tagging algorithm can be found in Ref. [23]. The

parametrizations used in this analysis are identical to those used in the cross-section analysis for which the b-tagging parametrizations were determined, described in the same note.

b-tagging was used in the matrix element method in the following two ways:

1. to determine weighting factors for the probabilities corresponding to the multiple combinations of assigning jets in the detector to quarks in the final state, and

2. to correctly normalize P_{sgn} and P_{bkg} depending on the number of b-tagged jets in the event.

A single likelihood was generated using all events, including events with no b-tagged jets, to most efficiently use the available statistics.

In ensemble testing, tagging of jets is simulated by picking a random number between 0 and 1, and tagging the jet if the per-jet tagging probability, η^{tag}, is greater than the random number.

Comparisons of Signal and Background Probabilities

The likelihood (see Eqn. 5.2) is not affected if P_{sgn} and P_{bkg} are both multiplied by a constant factor. Even if the factor varies event-by-event, there is no effect on the fit as long as the factor does not vary with m_t, JES, or f_{top}. Thus the ratio of P_{sgn} to P_{bkg} is an important quantity for an event, and, as the relative probability for the event to be a signal event, it can be used to judge the ability of the method to discriminate between signal and background.

For properly normalized probabilities, signal events should tend to have values of P_{sgn}/P_{bkg} greater than 1, while background events should have P_{sgn}/P_{bkg} values less than 1. Figures 5.5 and 5.6 show $\log_{10}(P_{sgn})$ vs. $\log_{10}(P_{bkg})$ for top MC events (m_t = 175 GeV/c^2), $Wjjjj$, and $Wbbjj$ MC events.

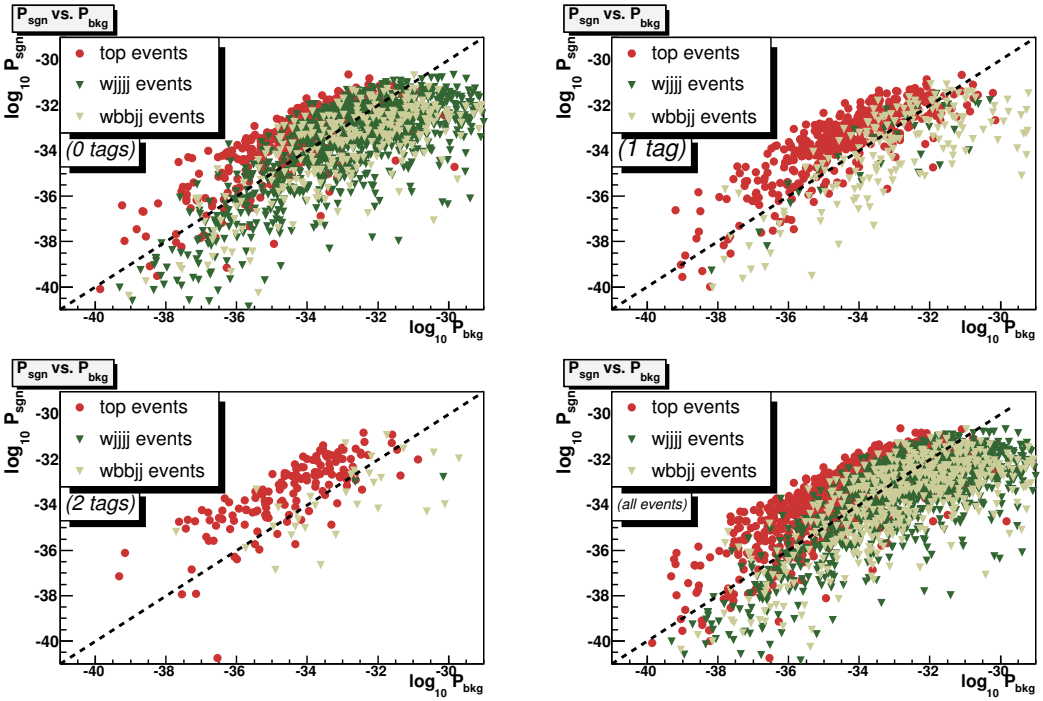

Fig. 5.5. Signal vs. background probabilities for top, $Wjjjj$, and $Wbbjj$ MC events, e+jets (0, 1, $\geq$2 tags, and all-inclusive).

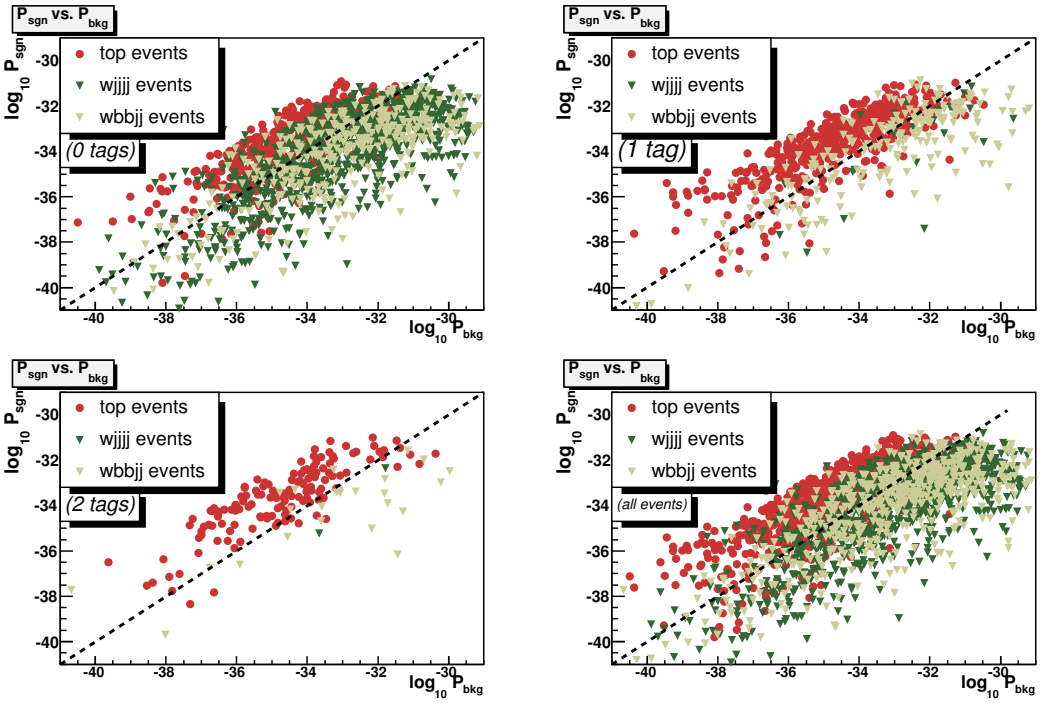

Fig. 5.6. Signal vs. background probabilities for top, $Wjjjj$, and $Wbbjj$ MC events, μ+jets (0, 1, $\geq$2 tags, and all-inclusive).

Bias in Signal Fraction Estimation Top MC events are clearly discriminated as signal events, whereas background MC events are not as well discriminated. It is expected that this will result in systematic overestimations of signal fractions, since most of the signal events look like signal and a large fraction of background events do as well. In addition, it is expected that $t\bar{t}$ events which contain extra jets, whether due to gluon splitting or $t\bar{t}$ production in association with extra jets, may have worse discrimination than $t\bar{t}$ events in which all four jets came directly from the four final-state quarks.

To see the effect, events are selected in which all four jets have been matched to a $\Delta R = 0.5$ cone to the final state quarks. Note that this type of *jet-parton matching* is not the same type of matching that will be used for background MC events. Events are binned in $\log_{10}(P_{sgn}/P_{bkg})$. As Figures 5.7 and 5.8 show, the discrimination of events as signal events is slightly degraded for events that are not jet-parton matched, but these events still tend to have P_{sgn}/P_{bkg} greater than one.

Ensemble testing (Chapt. 6) shows that there is indeed a bias in the fitted signal fraction, but it has no significant effect on the m_t determination.

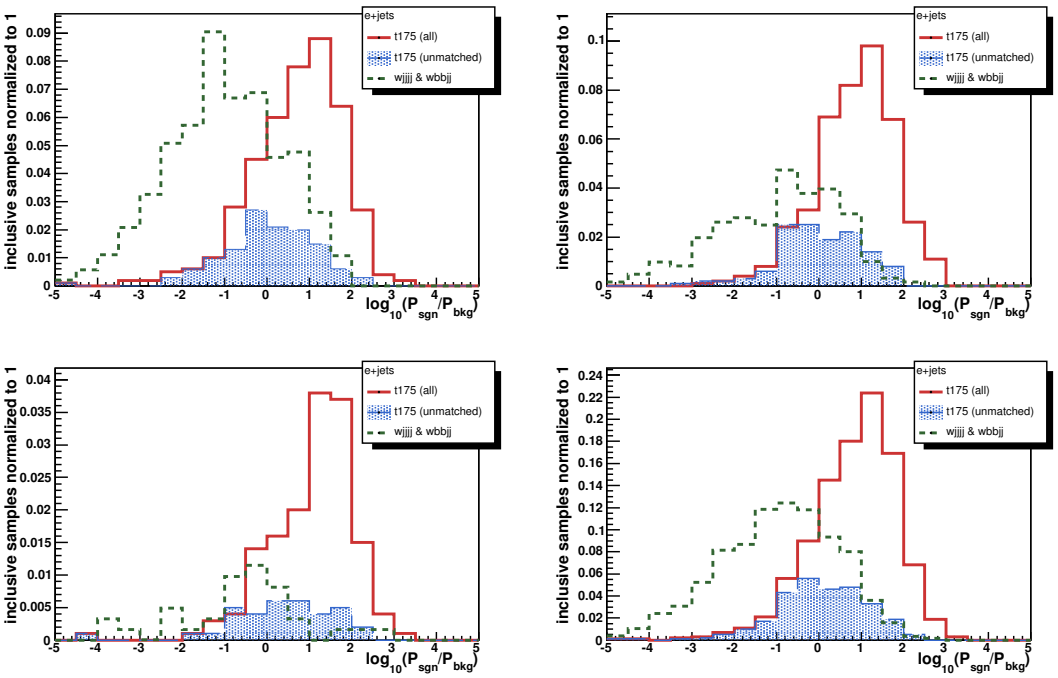

Fig. 5.7. Signal vs. background probabilities for top, $Wjjjj$, and $Wbbjj$ MC events, e+jets (0, 1, $\geq$2 tags, and all-inclusive).

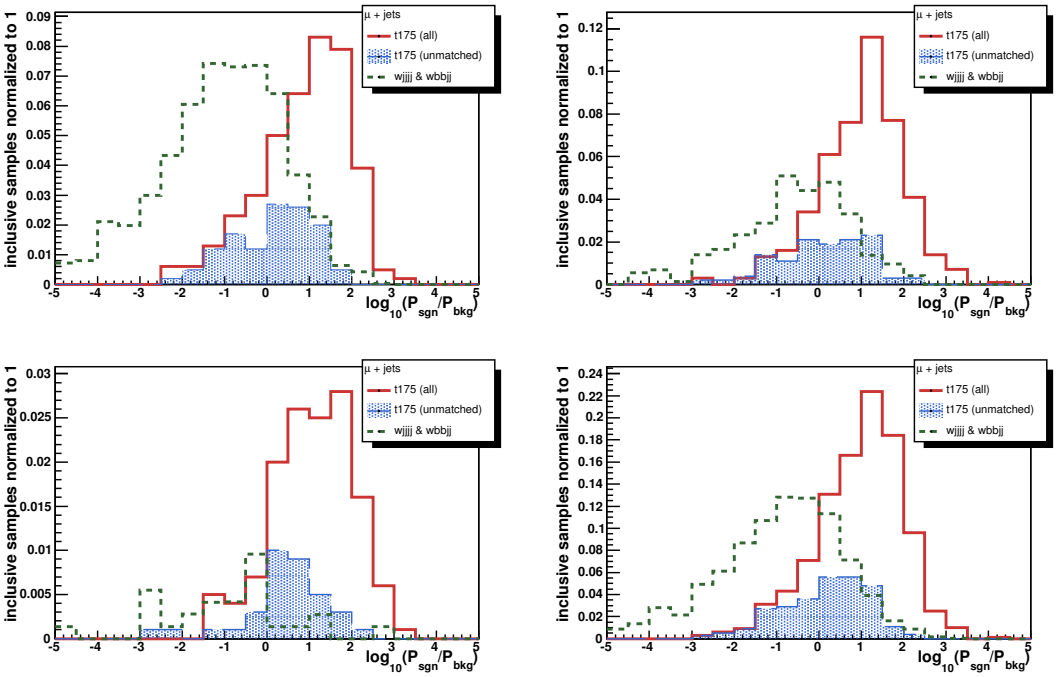

Fig. 5.8. Signal vs. background probabilities for top, $Wjjjj$, and $Wbbjj$ MC events, μ+jets (0, 1, $\geq$2 tags, and all-inclusive).

5.4 Likelihood Fitting

5.4.1 Event likelihood and signal fraction

P_{sgn} and P_{bkg}, properly normalized, are used to construct probabilities for each event. These event probabilities are combined to form a total likelihood for the entire data sample. Since this likelihood is a function of m_t and JES, the most likely values of m_t and JES can be found by maximizing the likelihood with respect to these two variables.

The event probability for the i^{th} event is expressed as:

$$P^i_{evt}(m_t, JES, f_{top}) = \\ f_{sgn}\eta^{sgn}_{btag}P^i_{sgn}(m_t, JES) + (1 - f_{sgn})\eta^{bkg}_{btag}P^i_{bkg}. \quad (5.20)$$

The variable f_{sgn}, the expected signal fraction, is allowed to float in the minimization process.

Note that the b-tagging efficiencies, η^{sgn}_{btag} and η^{bkg}_{btag}, are calculated assuming that the event is, respectively, signal or background. This can result in different tagging efficiencies, since the flavor compositions of the signal and various background samples vary and b-tagging efficiencies are flavor-dependent.

For a set of N data events, the likelihood is defined as the product of the individual probabilities:

$$L(m_t, JES, f_{top}) = \prod_{i=1}^{N} P^i_{evt}(m_t, JES, f_{top}). \quad (5.21)$$

It is easier to minimize the negative logarithm of L, so the following is used instead:

$$-\ln\ L(m_t, JES, f_{top}) = -\sum_{i=1}^{N} \ln\ P^i_{evt}(m_t, JES, f_{top}). \quad (5.22)$$

5.4.2 m_t, JES, and f_{top} fit

The ln L curve must be minimized simultaneously in 3 dimensions. This is done by first minimizing $-\ln\ L$ with respect to f_{sgn} for each value of m_t and JES. The result is a 2-dimensional likelihood, $-\ln\ L_{2D}(m_t, \text{JES})$. Then $-\ln\ L_{2D}$ is fit to a 2-dimensional 4^{th}-order polynomial in the vicinity of the peak to find the minima in m_t^{fit} and JES^{fit}. This is done in the following way:

1. All bins with likelihood values within 0.75 of the minimum likelihood value are selected
2. If the bin is on the edge of the histogram (i.e. at the maximum or minimum in the range of JES and m_t values), the bin is not used
3. If there are less than three bins in either dimension, an extra one or two bins are added on the side closest to the central value
4. The peak is then fit to a 2-dimensional 2^{nd}-order polynomial:

$$-\ln\ L_{2D}(m_t, JES) = p_0 + \frac{1}{2(1-\rho^2)}(A^2 + B^2 - 2\rho AB), \tag{5.23}$$

where

$$\begin{aligned} A &= \frac{JES - JES^{fit}}{\sigma_{JES}}, \\ B &= \frac{m_t - m_t^{fit}}{\sigma_{m_t}}, \end{aligned} \tag{5.24}$$

and p_0, ρ, JES^{fit}, m_t^{fit}, σ_{JES}, and σ_{m_t} are the fit parameters.

5. If there are at least 4×4 bins in m_t and JES, the peak is fit to a 2-dimensional 4^{th}-order polynomial

$$
\begin{aligned}
-\ln\ L(m_t, JES) = p_0 + \frac{A^2}{p_3^2} + \frac{B^2}{p_5^2} \\
+ p_6(A^4 + p_7 A^3 B + p_8 A^2 B^2 + p_9 A B^3 + p_{10} B^4) \\
+ p_{11}(A^3 + p_{12} A^2 B + p_{13} A B^2 + p_{14} B^3).
\end{aligned} \tag{5.25}
$$

Figure 5.9 shows the fit of 41 (e+jets) and 26 (μ+jets) $t\bar{t}$ MC events generated with $m_t = 175$ GeV/c^2. These numbers were chosen because they are the expected number of signal events in the data sample. Figures 5.10- 5.11 show slices of $-\ln\ L_{2D}$ for fixed JES and m_t values for the sample sample.

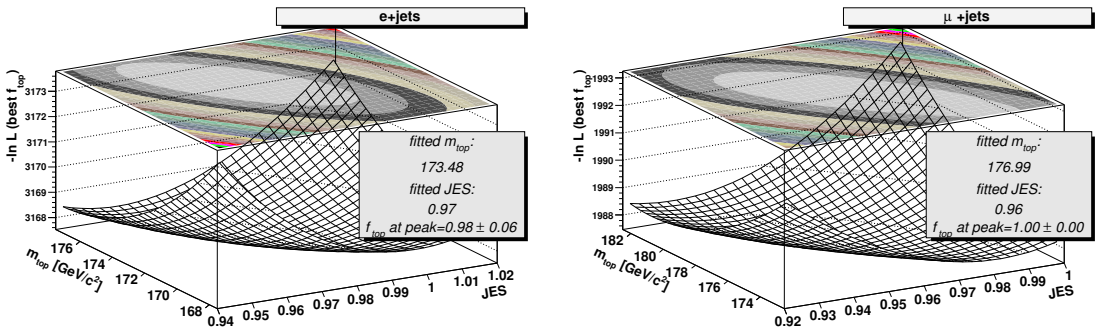

Fig. 5.9. $-\ln\ L_{2D}(m_t, JES)$ for actual $m_t = 175$ GeV/c^2, $JES = 1.0$ MC (e+jets and μ+jets).

5.4.3 Error estimation

Errors in m_t, JES, and f_{sgn} not only are asymmetric, but also are highly correlated. To account for this, the 68% confidence interval around the peak is calculated by integrating the

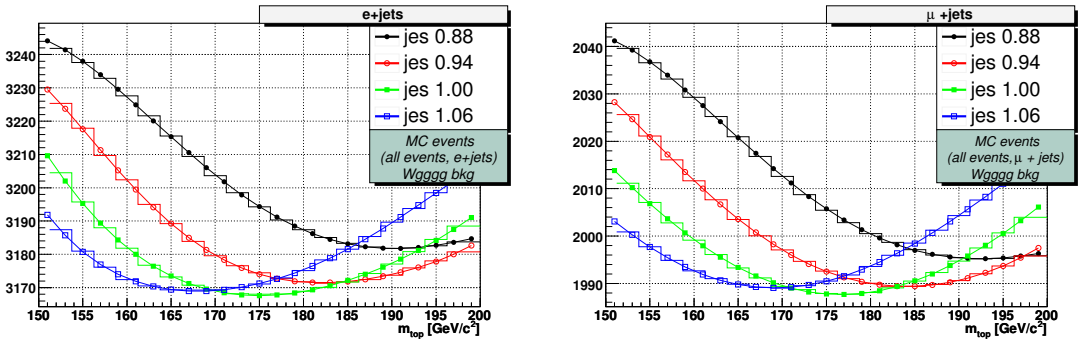

Fig. 5.10. $-\ln\ L_{2D}(m_t, JES)$ vs. m_t for fixed values of JES for actual $m_t = 175$ GeV/c^2, $JES = 1.0$ MC (e+jets and μ+jets).

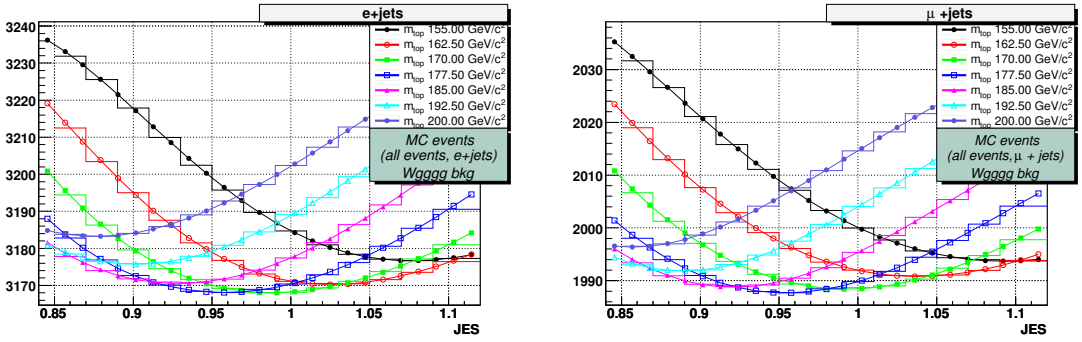

Fig. 5.11. $-\ln\ L_{2D}(m_t, JES)$ vs.JES for fixed values of m_t for actual $m_t = 175$ GeV/c^2, $JES = 1.0$ MC (e+jets and μ+jets).

3-dimensional volume under $L(m_t, JES, f_{sgn})$. Plots of L vs. f_{sgn} for fixed m_t and JES values are Gaussian, so

$$L_{2D}^{proj}(m_t, \text{JES}) = \int L(m_t' = m_t, \text{JES}' = \text{JES}, f_{sgn}')\ \mathrm{d}f_{sgn}' \tag{5.26}$$

$$\approx \frac{L_{peak}}{\sqrt{2\pi}\sigma_{f_{sgn}}}. \tag{5.27}$$

(L_{peak} is the peak value of L vs. f_{sgn}, and $\sigma_{f_{sgn}}$ is the width of the Gaussian.) The final likelihood curve used to calculate asymmetric errors is:

$$L_{1D}^{proj}(m_t) = \int L_{2D}^{proj}(m_t' = m_t, \text{JES}')\ \mathrm{d}(\text{JES'}). \tag{5.28}$$

This integral is done by projecting the 2-dimensional histogram of L_{2D}^{proj} onto the m_t axis, summing over JES bins for each m_t bin. The JES projection is also done to obtain the correlated JES error. These are shown in Figures 5.12 and 5.13. The following plots show the likeli-

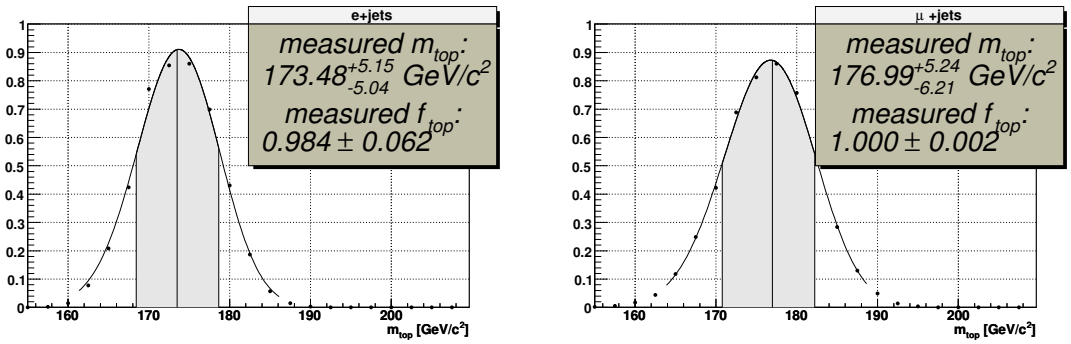

Fig. 5.12. Projection onto m_t axis of $-\ln\ L_{2D}(m_t$,JES) for actual $m_t = 175$ GeV/c^2, JES= 1.0 MC (e+jets and μ+jets).

hood fit for the same $t\bar{t}$ events with b-tagging incorporated into the likelihood as described in Section 5.3.3.

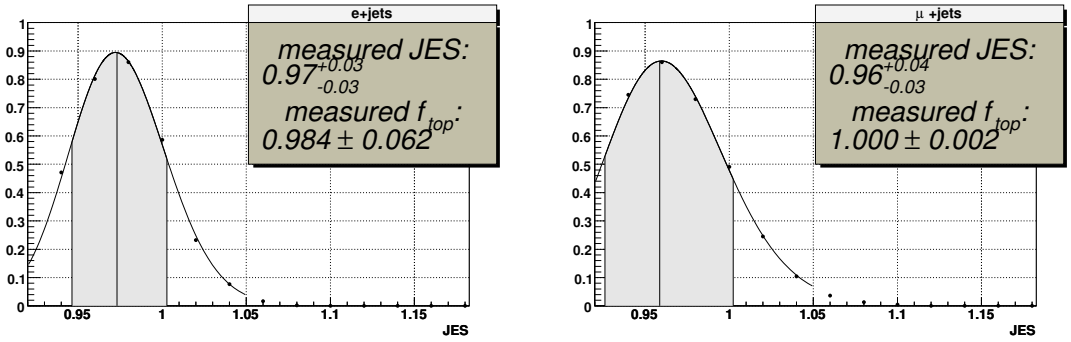

Fig. 5.13. Projection onto JES axis of $-\ln\ L_{2D}(m_t$,JES) for actual $m_t = 175$ GeV/c^2, JES= 1.0 MC (e+jets and μ+jets).

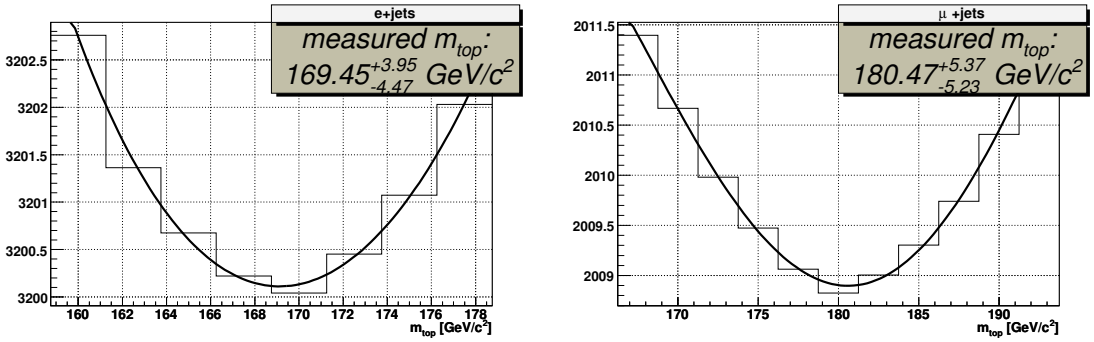

Fig. 5.14. Projection onto m_t axis of $-\ln\ L_{2D}(m_t$,JES) for actual $m_t = 175$ GeV/c^2, JES= 1.0 MC, L includes b-tagging (e+jets and μ+jets).

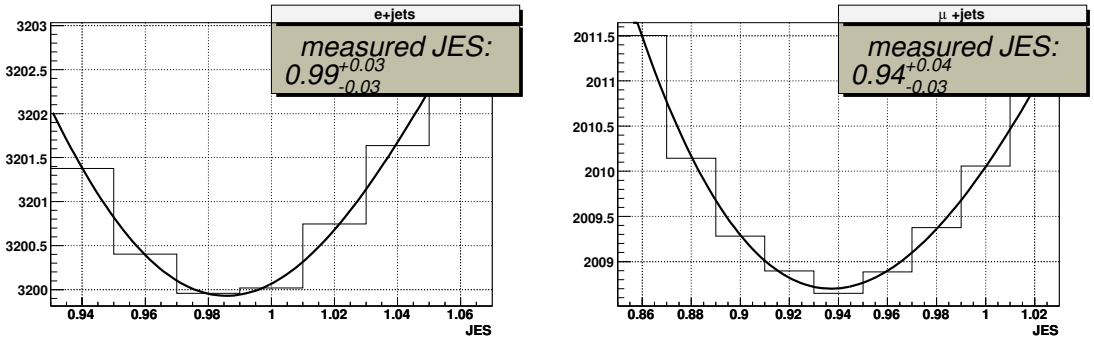

Fig. 5.15. Projection onto JES axis of $-\ln\ L_{2D}(m_t$,JES) for actual $m_t = 175$ GeV/c^2, JES= 1.0 MC, L includes b-tagging (e+jets and μ+jets).

6. TOP QUARK MASS MEASUREMENT

The matrix element method, described in Chapter 5, is tested and calibrated using Monte Carlo-simulated events prior to analyzing data. The statistics available for testing the method is limited not by the number of Monte Carlo (MC) events, however, but by the number of events for which event probabilities have been calculated. The calculation of event probabilities is very CPU-intensive, and evaluating the probabilities for every MC event is not feasible. To maximize the use of all available statistics, *ensemble testing* is used.

In ensemble testing, a set of pseudo-experiments to that the average behavior of a statistical ensemble of pseudo-experiments can be evaluated. Each pseudo-experiment is a simulation of a possible data sample and contains approximately the same numbers of signal and background events as the real data sample. The matrix element method described in the last chapter is applied to each and every pseudo-experiment in the ensemble, and this is used to characterize the behavior of the method. The matrix element method is completely tested and calibrated with ensemble testing prior to application to data to determine the top mass.

The following sections describe the use of ensemble testing, including MC event generation, determination of sample composition, and final calibration of the matrix element method.

6.1 Monte Carlo Samples

6.1.1 Event Generation

The $t\bar{t}$ signal and W+jets background samples were generated using the generation parameters and parton-level cuts prescribed by the "Common Alpgen+Pythia Study" (CAPS)

Generation Parameters	$t\bar{t}$	W+jets
PDF	CTEQ6.LM	CTEQ5L
Q^2	m_t^2	$M_W^2 + \sum p_{T_q}^2$
Underlying event	Tune A	Tune A
light- and c-quark p_T	none	≥ 8 GeV
light- and c-quark $\|\eta\|$	none	≤ 3.5
$\Delta R(q_1, q_2)$	none	≥ 0.4
lepton p_T	none	none
lepton $\|\eta\|$	none	≤ 10
neutrino p_T	none	none

Table 1
Generation parameters used in $t\bar{t}$ and W+jets production.

group. [92] ALPGEN v1.3 [37] was used for the hard-scatter event generation, while PYTHIA v6.2 [38] was used for subsequent parton-showering and introduction of initial- and final-state radiation (ISR and FSR). The parton distribution functions used by PYTHIA were the CTEQ5L set. [39] All event generation parameters are summarized in Table 1.

EVTGEN [40] was used to provide branching fractions and lifetimes for B^0, B^+, B_s^0, B_c^+, and Λ_b. Samples were generated with all lepton + jets final states, including taus. Tau leptons were allowed to decay inclusively for $t\bar{t}$ samples, and forced to decay leptonically for W+jets. In both cases, tau decay was simulated using TAUOLA. [41] Large $t\bar{t}$ samples were generated using each of the following top quark masses: 160, 170, 175, 180, and 190 GeV/c^2.

W+jets samples were generated separately for each combination of flavored quarks. The samples used were $Wjjjj$, $Wcjjj$, $Wc\bar{c}Jj$, and $Wb\bar{b}Jj$, where J corresponds to any of u, d, s, g, c partons, and j is any of u, d, s, g partons. $Wc\bar{c}Jjj$ and $Wb\bar{b}Jjj$ samples were also generated. Events were selected which had only 4 jets in the reconstructed final state, and only 1 b- or c-jet. To simplify the nomenclature, the samples are referred to respectively as $Wjjjj$, $Wcjjj$, $Wccjj$, $Wbbjj$, $W(cc)jjj$, and $W(bb)jjj$.

After hadronization, all events had additional minimum bias $p\overline{p}$ events overlayed. The number of events added was taken from a Poisson distribution with a mean of 0.4 events.

The events were then processed through reconstruction release-p14 GEANT (**d0gstar**) to simulate the DØ detector, and p14 **d0sim** to digitize the **d0gstar** signals. p14.06.00 **d0reco** was used to reconstruct the events.

6.1.2 Combining Heavy-Flavor W+jets Background Samples

The W+jets background was simulated using a combination of ALPGEN for hard-scatter event generation and PYTHIA for showering, underlying event, and minimum bias event overlay. Several theoretical and practical difficulties arise from the combination of two separate packages for hard-scatter event generation and parton-showering:

- Cuts at the generator level are necessary to avoid divergences due to soft and collinear gluon radiation. Significant regions of phase space are missing in ALPGEN event generation, and consequently all cross-sections will be underestimated. This results in errors in the relative background fractions as high as 50%, since the cross-sections are used to determine relative contributions of the various backgrounds to the total background.

- PYTHIA effectively corrects for this through parton showering for initial- and final-state radiation, but, in so doing, it changes the jet multiplicity and/or flavor composition for individual events. This is attributed to gluon radiation and splitting, fragmentation and hadronization, as well as detector acceptance of final-state jets.

Ensemble testing relies on the use of samples that accurately simulate the data sample. b-tagging of events is simulated using the b-tagging efficiencies for individual jets, which depend on the flavors of the jets (see Sect. 6.1.4). Thus, it is crucial that the samples used to generate the ensembles have the correct flavor composition, and also that the flavors of heavy jets are known. This requires the use of a prescription for selecting heavy-flavor Monte Carlo events. The prescription used is identical to the *ad hoc* matching procedure of Ref. [23]:

1. The flavor of a jet is determined by matching at least one meson to the jet within a $\Delta R < 0.5$ cone. If there is at least one B-meson in the cone, the jet is considered to be a b-jet. If there is no B-meson and at least one C-meson, the jet is a c-jet. Otherwise, the jet is considered to be a light jet.

2. For any hard-scatter matrix element process not involving gluon splitting (i.e. any but $Wb\overline{b}+X$ and $Wc\overline{c}+X$), the number of jets must be equal to the number of partons arising from the hard-scatter process.

3. For matrix element processes involving gluon splitting, the number of jets must be equal to or one less than the number of hard-scatter partons.

4. b-jets are not required to be matched to b-quarks from the hard-scatter process since there are no parton level cuts in ALPGEN for b-quarks.

The samples are identical to the ones used in the b-tagged cross-section analysis. [23] These samples are run through the same preselection as data events (see Chapter 4), and then integrated to obtain per-event signal probabilities. The samples used, along with numbers of events integrated and available to use in ensembles, are listed in Table 2. Events are counted for which both signal and background probabilities exist. Also shown in the table are the numbers of events before and after jet-parton matching.

6.1.3 W+jets Background Fractions

The fractional contributions of the heavy- and light-flavor background types to the total W+jet background are determined from the cross-sections generated by ALPGEN. These background fractions, obtained from Ref. [23], are shown in Table 3.

	# events integrated			
sample	parton-matched		not parton-matched	
	e+jets	μ+jets	e+jets	μ+jets
$t\bar{t}$(160 GeV)	689	737	311	263
$t\bar{t}$(170 GeV)	711	733	289	267
$t\bar{t}$(175 GeV)	713	716	287	284
$t\bar{t}$(180 GeV)	724	739	276	261
$t\bar{t}$(190 GeV)	747	730	252	270
$Wjjjj$	137	137	863	862
$Wb\bar{b}Jj$	75	93	425	502
$Wc\bar{c}Jj$	97	114	603	756
$W(b\bar{b})jjj$	66	78	309	370
$W(c\bar{c})jjj$	28	39	182	181
$Wcjjj$	116	126	871	874

Table 2
Number of events integrated for each MC sample (number of events available for ensembles).

Subprocess	Relative fraction (%)
$Wb\bar{b}$	2.72 ± 0.11
$Wc\bar{c}$	4.31 ± 0.20
$W(c\bar{c})$	2.70 ± 0.15
$W(b\bar{b})$	4.69 ± 0.36
Wc	4.88 ± 0.17
W+jjjj	80.71 ± 0.43

Table 3
Fractions of different flavor subprocesses contributing to the W+jet sample.

6.1.4 b-tagging in MC

The SVX tagger used for identifying jets likely to have come from the hadronization of b-quarks (see Sect. 4.5) behaves differently in MC and data. For this reason, tag rate functions are used to simulate the effects of b-tagging in MC. Tag rate functions for jets are parameterized in jet p_T and η, and are expressed as a product of two terms: *taggability* and *tagging efficiency*. The taggability is the probability for the jet to be "taggable", and is determined by the ability to match the calorimeter jet to a track in the central tracking system. The tagging efficiency is the probability for a taggable jet to be tagged as a b-jet. These both depend upon the flavor of the jet (b, c, or light jet). The tag rate parametrizations used in the matrix element method were derived for use in the cross-section analysis using b-tagging, described in Ref. [23], and more details may be found there.

6.1.5 Data-MC Comparisons

Plots of kinematic variables are used to determine the level of agreement between data and MC. The plots shown in Appendix A show the agreement between the data sample requiring at least 1 b-tagged jet in the event. Additional plots can be found in Ref. [22].

6.2 Sample Composition

After passing the event selection described in Chapter 4, the data samples have a large fraction of high p_T isolated leptons arising from the decay of W bosons produced in association with jets. These events, called W+jets events, are the primary source of physics background events. In addition, QCD multijet events in which either a jet is misidentified as an electron, or a muon from the semileptonic decay of a heavy quark appears as a isolated muon, are the

instrumental backgrounds. In both of the last two, the missing transverse energy ($\not\!\!E_T$) arises from a mismeasurement of jet energies in the calorimeter.

The modeling of the background in the matrix element method is described in Sect. 5.3.2. The fraction of signal events, f_{sgn}, is fit using the matrix element-based likelihood (Eqn. 5.2). However, for testing the matrix element method, it is important to generate ensembles with the correct proportions of signal and background events. For this reason, the *Matrix Method* [93] (not to be confused with the matrix element method) is used to first estimate the number of QCD events, and then a topological likelihood fit is used to estimate the number of signal events.

It is stressed, however, that the results of the Matrix Method and the topological discriminant have no direct input into the matrix element method. Only an indirect effect arises determining the calibration using ensembles with the expected sample composition.

6.2.1 The Matrix Method

The Matrix Method relies on the differences in behavior of the lepton isolation variables between the QCD multijet (QCD) events and the remaining events $t\bar{t}$ and W+jets ($N^{W+t\bar{t}}$) to determine the number of QCD events (N^{QCD}). The electron and muon isolation variables are described in Sections 4.3.1 and 4.4.1, respectively. With N_l for the number of events passing the loose lepton isolation criteria, N_t for the number of events with tight leptons, and ϵ_{sgn} and ϵ_{QCD} for the efficiencies for real leptons and non-isolated (μ+jets)/fake (e+jets) leptons, respectively, to pass the isolation cuts, the following equation is used:

$$\begin{pmatrix} N_l \\ N_t \end{pmatrix} = \begin{pmatrix} 1 & 1 \\ \epsilon_{sgn} & \epsilon_{QCD} \end{pmatrix} \begin{pmatrix} N_l^{W+t\bar{t}} \\ N_l^{QCD} \end{pmatrix} \tag{6.1}$$

The values of ϵ_{sgn} are determined using W+jets MC events, and corrected with a data-to-MC scale factor derived comparing $Z \rightarrow ll$ MC events to data. All MC samples have the same

	e+jets	μ+jets
ϵ_{sgn}	0.817 ± 0.011	$0.810^{+0.021}_{-0.017}$
ϵ_{QCD}	0.160 ± 0.040	$0.085^{+0.034}_{-0.030}$

Table 4
Lepton isolation efficiencies for real leptons (ϵ_{sgn}) and for non-isolated muons (μ+jets) or fake electrons (e+jets) (both ϵ_{QCD}).

preselection (except lepton isolation, of course) used in the top mass analysis event selection. The values of ϵ_{QCD} are determined using a sample with an inverted $\not\!\!E_T$ cut. Values are taken directly from Ref. [22] and shown in Table 4.

With N_l, N_t, and the two values of isolation efficiencies known, one can solve directly for N_l^{QCD}. Then multiplication by ϵ_{QCD} easily gives N_t^{QCD}, the number of QCD events in the preselected tight sample.

6.2.2 Topological Likelihood

The topological discriminant used to calculate the $t\bar{t}$ production cross section [23] is rederived for the top mass analysis, which has only four jets. Six event shape variables, chosen to give good discrimination between W+jets and $t\bar{t}$ events, are used to form a topological likelihood. The QCD fraction is constrained using the results of the Matrix Method. The six likelihood variables are described and the results for a slightly smaller data sample are shown in Ref. [22]. The final sample compositions are taken from Ref. [88] and shown in Table 5.

6.3 Ensemble Testing

Ensemble testing is used for the following reasons:

1. to verify proper behavior of the mass fitting algorithms,

2. to determine the expected statistical uncertainty, and

	e+jets	μ+jets
W+jets	$30.5^{+9.7}_{-9.0}$	$58.7^{+9.6}_{-9.2}$
QCD	$15.2^{+2.0}_{-1.9}$	$4.6^{+0.8}_{-0.8}$
total bkgd	$45.7^{+9.9}_{-9.2}$	$63.3^{+9.6}_{-9.2}$
$t\bar{t} \to l$+jets	$40.6^{+9.4}_{-9.1}$	$25.8^{+8.6}_{-8.1}$
total	$86.3^{+13.7}_{-12.9}$	$89.1^{+12.9}_{-12.3}$
f_{sgn}	0.470	0.290

Table 5
Expected signal and background contributions.

3. to study systematic shifts in the measured top mass.

The details of the use of ensemble testing for validating and calibrating the matrix element method is described in the following sections.

6.3.1 Event selection for ensembles

To get an event for a pseudo-experiment, an event is chosen from the integration pool (see Table 2) at random, and then a decision is made to either use or reject the event based on the trigger efficiency. Whether the event is chosen or not, it is returned to the pool for later selection. Thus, ensembles may contain duplicated events. The number of events per ensemble is small compared to the number of events available in the pool, so this is not expected to be a problem.

As described in Ref. [23], each jet has a tagging probability that is a product of its taggability and its tagging efficiency. The tagging of a jet within an event is simulated by choosing a random number within a range determined by the lowest and highest tagging probability for the sample. This number is compared to the tagging probability for the jet, and the jet is "tagged" if the random number is less than the tagging probability. Tagging probabilities are used on a per-jet basis in this way primarily because it allows simulation of tagged jets in the event.

Tagging information is also used to weight the 12 jet-parton combinations used in calculating the signal probabilities, and the 24 jet-parton combinations used for the background probabilities.

6.3.2 Types of ensembles

The following ensembles are generated for ensemble testing:

- signal-only ($t\bar{t} \rightarrow l\nu$+jets)

  - jet-parton matching for $t\bar{t}$, *ad hoc* for heavy-flavor W+jets background
  - *ad hoc* matching used for heavy-flavor background only

- 40% signal and 60% background, with the following background selections (*ad hoc* matching for heavy-flavor background events):
  - all $Wjjjj$ events
  - $Wjjjj$, $Wcjjj$, $Wc\bar{c}jj$, $Wb\bar{b}jj$, $W(b\bar{b})jjj$, $W(c\bar{c})jjj$ (see Table 3)
  - QCD events included

6.3.3 Signal-only ($t\bar{t}$) ensembles (no b-tagging)

Ensembles were generated containing signal events only with jet-parton matching to gauge the performance of the matrix element method in the absence of background events and with all particles in the final state coming directly from partons arising directly from the hard scatter $t\bar{t}$ process modeled by P_{sgn}. Then ensembles were generated without jet-parton matching to see the effect of having events with extra gluons in the final state (FSR).

With jet-parton matching

The first ensemble testing was done on ensembles consisting entirely of signal events. Jets were matched to partons using the procedure described in Section 6.1.2. Results are shown in Figures 6.1 and 6.2.

Without jet-parton matching

Next, in order to show the bias that results from using all MC events for the signal samples, ensembles were generated without parton-matching. Results are shown in Figures 6.3. As

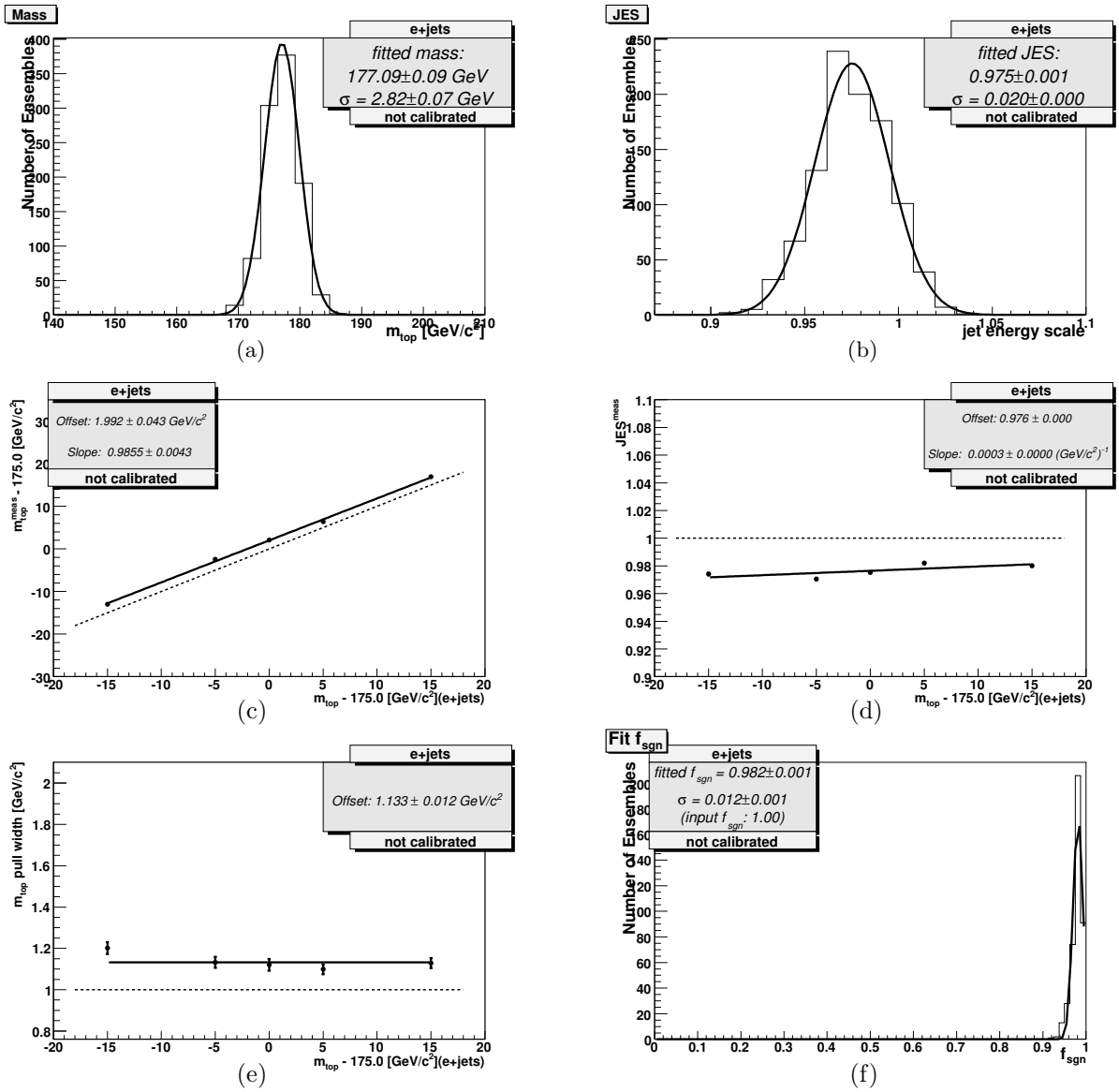

Fig. 6.1. Results of ensemble testing for **signal-only ensembles** (f_{top}=1.0), **with jet-parton matching**, input mass 175 GeV/c^2 (e+jets): (a) output m_{top}, (b) output JES, (c) output mass vs. input mass, (d) output JES vs. input mass, (e) m_{top} pull vs. input mass, and (f) output f_{top},

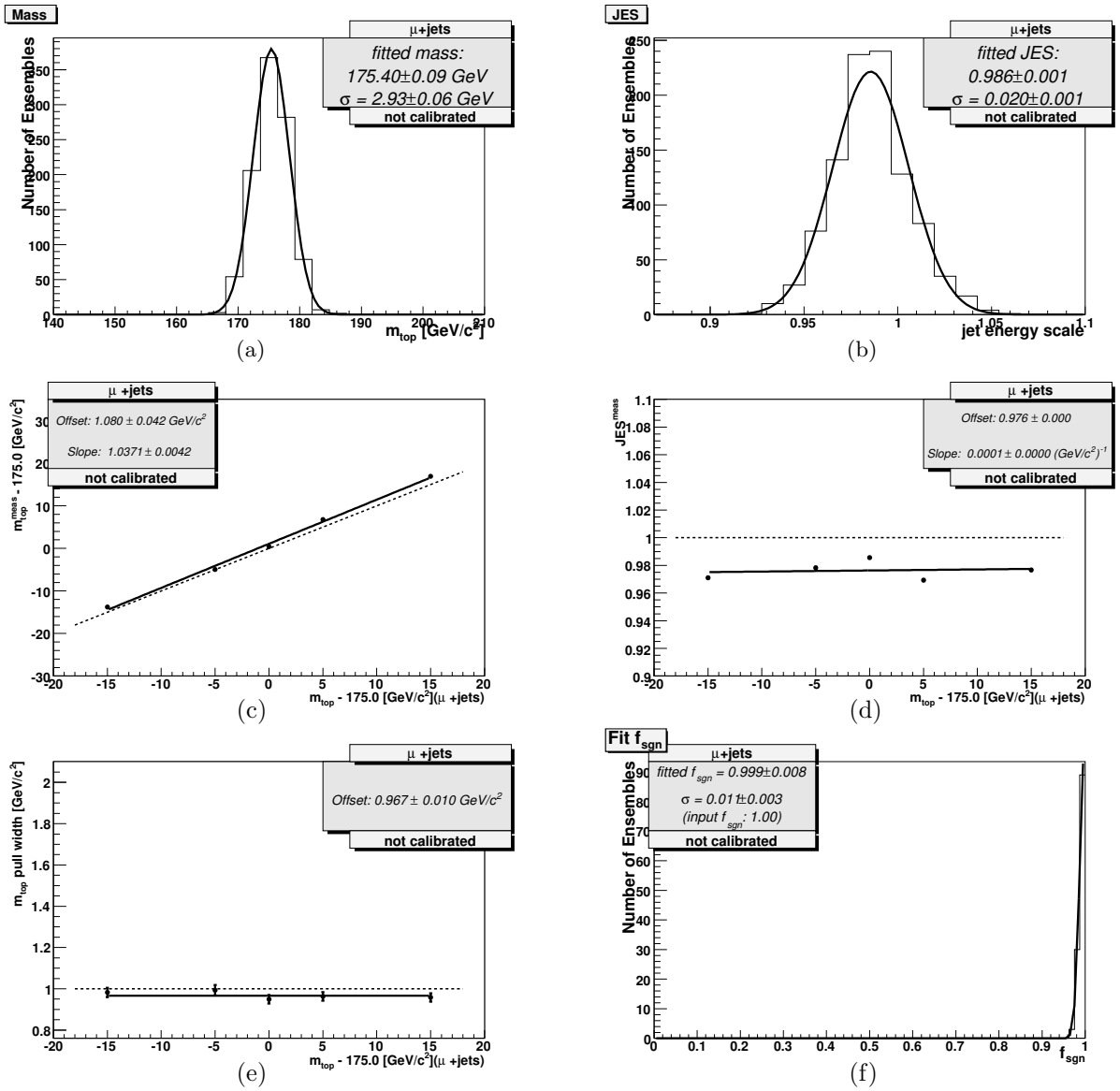

Fig. 6.2. Results of ensemble testing for **signal-only ensembles** (f_{top}=1.0), **with jet-parton matching**, input mass 175 GeV/c^2 (μ+jets): (a) output m_{top}, (b) output JES, (c) output mass vs. input mass, (d) output JES vs. input mass, (e) m_{top} pull vs. input mass, and (f) output f_{top},

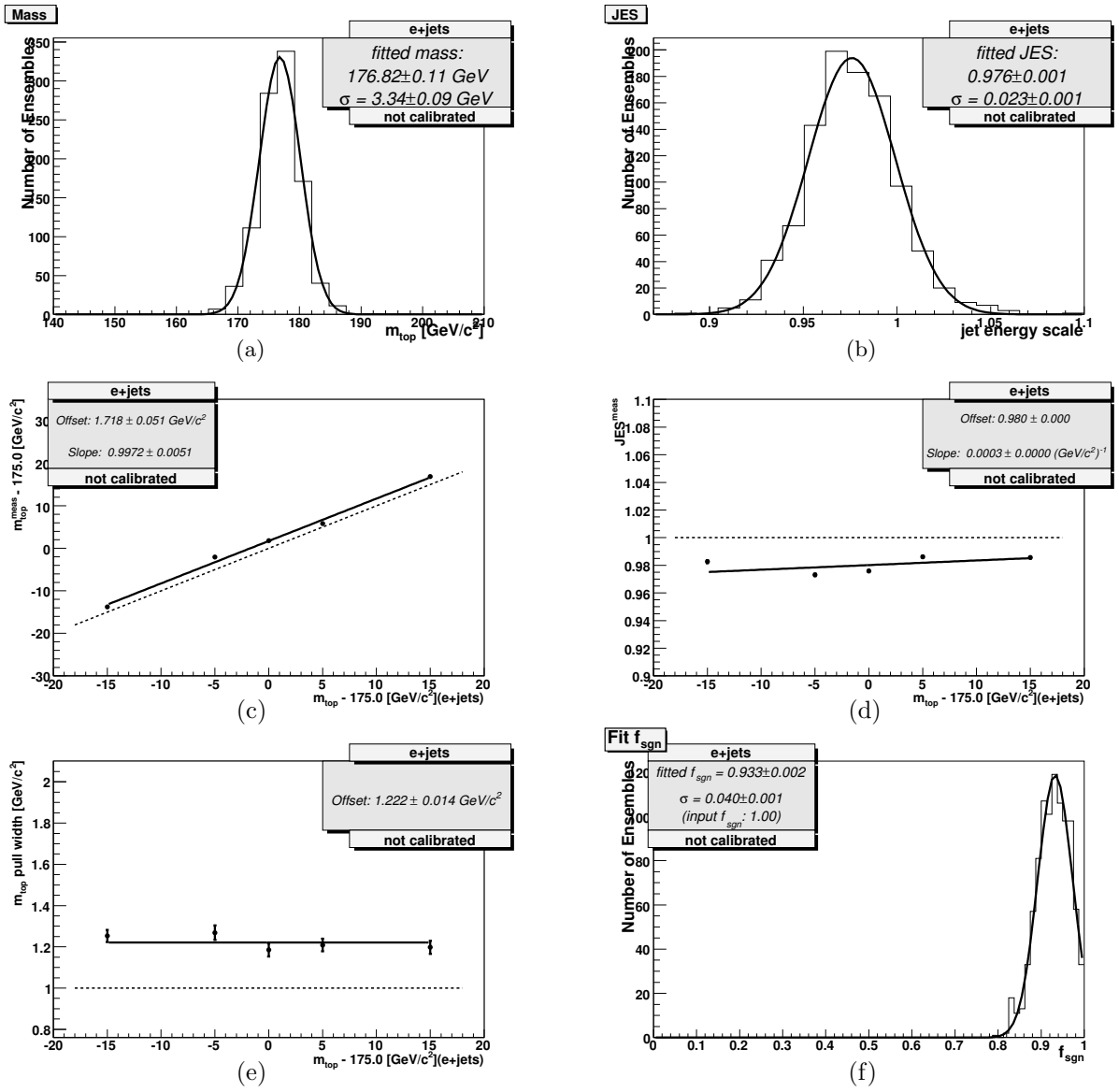

Fig. 6.3. Results of ensemble testing for **signal-only ensembles** (f_{top}=1.0), **no jet-parton matching**, input mass 175 GeV/c^2 (e+jets): (a) output m_{top}, (b) output JES, (c) output mass vs. input mass, (d) output JES vs. input mass, (e) m_{top} pull vs. input mass, and (f) output f_{top},

expected, there is a small decrease in the fitted signal fraction. The effect on the fitted m_t is small. Results are shown in Figures 6.3 and 6.4.

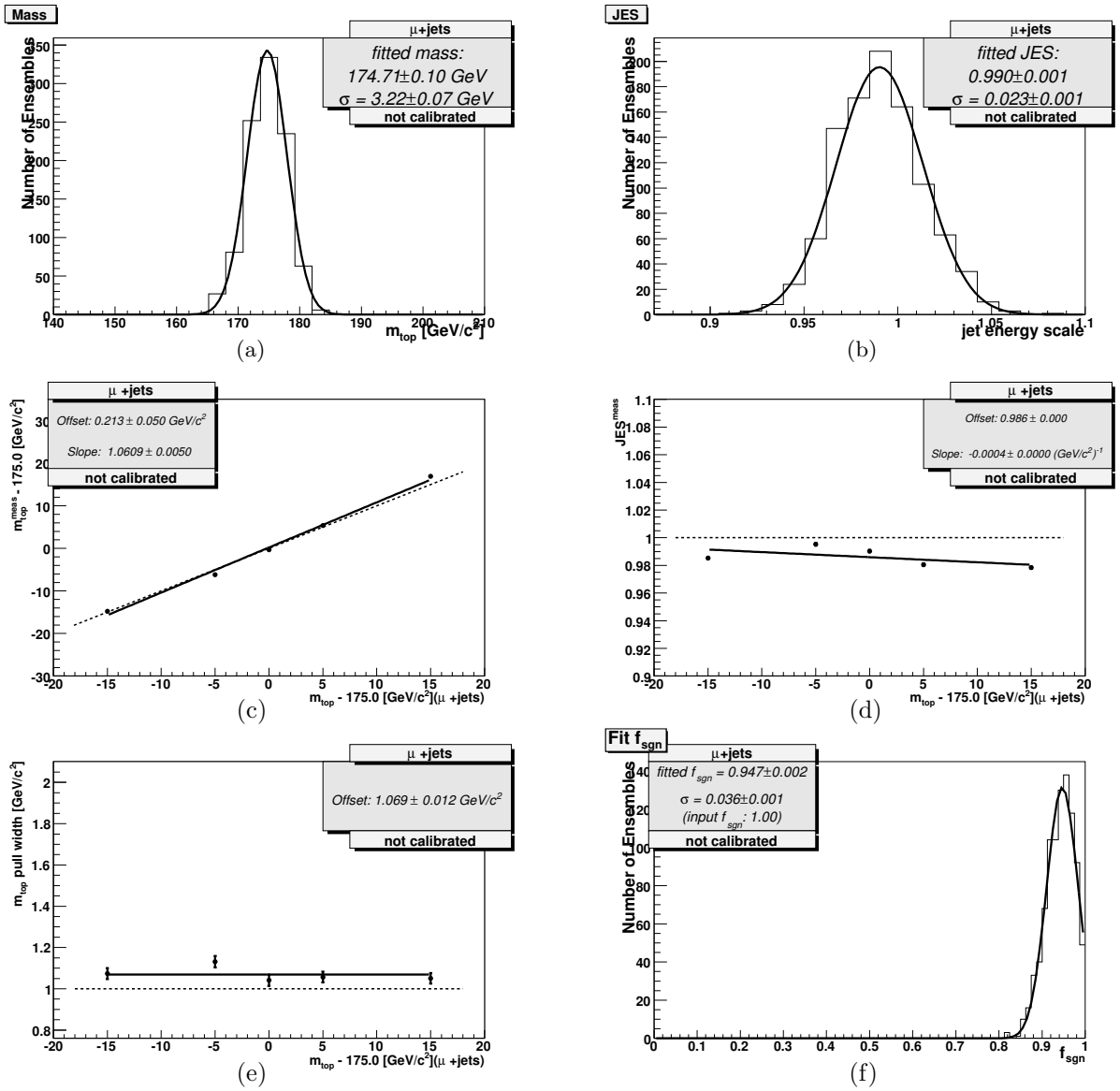

Fig. 6.4. Results of ensemble testing for **signal-only ensembles** (f_{top}=1.0), **no jet-parton matching**, input mass 175 GeV/c^2 (μ+jets): (a) output m_{top}, (b) output JES, (c) output mass vs. input mass, (d) output JES vs. input mass, (e) m_{top} pull vs. input mass, and (f) output f_{top},

6.3.4 Ensemble testing with background (no b-tagging)

Next, ensembles were generated containing background events in approximately the same proportions expected in the data sample. As explained in Sect. 5.3.2, the likelihood consists of matrix elements for $Wgggg$ and $Wbbgg$ processes, weighted by b-tagging efficiencies. If b-tagging is not used, the background probability comes entirely from the $Wgggg$ matrix elements, so discrimination is not expected to be very good for heavy-flavor background events. Ensembles are generated with and without heavy-flavor background events. In addition, to simulate the full background, ensembles are generated with QCD events in the expected proportions.

All $Wjjjj$ background

Only light-flavor background events were used, with the total number of background events as expected in the data samples. Results are shown in Figures 6.5 and 6.6.

Heavy-flavor background, without QCD

In anticipation of the use of b-tagging in the likelihood, it is necessary to include heavy flavor background events in the ensembles. Events in the expected proportions (see Table 3) were used in heavy-flavor background ensembles. Results are shown in Figures 6.7 and 6.8.

Heavy-flavor background, with QCD

Ensembles were created containing QCD events in the expected proportions. Results are shown in Figures 6.9 and 6.10.

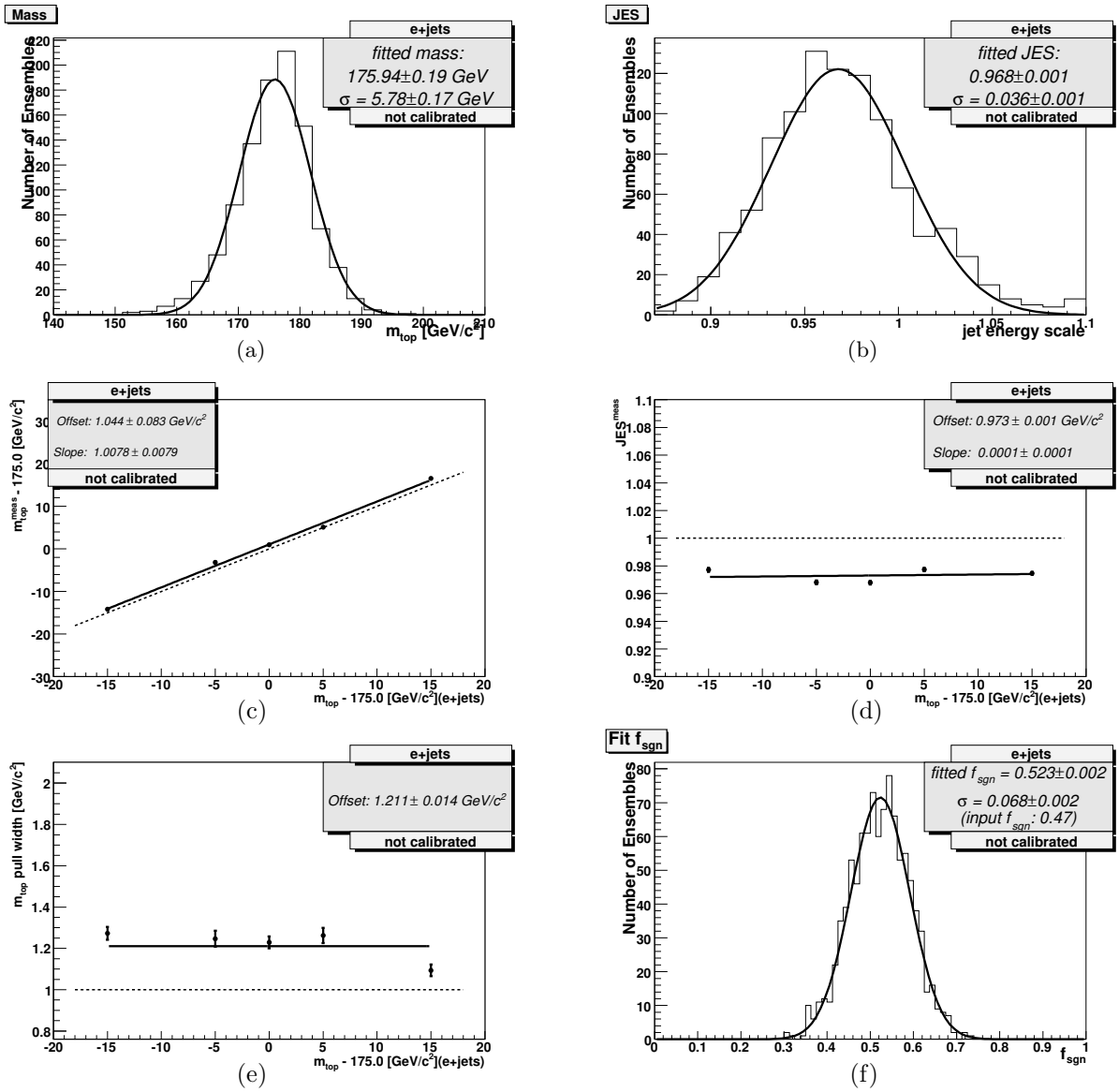

Fig. 6.5. Results of ensemble testing for ensembles with normal background fraction, **all** $Wjjjj$ **background**, input mass 175 GeV/c^2 (e+jets): (a) output m_{top}, (b) output JES, (c) output mass vs. input mass, (d) output JES vs. input mass, (e) m_{top} pull vs. input mass, and (f) output f_{top},

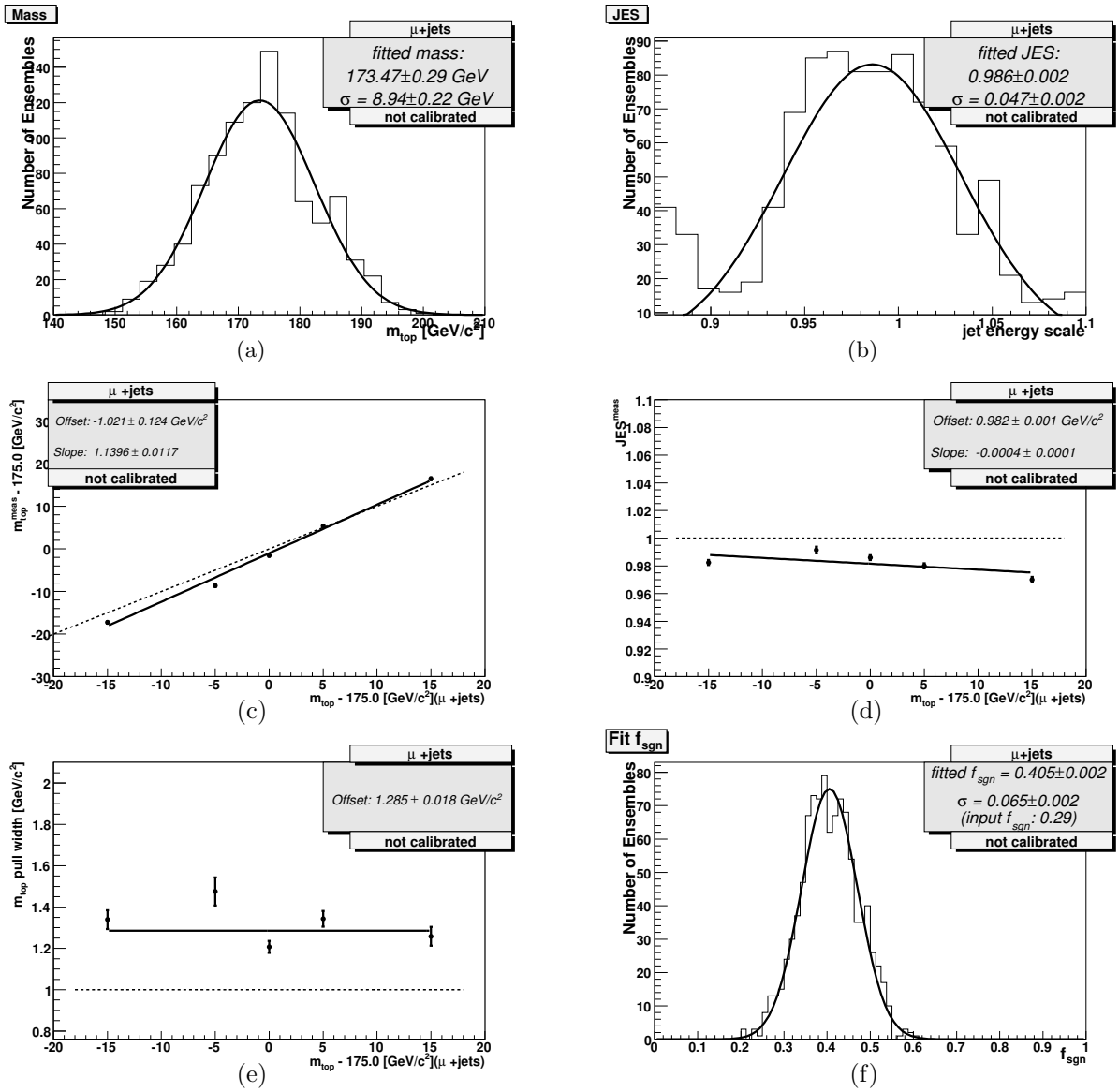

Fig. 6.6. Results of ensemble testing for ensembles with normal background fraction, **all** $Wjjjj$ **background**, input mass 175 GeV/c^2 (μ+jets): (a) output m_{top}, (b) output JES, (c) output mass vs. input mass, (d) output JES vs. input mass, (e) m_{top} pull vs. input mass, and (f) output f_{top},

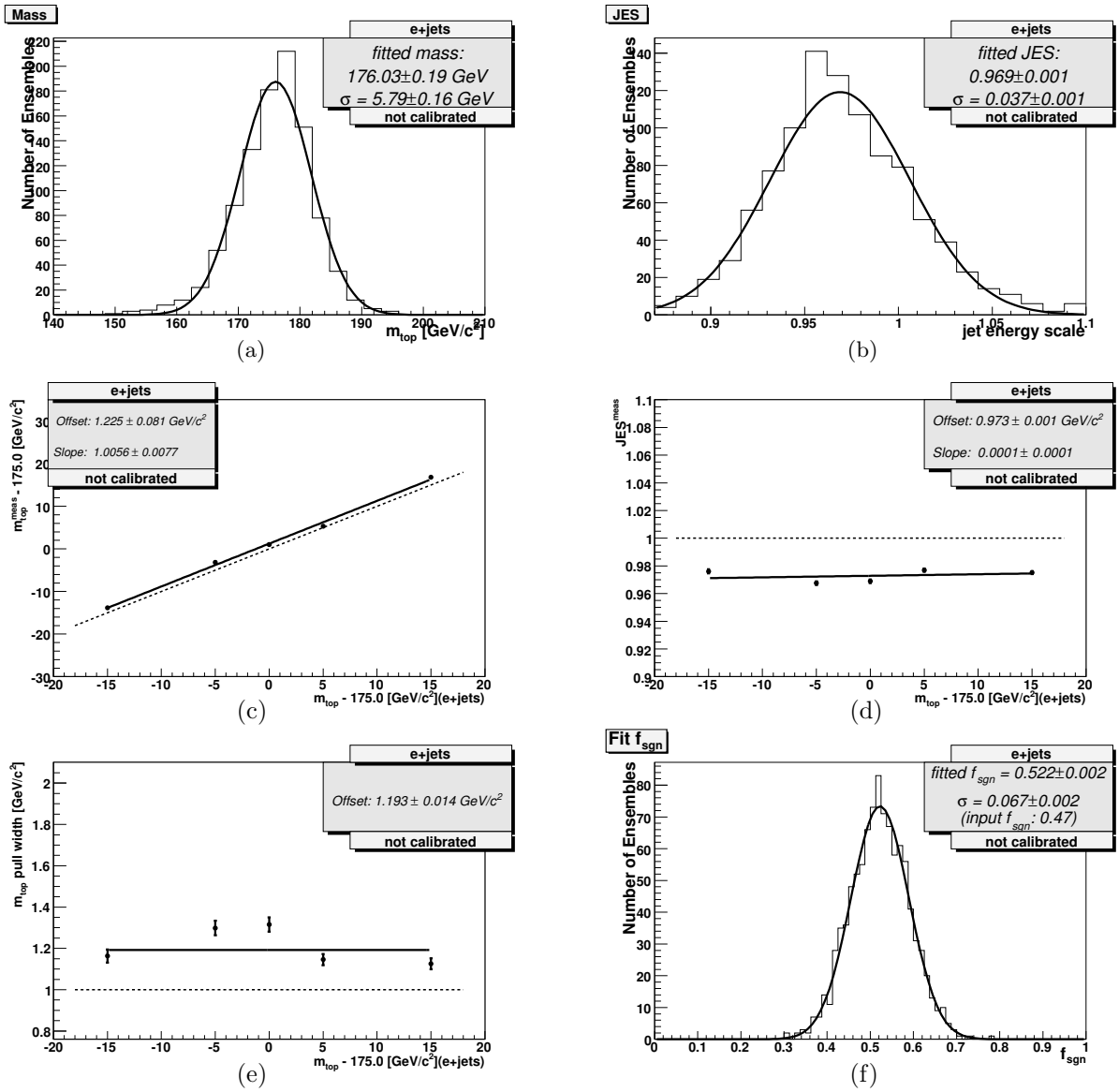

Fig. 6.7. Results of ensemble testing for ensembles with normal background fraction, **heavy-flavor background included**, input mass 175 GeV/c^2 (e+jets): (a) output m_{top}, (b) output JES, (c) output mass vs. input mass, (d) output JES vs. input mass, (e) m_{top} pull vs. input mass, and (f) output f_{top},

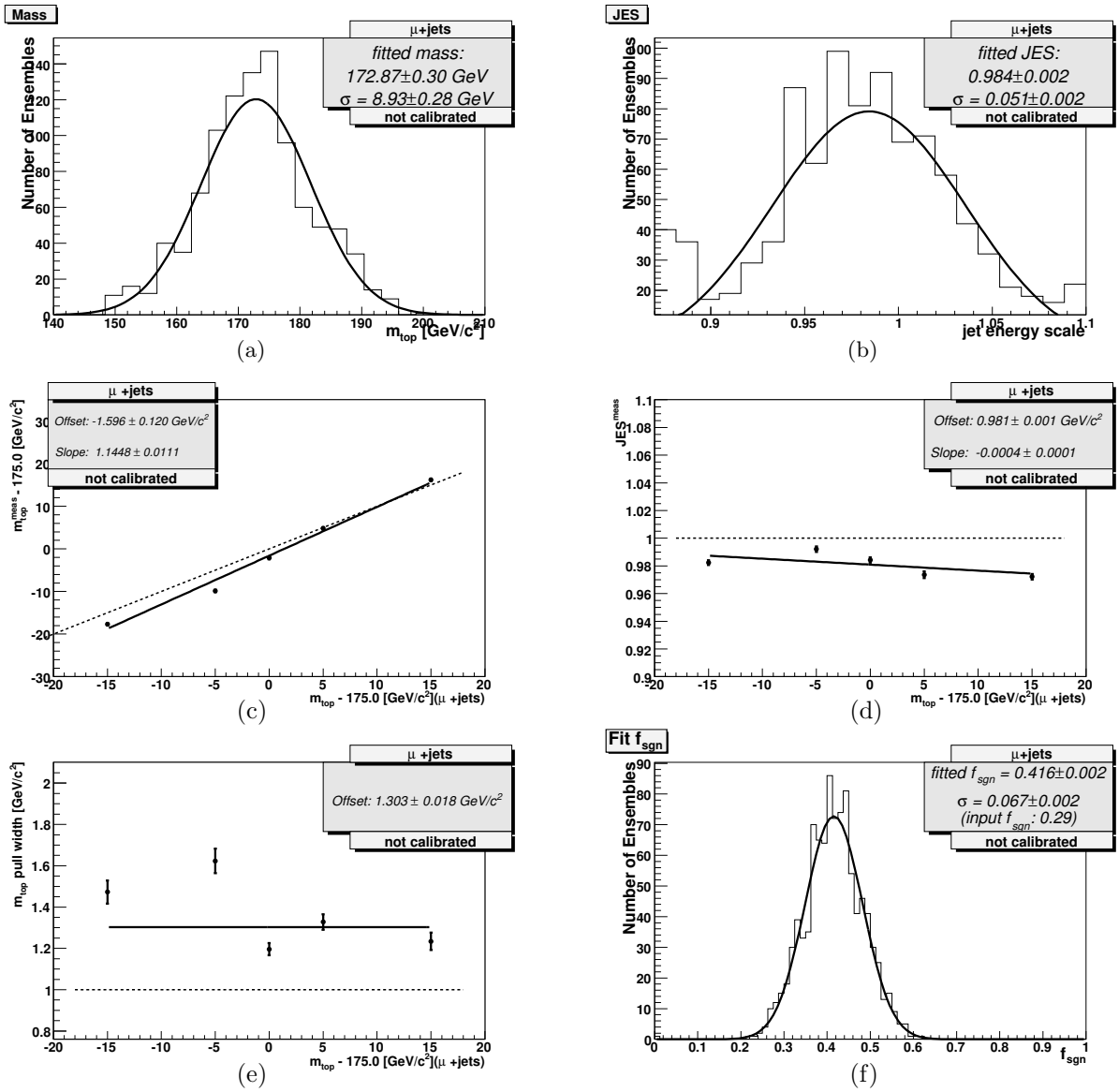

Fig. 6.8. Results of ensemble testing for ensembles with normal background fraction, **heavy-flavor background included**, input mass 175 GeV/c^2 (μ+jets): (a) output m_{top}, (b) output JES, (c) output mass vs. input mass, (d) output JES vs. input mass, (e) m_{top} pull vs. input mass, and (f) output f_{top},

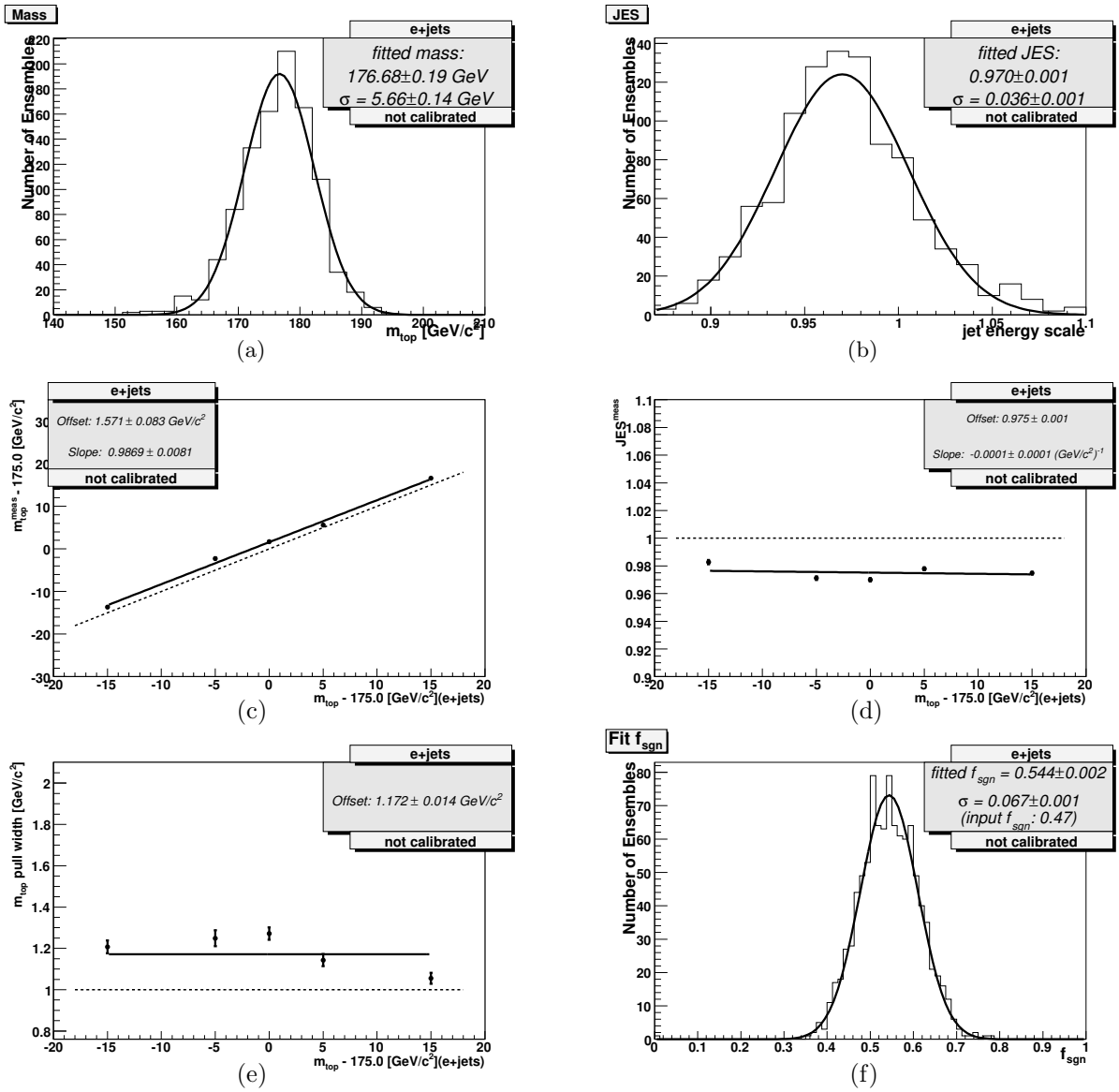

Fig. 6.9. Results of ensemble testing for ensembles with normal background fraction, **heavy-flavor background and QCD included**, input mass 175 GeV/c^2 (e+jets): (a) output m_{top}, (b) output JES, (c) output mass vs. input mass, (d) output JES vs. input mass, (e) m_{top} pull vs. input mass, and (f) output f_{top},

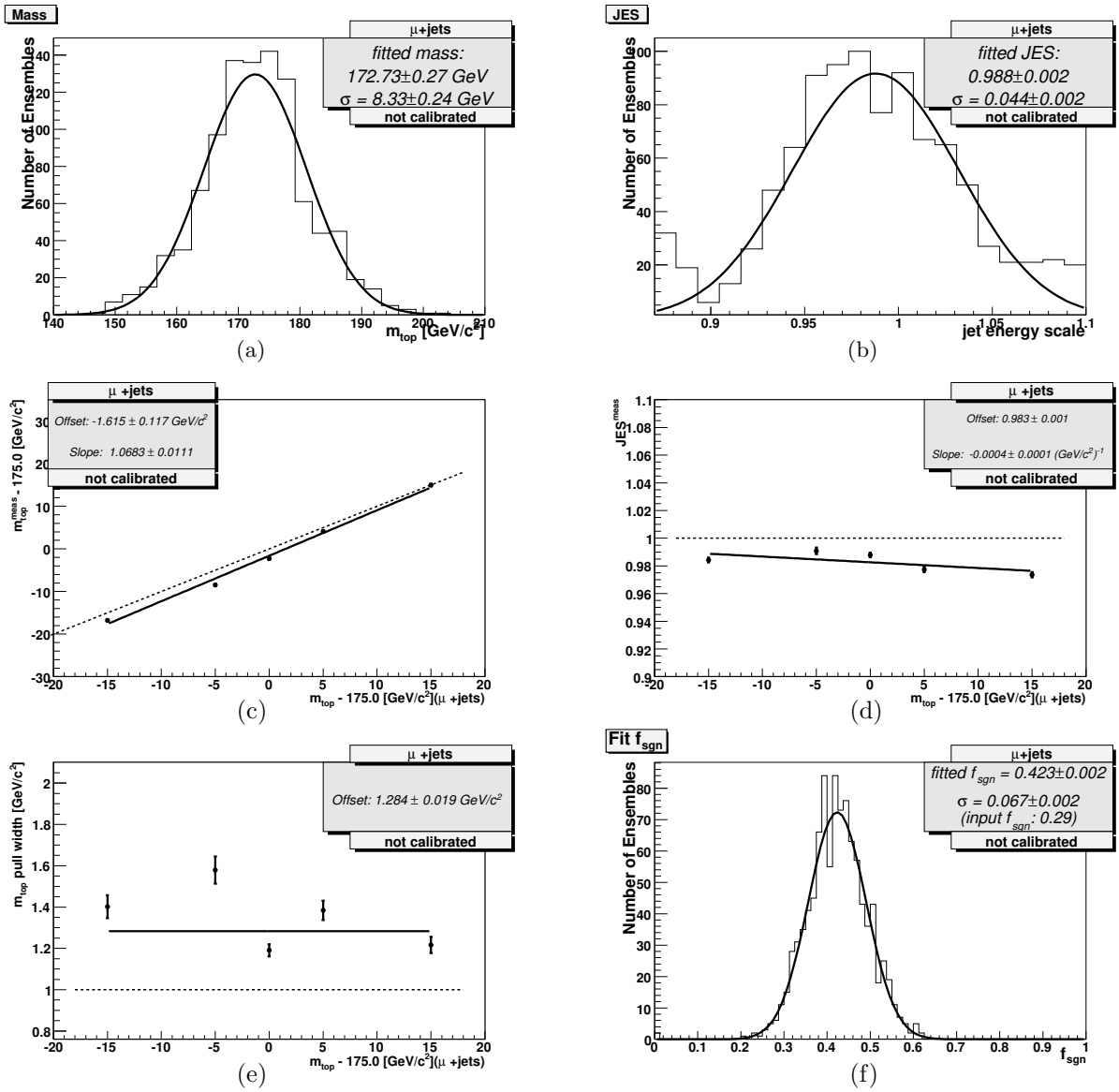

Fig. 6.10. Results of ensemble testing for ensembles with normal background fraction, **heavy-flavor background and QCD included**, input mass 175 GeV/c^2 (μ+jets): (a) output m_{top}, (b) output JES, (c) output mass vs. input mass, (d) output JES vs. input mass, (e) m_{top} pull vs. input mass, and (f) output f_{top},

6.3.5 Ensemble testing with b-tagging

The tagging of a jet within an event is simulated by choosing a random number within a range determined by the lowest and highest tagging probability (see Sect. 6.1.4) for the sample. This number is compared to the tagging probability for the jet, and the jet is "tagged" if the random number is less than the tagging probability. Tagging probabilities are used on a per-jet basis in this way primarily because it allows simulation of tagged jets in the event.

The results for the full ensembles with b-tagging are shown in Figures 6.11 and 6.12. A comparison of these with Figures 6.9 and 6.10 shows a marked improvement with the use of b-tagging.

6.3.6 Determination of calibration parameters

The final ensembles, consisting of signal and background compositions expected in data, were used to determine fitted mass calibrations as functions of fitted m_{top} and fitted f_{top}. Calibration parameters for b-tagged and untagged, e+jets and μ+jets likelihoods, were determined in the following manner:

1. m_{top}^{in} values of 160, 170, 175, 180, and 190 GeV/c^2 were used.

2. f_{top}^{in} values were varied over the following ranges, inclusively, in .01 steps:

   - e+jets: 0.34-0.59 (expected f_{top}=0.47$\pm$0.13)
   - μ+jets: 0.19-0.39 (expected f_{top}=0.29$\pm$0.10)

3. For a given f_{top}^{in} hypothesis, the mass bias ($\Delta m_{top} = m_{top}^{out}$ - m_{top}^{in}) as a function of m_{top}^{out} was fit to a line. The average f_{top}^{out} is determined as well.

4. The slopes and intercepts were fit separately to 1^{st}-order polynomials as functions of the average f_{top}^{out} values.

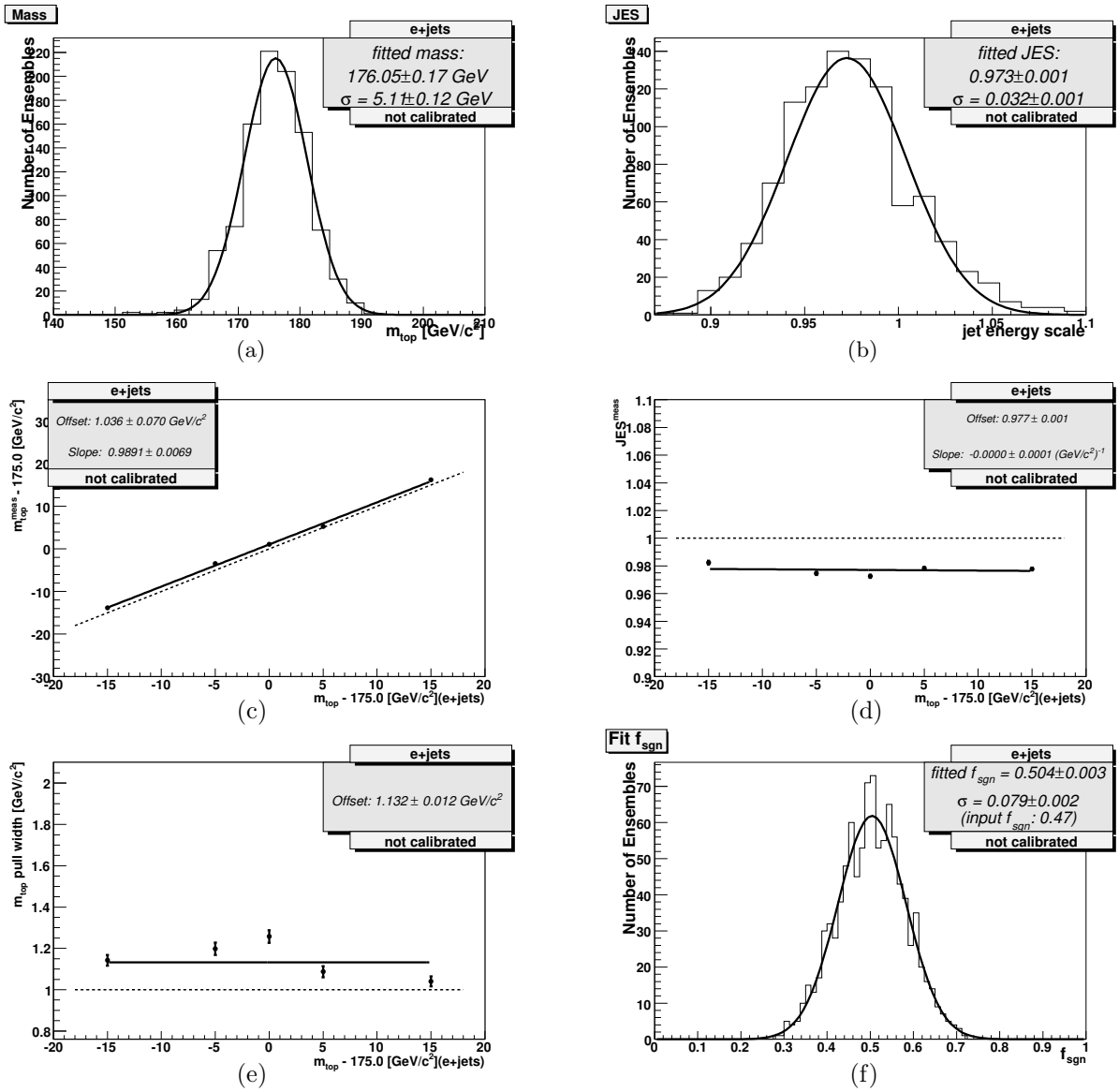

Fig. 6.11. Results of ensemble testing for ensembles with normal background fraction, heavy-flavor background and QCD included, b-**tagged**, input mass 175 GeV/c^2 (e+jets): (a) output m_{top}, (b) output JES, (c) output mass vs. input mass, (d) output JES vs. input mass, (e) m_{top} pull vs. input mass, and (f) output f_{top},

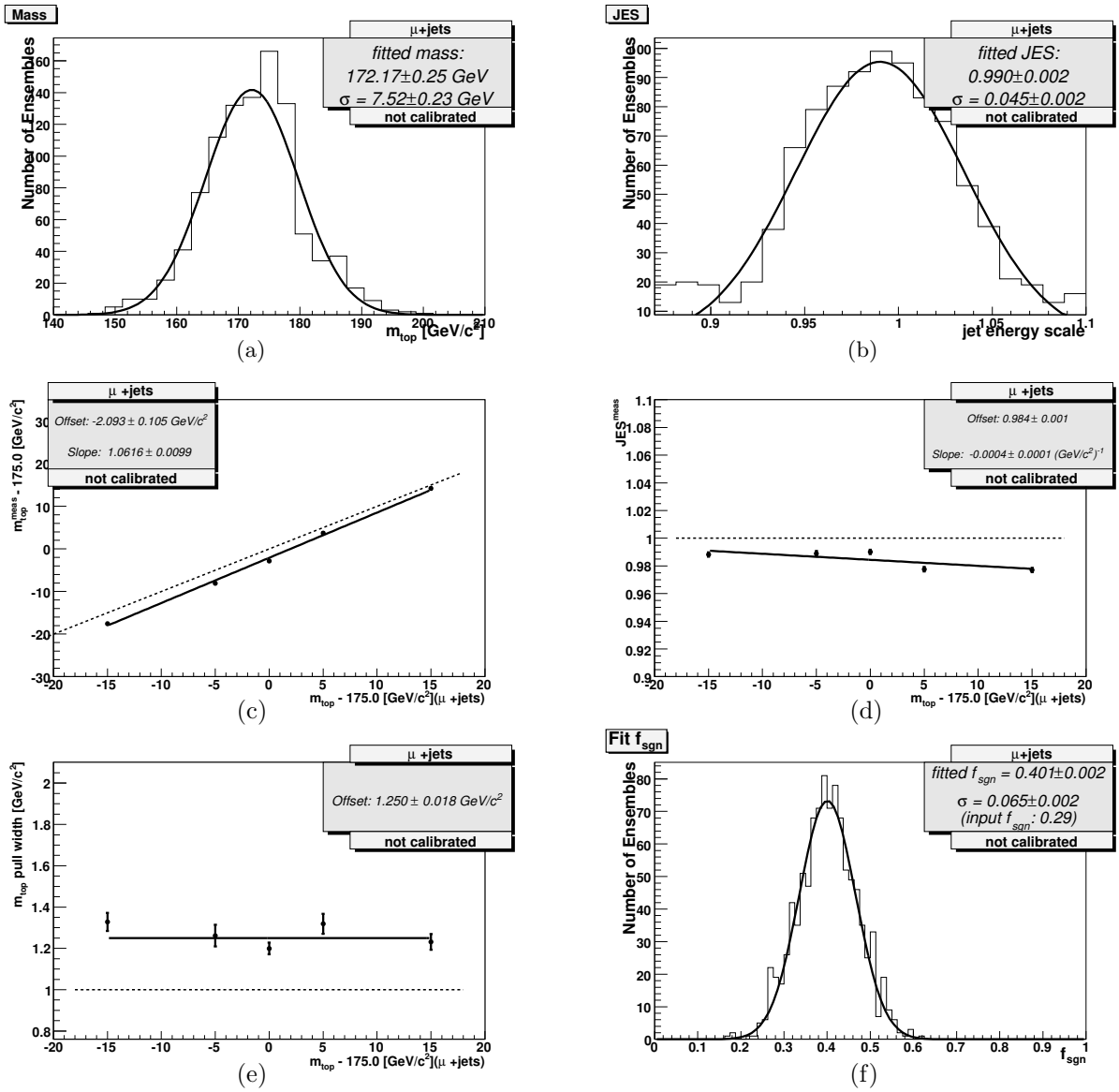

Fig. 6.12. Results of ensemble testing for ensembles with normal background fraction, heavy-flavor background and QCD included, b-**tagged**, input mass 175 GeV/c^2 (μ+jets): (a) output m_{top}, (b) output JES, (c) output mass vs. input mass, (d) output JES vs. input mass, (e) m_{top} pull vs. input mass, and (f) output f_{top},

	e+jets channel		μ+jets channel	
	b-tagged	untagged	b-tagged	untagged
p_0	0.856±0.143	2.544±0.199	-7.067±0.276	-6.025±0.282
p_1	0.249±0.272	-1.536±0.352	12.108±0.631	10.100±0.643
p_2	-0.081±0.015	-0.159±0.020	-0.027±0.023	0.039±0.024
p_3	0.120±0.028	0.213±0.036	0.150±0.054	0.019±0.055

Table 6
Parametrization of m_t calibration with respect to fitted m_t and f_{sgn} (see Eqn. 6.2).

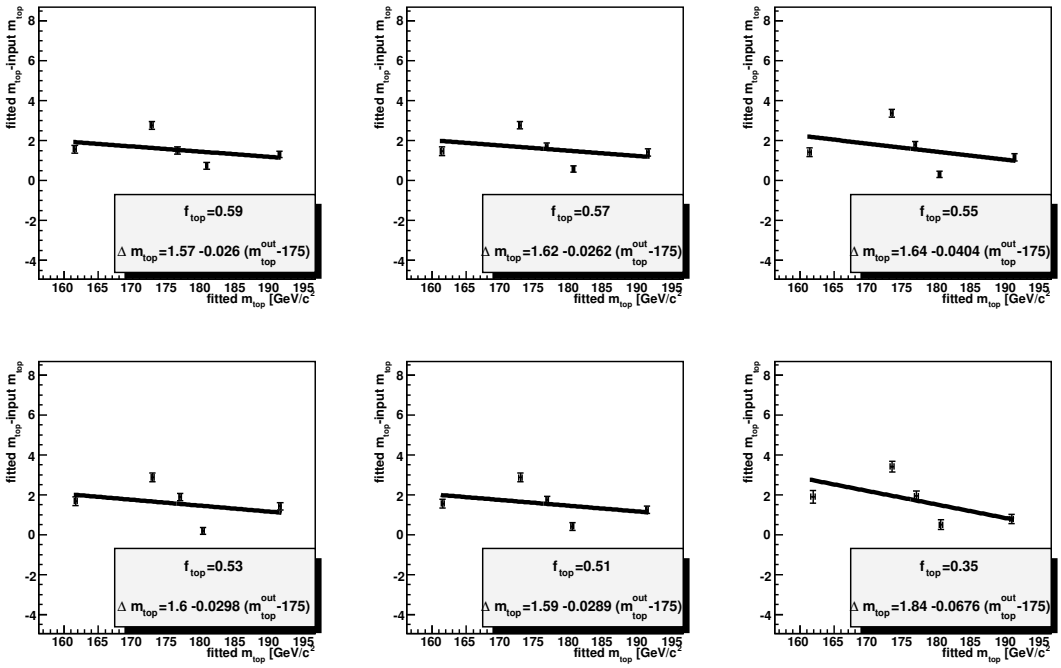

Fig. 6.13. Linear fit as a function of m_{top}^{out} of the mass bias for various f_{top}^{in} values, e+jets

The result is a 2-dimensional parametrization of the mass calibration, given by Eqn. 6.2. Results are shown in Figures 6.13 through 6.20, and summarized in Table 6.3.6.

$$\Delta m_{top} = p_0 + p_1 f_{top}^{fit} + (p_2 + p_3 f_{top}^{fit})(m_{top}^{fit} - 175) \tag{6.2}$$

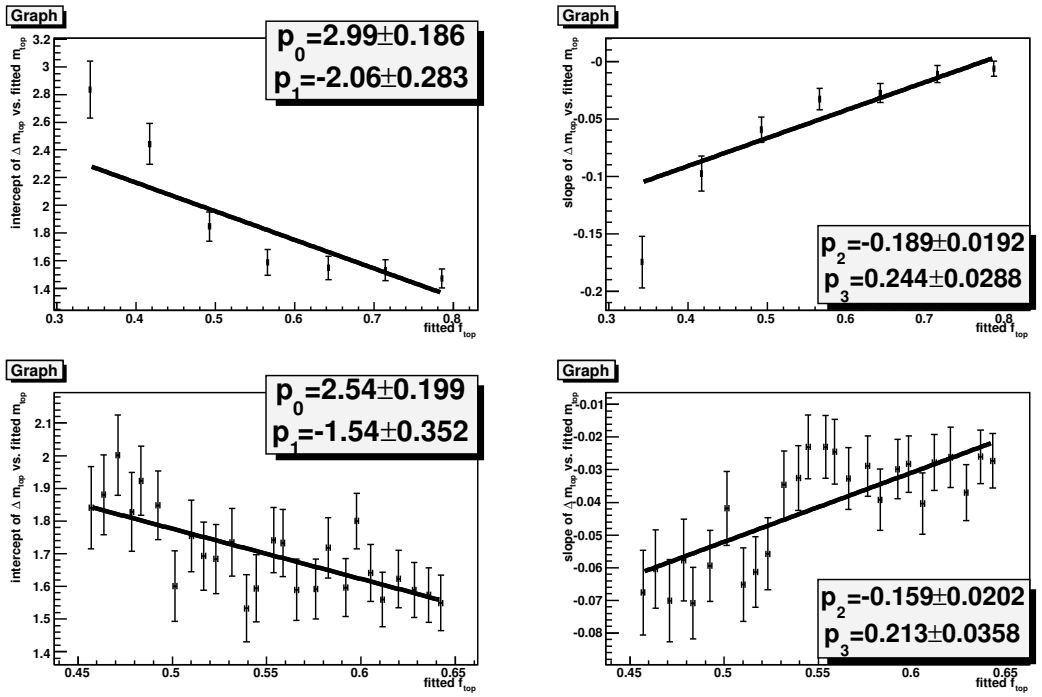

Fig. 6.14. Linear fits as functions of f_{top}^{out} of the slopes and intercepts from fixed f_{top}^{in} mass bias vs. m_{top}^{out} plots, e+jets

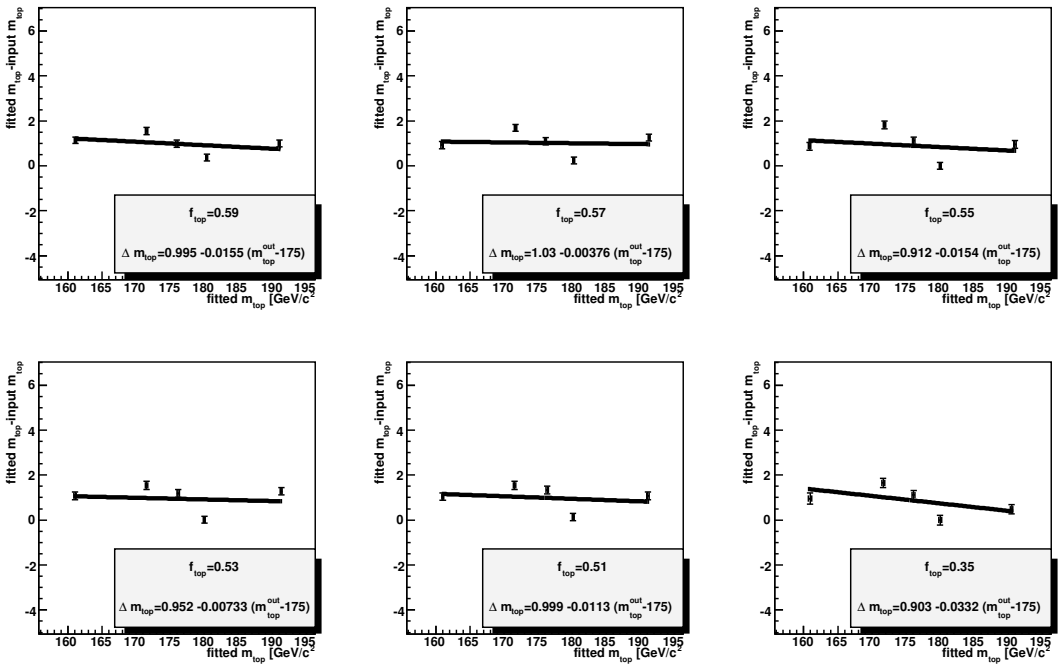

Fig. 6.15. Linear fit as a function of m_{top}^{out} of the mass bias for various f_{top}^{in} values, e+jets with b-tagging

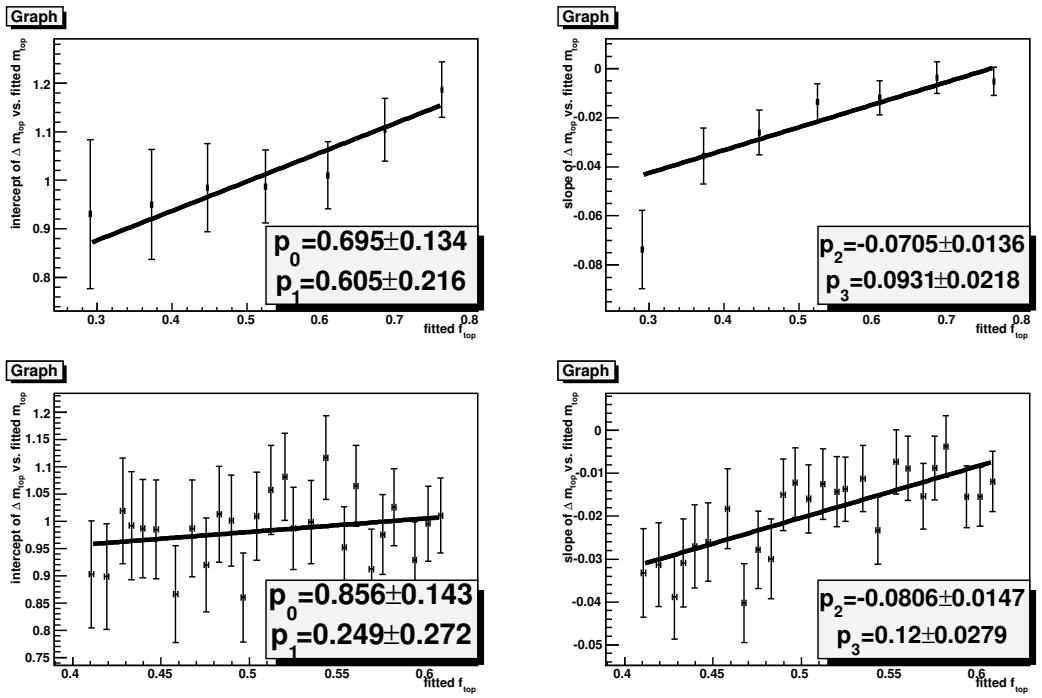

Fig. 6.16. Linear fits as functions of f_{top}^{out} of the slopes and intercepts from fixed f_{top}^{in} mass bias vs. m_{top}^{out} plots, e+jets with b-tagging

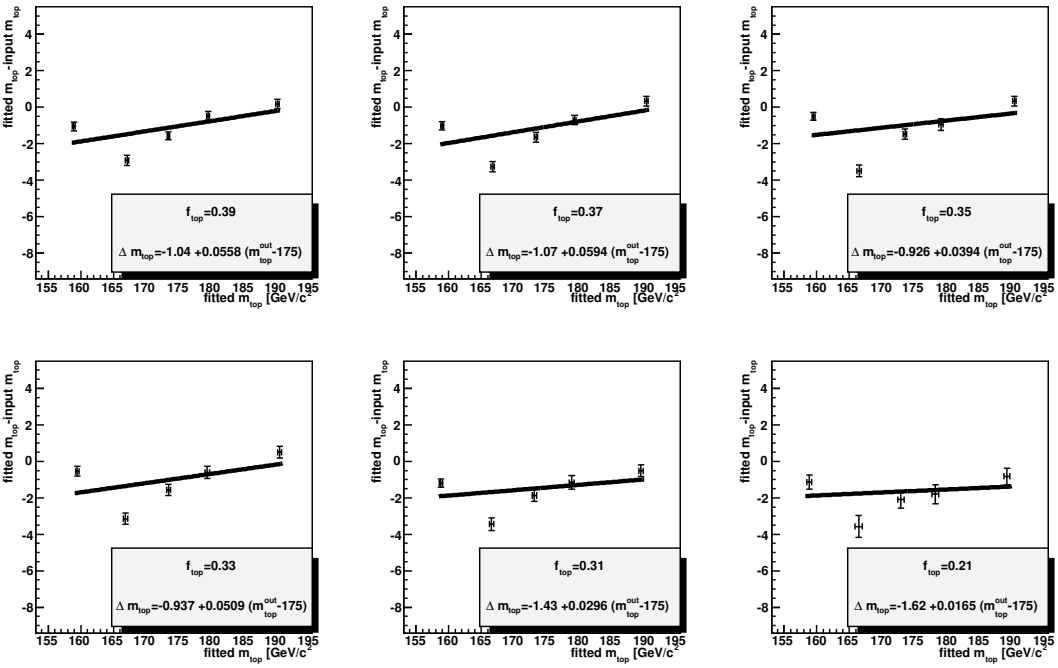

Fig. 6.17. Linear fit as a function of m_{top}^{out} of the mass bias for various f_{top}^{in} values, μ+jets

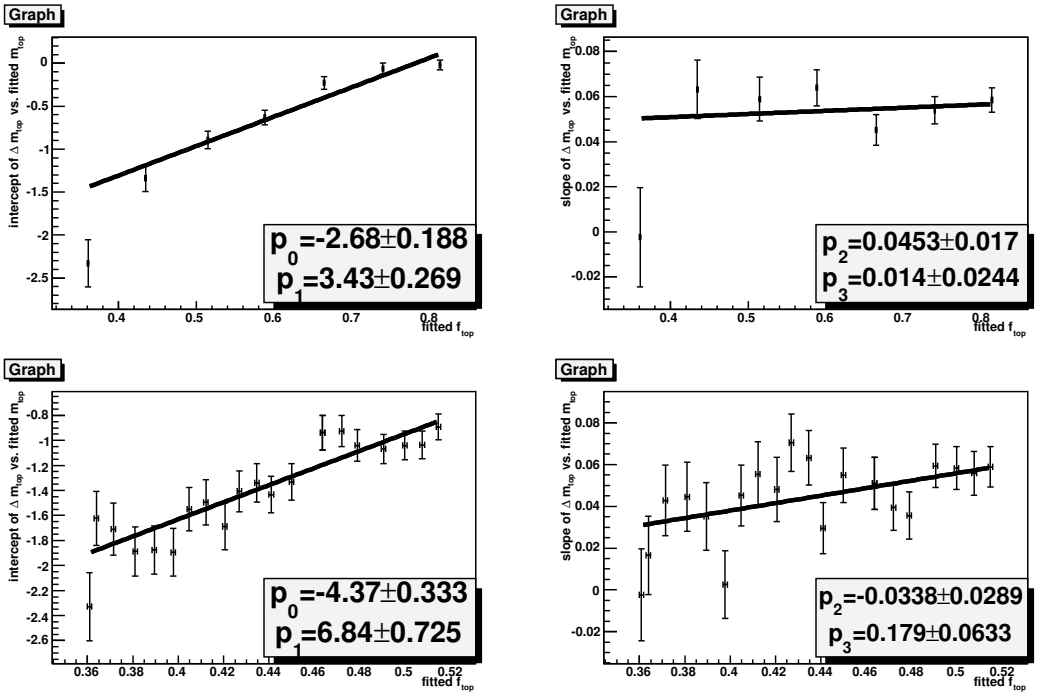

Fig. 6.18. Linear fits as functions of f_{top}^{out} of the slopes and intercepts from fixed f_{top}^{in} mass bias vs. m_{top}^{out} plots, μ+jets

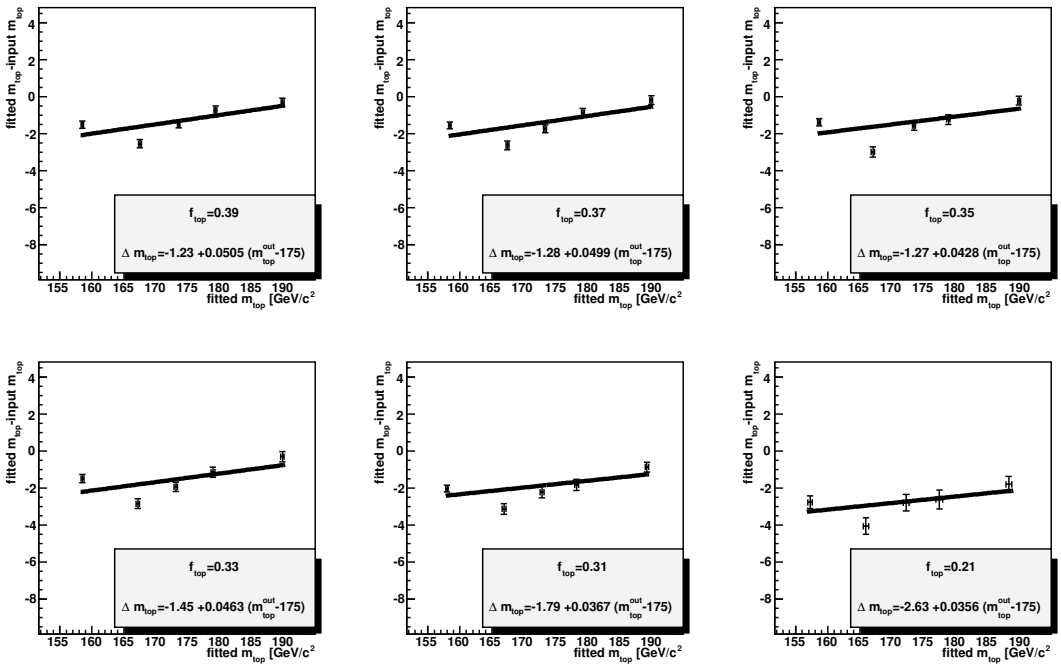

Fig. 6.19. Linear fit as a function of m_{top}^{out} of the mass bias for various f_{top}^{in} values, μ+jets with b-tagging

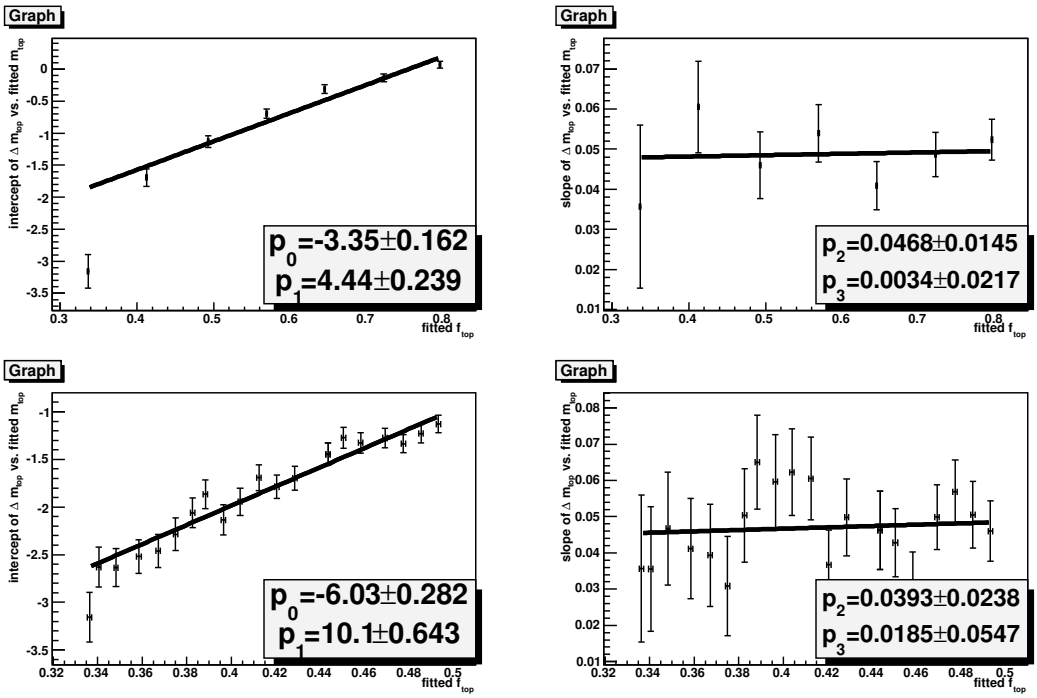

Fig. 6.20. Linear fits as functions of f_{top}^{out} of the slopes and intercepts from fixed f_{top}^{in} mass bias vs. m_{top}^{out} plots, μ+jets with b-tagging

6.3.7 Results of Final Calibration

The calibrations were applied to the likelihood curves for e+jets and μ+jets events separately according to the fitted m_{top} and fitted f_{top} values. These likelihoods were then combined to get a single likelihood for the l+jets ensemble. Results are shown in Figures 6.21 through 6.26.

The pull for a pseudo-experiment is calculated as

$$\text{pull} = \frac{(m_t^{fit} - m_t^{actual})}{\Delta m_t}, \tag{6.3}$$

where Δm_t is the m_t error estimated by the likelihood fit for the pseudo-experiment. The pull distributions show the pulls for all pseudo-experiments within the ensemble. The width of the pull distribution is 1.0 if the errors are estimated correctly. The errors in the next section were all corrected by multiplying by the average pull width, obtain by averaging over the ensembles for the five input top quark masses. The pull corrections applied to data are:

$$\begin{aligned}
(\text{pull width})^{e+\text{jets}} &= 1.30 \quad (\text{pull width})^{e+\text{jets}}_{b-\text{tag}} = 1.22 \\
(\text{pull width})^{\mu+\text{jets}} &= 1.17 \quad (\text{pull width})^{\mu+\text{jets}}_{b-\text{tag}} = 1.15 \\
(\text{pull width})^{l+\text{jets}} &= 1.26 \quad (\text{pull width})^{l+\text{jets}}_{b-\text{tag}} = 1.22
\end{aligned} \tag{6.4}$$

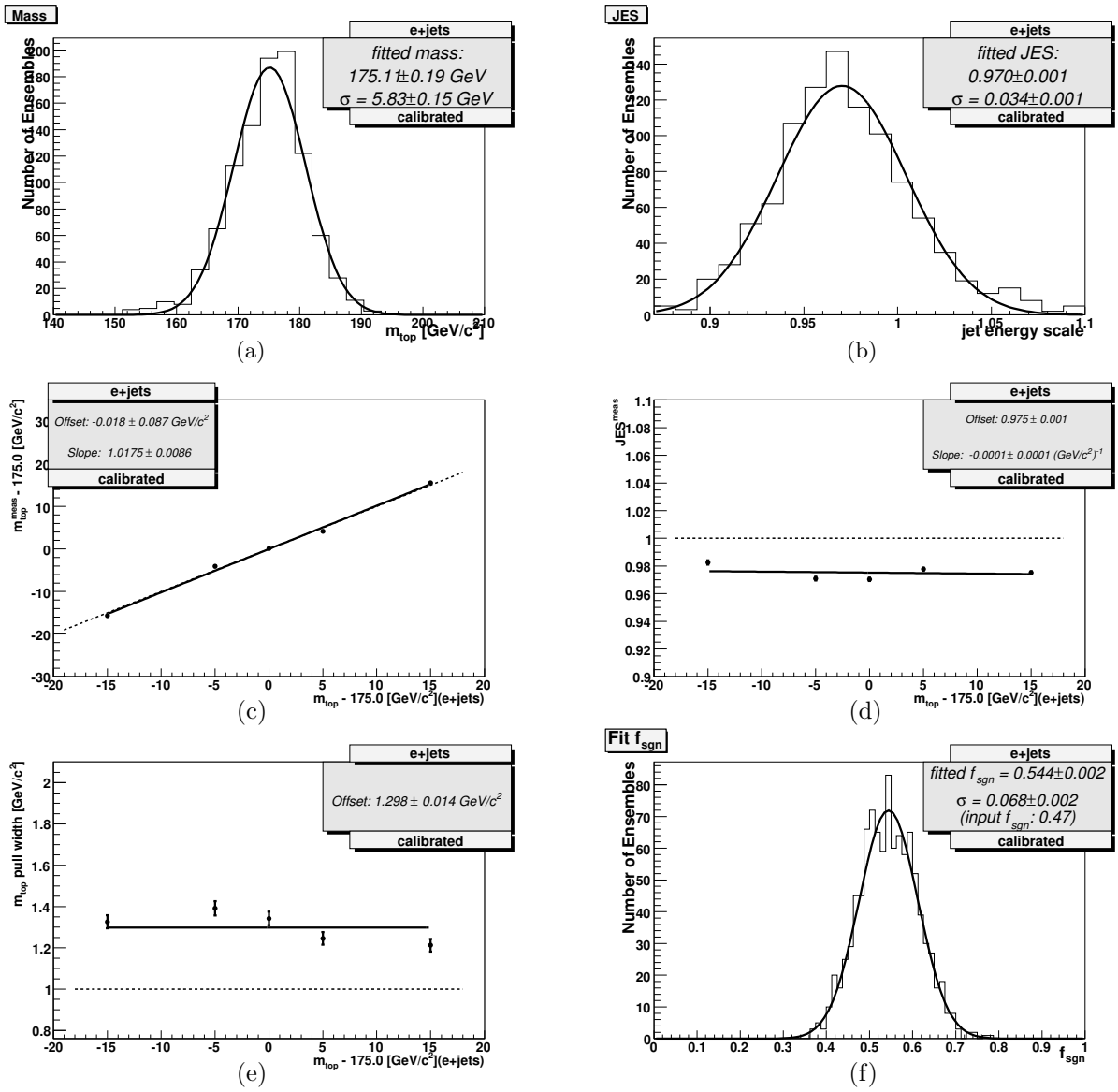

Fig. 6.21. Results of ensemble testing for ensembles with normal background fraction, **heavy-flavor background and QCD included, e+jets (calibrated)**, input mass 175 GeV/c^2 (e+jets): (a) output m_{top}, (b) output JES, (c) output mass vs. input mass, (d) output JES vs. input mass, (e) m_{top} pull vs. input mass, and (f) output f_{top},

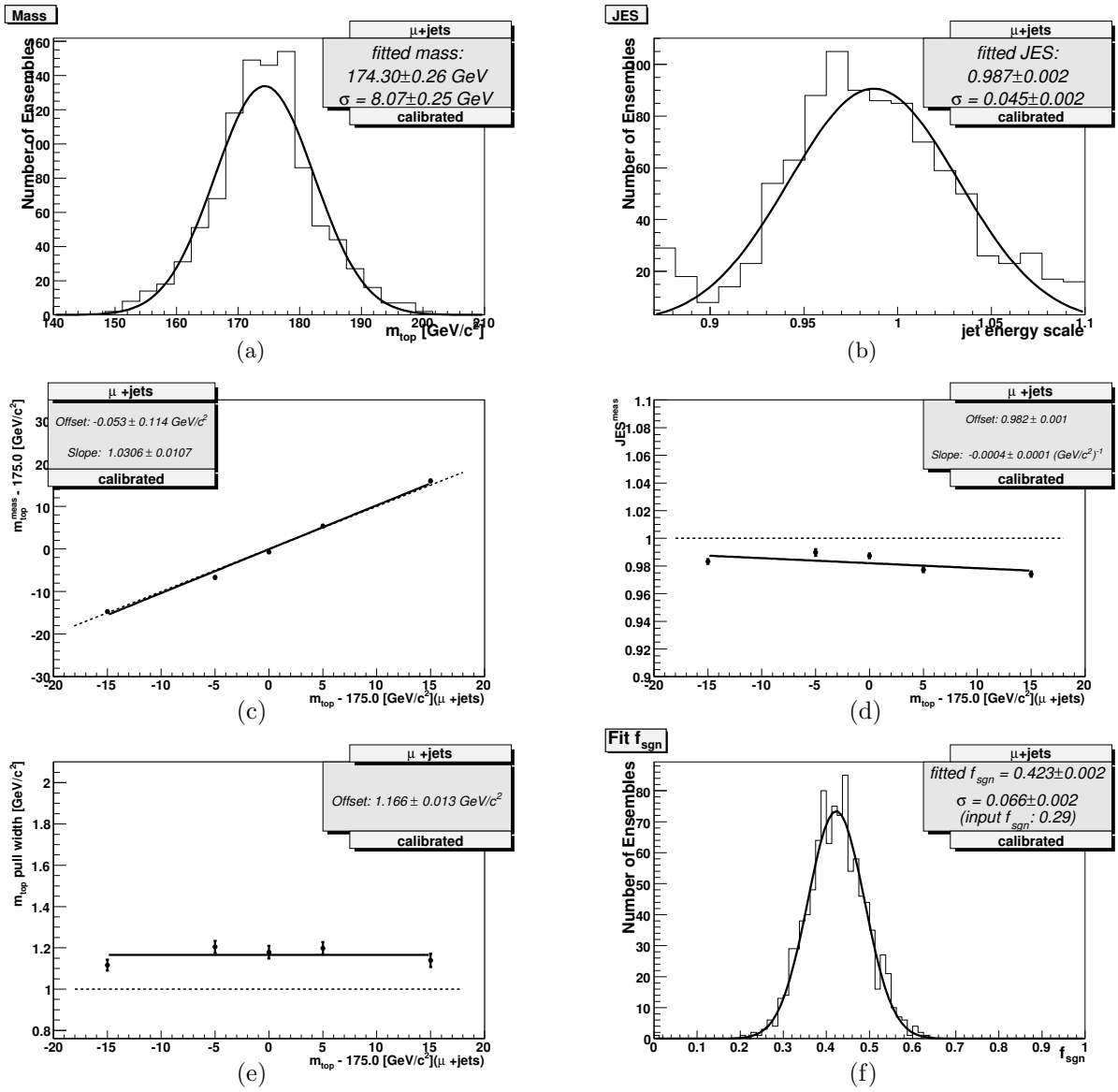

Fig. 6.22. Results of ensemble testing for ensembles with normal background fraction, **heavy-flavor background and QCD included, μ+jets (calibrated)**, input mass 175 GeV/c^2 (μ+jets): (a) output m_{top}, (b) output JES, (c) output mass vs. input mass, (d) output JES vs. input mass, (e) m_{top} pull vs. input mass, and (f) output f_{top},

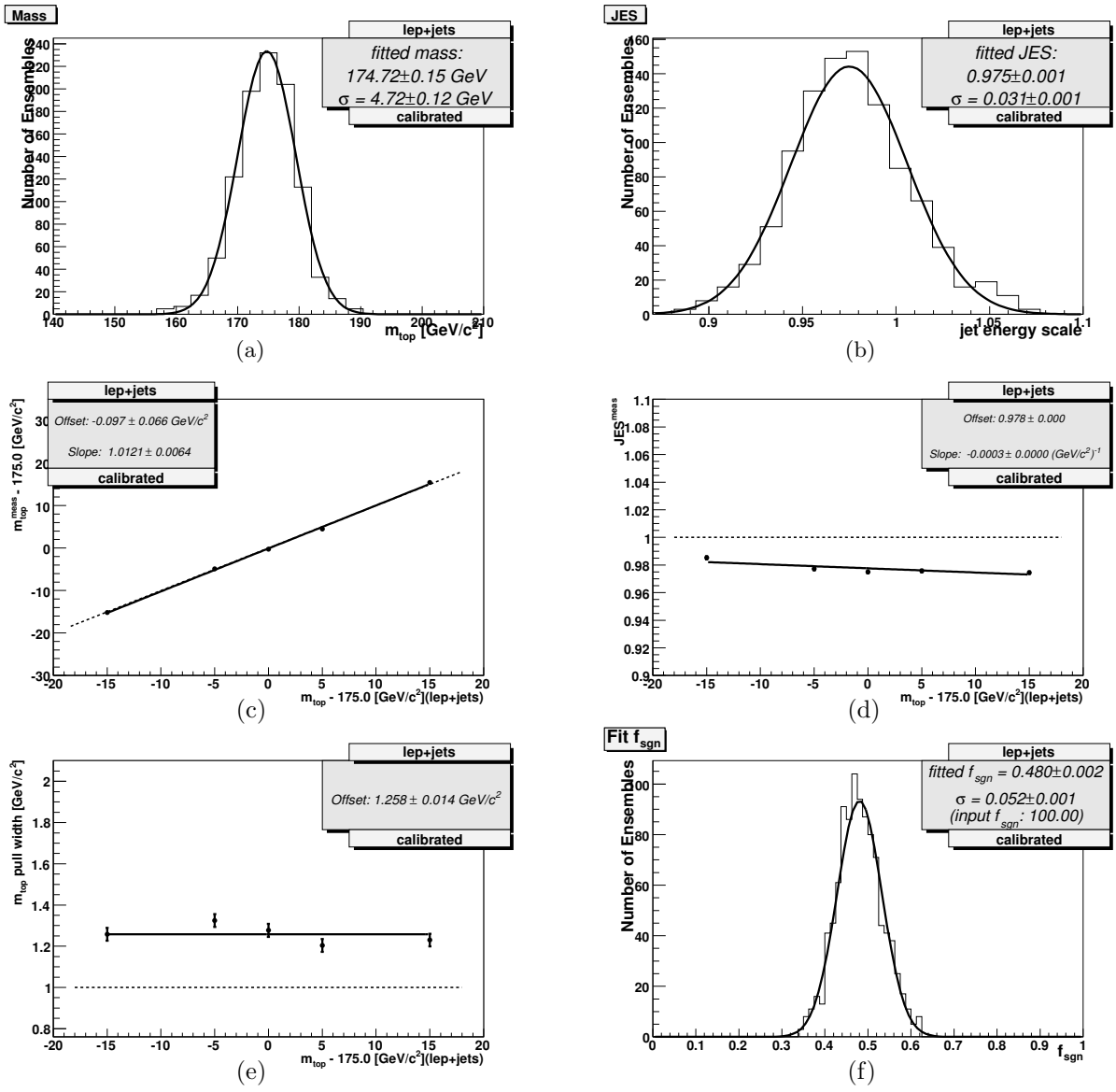

Fig. 6.23. Results of ensemble testing for ensembles with normal background fraction, **heavy-flavor background and QCD included, l+jets (calibrated)**, input mass 175 GeV/c^2 (μ+jets): (a) output m_{top}, (b) output JES, (c) output mass vs. input mass, (d) output JES vs. input mass, (e) m_{top} pull vs. input mass, and (f) output f_{top},

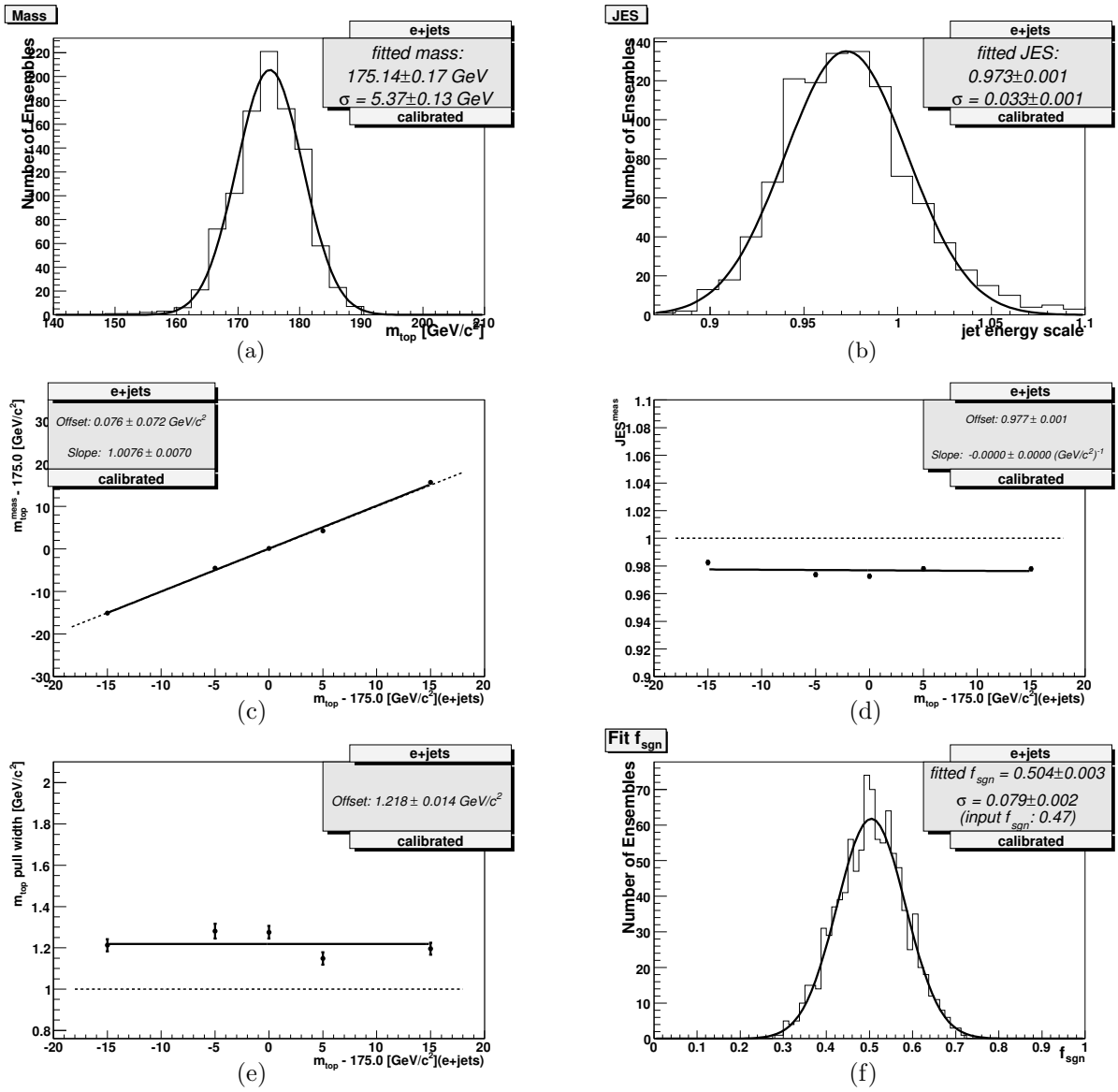

Fig. 6.24. Results of ensemble testing for ensembles with normal background fraction, **heavy-flavor background and QCD included, b-tagging applied, e+jets (calibrated)**, input mass 175 GeV/c^2 (e+jets): (a) output m_{top}, (b) output JES, (c) output mass vs. input mass, (d) output JES vs. input mass, (e) m_{top} pull vs. input mass, and (f) output f_{top},

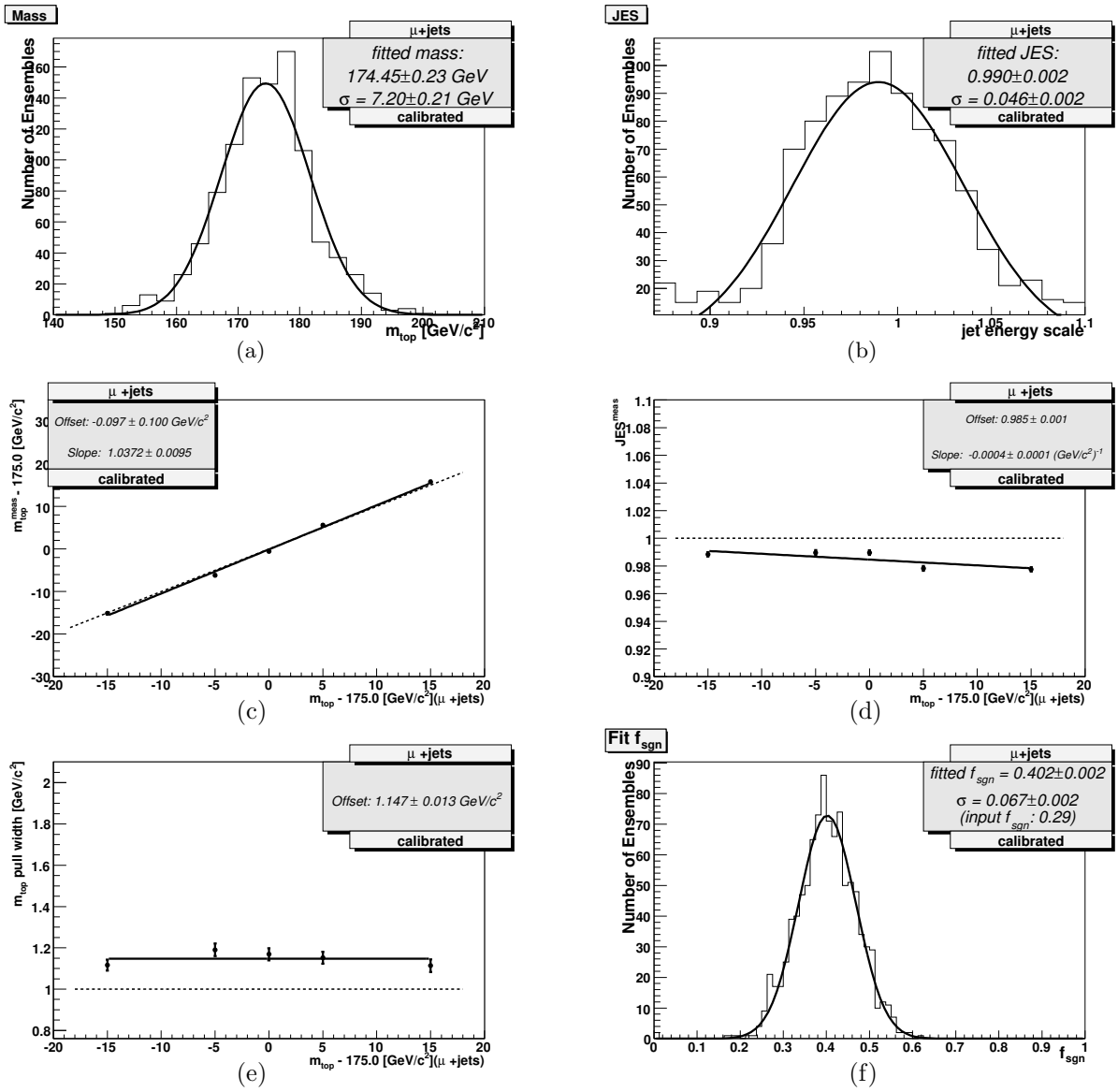

Fig. 6.25. Results of ensemble testing for ensembles with normal background fraction, **heavy-flavor background and QCD included, b-tagging applied, μ+jets (calibrated)**, input mass 175 GeV/c^2 (μ+jets): (a) output m_{top}, (b) output JES, (c) output mass vs. input mass, (d) output JES vs. input mass, (e) m_{top} pull vs. input mass, and (f) output f_{top},

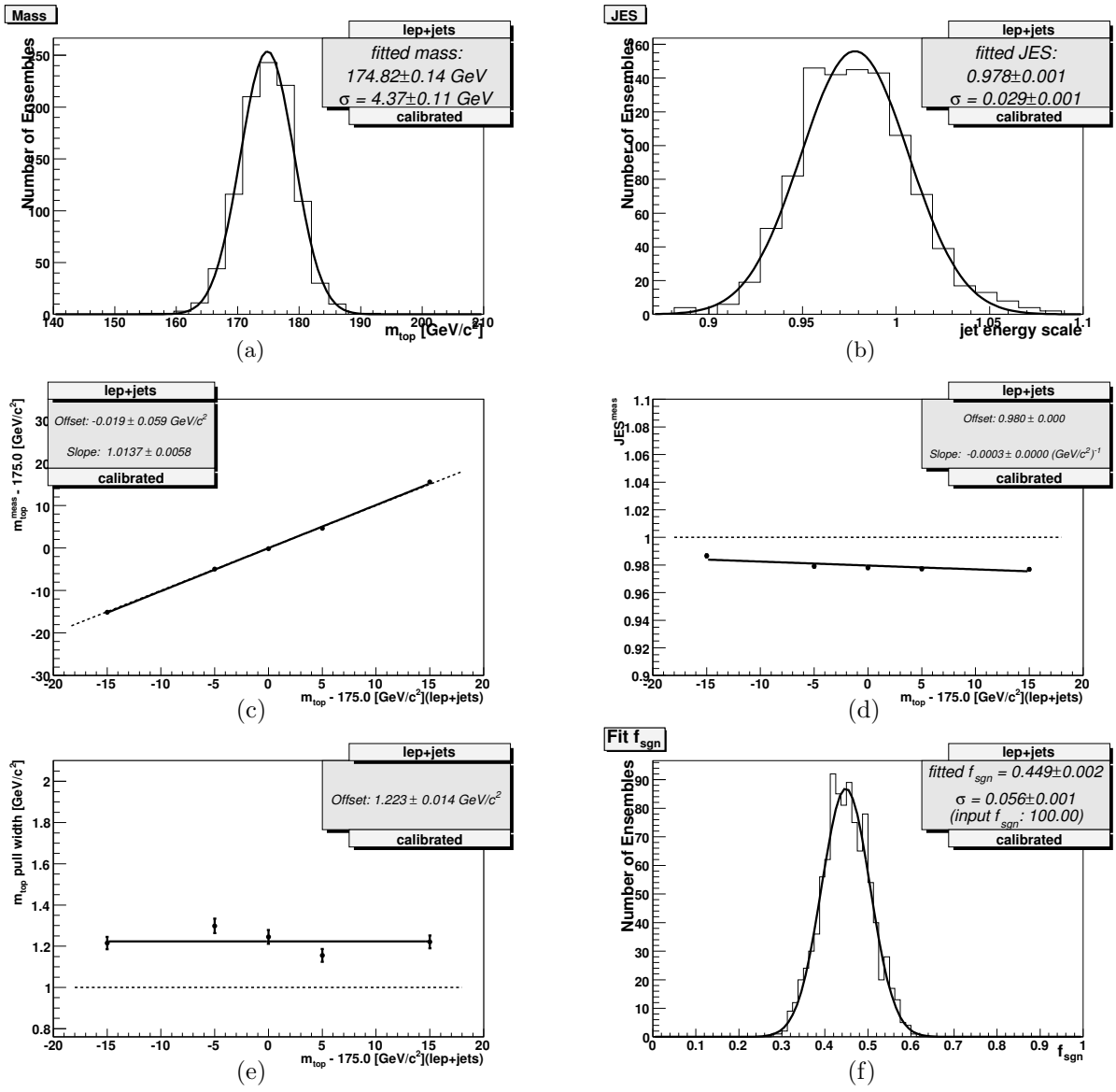

Fig. 6.26. Results of ensemble testing for ensembles with normal background fraction, **heavy-flavor background and QCD included, b-tagging applied, l+jets (calibrated)**, input mass 175 GeV/c^2 (μ+jets): (a) output m_{top}, (b) output JES, (c) output mass vs. input mass, (d) output JES vs. input mass, (e) m_{top} pull vs. input mass, and (f) output f_{top},

6.4 Results

6.4.1 No b-tagging

The results of applying the likelihood fit to data without the use of b-tagging information are shown in Figures 6.27 and 6.28. These are projections of the 2-dimensional likelihood onto the m_{top} and JES axes for e+jets and μ+jets, respectively. All likelihood curves were shifted by the calibrations which depend upon the fitted values of m_{top} and f_{top}. Also shown in Figure 6.29

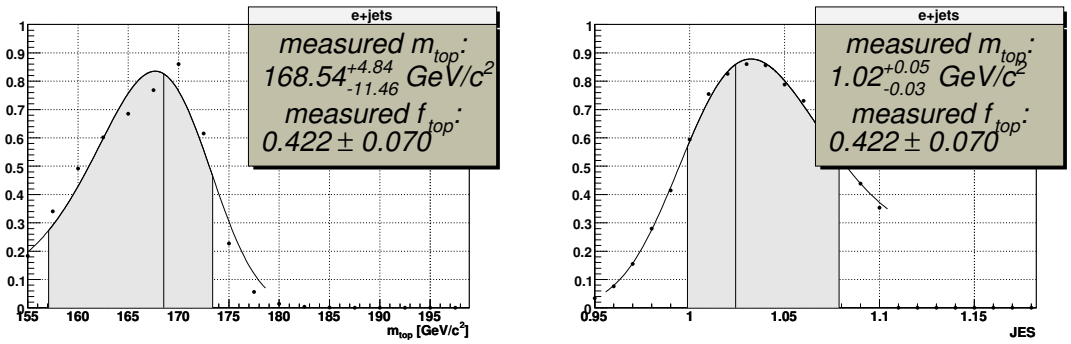

Fig. 6.27. Projection onto m_{top} axis and JES axis of $-ln\ L_{2D}(m_{top}, JES)$ for data events, NO B-TAGGING APPLIED (e+jets).

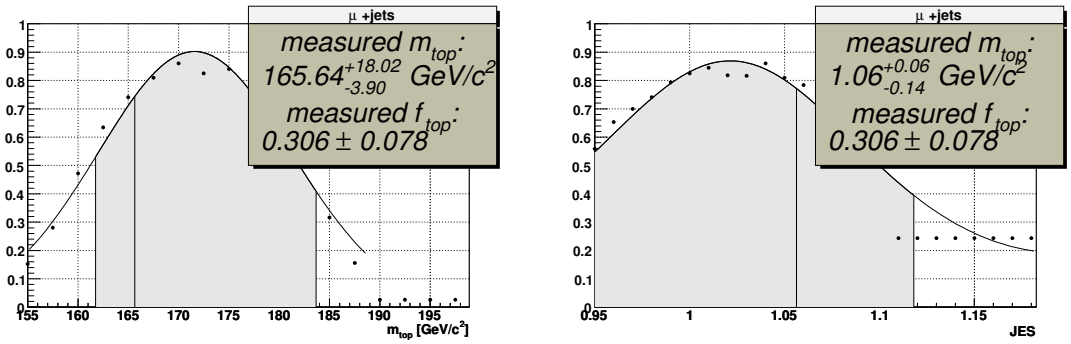

Fig. 6.28. Projection onto m_{top} axis and JES axis of $-ln\ L_{2D}(m_{top}, JES)$ for data events, NO B-TAGGING APPLIED (μ+jets).

are the projections onto the m_{top} and JES axes for the combination of e+jets and μ+jets.

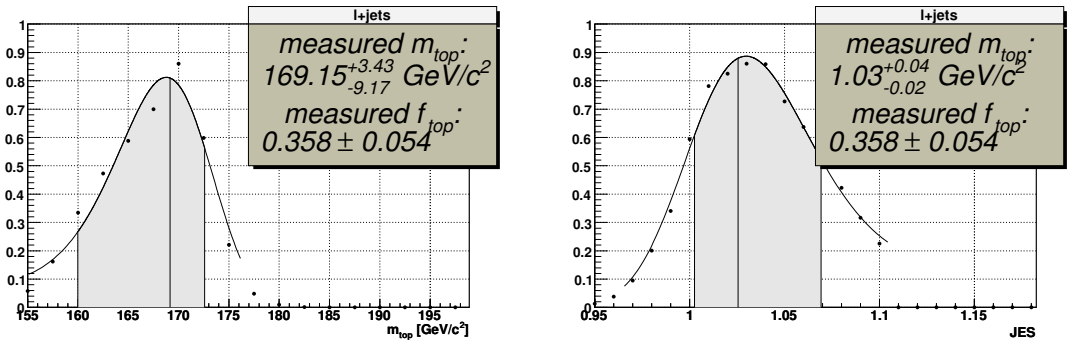

Fig. 6.29. Projection onto JES axis of $-ln\ L_{2D}(m_{top}, JES)$ for lepton+jets data events, NO B-TAGGING APPLIED (e+jets and μ+jets combined).

6.4.2 With b-tagging

The results on data of the likelihood fit using b-tagging information are shown in Figures 6.30 and 6.31. These are projections of the 2-dimensional likelihood onto the m_{top} and JES axes for e+jets and μ+jets, respectively. Also shown in Figure 6.32 are the projections onto the m_{top}

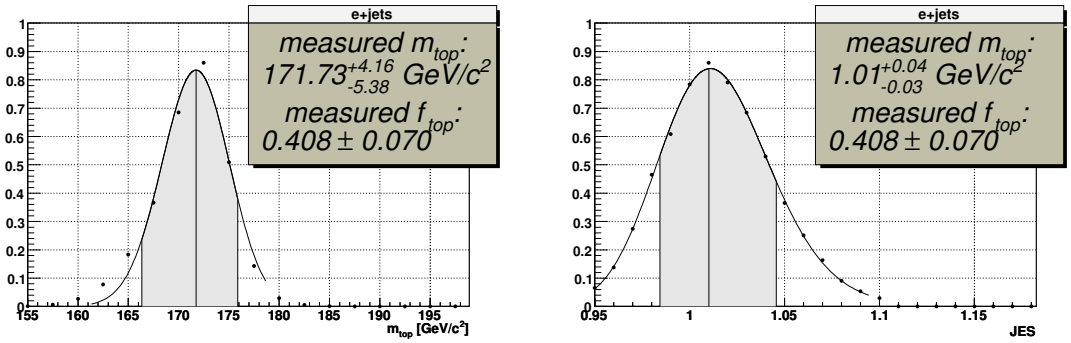

Fig. 6.30. Projection onto m_{top} axis and JES axis of $-ln\ L_{2D}(m_{top}, JES)$ for data events, B-TAGGING APPLIED (e+jets).

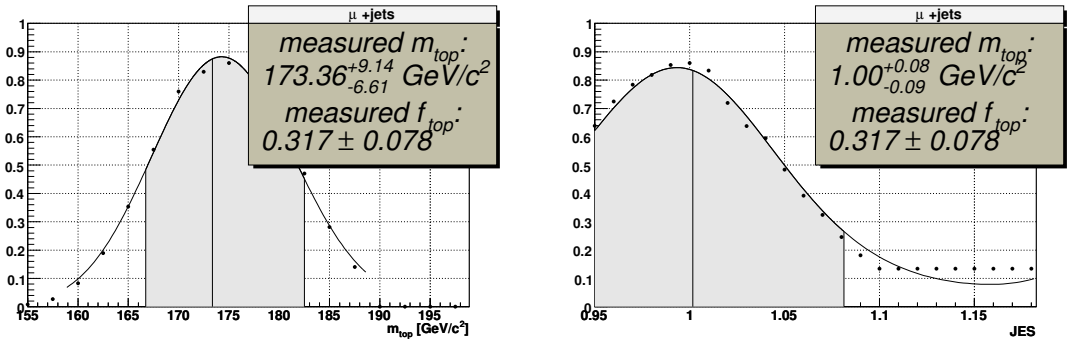

Fig. 6.31. Projection onto m_{top} axis and JES axis of $-ln\ L_{2D}(m_{top}, JES)$ for data events, B-TAGGING APPLIED (μ+jets).

and JES axes for the combination of e+jets and μ+jets.

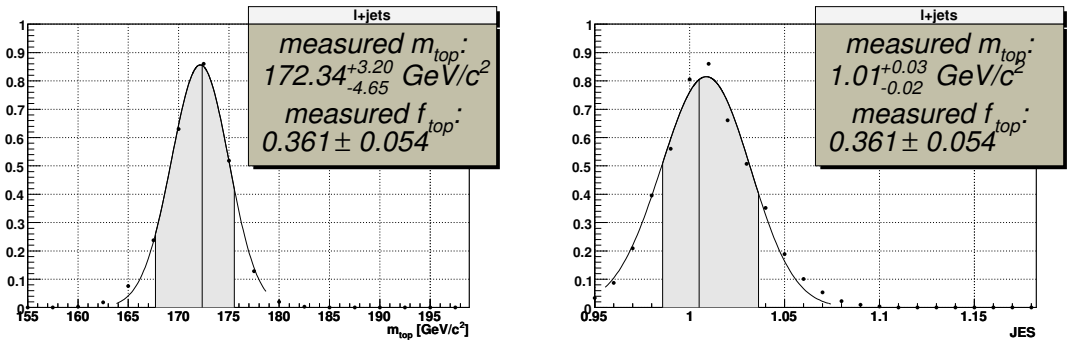

Fig. 6.32. Projection onto JES axis of $-ln\ L_{2D}(m_{top}, JES)$ for lepton+jets data events, B-TAGGING APPLIED (e+jets and μ+jets combined).

6.5 Systematic Errors/Uncertainties

Systematic errors are summarized in Table 7. Details of individual systematic errors are explained below.

	no b-tagging			with b-tagging		
	e+jets	μ+jets	l+jets	e+jets	μ+jets	l+jets
Statistical uncertainty and JES uncertainty	$^{+4.84}_{-11.5}$	$^{+18.0}_{-3.90}$	$^{+3.43}_{-9.17}$	$^{+4.16}_{-5.38}$	$^{+9.14}_{-6.61}$	$^{+3.20}_{-4.65}$
Physics modeling:						
signal modeling	+0.18	+0.40	+0.34	+0.15	+0.34	+0.21
background modeling	±0.66	±2.82	±0.32	±0.66	±2.82	±0.40
PDF uncertainty	± 0.67	± 0.83	± 0.68	± 0.45	± 0.67	± 0.55
b-fragmentation	± 1.29	± 1.04	± 0.76	± 1.26	± 1.45	± 0.61
Detector modeling:						
JES	$^{+2.04}_{-10.6}$	$^{+17.2}_{-0.0}$	$^{+1.16}_{-8.58}$	$^{+2.57}_{-4.27}$	$^{+8.05}_{-5.01}$	$^{+2.45}_{-4.17}$
JES p_T	±0.43	±0.45	±0.46	±0.31	±0.30	±0.35
b response (h/e)	$^{+1.12}_{-0.24}$	$^{+0.53}_{-0.72}$	$^{+0.91}_{-0.39}$	$^{+1.06}_{-0.45}$	$^{+0.44}_{-1.00}$	$^{+0.73}_{-0.71}$
trigger	±0.14	±0.32	±0.16	±0.19	±0.26	±0.12
b-tagging	-	-	-	± 0.42	± 0.36	± 0.26
Method:						
QCD fraction	± 0.27	± 0.04	± 0.68	± 0.26	± 0.08	± 0.71
MC calibration	±0.38	±1.62	±0.86	±0.39	±1.37	±0.61
Total systematic uncertainty (incl. JES)	$^{+2.9}_{-10.7}$	$^{+17.6}_{-3.6}$	$^{+2.2}_{-8.7}$	$^{+3.2}_{-4.6}$	$^{+8.8}_{-6.2}$	$^{+2.9}_{-4.4}$
Systematic uncertainty without JES	$^{+2.1}_{-1.7}$	$^{+3.6}_{-3.6}$	$^{+1.8}_{-1.7}$	$^{+2.0}_{-1.7}$	$^{+3.6}_{-3.7}$	$^{+1.6}_{-1.6}$
Total uncertainty (stat. + syst.)	$^{+5.3}_{-11.6}$	$^{+18.4}_{-5.3}$	$^{+3.9}_{-9.3}$	$^{+4.6}_{-5.6}$	$^{+9.8}_{-7.6}$	$^{+3.6}_{-4.9}$

Table 7
Systematic uncertainties (GeV/c^2).

6.5.1 Physics modeling

Signal Modeling

The P_{sgn} calculation makes the assumption that all 4 jets arise from $t\bar{t}$ decay. The pre-selection applied to data and MC requires events with exactly 4 jets, so, for most $t\bar{t}$ events, this is a good assumption. If, however, a number of extra jets arise through various NLO and higher-order processes, and then the same number of jets is lost through jet merging or failure to pass jet ID, then 1 or more jets will be misinterpreted as coming from $t\bar{t}$ decay contrary to the P_{sgn} assumption.

To estimate the error due to the presence of jets not coming directly from the $q\bar{q} \rightarrow t\bar{t}$ process, a dedicated sample was generated using ALPGEN so that it contains events with 1 extra parton accompanying the $t\bar{t}$ pair. These $t\bar{t}j$ samples were passed through the normal simulation chain (PYTHIA for showering and the GEANT-based DØ detector simulation). It was found that the p_T spectrum for jets not coming from $t\bar{t}$ decay is harder for the $t\bar{t}j$ sample than for the $t\bar{t}$ sample, so it is expected that these events can result in a larger fitted mass from using a leading order (LO) matrix element for P_{sgn}.

The expected $f_{t\bar{t}j}$ values were determined by multiplying the event selection efficiencies (from Ref. [22]),

$$\begin{aligned} \epsilon_{t\bar{t}}^{e+\text{jets}} &= 9.93 \pm 0.12\% \qquad \epsilon_{t\bar{t}j}^{e+\text{jets}} = 10.22 \pm 0.24\% \\ \epsilon_{t\bar{t}}^{\mu+\text{jets}} &= 10.25 \pm 0.13\% \qquad \epsilon_{t\bar{t}j}^{\mu+\text{jets}} = 9.71 \pm 0.24\%. \end{aligned} \tag{6.5}$$

by the LO ALPGEN cross-section estimates. The cross-sections for $t\bar{t}$ production in association with another parton and $t\bar{t}$ only are 2.5 and 6.0 pb, respectively, so the fractions of $t\bar{t}j$ events expected after preselection are

$$f_{t\bar{t}j}^{e+\text{jets}} = 30.3\%$$
$$f_{t\bar{t}j}^{\mu+\text{jets}} = 27.9\%$$
$$f_{t\bar{t}j}^{l+\text{jets}} = 29.1.\%$$

Ensembles were generated with $t\bar{t}$ fractions varying from 0-100% such that the total signal fractions ($f_{t\bar{t}}$ plus $f_{t\bar{t}j}$) were fixed at the expected value. The mass bias Δm_{top} was plotted vs. $f_{t\bar{t}j}$ and fit to a line. These fits, shown in Fig. 6.33 and 6.33, were used to determine the mass bias at the expected $f_{t\bar{t}j}$ values.

The final results are:

$$\begin{aligned}
(\Delta m_t)^{e+\text{jets}} &= +0.18\text{GeV}/c^2 \quad & (\Delta m_t)_{b-\text{tag}}^{e+\text{jets}} &= +0.15\text{GeV}/c^2 \\
(\Delta m_t)^{\mu+\text{jets}} &= +0.40\text{GeV}/c^2 \quad & (\Delta m_t)_{b-\text{tag}}^{\mu+\text{jets}} &= +0.34\text{GeV}/c^2 \\
(\Delta m_t)^{l+\text{jets}} &= +0.34\text{GeV}/c^2 \quad & (\Delta m_t)_{b-\text{tag}}^{l+\text{jets}} &= +0.21\text{GeV}/c^2
\end{aligned} \tag{6.6}$$

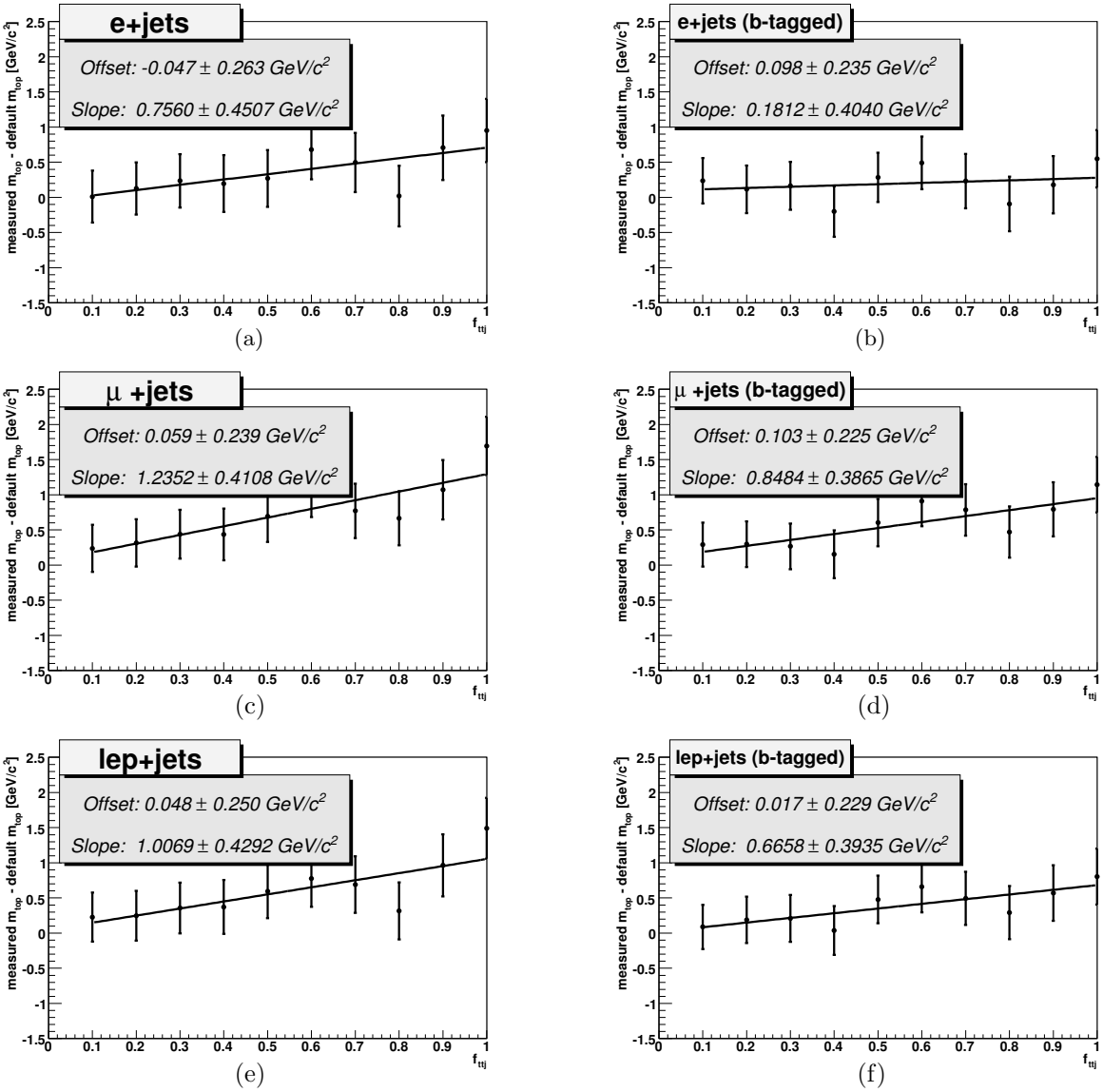

Fig. 6.33. Measured Δm_t vs. $f_{t\bar{t}j}$, untagged (*left*) and b-tagged(*right*), e+jets (*top*), μ+jets(*middle*), and l+jets(*bottom*)

Background Modeling

The default MC samples use the factorization scale

$$Q^2 = m_W^2 + \sum_j p_{T,j}^2. \tag{6.7}$$

To study the effect of alternate factorization scales, the analysis described in Ref. [22] used a $Wjjjj$ sample generated with the factorization scale

$$Q'^2 = \langle p_{T,j} \rangle^2 . \tag{6.8}$$

A single large ensemble was generated with the alternate $Wjjjj$ events, giving the following results (the l+jets results are from Ref. [88]):

$$\begin{aligned} (\Delta m_t)^{e+\text{jets}} &= \pm 0.66 \text{GeV}/c^2 \\ (\Delta m_t)^{\mu+\text{jets}} &= \pm 2.82 \text{GeV}/c^2 \\ (\Delta m_t)^{l+\text{jets}} &= \pm 0.32 \text{GeV}/c^2 \quad (\Delta m_t)^{l+\text{jets}}_{b-\text{tag}} = \pm 0.40 \text{GeV}/c^2 \end{aligned} \tag{6.9}$$

These results are quoted for the systematic uncertainty associated with background modeling. The b-tagged μ+jets and e+jets uncertainties are assumed to be the same as the uncertainties obtained without b-tagging.

An additional study was done in which the background W+jet events, including those with heavy-flavor jets, were reweighted using alternate factorization scales. To do this, the parton-

level kinematics were used to calculate the factorization scales using the original scale choice (Eqn. 6.7) and three alternate choices:

$$Q'^2 = \langle p_{T,j} \rangle^2 \tag{6.10}$$

$$Q'^2 = m_W^2 + p_{T,W}^2 \tag{6.11}$$

$$Q'^2 = m_W^2. \tag{6.12}$$

These studies gave uncertainties smaller than the e+jets and μ+jets uncertainties from Ref. [22]. However, since this method of rescaling factorization scales does not properly simulate the behavior in PYTHIA that would be expected from an alternate factorization scale choice, the uncertainties were not used in the final quoted systematic uncertainty to be conservative.

In addition, ensembles were generated using a global reweighting of the factorization scale by factors of 2 and 1/2. The larger of the two shifts are used to form the symmetrized uncertainties:

$$\begin{aligned}
(\Delta m_t)^{e+\text{jets}} &= \pm 0.44 \text{GeV}/c^2 \quad & (\Delta m_t)^{e+\text{jets}}_{b-\text{tag}} &= \pm 0.19 \text{GeV}/c^2 \\
(\Delta m_t)^{\mu+\text{jets}} &= \pm 0.53 \text{GeV}/c^2 \quad & (\Delta m_t)^{\mu+\text{jets}}_{b-\text{tag}} &= \pm 0.63 \text{GeV}/c^2 \\
(\Delta m_t)^{l+\text{jets}} &= \pm 0.35 \text{GeV}/c^2 \quad & (\Delta m_t)^{l+\text{jets}}_{b-\text{tag}} &= \pm 0.25 \text{GeV}/c^2
\end{aligned} \tag{6.13}$$

These are consistent with the shifts observed with the alternate factorization scale parametrization, and are also not used in the final quoted systematic uncertainty.

PDF Uncertainty

The calculations of P_{sgn} and P_{bkg} use leading order (LO) matrix elements, and a LO parton distribution function (PDF). The PDFs were evaluated using CTEQ5L. [39] To estimate the effect on m_t due to PDF uncertainties, the standard $t\bar{t}$ and W+jets MC samples were reweighted

using the CTEQ6M PDF set. The CTEQ6M set contains up and down variations along 20 eigenvectors corresponding to 20 free parameters in the PDF parametrization.

Since the uncertainties due to PDF variations are very small, they were evaluated using ensembles generated with strong correlations so that differences between ensembles arise almost entirely from the small PDF variations. The seeds used for the random selection of events for the pseudo-experiments within each ensemble were determined by the pseudo-experiment number and the order of event selection within the pseudo-experiment. The event that was chosen was then either accepted or rejected using a weight that depends on the PDF evaluated using the incoming parton momenta. Events were chosen from the pool until one was selected. In this way, the only differences between events are from PDF variations rather than statistical fluctuations.

Each PDF variation was compared to an ensemble which was first reweighted to the base CTEQ6M set. For each of 40 variations, a scatter plot was made consisting of entries in the varied ensemble versus the base ensemble. Each entry was a pairing of the output mass for a pseudo-experiment within one ensemble and the output mass of the corresponding pseudo-experiment within the second ensemble. A typical scatter plot is shown in Figure 6.34. The points were fit to a line with the slope fixed at 1.0. The offset and the error in the calculated offset were added in quadrature to get the systematic uncertainty due to the PDF variation . The larger of the two variations (up and down) for each of the 20 CTEQ6M eigenvectors are given in Table 8.

The total uncertainties due to the choice of PDF obtained by adding the 20 errors in quadrature are:

$$\begin{aligned}
(\Delta m_t)^{e+\text{jets}} &= \pm 0.67\text{GeV}/c^2 \quad & (\Delta m_t)^{e+\text{jets}}_{b-\text{tag}} &= \pm 0.45\text{GeV}/c^2 \\
(\Delta m_t)^{\mu+\text{jets}} &= \pm 0.83\text{GeV}/c^2 \quad & (\Delta m_t)^{\mu+\text{jets}}_{b-\text{tag}} &= \pm 0.67\text{GeV}/c^2 \\
(\Delta m_t)^{l+\text{jets}} &= \pm 0.68\text{GeV}/c^2 \quad & (\Delta m_t)^{l+\text{jets}}_{b-\text{tag}} &= \pm 0.55\text{GeV}/c^2
\end{aligned} \tag{6.14}$$

	no b-tagging			with b-tagging		
Variation	e+jets	μ+jets	l+jets	e+jets	μ+jets	l+jets
1	0.05	0.12	0.03	0.05	0.12	0.04
2	0.05	0.07	0.03	0.03	0.07	0.03
3	0.05	0.20	0.04	0.05	0.14	0.03
4	0.05	0.11	0.04	0.03	0.08	0.03
5	0.09	0.13	0.05	0.08	0.10	0.08
6	0.13	0.18	0.21	0.12	0.18	0.16
7	0.15	0.14	0.17	0.08	0.15	0.13
8	0.16	0.22	0.11	0.12	0.17	0.10
9	0.09	0.16	0.10	0.11	0.17	0.10
10	0.11	0.22	0.11	0.09	0.1	0.09
11	0.09	0.11	0.10	0.05	0.11	0.08
12	0.06	0.17	0.07	0.05	0.12	0.09
13	0.11	0.27	0.16	0.06	0.25	0.12
14	0.07	0.19	0.14	0.05	0.13	0.07
15	0.50	0.27	0.49	0.31	0.26	0.40
16	0.05	0.09	0.05	0.05	0.14	0.06
17	0.14	0.18	0.12	0.10	0.12	0.07
18	0.08	0.13	0.11	0.06	0.11	0.08
19	0.18	0.37	0.11	0.09	0.19	0.09
20	0.10	0.10	0.09	0.04	0.10	0.06
total	$\pm$0.67	$\pm$0.83	$\pm$0.68	$\pm$0.45	$\pm$0.67	$\pm$0.55

Table 8
Systematic uncertainties (GeV/c^2) due to PDF variations.

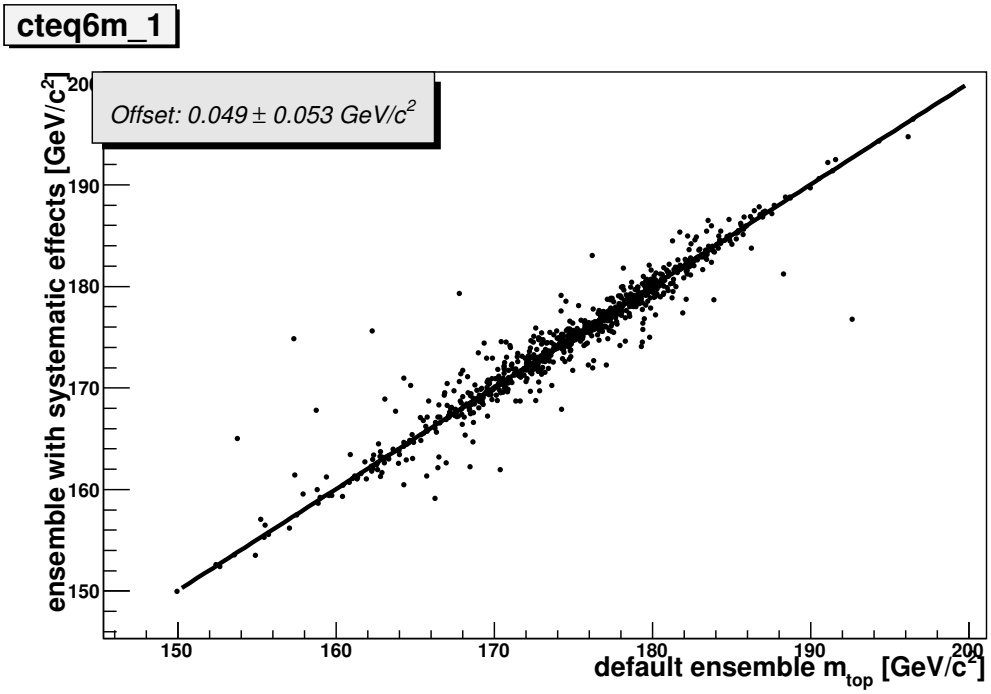

Fig. 6.34. Scatter plot of fitted m_t for an ensemble generated with a variation of one of the 20 eigenvalues of the CTEQ6M PDF set vs. an ensemble reweighted with the standard CTEQ6M PDF set.

b-fragmentation Model

The standard MC samples use in the event generators the Bowler fragmentation scheme [98] with $r_t = 1.0$. Two additional $t\bar{t}$ samples were generated with the following b-fragmentation models:

- Peterson fragmentation [99], $\epsilon = 0.00191$
- Bowler fragmentation, $r_t = 0.69$ ("B069-sample")

b-fragmentation	no b-tagging			with b-tagging		
	e+jets	μ+jets	l+jets	e+jets	μ+jets	l+jets
Peterson, $\epsilon = 0.00191$	1.11	0.39	0.75	1.05	0.51	0.59
Bowler, $r_t = 0.69$	0.66	0.96	0.15	0.69	1.36	0.17
final	$\pm$1.29	$\pm$1.04	$\pm$0.76	$\pm$1.26	$\pm$1.45	$\pm$0.61

Table 9
Systematic errors (GeV/c^2) due to b-fragmentation modeling.

Systematic errors were estimated using the same type of correlated sampling used to evaluate systematic uncertainties due to PDF uncertainties. Errors from the two b-fragmentation models, shown in Table 9, were added in quadrature to get:

$$\begin{aligned} (\Delta m_t)^{e+\text{jets}} &= \pm 1.29 \text{GeV}/c^2 \quad (\Delta m_t)^{e+\text{jets}}_{b-\text{tag}} = \pm 1.26 \text{GeV}/c^2 \\ (\Delta m_t)^{\mu+\text{jets}} &= \pm 1.04 \text{GeV}/c^2 \quad (\Delta m_t)^{\mu+\text{jets}}_{b-\text{tag}} = \pm 1.45 \text{GeV}/c^2 \\ (\Delta m_t)^{l+\text{jets}} &= \pm 0.76 \text{GeV}/c^2 \quad (\Delta m_t)^{l+\text{jets}}_{b-\text{tag}} = \pm 0.61 \text{GeV}/c^2 \end{aligned} \tag{6.15}$$

6.5.2 Detector Modeling

Jet Energy Scale

The two-dimensional likelihood fit gives an error with includes a systematic uncertainty in the top mass measurement due to errors in the jet energy scale. To estimate the systematic error due to JES alone, the JES hypothesis was fixed to 1.0 and the one-dimensional likelihood fits were used to determine top mass errors which are statistical only. Results of likelihood fits

for JES=1.0 are shown in Figures 6.35 through 6.37. The JES contributions to the error on m_{top} are:

$$\begin{array}{llll} (\Delta m_t)^{e+\text{jets}} & =^{+2.04}_{-10.6}\ \text{GeV}/c^2 & (\Delta m_t)^{e+\text{jets}}_{b-\text{tag}} & =^{+2.57}_{-4.27}\ \text{GeV}/c^2 \\ (\Delta m_t)^{\mu+\text{jets}} & =^{+17.2}_{-0.0}\ \text{GeV}/c^2 & (\Delta m_t)^{\mu+\text{jets}}_{b-\text{tag}} & =^{+8.05}_{-5.01}\ \text{GeV}/c^2 \\ (\Delta m_t)^{l+\text{jets}} & =^{+1.16}_{-8.58}\ \text{GeV}/c^2 & (\Delta m_t)^{l+\text{jets}}_{b-\text{tag}} & =^{+2.45}_{-4.17}\ \text{GeV}/c^2 \end{array} \tag{6.16}$$

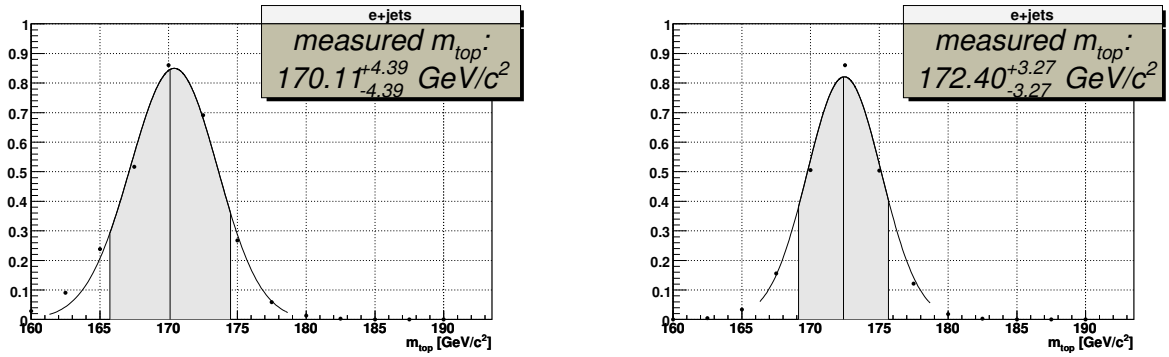

(a) (b)

Fig. 6.35. $-ln\ L(m_{top})$ for e+jets data events with JES fixed at 1.0, (a) without b-tagging, and (b) with b-tagging applied.

JES p_T dependence

Errors in the jet energy scale parametrizations as functions of detector $|\eta|$ and p_T were considered as sources of systematic uncertainties in the m_t measurement. The dependence on jet transverse energy, p_T^{jet}, was varied up by 1 σ, and the standard MC samples were reanalyzed

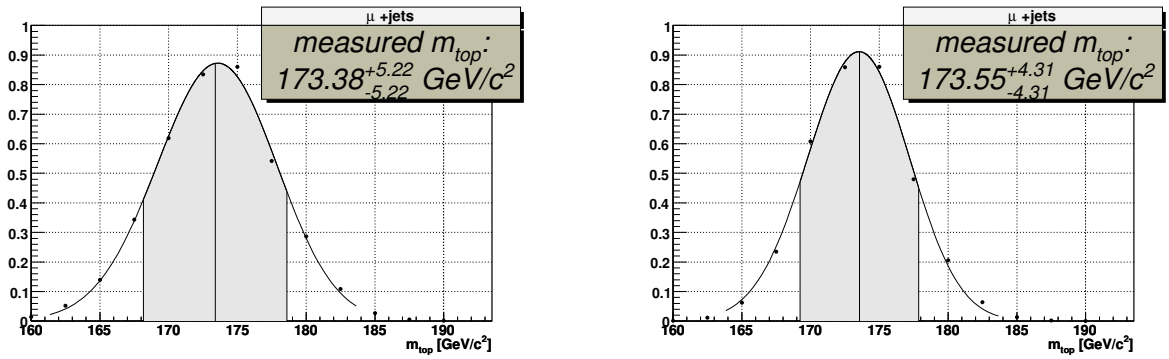

(a) (b)

Fig. 6.36. $-ln\ L(m_{top})$ for μ+jets data events with JES fixed at 1.0, (a) without b-tagging, and (b) with b-tagging applied.

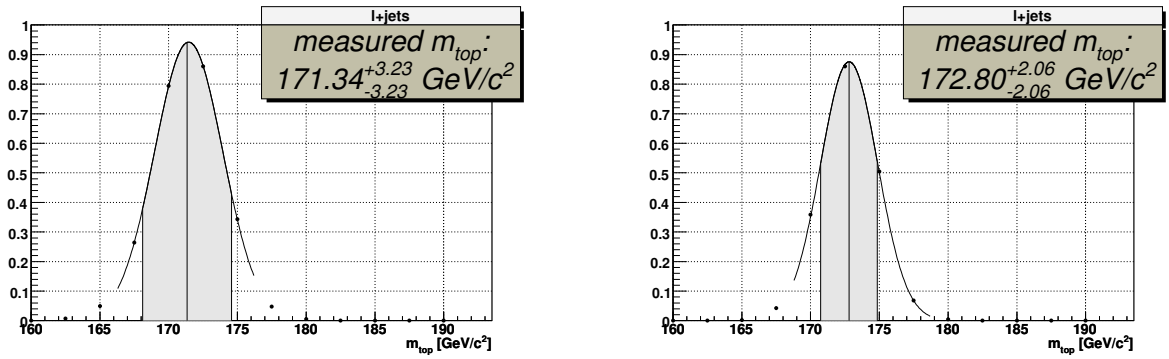

(a) (b)

Fig. 6.37. $-ln\ L(m_{top})$ for l+jets data events (e+jets and μ+jets combined after separate calibrations) with JES fixed at 1.0, (a) without b-tagging, and (b) with b-tagging applied.

using the normal matrix element procedure. The results, assumed to be symmetric for variations up and down, are:

$$\begin{aligned}
(\Delta m_t)^{e+\text{jets}} &= \pm 0.43\text{GeV}/c^2 \quad (\Delta m_t)^{e+\text{jets}}_{b-\text{tag}} = \pm 0.31\text{GeV}/c^2 \\
(\Delta m_t)^{\mu+\text{jets}} &= \pm 0.45\text{GeV}/c^2 \quad (\Delta m_t)^{\mu+\text{jets}}_{b-\text{tag}} = \pm 0.30\text{GeV}/c^2 \\
(\Delta m_t)^{l+\text{jets}} &= \pm 0.46\text{GeV}/c^2 \quad (\Delta m_t)^{l+\text{jets}}_{b-\text{tag}} = \pm 0.35\text{GeV}/c^2.
\end{aligned} \tag{6.17}$$

Earlier studies [22] show no effect from varying the dependence of JES on detector $|\eta|$.

h/e Calorimeter Response

Signal and background probabilities use different transfer function for b and light jets. These transfer functions are corrections to the overall JES which is derived using an inclusive γ+jets sample, and are derived using the same MC samples used for ensemble testing. These corrections are, however, only as good as the MC simulation.

Differences in responses of the DØ calorimeter to hadronic and electromagnetic particles give different detector responses to light and heavy-flavor jets. A variation of 15% in the h/e response is expected to result in a b-to-light jet response variation of +1.5 -1.3% for $20 < p_T^{jet} < 92$ [94]. Ensemble testing was done using the normal b-to-light response, and also with the b-jets scaled up and down by 3% in the $t\bar{t}$ events within the ensemble. These were used to derive a calibration, and the quoted errors were calculated using +1.5 -1.3% variations in the b-to-light response. Calibrations are shown in Figure 6.38.

Final uncertainties due to h/e calorimeter response are:

$$\begin{aligned}
(\Delta m_t)^{e+\text{jets}} &= ^{+1.12}_{-0.24}\ \text{GeV}/c^2 \quad (\Delta m_t)^{e+\text{jets}}_{b-\text{tag}} = ^{+1.06}_{-0.45}\ \text{GeV}/c^2 \\
(\Delta m_t)^{\mu+\text{jets}} &= ^{+0.53}_{-0.72}\ \text{GeV}/c^2 \quad (\Delta m_t)^{\mu+\text{jets}}_{b-\text{tag}} = ^{+0.44}_{-1.00}\ \text{GeV}/c^2 \\
(\Delta m_t)^{l+\text{jets}} &= ^{+0.91}_{-0.39}\ \text{GeV}/c^2 \quad (\Delta m_t)^{l+\text{jets}}_{b-\text{tag}} = ^{+0.73}_{-0.71}\ \text{GeV}/c^2
\end{aligned} \tag{6.18}$$

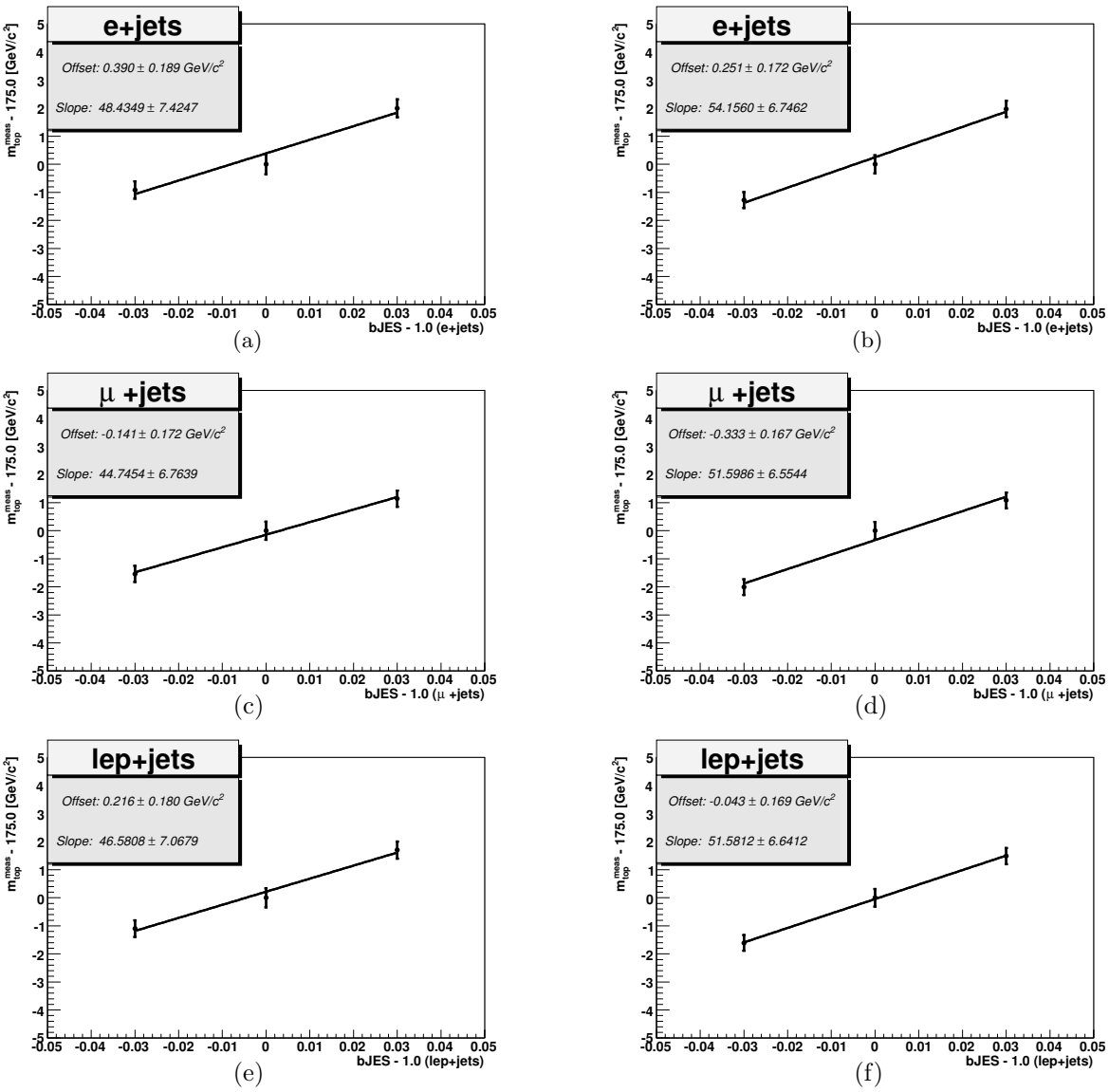

Fig. 6.38. Fitted m_{top} vs. b-jet energy scales for 1000 ensembles, normal signal and background composition, untagged (*left*) and b-tagged(*right*), e+jets (*top*), μ+jets(*middle*), and l+jets(*bottom*)

Trigger

The trigger efficiencies are used to simulate the effect of the DØ trigger system on event selection. Trigger efficiencies are used in the calculations of event probability normalizations as described in Sect. 5.3.3 using a dedicated tool developed within the DØ top group. [26] The **top_trigger** package determines average trigger efficiencies for different periods of data collection by considering all trigger versions in use during the data collection period, and weighting each trigger version by the luminosity collected using that trigger version. A turn-on curve is provided for each of the three levels of the trigger system for EM objects, muons, and jets as functions of particle momentum and η. Systematic variations are also provided.

For determining systematic uncertainties due to these trigger variations, trigger efficiencies used to select events for ensembles (see Sect. 6.3.1) were varied up and down for each of the 9 turn on curves. The correlated event selection used for PDF uncertainties was used, giving the values shown in Table 10. The final values are

$$\begin{aligned}
(\Delta m_t)^{e+\text{jets}} &= \pm 0.14\text{GeV}/c^2 \quad & (\Delta m_t)^{e+\text{jets}}_{b-\text{tag}} &= \pm 0.19\text{GeV}/c^2 \\
(\Delta m_t)^{\mu+\text{jets}} &= \pm 0.32\text{GeV}/c^2 \quad & (\Delta m_t)^{\mu+\text{jets}}_{b-\text{tag}} &= \pm 0.26\text{GeV}/c^2 \\
(\Delta m_t)^{l+\text{jets}} &= \pm 0.16\text{GeV}/c^2 \quad & (\Delta m_t)^{l+\text{jets}}_{b-\text{tag}} &= \pm 0.12\text{GeV}/c^2.
\end{aligned} \tag{6.19}$$

	Δm_{top}					
	no b-tagging			with b-tagging		
	e+jets	μ+jets	l+jets	e+jets	μ+jets	l+jets
EM Level1	0.08	0.04	0.04	0.12	0.05	0.06
EM Level2	0.04	0.04	0.04	0.05	0.05	0.02
EM Level3	0.04	0.04	0.04	0.09	0.05	0.03
MU Level1	0.03	0.13	0.04	0.04	0.10	0.03
MU Level2	0.03	0.16	0.05	0.04	0.09	0.03
MU Level3	0.03	0.04	0.04	0.04	0.05	0.02
JT Level1	0.04	0.04	0.04	0.04	0.05	0.02
JT Level2	0.03	0.04	0.04	0.04	0.05	0.02
JT Level3	0.04	0.23	0.10	0.05	0.18	0.08
final	$\pm$0.14	$\pm$0.32	$\pm$0.16	$\pm$0.19	$\pm$0.26	$\pm$0.12

Table 10
Systematic errors due to trigger selection efficiencies

b-Tagging Uncertainties

Uncertainties in b-tagging arise from a number of sources. The event tagging probabilities are evaluated in Monte Carlo, and limited MC statistics give uncertainties in the taggability and tagging efficiencies. Each of the following parameters were varied up and down within their uncertainties:

- taggability in data,
- taggability flavor-dependence,
- b-tagging efficiency in MC,
- c-tagging efficiency in MC,
- semileptonic b-tagging efficiency in MC,
- semileptonic b-tagging efficiency in data,
- negative tag rate, and
- light flavor scale factor in MC.

Ensembles were generated to evaluate the uncertainty due to each parameter variation. Results are given in Table 11. Uncertainties due to b-tagging are:

$$\begin{aligned} (\Delta m_t)^{e+\text{jets}}_{b-\text{tag}} &= \pm 0.42 \text{GeV}/c^2 \\ (\Delta m_t)^{\mu+\text{jets}}_{b-\text{tag}} &= \pm 0.36 \text{GeV}/c^2 \\ (\Delta m_t)^{l+\text{jets}}_{b-\text{tag}} &= \pm 0.26 \text{GeV}/c^2. \end{aligned} \tag{6.20}$$

	e+jets	μ+jets	l+jets
taggability	$\pm$0.16	0.11	0.08
taggability flavor-dep	$\pm$0.15	0.11	0.06
b-tag eff	$\pm$0.14	0.11	0.08
c-tag eff	$\pm$0.14	0.14	0.10
semilept b MC	$\pm$0.15	0.12	0.08
semilept b data	$\pm$0.14	0.15	0.15
neg tag rate	$\pm$0.17	0.13	0.08
light scale factor	$\pm$0.14	0.13	0.08
final	$\pm$0.42	0.36	0.26

Table 11
Systematic errors due to tagging probability uncertainties

	Δm_{top}					
	no b-tagging			with b-tagging		
	e+jets	μ+jets	l+jets	e+jets	μ+jets	l+jets
f_{QCD}+δf_{QCD}	0.27±0.37	0.04±0.52	0.68±0.35	0.26±0.33	0.07±0.47	0.71±0.32
f_{QCD}-δf_{QCD}	0.18±0.35	0.02±0.53	0.39±0.33	0.11±0.32	-0.08±0.48	0.44±0.32
final	± 0.27	±0.04	± 0.68	± 0.26	±0.08	± 0.71

Table 12
Systematic errors due to errors in f_{QCD} estimation

6.5.3 Method

QCD fraction

The expected QCD fractions, f_{QCD}, and errors in f_{QCD} were determined using the topological discriminant described in Ref. [22]. To determine the systematic uncertainty due to errors in f_{QCD}, ensemble testing was repeated using values of f_{QCD} varied up and down within the errors. The differences between the fitted masses in the normal ensembles and ensembles generated with f_{QCD} varied up and down were determined, and the larger of the two differences is quoted as the systematic error for each sample type. Results are summarized in Table 12.

MC Calibration

The calibration parameters were varied up and down by 1 σ and the ensembles with normal sample composition were re-evaluated. The maximum Δm_t was taken for the variation of each parameter. These values are shown in Table 13, and results of adding these in quadrature are:

$$\begin{aligned}
(\Delta m_t)^{e+\text{jets}} &= \pm 0.38\text{GeV}/c^2 \quad (\Delta m_t)^{e+\text{jets}}_{b-\text{tag}} = \pm 0.39\text{GeV}/c^2 \\
(\Delta m_t)^{\mu+\text{jets}} &= \pm 1.62\text{GeV}/c^2 \quad (\Delta m_t)^{\mu+\text{jets}}_{b-\text{tag}} = \pm 1.37\text{GeV}/c^2 \\
(\Delta m_t)^{l+\text{jets}} &= \pm 0.86\text{GeV}/c^2 \quad (\Delta m_t)^{l+\text{jets}}_{b-\text{tag}} = \pm 0.61\text{GeV}/c^2.
\end{aligned} \tag{6.21}$$

	no b-tagging			with b-tagging		
	e+jets	μ+jets	l+jets	e+jets	μ+jets	l+jets
e+jets p_0	0.24	0.00	0.34	0.24	0.00	0.25
e+jets p_1	0.23	0.00	0.32	0.23	0.00	0.24
e+jets p_2	0.13	0.00	0.28	0.15	0.00	0.19
e+jets p_3	0.13	0.00	0.26	0.15	0.00	0.15
μ+jets p_0	0.00	0.91	0.34	0.00	0.76	0.25
μ+jets p_1	0.00	0.89	0.34	0.00	0.75	0.25
μ+jets p_2	0.00	0.70	0.27	0.00	0.61	0.20
μ+jets p_3	0.00	0.71	0.28	0.00	0.60	0.18
final	$\pm$0.38	$\pm$1.62	$\pm$0.86	$\pm$0.39	$\pm$1.37	$\pm$0.61

Table 13
Systematic errors due to uncertainties in e+jets and μ+jets calibration parameters.

Expected errors from ensemble testing

The 2-dimensional likelihood fit gives an error estimation that combines the statistical and jet energy scale error. The error determined in the measurement on data can be compared to the expected errors obtained from ensemble testing. For each of the 1000 pseudo-experiments within a standard ensemble, asymmetric errors are calculated. The positive and negative errors are plotted as a histogram, and the actual errors from data are shown superimposed on the histogram. These are shown in Figure 6.39. Some of the actual errors are out of range for the e+jets, μ+jets, and combined l+jets channels analyzed without the use of b-tagging.

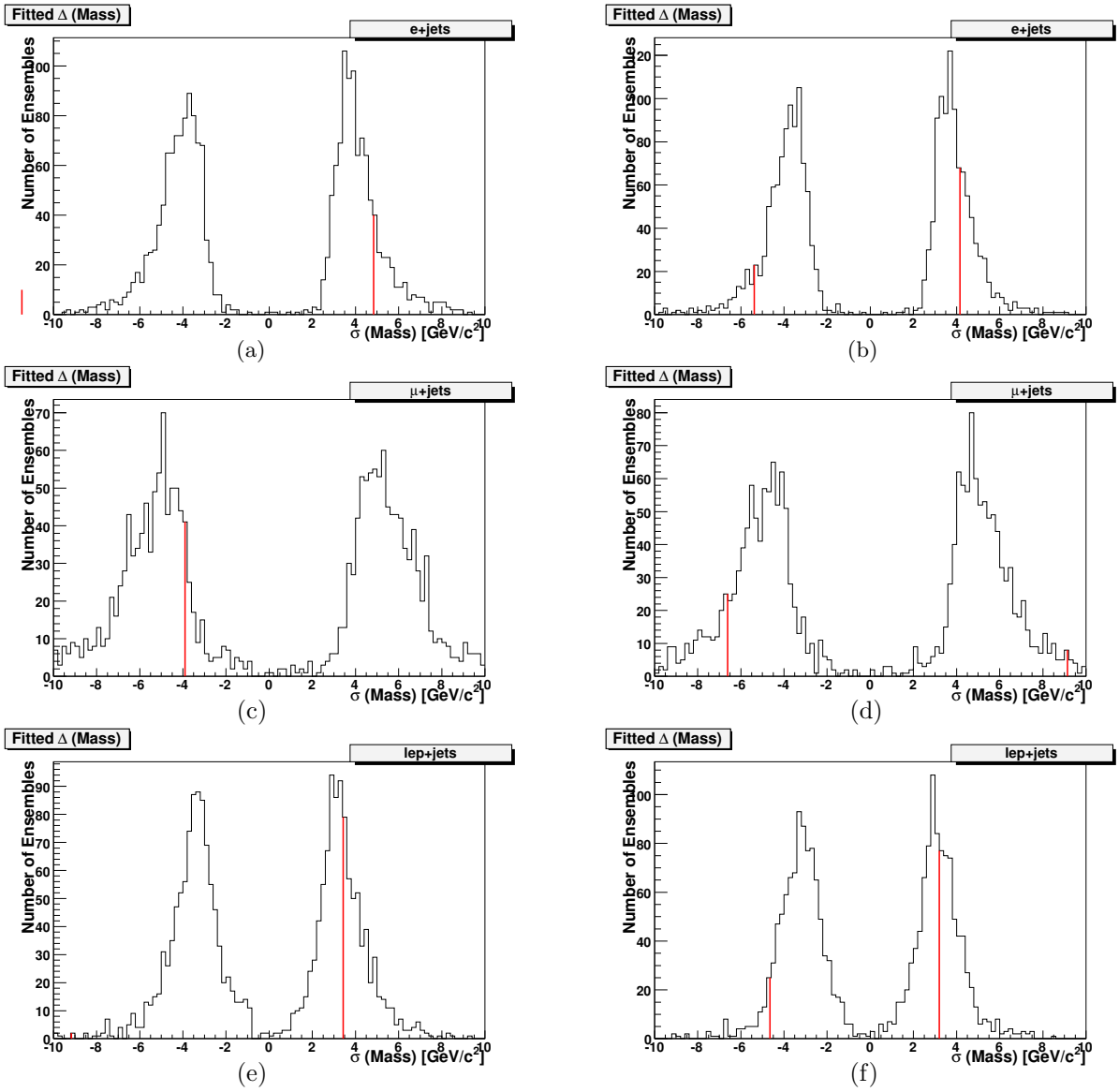

Fig. 6.39. Actual errors from data (vertical lines) and error distribution from ensemble testing, untagged (*left*) and b-tagged(*right*), e+jets (*top*), μ+jets(*middle*), and l+jets(*bottom*)

7. CONCLUSIONS

The final results for the combined l+jets channels using 425 pb^{-1} of DØ Run II data are:

$$m_{top} = 169.2\ ^{+3.4}_{-9.2}(stat + JES)\ ^{+1.8}_{-1.7}(syst)\ \text{GeV}/c^2 \tag{7.1}$$

$$m_{top}^{btag} = 172.2\ ^{+3.2}_{-4.6}(stat + JES)\ \pm 1.6(syst)\ \text{GeV}/c^2, \tag{7.2}$$

or, alternately,

$$m_{top} = 169.2\ \pm 3.2(stat)\ ^{+2.2}_{-8.7}(syst)\ \text{GeV}/c^2 \tag{7.3}$$

$$m_{top}^{btag} = 172.2\ \pm 2.1(stat)\ ^{+2.9}_{-4.4}(syst)\ \text{GeV}/c^2, \tag{7.4}$$

These results are consistent with the earlier DØ result on the same data set, also using a matrix element method: [88]

$$m_{top} = 169.2\ ^{+5.0}_{-7.4}(stat + JES)\ ^{+1.5}_{-1.4}(syst)\ \text{GeV}/c^2 \tag{7.5}$$

$$m_{top}^{btag} = 170.3\ ^{+4.1}_{-4.5}(stat + JES)\ ^{+1.2}_{-1.8}(syst)\ \text{GeV}/c^2 \tag{7.6}$$

and also consistent with the current world average: [100]

$$m_{top} = 171.4\ \pm 1.2(stat)\ \pm 1.8(syst)\ \text{GeV}/c^2. \tag{7.7}$$

The systematic uncertainties are also comparable with the uncertainties of the earlier DØ result.

The important difference between the two versions of the matrix element method is in the calculation and normalization of the background probabilities. In the analysis described in Ref. [88], the background probabilities were normalized by varying the normalization constant until the output signal fraction matched the input signal fraction for an ensemble made with known signal fractions. While this method is easier to implement, there is a risk of incorrectly normalizing the background probabilities if the background fractions are too high.

The plots of P_{sgn} vs. P_{bkg} show that background events have worse discrimination than signal events, and around half of them actually look like signal events (see Fig. 5.5, for example). Output signal fractions tend to be overestimated for this reason. This would give more weight to background events in the likelihood function, which will shift the fitted m_t either up or down depending on where m_t peaks in the background events. There is some confidence that the final calibration will correct for this effect, but this means the implementation of the matrix element has a strong dependence on the Monte Carlo simulation.

There are two benefits to the alternate background probability calculation. The first is a decrease in the CPU time to calculate background probabilities. The second is an incorporation of heavy-flavor background events in such a way that excessive CPU resources are not required. $Wgggg$ and $Wbbgg$ matrix elements only were used in the analysis presented here, but additional matrix elements can easily be added to give better discrimination or to add backgrounds other than W+jets (diboson, for example). Future versions of the matrix element method will likely be used exclusively on events with b-tagging requirements, so the incorporation of heavy-flavor background matrix elements is essential.

There are a few ways in which the matrix element can be improved for use in future top quark mass analyses. While the current version is excellent for measuring an observable on a small number of data events, the matrix element method in its current form is perhaps not very practical for larger data samples. As data samples get larger, the numbers of MC events required to do adequate ensemble testing also get larger. The CPU time required to integrate

event probabilities for all signal and background events is already becoming prohibitively large with the 1 fb^{-1} dataset. The event probability calculation is a large drain on the experiment's resources, and, once they're calculated, keeping track of them is a logistical nightmare.

The situation can be improved by imposing tighter selection cuts to reduce the size of the data sample, but this is difficult because of the inherent difficulties in optimizing the event selection for such a time-consuming measurement method. A version of the matrix element method could be developed that would be quicker and more flexible, although not as precise as the full analysis version. The event probability calculation can be sped up through a number of ways, some of which are listed below:

1. The current calculations are done separately for different m_t and JES hypotheses, and each probability is calculated to the same accuracy. This results in spending a great deal of time performing integrations for m_t and JES values that are far away from the most likely values. It would be more efficient to first determine the approximate location of the maximum in the likelihood with respect to m_t and JES, and then calculate the event probabilities with greater accuracy in that region.

2. Instead of evaluating event probabilities for discrete m_t and JES hypotheses, the event probability (or negative log-likelihood) can instead be parametrized as a function of m_t and JES for each event, and the functions can be combined at the end to form the total likelihood. This has the advantage not only of saving time integrating unnecessary m_t and JES hypotheses, but also of allowing for maximum probabilities over larger ranges of m_t and JES. This will remove the need to extrapolate the integrated probabilities outside the current integration ranges.

3. While the full integration over all parton momenta will probably be desired for a final high-precision measurement, it is probably not necessary for testing and event selection optimization. It might be useful to do a "smearing" of the reconstructed particle energies

to approximate the parton energies, and take an average over a number of smearings of the probabilities determined for each set of smeared parton momenta. This is already done in the VECBOS-based background probability estimate used in the analysis of Ref. [88].

Finally, it is important to calculate event kinematics in such a way that the transverse momentum of the $t\bar{t}$ system is not constrained to zero. This will eventually allow the use of next-to-leading order matrix element calculations in the method which is, of course, necessary for higher precision top quark mass measurements. This gives another degree of freedom to an already under-constrained system, which increases the integration time even further. So this is another reason to find ways to reduce the integration time.

APPENDIX

A. DATA-MC COMPARISON PLOTS

Since Monte Carlo (MC) events are used to test and calibrate the matrix element method, it is important to verify that the kinematic distributions in data agree well with the MC. Validation plots for the data and MC samples with no b-tagging requirements in the event selection can be found in Ref. [22]. Given here are several kinematic distributions for data samples with at least 1 b-tagged jet in the event. MC events are weighted with b-tagging efficiencies. See Sect. 4.5 for a description of the Secondary Vertex Tagging algorithm.

The estimation of the QCD multijet background uses the Matrix Method, described in Sect. 6.2. The MC events are normalized to agree in each jet multiplicity bin with the data after QCD subtraction.

A.1 μ+jets Data-MC Comparison Plots

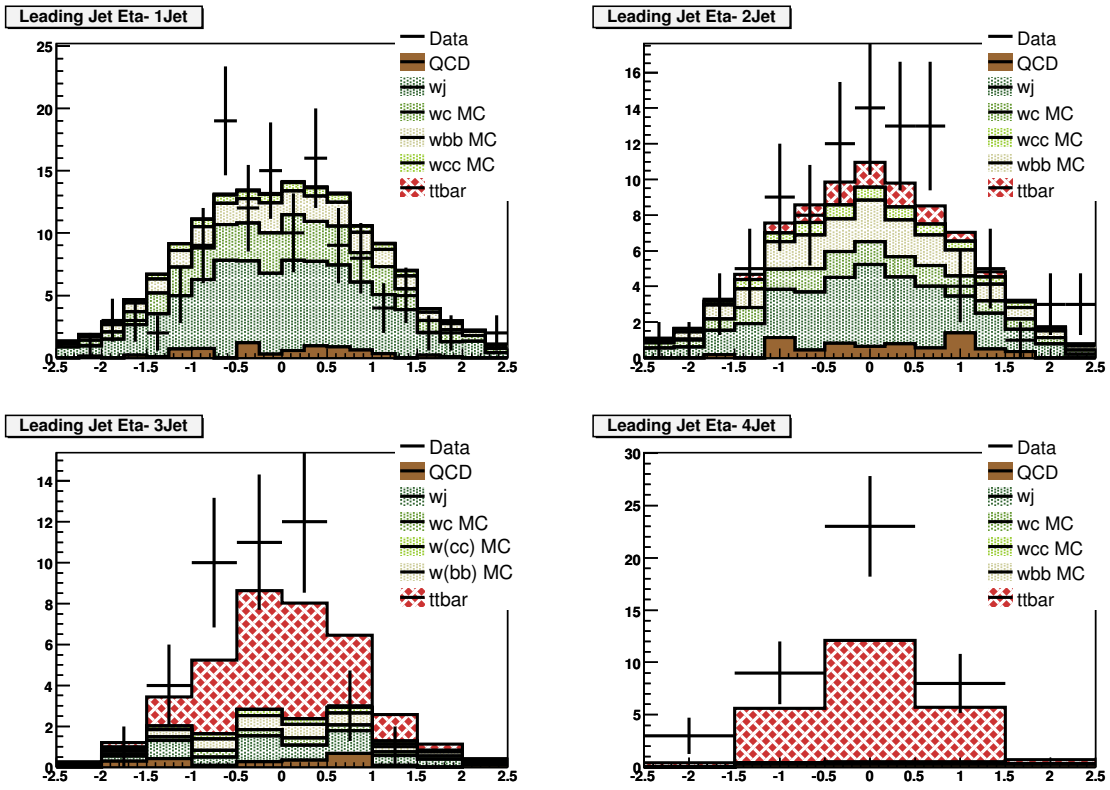

Fig. A.1. e+jets: Leading jet $|\eta|$.

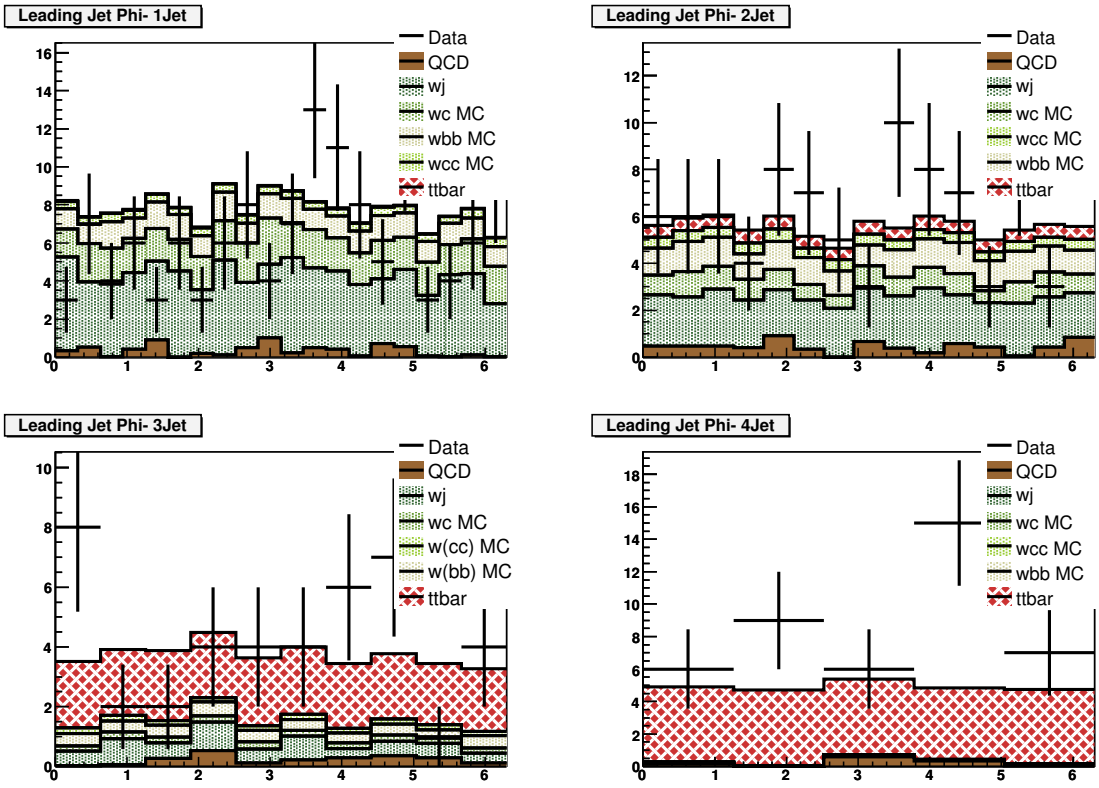

Fig. A.2. e+jets: Leading jet ϕ.

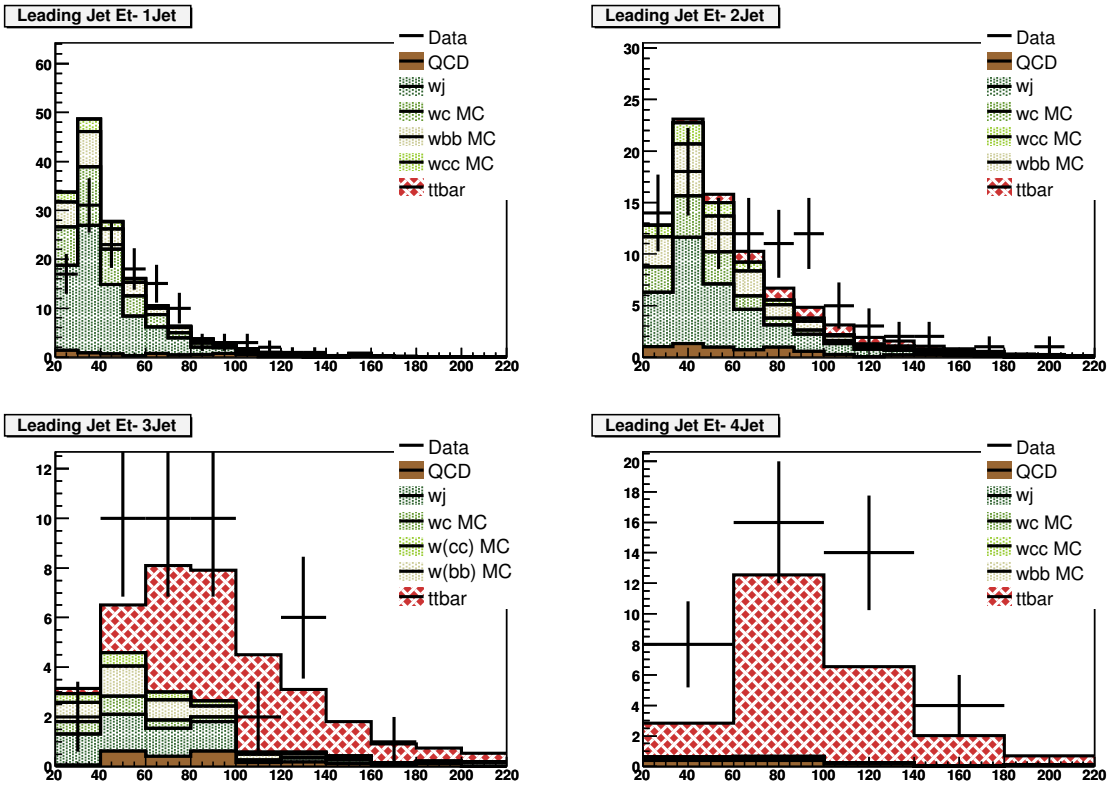

Fig. A.3. e+jets: Leading jet p_T.

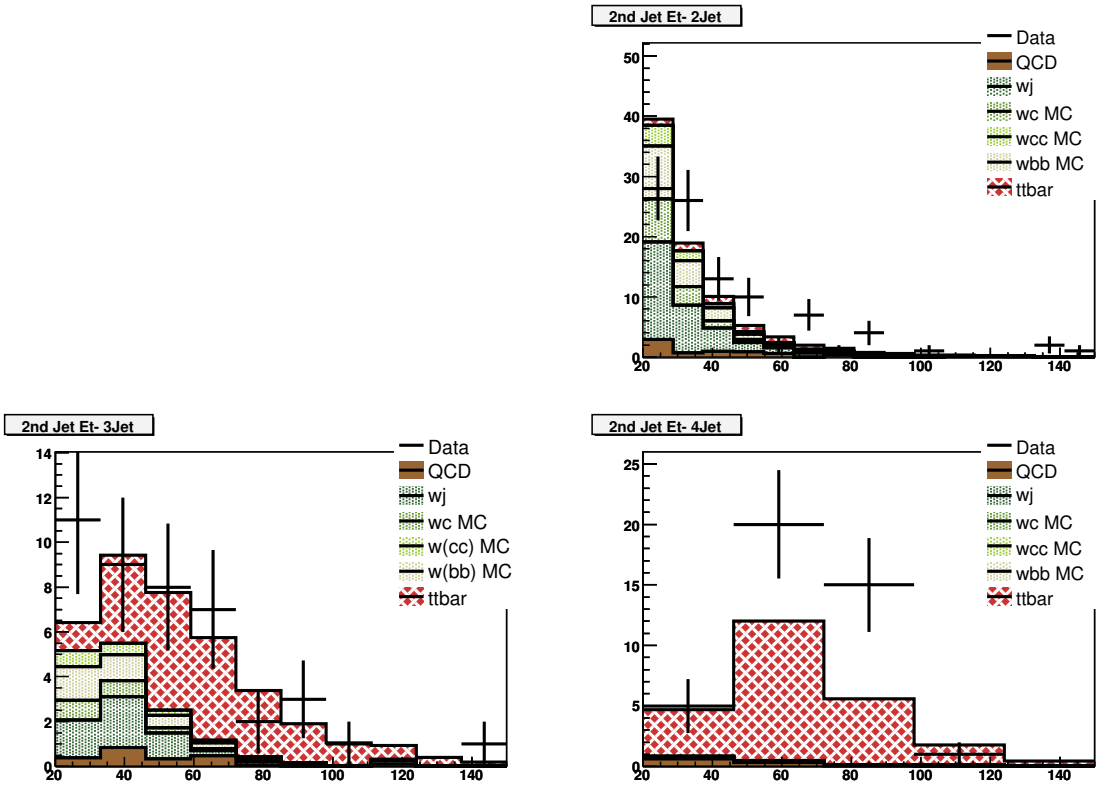

Fig. A.4. e+jets: 2nd leading jet p_T.

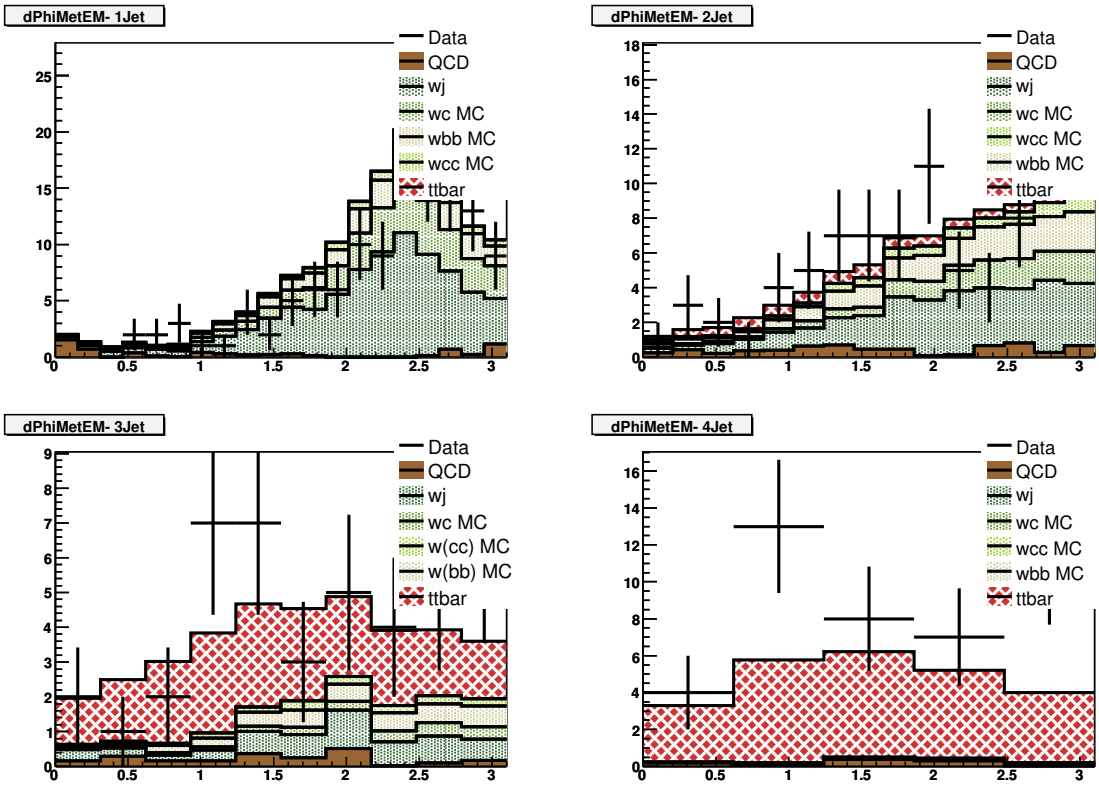

Fig. A.5. e+jets: $\Delta\phi(electron, missing E_T)$.

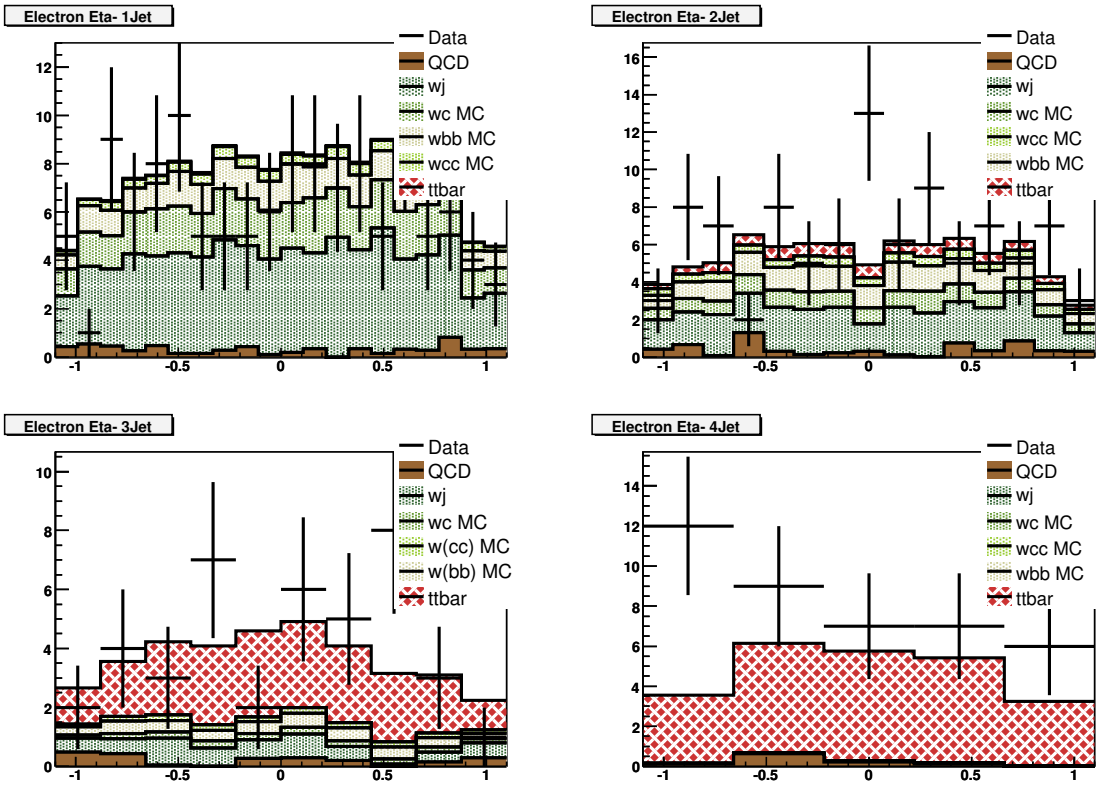

Fig. A.6. e+jets: electron $|\eta|$.

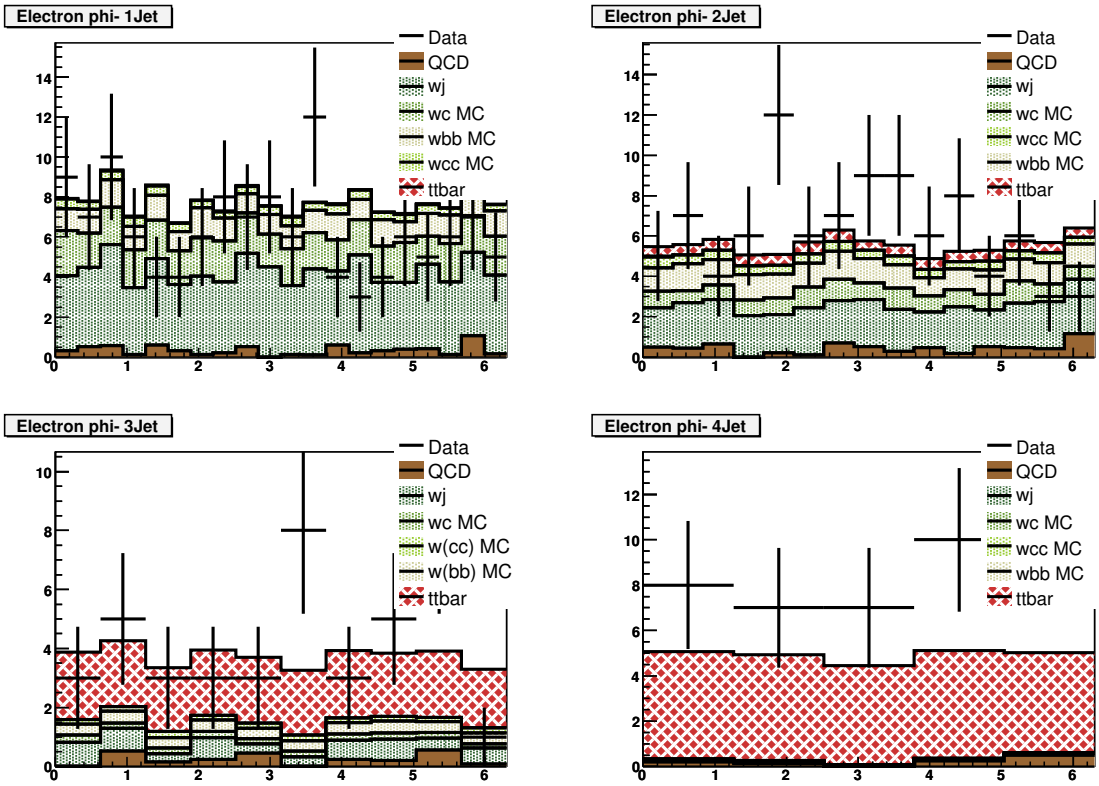

Fig. A.7. e+jets: Electron ϕ.

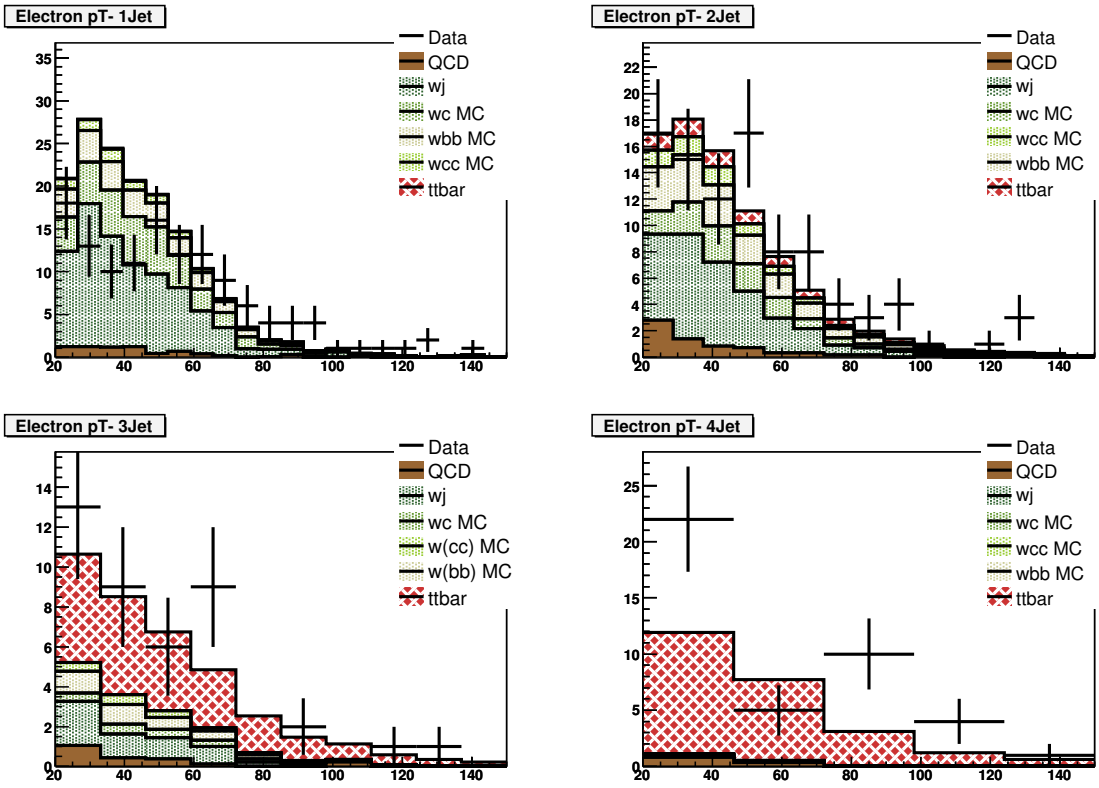

Fig. A.8. e+jets: Electron p_T.

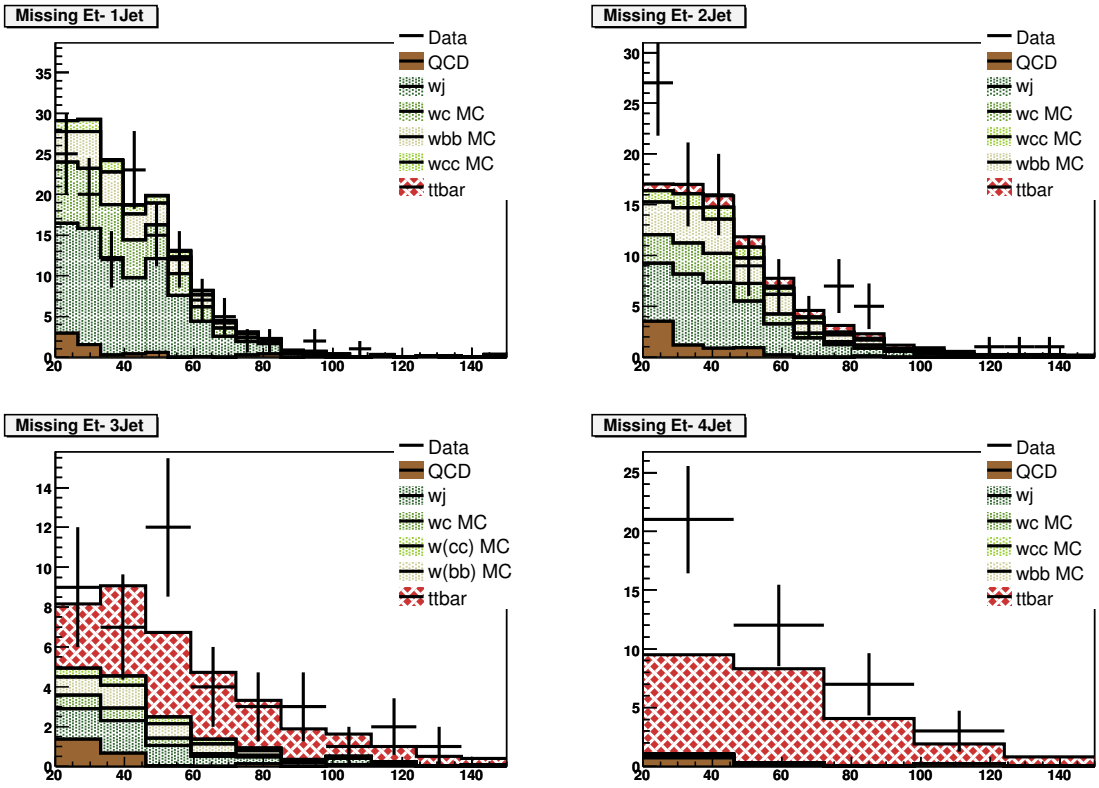

Fig. A.9. e+jets: Missing E_T.

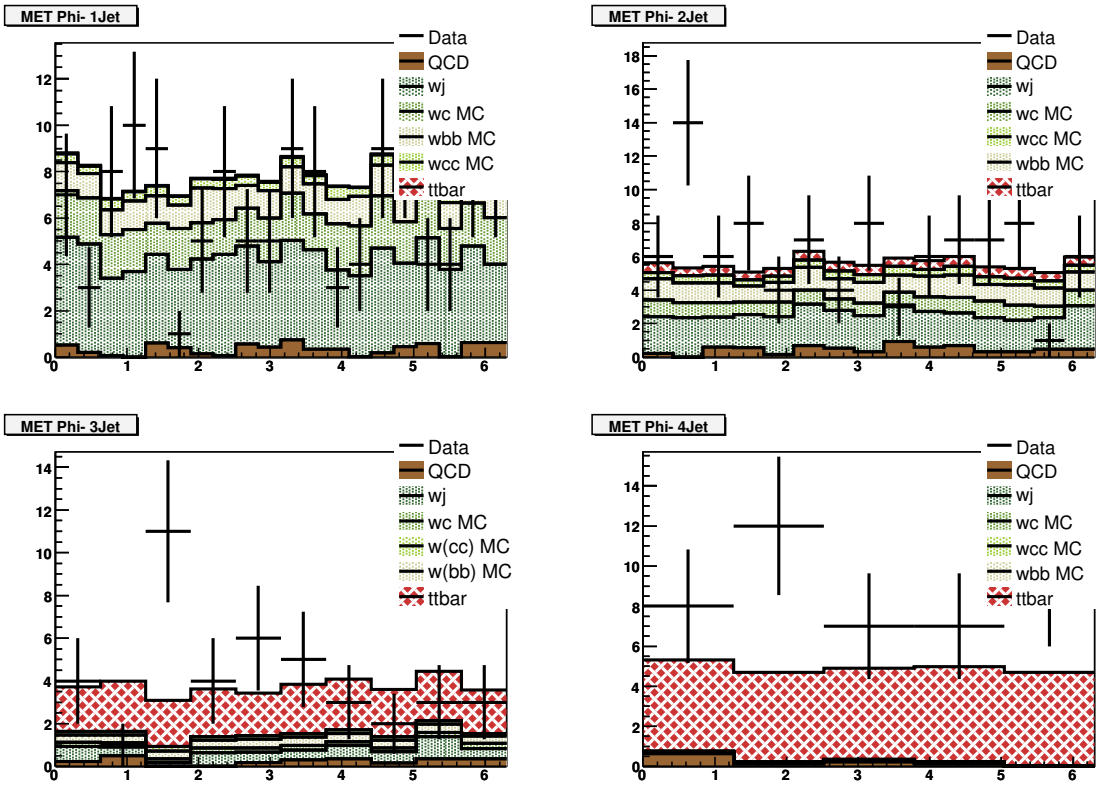

Fig. A.10. e+jets: ϕ of missing E_T.

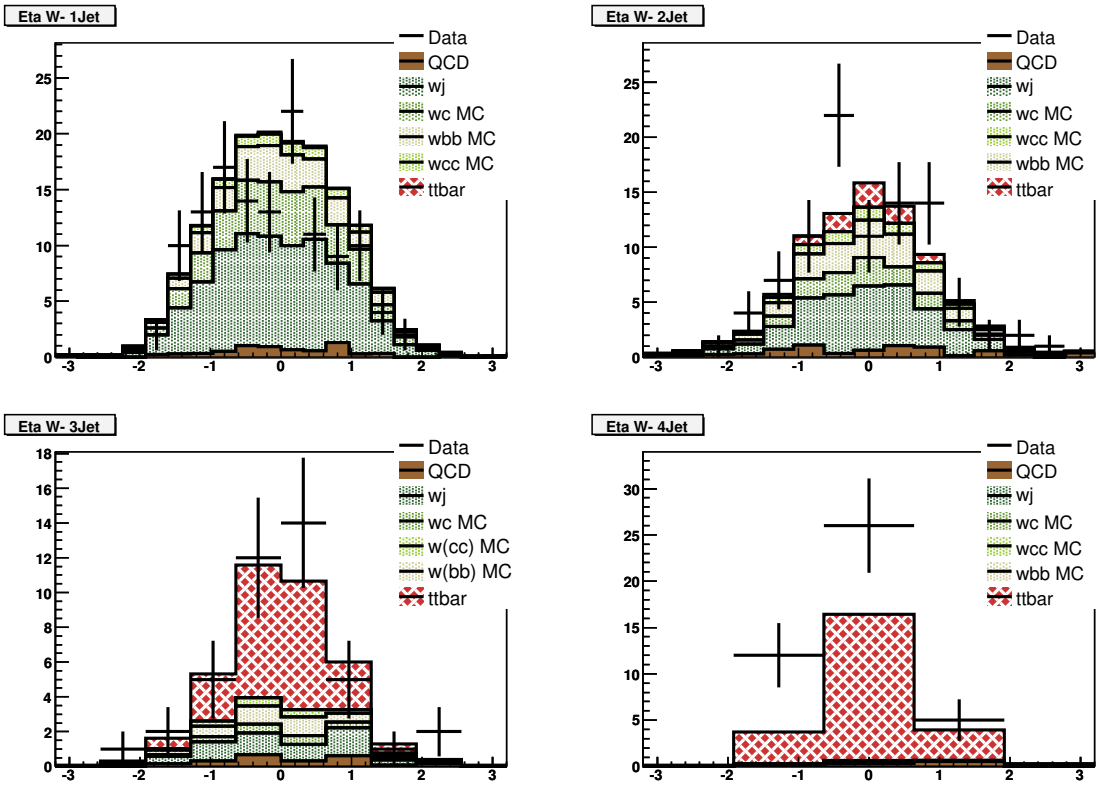

Fig. A.11. e+jets: W boson η.

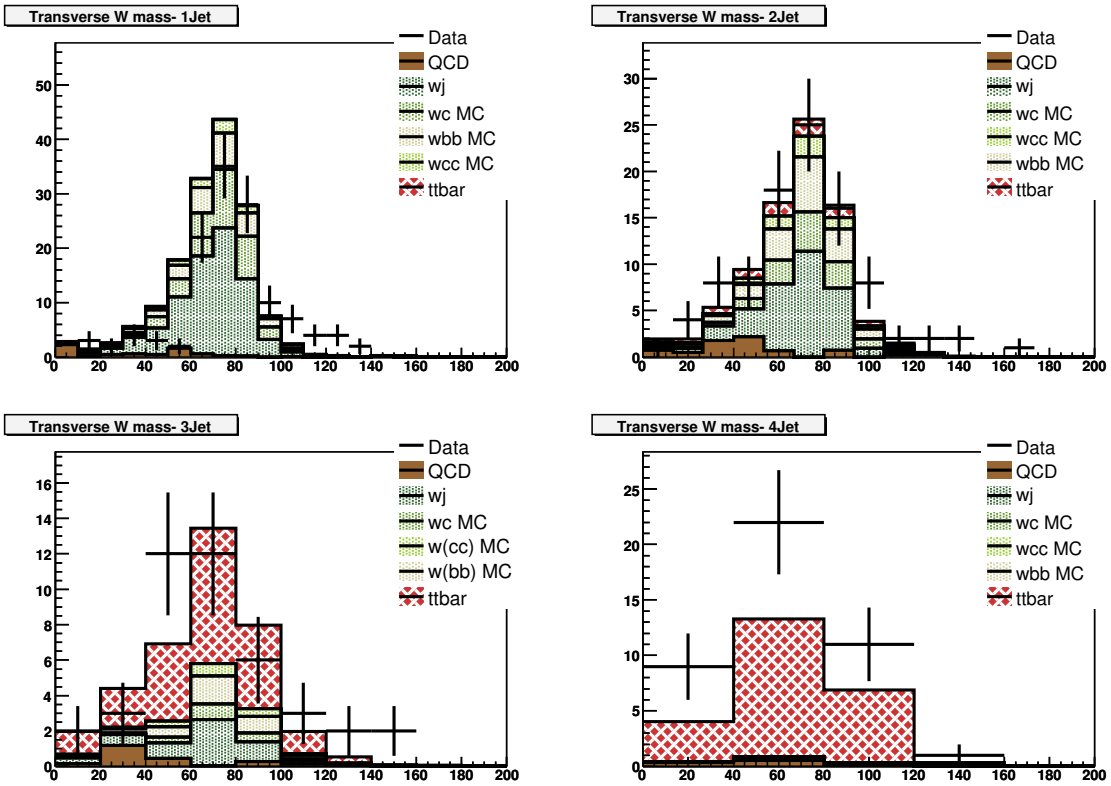

Fig. A.12. e+jets: W boson transverse mass.

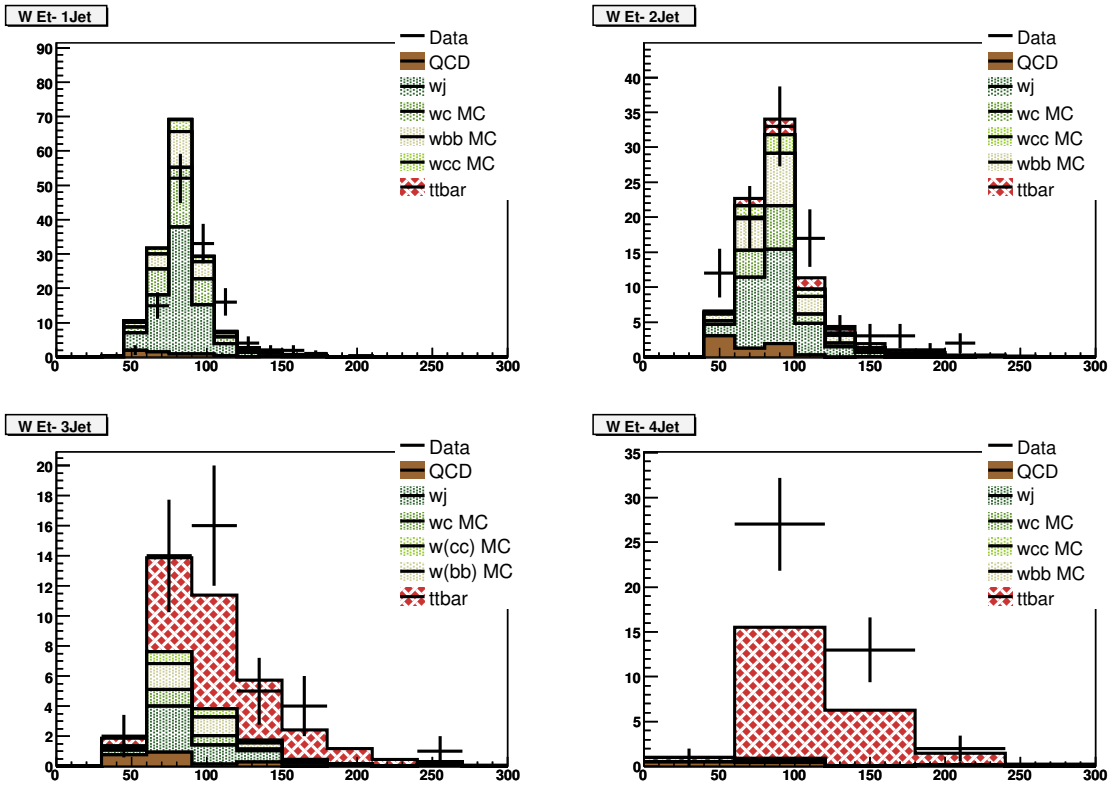

Fig. A.13. e+jets: W boson E_T.

A.2 μ+jets Data-MC Comparison Plots

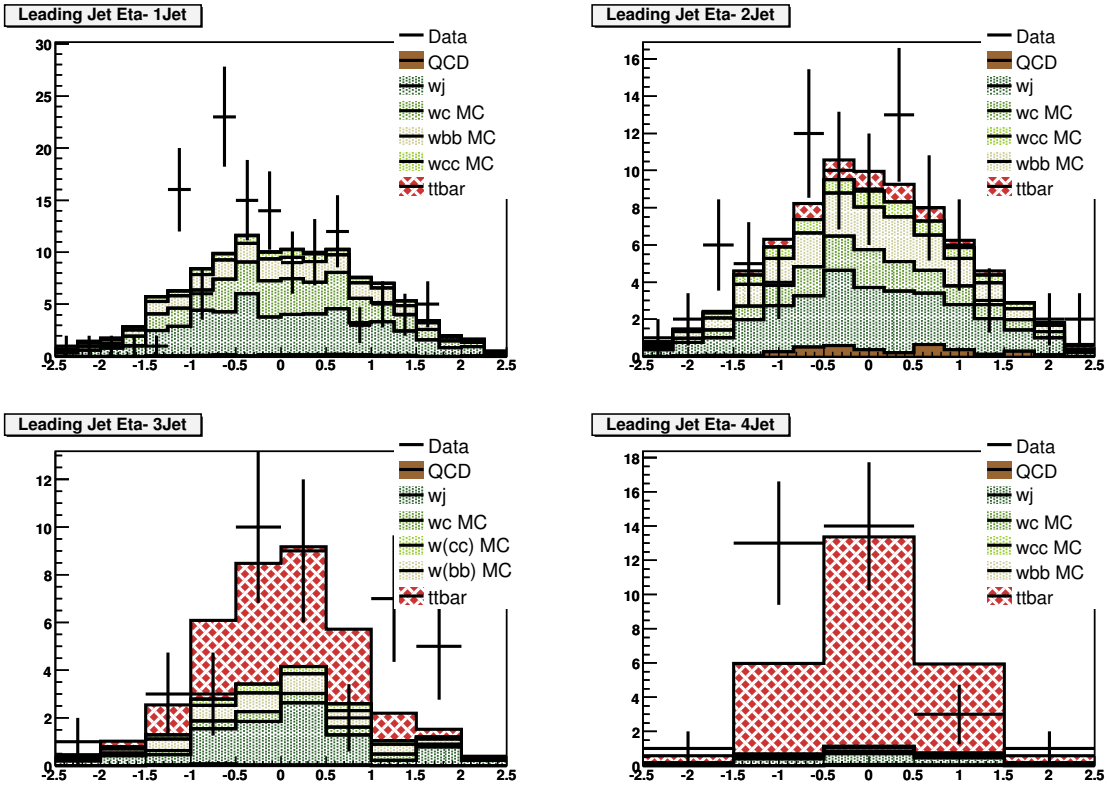

Fig. A.14. μ+jets: Leading jet $|\eta|$.

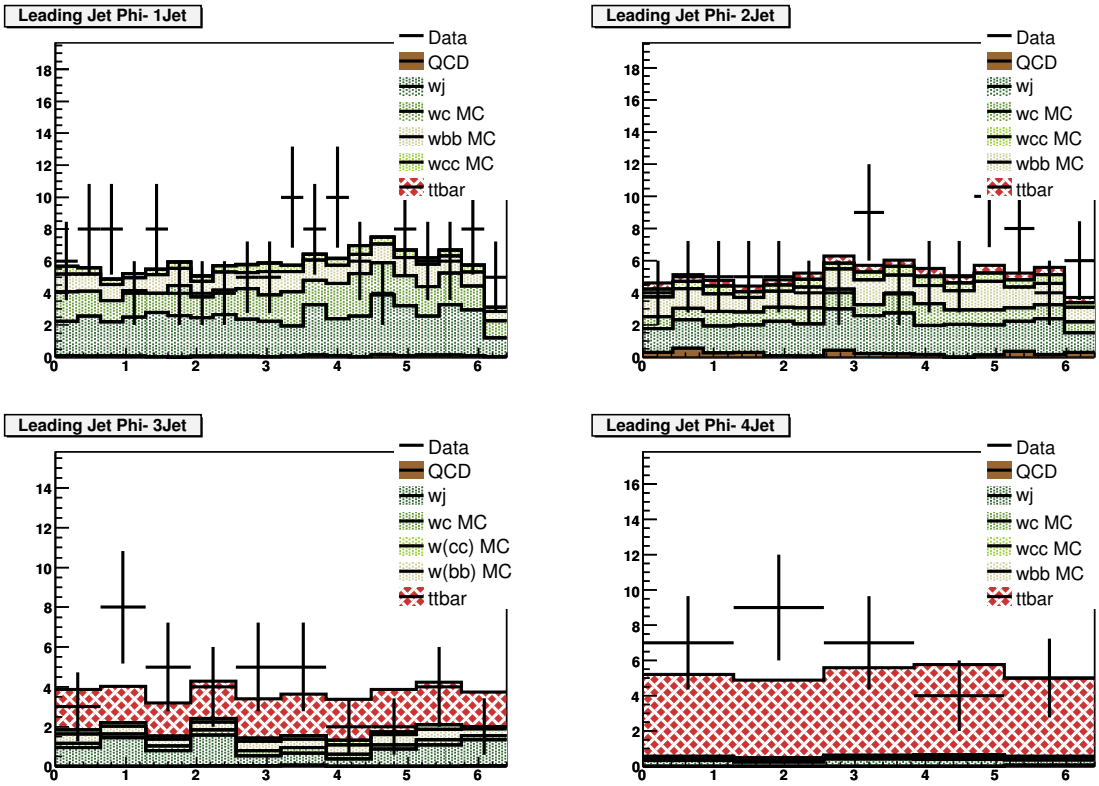

Fig. A.15. μ+jets: Leading jet ϕ.

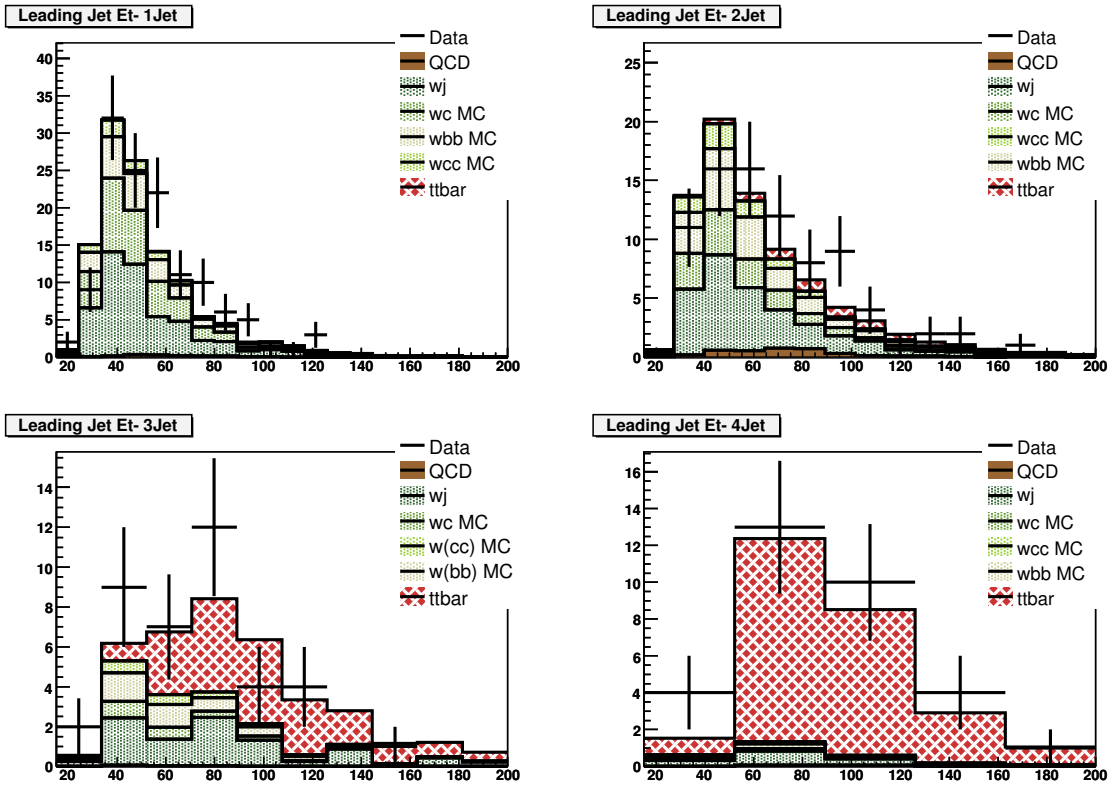

Fig. A.16. μ+jets: Leading jet p_T.

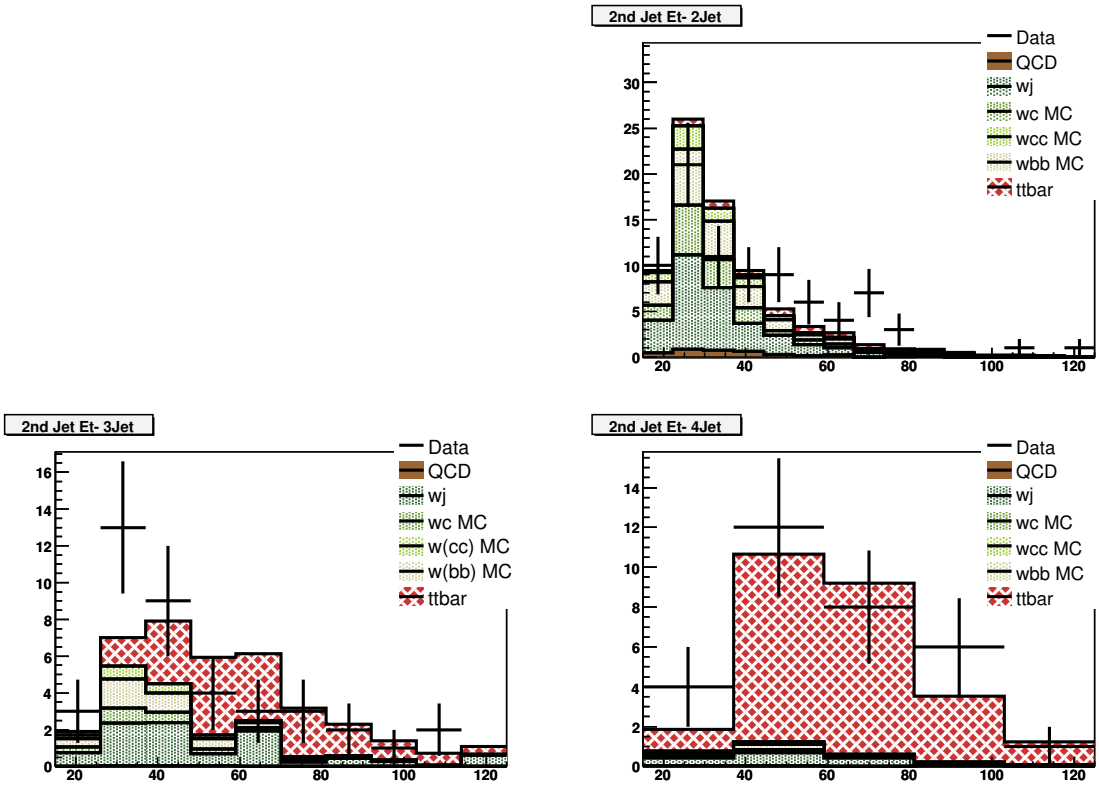

Fig. A.17. μ+jets: 2nd leading jet p_T.

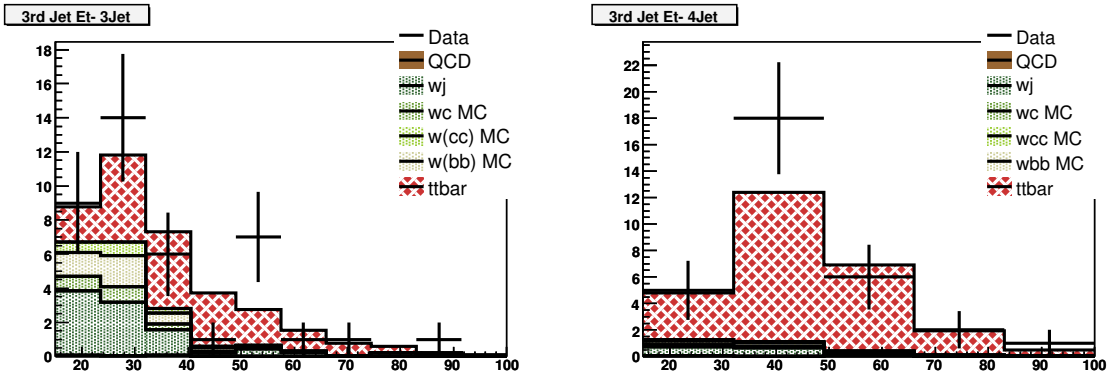

Fig. A.18. μ+jets: 3rd leading jet p_T.

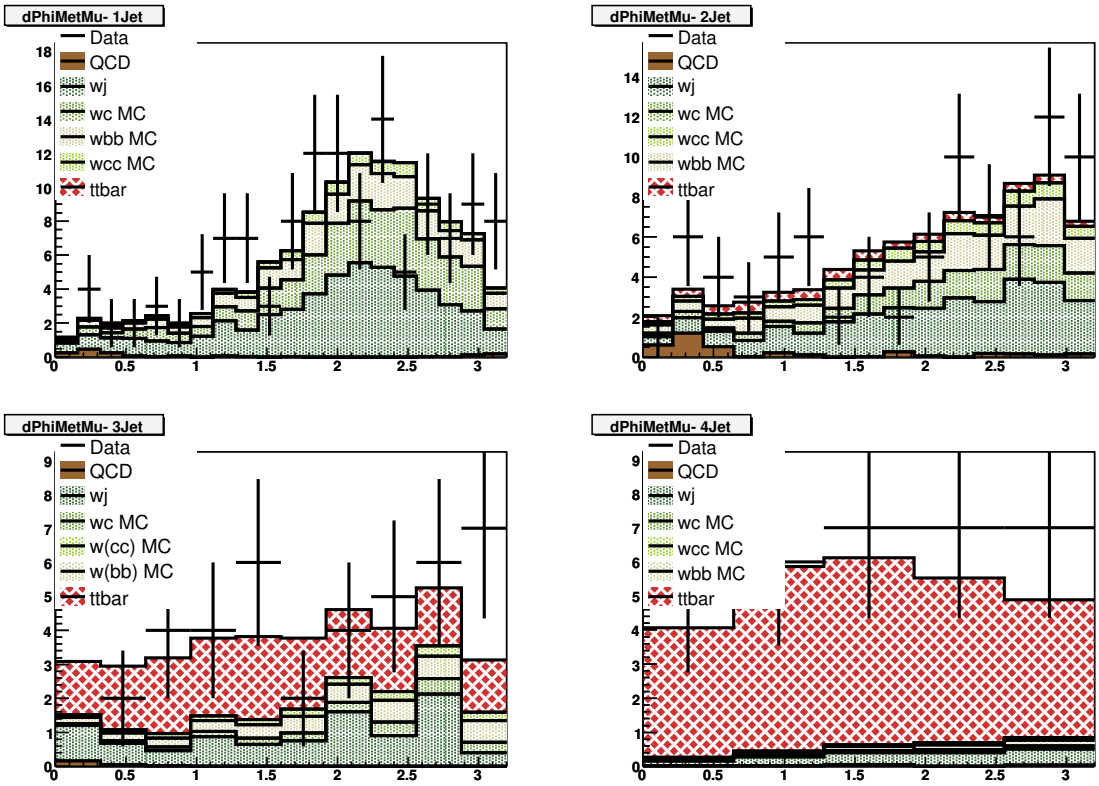

Fig. A.19. μ+jets: $\Delta\phi(muon, missing E_T)$.

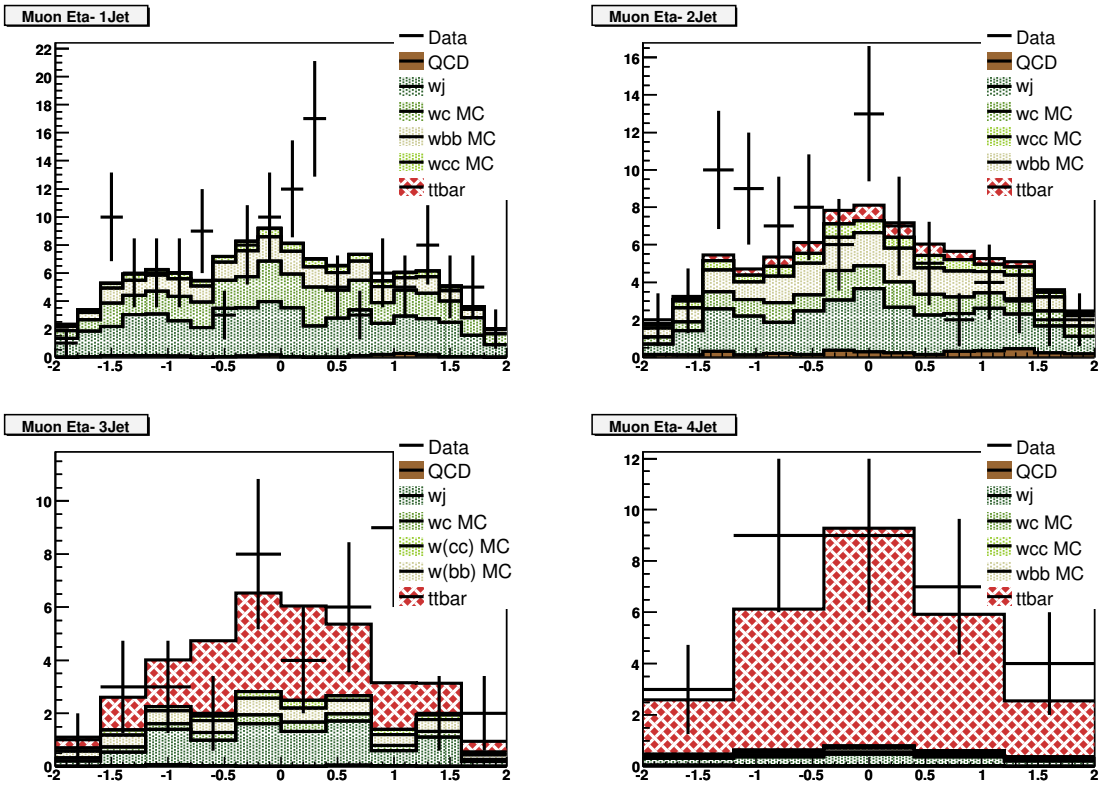

Fig. A.20. μ+jets: muon $|\eta|$.

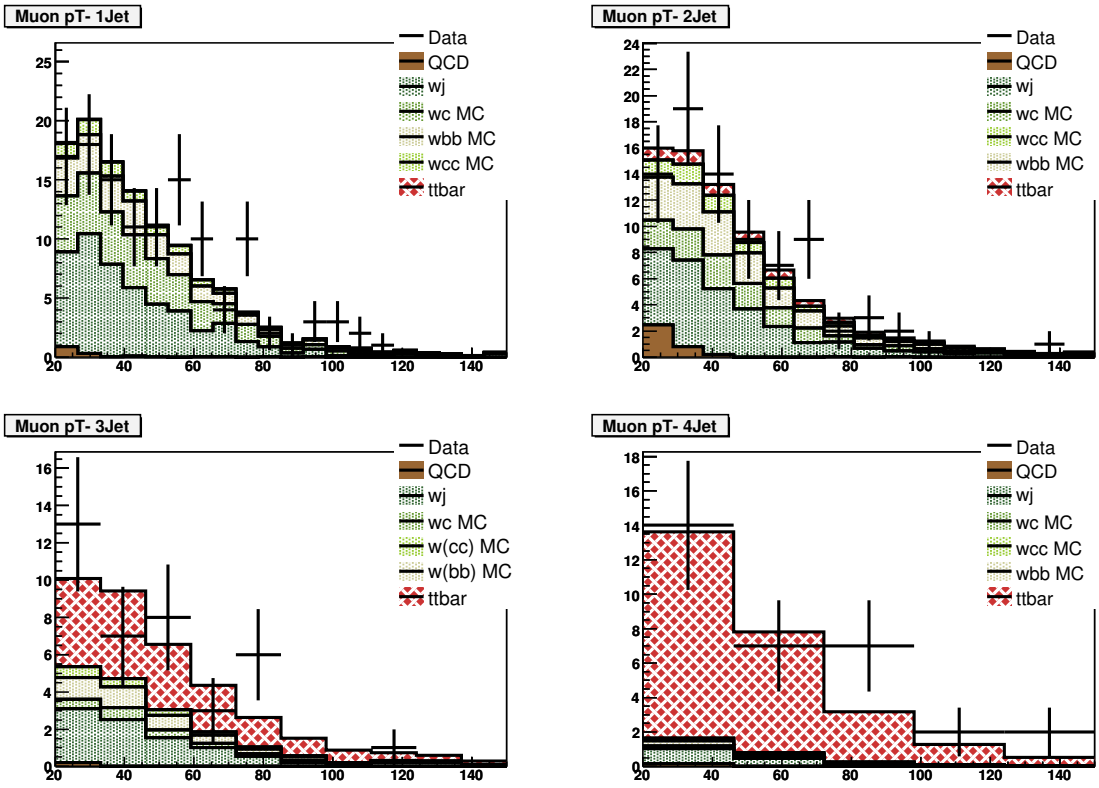

Fig. A.21. μ+jets: Electron p_T.

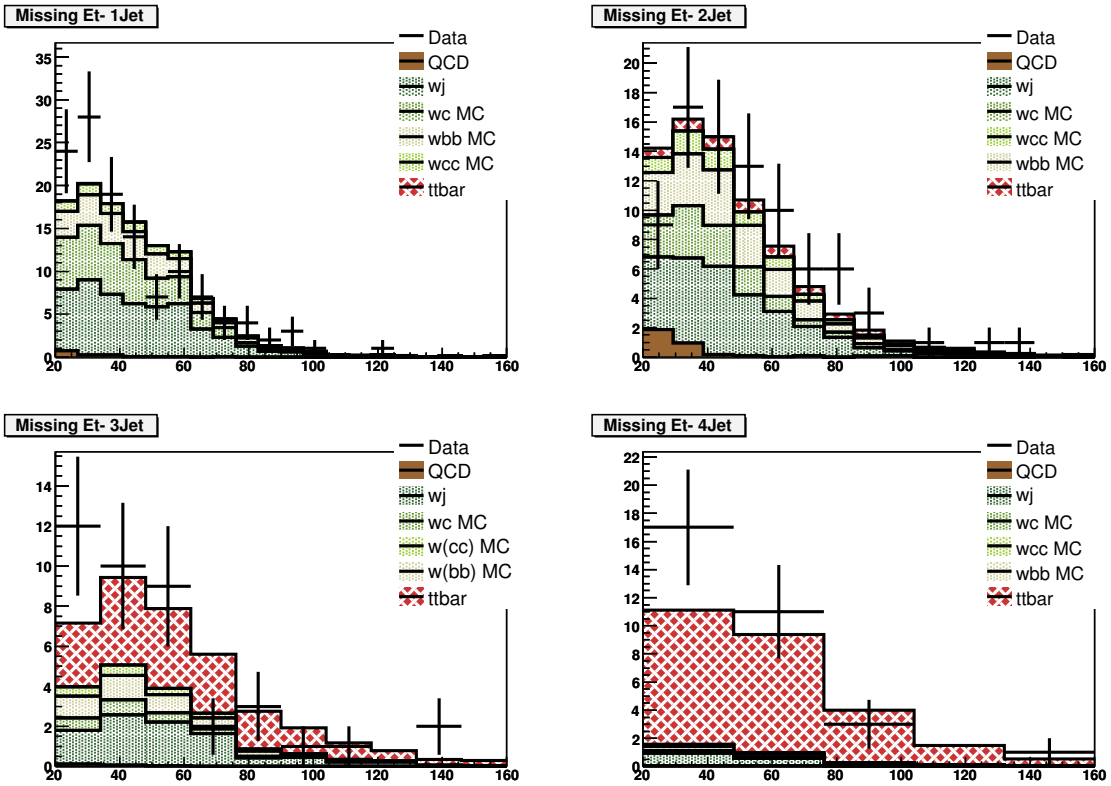

Fig. A.22. μ+jets: Missing E_T.

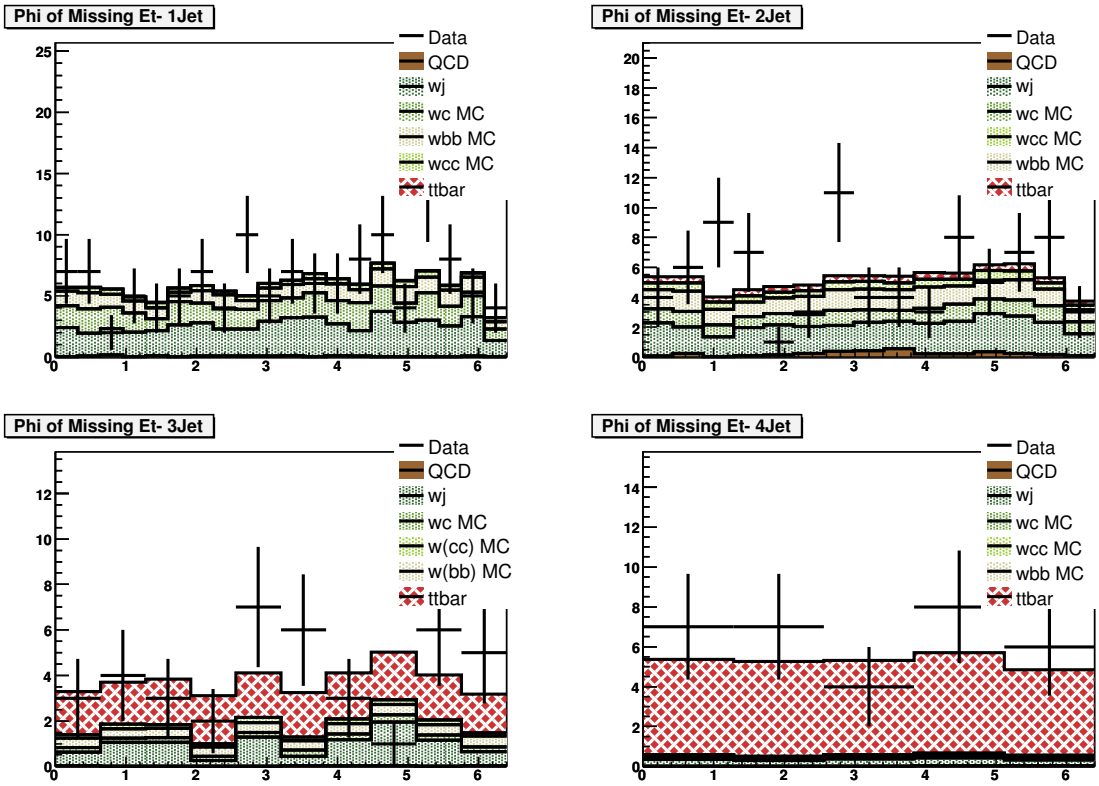

Fig. A.23. μ+jets: ϕ of missing E_T.

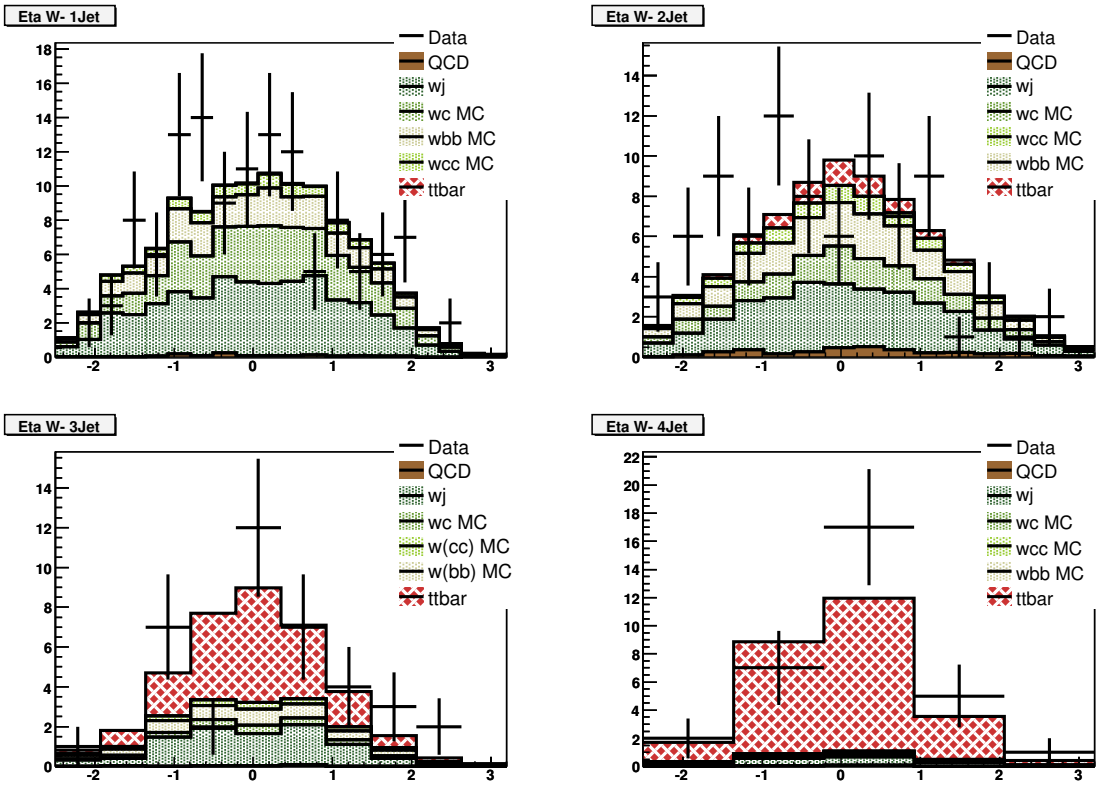

Fig. A.24. μ+jets: W boson η.

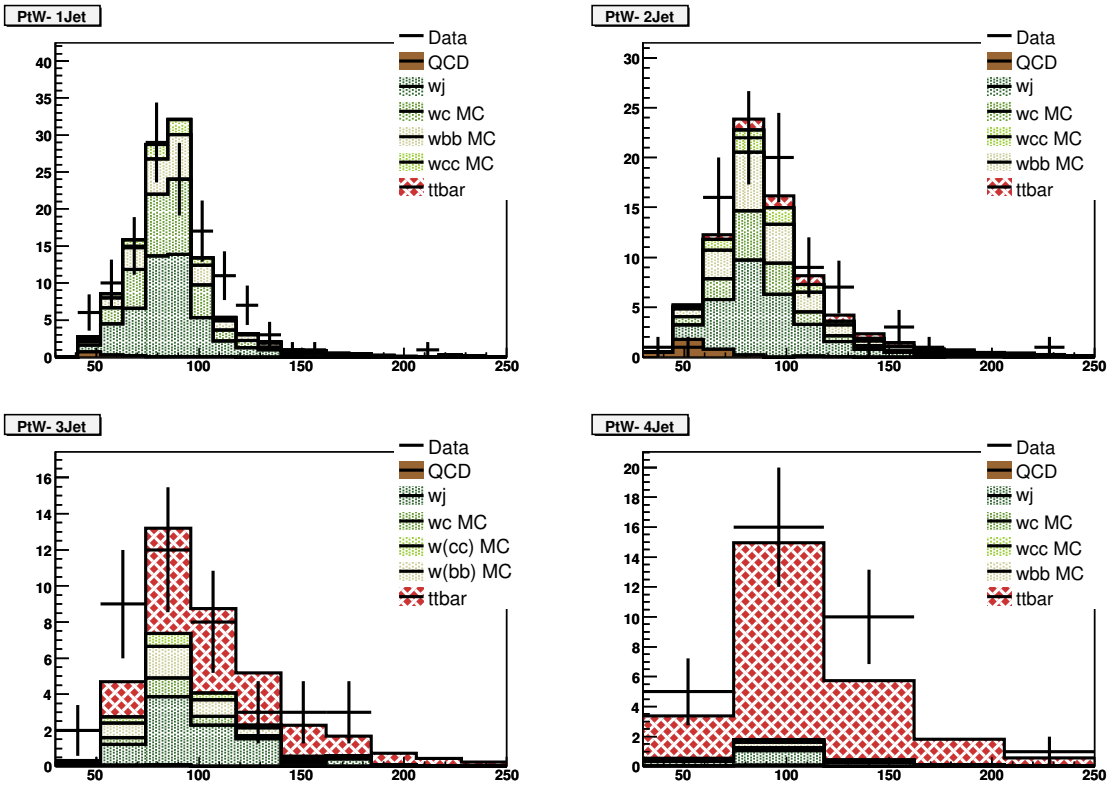

Fig. A.25. μ+jets: W boson E_T.

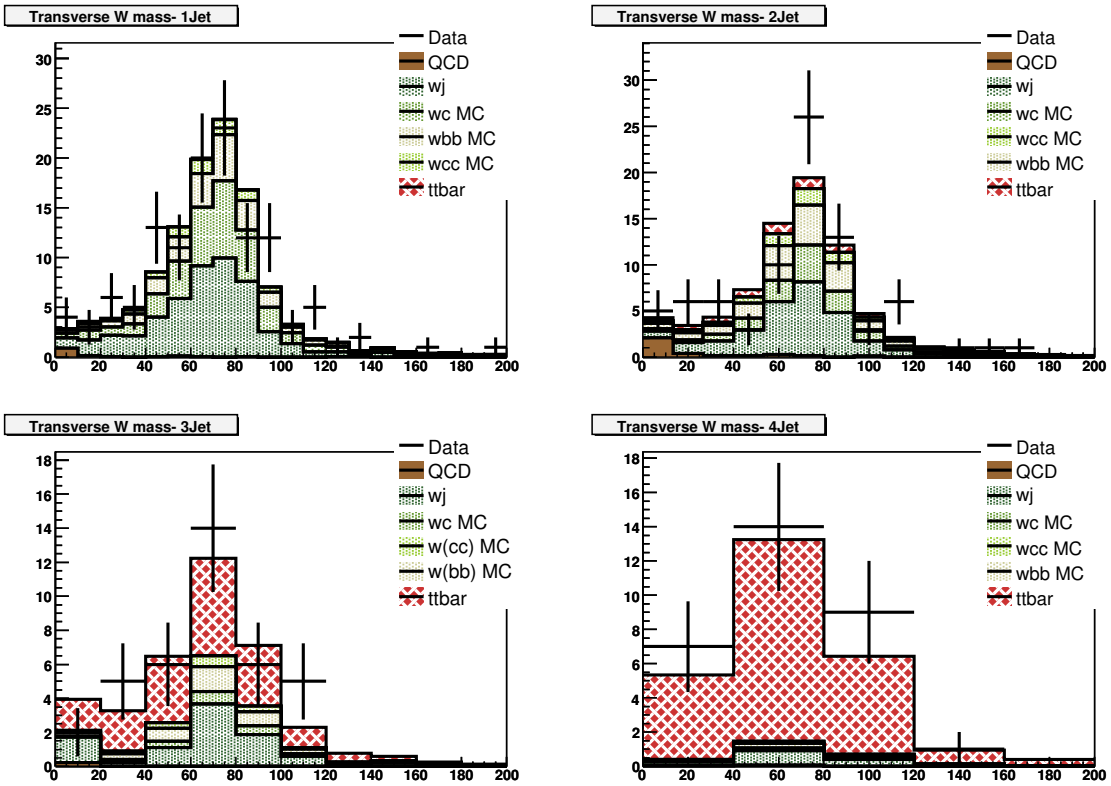

Fig. A.26. μ+jets: W boson transverse mass..

B. LIKELIHOOD FUNCTION

For N total events in a data sample, D, there will be N_s actual signal events and N_b background events such that $N = N_s + N_b$. These values of N are different from the expected number of events, which are denoted with lower-case n_s and n_b.

The probability $p(n_s, n_b, m_t, \text{JES}|D)$ is the probability that a particular set of n_s, n_b, m_t, and JES is correct given the data sample. This cannot be calculated directly, but is related to the likelihood of having a data sample D given the expected numbers of signal and background and a top mass hypothesis, $\mathcal{L}(D|n_s, n_b, m_t, \text{JES})$, through Bayes' Theorem. Thus the first step is to calculate $\mathcal{L}(D|n_s, n_b, m_t, \text{JES})$.

B.1 $\mathcal{L}(D|\, n_s, n_b, m_t, \textbf{JES})$

The likelihood $\mathcal{L}(D|n_s, n_b, m_t, \text{JES})$ can be expanded by summing over all possible combinations of N_s and N_b and applying the product rule:

$$\mathcal{L}(D|n_s, n_b, m_t, \text{JES}) = \sum_{N_s=0}^{N} \mathcal{L}(D|N_s, N_b, n_s, n_b, m_t, \text{JES})\, p(N_s, N_b|n_s, n_b, m_t, \text{JES}) \tag{B.1}$$

The second factor, the probability of having N_s and N_b given n_s and n_b, is the product of two Poisson terms. With

$$q(N, n) \equiv \frac{e^{-n}\, n^N}{N!},$$

$$p(N_s, N_b|n_s, n_b, m_t, \text{JES}) = q(N_s, n_s)\, q(N_b, n_b). \tag{B.2}$$

To evaluate the first term in Eqn. B.1, the following definitions are used:

$$s \equiv \text{an element of } 2^N \text{ ways to divide } N \text{ events}$$

$$\text{into signal and two backgrounds}$$

$$s_{N_s} \equiv \text{an element of the set of all } \binom{N}{N_s} \text{ ways of}$$

$$\text{picking } N_s \text{ signal events from } N \text{ in D}$$

Now $\mathcal{L}(D|N_s, N_b, m_t, \text{JES})$ can be written as

$$\begin{aligned}
&\mathcal{L}(D|N_s, N_b, m_t, \text{JES}) \\
&\quad = \sum_{s_{N_s}} \mathcal{L}(D|s_{N_s}, s_{N_b}, N_s, N_b, m_t, \text{JES}) p(s_{N_s}, s_{N_b}|N_s, N_b) \\
&\quad = \sum_{s_{N_s}} \mathcal{L}(D|s_{N_s}, s_{N_b}, m_t, \text{JES})\, p(s_{N_s}, s_{N_b}|N_s, N_b). \qquad \text{(B.3)}
\end{aligned}$$

Each of the $\binom{N}{N_s}$ ways of picking N_s and N_b events out of the N data events is equally likely, so the second term of Eqn. B.3 can be expressed as

$$p(s_{N_s}, s_{N_b}|N_s, N_b) = 1 \Big/ \binom{N}{N_s} = \frac{N_s! N_b!}{N!}. \qquad \text{(B.4)}$$

Combining equations B.3, B.2, and B.4,

$$\mathcal{L}(D|n_s, n_b, m_t, \text{JES}) = \sum_{s_{N_s}} \mathcal{L}(D|s, m_t, \text{JES}) \frac{N_s! N_b!}{N!}\, q(N_s, n_s)\, q(N_b, n_b). \qquad \text{(B.5)}$$

This can be simplified further by writing out the Poisson terms and canceling factorials. Some simple algebra gives the following:

$$\mathcal{L}(D|n_s, n_b, m_t, \text{JES}) = \sum_{s_{N_s}} q(N, n_s + n_b) \frac{{n_s}^{N_s} {n_b}^{N_b}}{(n_s + n_b)^N} \mathcal{L}(D|s, m_t, \text{JES}). \tag{B.6}$$

The probability $\mathcal{L}p(D|s, m_t, \text{JES})$ is the likelihood of getting a data sample, D, with a particular combination, s, of N_s and N_b. To calculate this, D is broken up into three subsets for the combination s. These are called $S(s)$, $B_1(s)$, and $B_2(s)$. Then the likelihood is calculated separately for each subset, and combined for the total likelihood.

With y_i as the set of kinematic variables for the i_{th} event, $p(\text{evt}|y_i, sgn, mt)$ and $p(\text{evt}|y_i, bkg)$ are the likelihoods for the event to exist given that it is a signal or background event, respectively, with the measured values of y_i. With these likelihoods,

$$\mathcal{L}(D|s, m_t, \text{JES}) = \prod_{i \in S(s)} \mathcal{L}(\text{evt}|y_i, \text{sgn}, m_t, \text{JES}) \prod_{i \in B(s)} \mathcal{L}(\text{evt}|y_i, \text{bkg})$$

Combining this with Eqn. B.6 and simplifying, one gets

$$\mathcal{L}(D|n_s, n_b, m_t, \text{JES}) = \\ q(N, n_s + n_b) \prod_{i=1}^{N} \frac{n_s \mathcal{L}(\text{evt}|y_i, \text{sgn}, m_t, \text{JES}) + n_b \mathcal{L}(\text{evt}|y_i, \text{bkg})}{n_s + n_b}. \tag{B.7}$$

B.2 P_{sgn} and P_{bkg}

Probabilities rather than likelihoods are calculated, so one must apply Bayes' Theorem to get:

$$\mathcal{L}(\text{evt}|y_i, \text{sgn}, m_t, \text{JES}) = \frac{p(y_i|\text{sgn}, m_t, \text{JES})}{p(y_i)}$$
$$\mathcal{L}(\text{evt}|y_i, \text{bkg}) = \frac{p(y_i|\text{bkg})}{p(y_i)} \tag{B.8}$$

So B.7 can be rewritten as:

$$\mathcal{L}(D|n_s, n_b, m_t, \text{JES}) =$$
$$q(N, n_s + n_b) \prod_{i=1}^{N} \frac{n_s p(y_i|\text{sgn}, m_t, \text{JES}) + n_b p(y_i|\text{bkg})}{(n_s + n_b)p(y_i)}. \tag{B.9}$$

The probabilities $p(y_i|\text{sgn}, m_t, \text{JES})$ and $p(y_i|\text{bkg})$ are written in terms of the differential cross-sections, which are measurements of $p(x|sgn, m_t)$ and $p(x|bkg)$. Here x represents the parton-level kinematics. Summing over all possible combinations of parton states, and taking into account the probability to observe the event, gives the following:

$$p(y_i|\text{sgn}, m_t, \text{JES}) = \text{Acc}(y_i)\eta_{trigg}(y_i)\eta_{btag}(y_i|\text{sgn}) \sum_x p(y_i|\text{sgn}, m_t) \tag{B.10}$$

$$p(y_i|\text{bkg}) = \text{Acc}(y_i)\eta_{trigger}(y_i)\eta_{btag}(y_i|\text{bkg}) \sum_x p(y_i|\text{bkg}). \tag{B.11}$$

With the following two changes to notation:

$$P^i_{sgn}(m_t, \text{JES}) \equiv p(y_i|\text{sgn}, m_t)$$
$$P^i_{bkg} \equiv p(y_i|\text{bkg}), \tag{B.12}$$

Eqn. B.9 becomes:

$$\mathcal{L}(D|n_s, n_b, m_t, \text{JES}) = q(N, n_s + n_b) \times \prod_{i=1}^{N} \frac{\text{Acc}(y_i)\eta_{trigg}(y_i)}{p(y_i)} \left(\frac{n_s \eta^{sgn}_{btag}(y) P^i_{sgn}(m_t, \text{JES}) + n_b \eta^{bkg}_{btag}(y) P^i_{bkg}}{(n_s + n_b)} \right). \tag{B.13}$$

Eqn. B.13 can be written in a more convenient form with the following definitions:

$$\begin{aligned} f_{sgn} &\equiv \frac{n_s}{n_s + n_b} \\ t &\equiv n_s + n_b. \end{aligned}$$

The result is

$$\mathcal{L}(D|f_{sgn}, t, m_t) = q(N, t) \times \prod_{i=1}^{N} \frac{\text{Acc}(y_i)\eta_{trigg}(y_i)}{p(y_i)} \left(f_{sgn} \eta^{sgn}_{tag}(y_i) P^i_{sgn}(m_t, \text{JES}) + (1 - f_{sgn}) \eta^{bkg}_{tag}(y_i) P^i_{bkg} \right). \tag{B.14}$$

One final application of Bayes' Theorem gives

$$\mathcal{L}(n_s, n_b, m_t|D) = \mathcal{L}(D|n_s, n_b, m_t) \frac{p(n_s, n_b, m_t)}{p(D)}. \tag{B.15}$$

The probability $p(n_s, n_b)$ is assumed to factor so that

$$p(n_s, n_b, m_t) = p(n_s)\, p(n_b)\, p(m_t). \tag{B.16}$$

Although it would be possible to take the background and/or signal estimates from the $t\bar{t}$ cross-section analysis, and use Gaussian priors for $p(n_s)$ and $p(n_b)$, this is not done for the

current version of the analysis. Instead, they are taken to be flat. For this reason, they can be dropped from the likelihood, since they will only contribute a constant term to the log-likelihood. The probability $p(D)$ is constant as well with respect to the parameters being varied.

The variable t could be used to determine the total expected number of events, which in turn could be used to measure the cross-section for $t\bar{t}$ or for either of the two backgrounds. This is not done for the mass analysis, so the first term $q(N,t)$ can also be dropped from the likelihood. The term $\mathrm{Acc}(y_i)\eta(y_i)/p(y_i)$ is also dropped since it does not vary with top mass and is the same for the signal as for the background probability, thus contributing only an additive term to the overall likelihood. The final result is:

$$\mathcal{L}(f_{sgn}, m_t, \mathrm{JES}) = \prod_{i=1}^{N} \frac{\mathrm{Acc}(y_i)\eta_{trigg}(y_i)}{p(y_i)} \left(f_{sgn}\eta_{tag}^{sgn}(y_i)P_{sgn}^{i}(m_t, \mathrm{JES}) + (1 - f_{sgn})\eta_{tag}^{bkg}(y_i)P_{bkg}^{i} \right). \tag{B.17}$$

C. EVENT PROBABILITIES

Appendix B gives the full derivation of the likelihood which contains P^i_{sgn} and P^i_{bkg}, the probabilities for the i^{th} event to be either signal or background. The full likelihood is given by eqn. B.17:

$$\mathcal{L}(f_{sgn}, m_t, \text{JES}) = \prod_{i=1}^{N} \frac{\text{Acc}(y_i)\eta_{trigg}(y_i)}{p(y_i)} \left(f_{sgn}\eta^{sgn}_{tag}(y_i)P^i_{sgn}(m_t, \text{JES}) + (1 - f_{sgn})\eta^{bkg}_{tag}(y_i)P^i_{bkg} \right).$$

The probabilities are defined by Eqns. B.12:

$$P^i_{sgn}(m_t, JES) = p(y_i|\text{sgn}, m_t, JES)$$
$$P^i_{bkg} = p(y_i|\text{bkg}) \tag{C.1}$$

The integrations used to obtain P_{sgn} and P_{bkg} are described in this section.

C.1 Transfer Functions

The matrix element is calculated using the momenta of the partons in the final state, but these are not known precisely. The probability is determined by summing over all possible points in the phase space of the final state partons (4 quarks, lepton, and neutrino), weighting

each point by the probability of having the parton momenta given the measured jet and lepton momenta. In Bayesian-speak, this is equivalent to:

$$P^i_{sgn}(m_t, \text{JES}) = p(y_i|\text{sgn}, m_t, \text{JES}) = \sum_x p(x|\text{sgn}, m_t, \text{JES}) p(y_i|x, JES)$$
$$P^i_{bkg} = p(y_i|\text{bkg}) = \sum_x p(x|\text{bkg}) p(y_i|x), \tag{C.2}$$

A change of notation replaces $p(y|x, JES)$ by $W(y, x, \text{JES})$, the *transfer function*. This function is defined as follows:

$$W(y, x, \text{JES}) = \frac{\delta^2(\Omega^{meas}_{lep} - \Omega_{lep})}{|\vec{p}^{meas}_{lep}|^2} W_{lep}(1/p^{meas}_{lep}, 1/p_{lep})$$
$$\times \prod_{i=1}^{4} \frac{\delta^2(\Omega_{jet_i} - \Omega_{q_i})}{|\vec{p}_{jet}|^2} W_{jet}(|\vec{p}_{jet_i}|, |\vec{p}_{q_i}|, \text{JES}), \tag{C.3}$$

where

$$W_{jet}(p_{jet}, p_q, \text{JES}) = \frac{1}{\sqrt{2\pi}(p_2 + p_3 p_5)} \left(\exp\left(\frac{-(p_q - p_{jet} - p_1)^2}{2p_2^2}\right) + p_3 \exp\left(\frac{-(p_q - p_{jet} - p_4)^2}{2p_5^2}\right) \right) \tag{C.4}$$

and

$$W_{lep}(1/p^{meas}_{lep}, 1/p_{lep}) =$$
$$\begin{cases} \delta(p^{meas}_{lep} - p_{lep}) = \delta(1/p^{meas}_{lep} - 1/p_{lep})/(p^{meas}_{lep})^2, & \mu + \text{jets channel} \\ \frac{1}{\sqrt{2\pi}\sigma_{lep}} \exp\left(\frac{-(1/p_{lep} - 1/p^{meas}_{lep})^2}{2\sigma^2_{lep}}\right), & e + \text{jets channel} \end{cases} \tag{C.5}$$

The JES factor is taken into account by rescaling the jet momentum, p_{jet}. JES is not varied for P_{bkg} calculations, so it is set to 1. Note that $W_{jet}(p_{q_i}, p_{jet_i})$ is normalized by construction. The terms $1/p_{jet}^2$ and $1/(p_{lep}^{meas})^2$ in Eqn. C.3 are necessary to ensure that $\int W(y,x)\ \mathrm{d}y = 1$, where

$$\begin{aligned}\mathrm{d}y &= |\vec{p}_{lep}^{meas}|^2\ \mathrm{d}|\vec{p}_{lep}^{meas}|\ \mathrm{d}\Omega_{lep}^{meas} \prod_{i=1}^{4} |\vec{p}_{jet_i}|^2\ \mathrm{d}|\vec{p}_{jet_i}|\ \mathrm{d}\Omega_{jet_i} \\ &= |\vec{p}_{lep}^{meas}|^4\ \mathrm{d}\left(\frac{1}{|\vec{p}_{lep}^{meas}|}\right)\ \mathrm{d}\Omega_{lep}^{meas} \prod_{i=1}^{4} |\vec{p}_{jet_i}|^2\ \mathrm{d}|\vec{p}_{jet_i}|\ \mathrm{d}\Omega_{jet_i}.\end{aligned}$$

C.2 Differential Cross-section

It is assumed that $p(x|\mathrm{sgn}, m_t, \mathrm{JES})$ and $p(x|\mathrm{bkg})$, appearing in Eqns. C.2, are proportional to the differential cross-section integrated over all possible incoming parton momenta. The differential cross-section $\mathrm{d}^n\sigma_{hs}$ for a hard-scatter interaction between two partons q_1 and q_2 decaying into an n-body final state is given by:

$$\begin{aligned}\mathrm{d}^n\sigma &= \frac{(2\pi)^4|\mathcal{M}|^2}{4\sqrt{(q_1\cdot q_2)^2 - m_1^2 m_2^2}}\mathrm{d}\Phi_n(q_1,q_2;p_1,...,p_n) \\ &\approx \frac{(2\pi)^4|\mathcal{M}|^2}{8|q_1||q_2|}\mathrm{d}\Phi_n(q_1,q_2;p_1,...,p_n).\end{aligned} \tag{C.6}$$

The resulting integrals for the event probabilities are:

$$P_{sgn}^i(m_t, \mathrm{JES}) = \frac{1}{\sigma_{norm}^{t\bar{t}}}\int \mathrm{d}x\ \mathrm{d}q_1\ \mathrm{d}q_2\ f(q_1)f(q_2)\frac{\mathrm{d}\sigma_{hs}^{t\bar{t}}}{\mathrm{d}x}W(y_i,x,\mathrm{JES}), \tag{C.7}$$

$$P_{bkg}^i = \frac{1}{\sigma_{norm}^{W+jet}}\int \mathrm{d}x\ \mathrm{d}q_1\ \mathrm{d}q_2\ f(q_1)f(q_2)\frac{\mathrm{d}\sigma_{hs}^{W+jet}}{\mathrm{d}x}W(y_i,x) \tag{C.8}$$

The normalization constants, σ_{norm}, are calculated in Section C.5.

C.3 P_{sgn}

Rewriting Eqn. C.7 for convenience,

$$\begin{aligned} P^i_{sgn}(m_t, \text{JES}) = & \\ & \frac{1}{\sigma^{t\bar{t}}_{norm}} \int \mathrm{d}x\ \mathrm{d}q_1\ \mathrm{d}q_2\ f(q_1)f(q_2)\frac{\mathrm{d}\sigma_{hs}}{\mathrm{d}x}^{t\bar{t}} W(y_i, x, \text{JES}) \\ & = \frac{1}{\sigma^{t\bar{t}}_{norm}} \int \mathrm{d}x_1\, \mathrm{d}x_2\, f'(x_1)\, f'(x_2) \frac{(2\pi)^4 |\mathcal{M}|^2}{8|q_1||q_2|}\ \mathrm{d}\Phi_6\, W(y_i, x, \text{JES}). \end{aligned} \tag{C.9}$$

The total phase space factor, $\mathrm{d}\Phi_6$, is calculated first:

$$\mathrm{d}\Phi_6 = \delta^4 \left(P - p_{lep} - p_\nu - \sum_{i=1}^{4} p_{q_i} \right) \frac{\mathrm{d}^3|\vec{p}_{lep}|\mathrm{d}^3|\vec{p}_\nu|}{(2\pi)^6 4 E_{lep} E_\nu} \prod_{i=1}^{4} \frac{\mathrm{d}^3|\vec{p}_{q_i}|}{(2\pi)^3 2 E_{q_i}}. \tag{C.10}$$

Integrating over $\mathrm{d}^3|\vec{p}_\nu|$ gives

$$\begin{aligned} \mathrm{d}\Phi_6 = & \\ & \delta \left(E - E_{lep} - E_\nu - \sum_{i=1}^{4} E_{q_i} \right) \frac{\mathrm{d}^3|\vec{p}_{lep}|}{(2\pi)^6 4 E_{lep} E_\nu} \prod_{i=1}^{4} \frac{\mathrm{d}^3|\vec{p}_{q_i}|}{(2\pi)^3 2 E_{q_i}} \\ & = \delta \left(E - E_{lep} - E_\nu - \sum_{i=1}^{4} E_{q_i} \right) \frac{|\vec{p}_{lep}|^2\ \mathrm{d}|\vec{p}_{lep}|\mathrm{d}^2\Omega_{lep}}{(2\pi)^6 4 E_{lep} E_\nu} \prod_{i=1}^{4} \frac{|\vec{p}_{q_i}|^2\ \mathrm{d}|\vec{p}_{q_i}|\mathrm{d}^2\Omega_{q_i}}{(2\pi)^3 2 E_{q_i}}. \end{aligned} \tag{C.11}$$

Rewriting Eqn. C.9, using the full definition of $W(y, x)$ from Eqn. C.3,

$$\begin{aligned} P^i_{sgn}(m_t, \text{JES}) = & \\ & \frac{1}{\sigma^{t\bar{t}}_{norm}} \int \mathrm{d}x_1\ \mathrm{d}x_2\ f'(x_1) f'(x_2) \frac{(2\pi)^4 |\mathcal{M}|^2}{8|q_1||q_2|}\, \delta \left(E - E_{lep} - E_\nu - \sum_{i=1}^{4} E_{q_i} \right) \\ & \times \frac{\delta^2(\Omega^{meas}_{lep} - \Omega_{lep})}{|\vec{p}^{meas}_{lep}|^2} \frac{|\vec{p}_{lep}|^2\ \mathrm{d}|\vec{p}_{lep}|\mathrm{d}^2\Omega_{lep}}{(2\pi)^6 4 E_{lep} E_\nu} W_{lep}(1/p^{meas}_{lep}, 1/p_{lep}) \\ & \times \prod_{i=1}^{4} \frac{\delta^2(\Omega_{jet_i} - \Omega_{q_i})}{|\vec{p}_{jet_i}|^2} \frac{|\vec{p}_{q_i}|^2\ \mathrm{d}|\vec{p}_{q_i}|\mathrm{d}^2\Omega_{q_i}}{(2\pi)^3 2 E_{q_i}} W_{jet}(p_{jet_i}, p_{q_i}, \text{JES}). \end{aligned} \tag{C.12}$$

Integrating over $\mathrm{d}^2\Omega_{q_i}$, $\mathrm{d}^2\Omega_{lep}$, and $\mathrm{d}\vec{p}_{lep}$ eliminates the corresponding δ-functions:

$$
\begin{aligned}
&P^i_{sgn}(m_t, \mathrm{JES}) = \\
&\quad \frac{1}{\sigma^{t\bar{t}}_{norm}} \int \mathrm{d}x_1 \; \mathrm{d}x_2 \; f'(x_1) f'(x_2) \frac{(2\pi)^4 |\mathcal{M}|^2}{8|q_1||q_2|} \, \delta\left(E - E_{lep} - E_\nu - \sum_{i=1}^{4} E_{q_i}\right) \\
&\quad \times \frac{1}{64(2\pi)^{18} E_{lep} E_\nu} \left| \frac{\vec{p}_{lep}}{\vec{p}^{\,meas}_{lep}} \right|^2 W_{lep}(1/p^{meas}_{lep}, 1/p_{lep}) \; \mathrm{d}|\vec{p}_{lep}| \\
&\quad \times \prod_{i=1}^{4} \frac{\mathrm{d}|\vec{p}_{q_i}|}{E_{q_i}} \left| \frac{\vec{p}_{q_i}}{\vec{p}_{jet_i}} \right|^2 W_{jet}(p_{jet_i}, p_{q_i}).
\end{aligned}
\tag{C.13}
$$

If W_{lep} is a δ-function, $\left|\frac{\vec{p}_{lep}}{\vec{p}^{\,meas}_{lep}}\right|^2 = 1$ and this term can be dropped with the integration over $\mathrm{d}|\vec{p}_{lep}|$. Otherwise it remains. To take care of the remaining δ-function, it is necessary to transform $\mathrm{d}x_1 \mathrm{d}x_2$ to two new integration variables, $\mathrm{d}E_{tot}\mathrm{d}(p_{tot})_z$. Note that

$$
\begin{aligned}
(p_{tot})_z &= \frac{\sqrt{s}}{2}(x_2 - x_1) \\
E_{tot} &= \frac{\sqrt{s}}{2}(x_2 + x_1), \\
\mathrm{d}x_1 \; \mathrm{d}x_2 &= \frac{2}{\sqrt{s}^2} \; \mathrm{d}E_{tot} \; \mathrm{d}(p_{tot})_z.
\end{aligned}
\tag{C.14}
$$

Using this in Eqn. C.13, carrying out the integral over $\mathrm{d}E_{tot}$ to eliminate the δ-function, gives

$$
\begin{aligned}
P^i_{sgn}(m_t, \mathrm{JES}) = \frac{1}{\sigma^{t\bar{t}}_{norm}} \int \mathrm{d}(p_{tot})_z \; & f'(x_1) f'(x_2) \frac{(2\pi)^4 |\mathcal{M}|^2}{8|q_1||q_2|} \frac{1}{32(2\pi)^{18}\sqrt{s}^2 E_{lep} E_\nu} \\
& \times \left| \frac{\vec{p}_{lep}}{\vec{p}^{\,meas}_{lep}} \right|^2 W_{lep}(1/p^{meas}_{lep}, 1/p_{lep}) \; \mathrm{d}|\vec{p}_{lep}| \\
& \times \prod_{i=1}^{4} \frac{\mathrm{d}|\vec{p}_{q_i}|}{E_{q_i}} \left| \frac{\vec{p}_{q_i}}{\vec{p}_{jet_i}} \right|^2 W_{jet}(p_{jet_i}, p_{q_i}).
\end{aligned}
\tag{C.15}
$$

Lastly, the variables $(p_z, p_{q_1}, \ldots, p_{q_4})$ are transformed into the variables $(p_{q_1}, m^2_{Whad}, m^2_{thad}, m^2_{tlep}, (p_{tlep})_z)$. The full calculation for the Jacobian is rather complicated, so the result from Ref. [22] is only quoted here:

$$|\det J| = \frac{\partial m^2_{\overline{d}\overline{u}}}{\partial |\vec{p}_{\overline{u}}|} \frac{\partial m^2_{\overline{b}\overline{d}\overline{u}}}{\partial |\vec{p}_{\overline{b}}|} \left(\frac{\partial m^2_{bl\nu}}{\partial |\vec{p}_b|} \frac{\partial p^z_{bl\nu}}{\partial p^z_\nu} - \frac{\partial p^z_{bl\nu}}{\partial |\vec{p}_b|} \frac{\partial m^2_{bl\nu}}{\partial p^z_\nu} \right). \tag{C.16}$$

The final result for P_{sgn} is

$$\begin{aligned} &P^i_{sgn}(m_t, \mathrm{JES}) = \\ &\quad \frac{1}{\sigma^{t\bar{t}}_{norm}} \int \mathrm{d}(p_{tlep})_z \; \mathrm{d}p_{q_2} \; \mathrm{d}m^2_{Whad} \; \mathrm{d}m^2_{thad} \; \mathrm{d}m^2_{tlep} \\ &\quad \frac{1}{|\det J|} f'(x_1) f'(x_2) \frac{(2\pi)^4 |\mathcal{M}|^2}{8|q_1||q_2|} \frac{1}{32(2\pi)^{18} \sqrt{s}^2 E_{lep} E_\nu} \left| \frac{\vec{p}_{lep}}{\vec{p}^{\,meas}_{lep}} \right|^2 W_{lep}(1/p^{meas}_{lep}, 1/p_{lep}) \\ &\quad \times \mathrm{d}|\vec{p}_{lep}| \prod_{i=1}^{4} \frac{1}{E_{q_i}} \left| \frac{\vec{p}_{q_i}}{\vec{p}_{jet_i}} \right|^2 W_{jet}(p_{jet_i}, p_{q_i}). \end{aligned} \tag{C.17}$$

C.3.1 Integration Limits for Signal Probabilities

- p_{q_1}: 0 to 500 GeV/c
- m^2_{thad}: 0 to 500^2 (GeV/c^2)^2
- m^2_{tlep}: 0 to 500^2 (GeV/c^2)^2
- m^2_{Whad}: 0 to 400^2 (GeV/c^2)^2
- $(p_{tlep})_z$): -980 to 980 GeV

The following checks are made to ensure energy doesn't exceed the maximum allowed at the initial $t\bar{t}$ vertex. These effectively place upper limits on m^2_{thad} and m^2_{tlep}, and both limits on $(p_{tlep})_z$.

$$E_{proton} \leq 980 \text{ GeV}/c^2$$

$$E_{antiproton} \leq 980 \text{ GeV}/c^2$$

$$E_{tlep} \leq 980 \text{ GeV}/c^2$$

To place an upper limit on m^2_{Whad} (and also a lower limit on m^2_{thad}):

$$m^2_{Whad} \leq (m_{thad} - m_b)^2$$

And, finally, the following check the neutrino momentum and energy:

$$p_\nu \leq E_\nu$$

It is also required that solutions for p_{blep} and p_{bhad} obtained from quadratic equations are real. This places the lower limit on m^2_{tlep}, and both limits on p_{q_1}.

C.4 P_{bkg}

Up through Eqn.C.15, the calculation of P_{bkg} is identical to that of P_{sgn}:

$$
\begin{aligned}
P^i_{bkg} = & \\
& \frac{1}{\sigma^{W+jet}_{norm}} \int \mathrm{d}(p_{tot})_z \; f'(x_1) f'(x_2) \frac{(2\pi)^4 |\mathcal{M}|^2}{8|q_1||q_2|} \frac{1}{32(2\pi)^{18}\sqrt{s}^2 E_{lep} E_\nu} \\
& \times \mathrm{d}|\vec{p}_{lep}| \left| \frac{\vec{p}_{lep}}{\vec{p}^{\,meas}_{lep}} \right|^2 W_{lep}(1/p^{meas}_{lep}, 1/p_{lep}) \\
& \times \prod_{i=1}^{4} \frac{\mathrm{d}|\vec{p}_{q_i}|}{E_{q_i}} \left| \frac{\vec{p}_{q_i}}{\vec{p}_{jet_i}} \right|^2 W_{jet}(p_{jet_i}, p_{q_i}).
\end{aligned}
\tag{C.18}
$$

The integral over $\mathrm{d}(p_{tot})_z$ is transformed into an integral over m^2_W using the following equation:

$$
\mathrm{d}(p_{tot})^z = \; \mathrm{d}(p^z_\nu) = \frac{\mathrm{d}m^2_W}{2|p_{lep}(u^z_\nu - u^z_{lep})|}.
\tag{C.19}
$$

Integrals over the narrow Breit-Wigner peaks and the somewhat narrow peaks in jet energy are transformed to improve the performance of the importance sampling technique (see App. E). Eqn. E.2 is used to transform the integrations over $|\vec{p}_{q_i}|$ and $1/|\vec{p}_{lep}|$, noting that the integrals

are over the parton rather than reco-level momenta, and Eqn. E.7 is used to transform $\mathrm{d}m^2$. The following equation results:

$$
\begin{aligned}
P^i_{bkg} = & \\
& \frac{1}{\sigma^{W+jet}_{norm}} \int \frac{\mathrm{d}r(m_W^2)}{2|p_{lep}(u^z_\nu - u^z_{lep})|h(m^2)} \; f'(x_1) f'(x_2) \\
& \frac{(2\pi)^4 |\mathcal{M}|^2}{8|q_1||q_2|} \frac{1}{32(2\pi)^{18}\sqrt{s}^2 E_{lep} E_\nu} \\
& \times \mathrm{d}r^{lep}_{gaus}(1/p_{lep}) \left| \frac{\vec{p}_{lep}}{\vec{p}^{meas}_{lep}} \right|^2 \frac{|p^{meas}_{lep}|^2 W_{lep}(1/p^{meas}_{lep}, 1/p_{lep})}{G_{lep}(1/p_{lep}, 1/p^{meas}_{lep}, \sigma_{lep})} \\
& \times \prod_{i=1}^{4} \frac{\mathrm{d}r_{gaus}(p_{q_i})}{E_{q_i}} \left| \frac{\vec{p}_{q_i}}{\vec{p}_{jet_i}} \right|^2 \frac{W_{jet}(p_{jet_i}, p_{q_i})}{G(p_{q_i}, p_{jet_i}, \sigma_i)}.
\end{aligned}
\tag{C.20}
$$

C.4.1 Parton-level Cuts and Approximations for Background Probabilities

This result would be correct if the matrix element could be calculated exactly. Due to singularities in the calculation of $|\mathcal{M}|^2$, though, it is necessary to put restrictions on the integration over the partonic phase space. This is done with Acc(x). Cuts are placed on the relative angles of the various partons, $\Delta R(quark_i, quark_j)$ and $\Delta R(quark_i, lepton)$, and the quark p_T. The quark $|\eta|$ cut, although done at the parton-level, is actually a reco-level cut, since quarks and jets are assumed to have the same angles. It is done at the parton-level only because it allows faster processing. Thus, Acc(x)=1 for the following conditions:

- $\Delta R(quark_i, quark_j) > 0.5$
- $\Delta R(quark_i, lepton) > 0.5$
- $p_T(quark_i) > 5$ GeV/c
- $|\eta| < 3.0$

and 0 otherwise.

The cuts are applied to partons in the lab rest frame. Note that they actually have no effect on the event probability integration, since quark angles are fixed by jet angles, and event selection criteria are tighter than or the same as parton-level cuts.

In addition, it is necessary to make an approximation since calculating the full $|\mathcal{M}|^2$ is very CPU intensive. Only the $u\overline{d} \to gggg$ contribution is included. To cut the time in half again, only the positive helicity states of the W are included. To account for this, the $|\mathcal{M}^+|^2$ term is multiplied by 2.

The final result is:

$$\begin{aligned} P_{bkg}(y_i) = \frac{1}{\sigma_{norm}^{W+jet}} \int \mathrm{d}(p_{tot})_z \; f'(x_1) f'(x_2) \frac{(2\pi)^4 2\mathrm{Acc}(x) |\mathcal{M}^+|^2}{8|q_1||q_2|} \frac{1}{32(2\pi)^{18}\sqrt{s}^2 E_{lep} E_\nu} \\ \times \; \mathrm{d}r_{gaus}^{lep}(1/p_{lep}) \left| \frac{\vec{p}_{lep}}{\vec{p}_{lep}^{meas}} \right|^2 \frac{|p_{lep}^{meas}|^2 W_{lep}(1/p_{lep}^{meas}, 1/p_{lep})}{G_{lep}(1/p_{lep}, 1/p_{lep}^{meas}, \sigma_{lep})} \\ \times \prod_{i=1}^{4} \frac{\mathrm{d}r_{gaus}(p_{q_i})}{E_{q_i}} \left| \frac{\vec{p}_{q_i}}{\vec{p}_{jet_i}} \right|^2 \frac{W_{jet}(p_{jet_i}, p_{q_i})}{G(p_{q_i}, p_{jet_i}, \sigma_i)}. \end{aligned} \tag{C.21}$$

C.4.2 Integration Limits for Background Probabilities

- $r_{gaus}(p_{q_i})$:

  The upper and lower limits of $r_{gaus}(p_{q_i})$ are such that p_{q_i} is between 0 and 500 GeV/c. For each parton, the upper limit is reduced further if necessary to prevent the total energy from exceeding $\sqrt{s}$ (1960 GeV/c^2) for all 4 partons. Eqn. E.2 is used to find $r_{gaus}^{max}(p_{q_i})$ and $r_{gaus}^{min}(p_{q_i})$. The value of 500 was chosen to be consistent with the upper limit for p_{q_1} used in the signal probability integration.

- $r_{gaus}^{lep}(1/p_{lep})$:

  The upper and lower limits of $r_{gaus}(1/p_{lep})$ are such that $1/p_{lep}$ is between 0.0001 and 2 $(\mathrm{GeV}/c)^{-1}$. Eqn. E.2 is used to find the limits of $r_{gaus}^{lep}(1/p_{lep})$.

- $r(m_W)$ (W mass):

  m_W^2 is allowed to vary from 0 to s (1960 GeV/c^2)^2. Eqn. E.7 is used to calculate $r^{max}(m_W)$ and $r^{min}(m_W)$.

The energies of the incoming proton and antiproton are checked to ensure they do not exceed 980 GeV/c^2. This is done by calculating x_1 and x_2 using the following:

$$x_1 = \frac{E_{tot} + (p_{tot})_z}{\sqrt{s}}$$
$$x_2 = \frac{E_{tot} - (p_{tot})_z}{\sqrt{s}}$$

and verifying that $x_1 \leq 1$ and $x_2 \leq 1$.

C.5 P_{sgn} and P_{bkg} Normalizations

The probabilities $p(y|\text{sgn}, m_t, \text{JES})$ and $p(y|\text{bkg})$ will be normalized if

$$\int p(y|\text{sgn}, m_t, \text{JES})\text{d}y = \int p(y|\text{bkg})\text{d}y = constant.$$

For simplicity, 1 is chosen for the normalization constant. This gives the integral for the normalization, which is equivalent to the cross-section after acceptance and tagging/trigger efficiencies applied:

$$\sigma_{norm} = \int \text{d}y\text{Acc}(y)\,\eta_{trigg}(y)\,\eta_{btag}(y) \times \int \text{d}x\ \text{d}q_1\ \text{d}q_2\ f(q_1)f(q_2)\frac{\text{d}^n\sigma}{\text{d}x}W(y,x). \quad \text{(C.22)}$$

The differential cross-section, $\mathrm{d}^n\sigma$, was defined in Eqn. C.6. Combining equations C.22 and C.6 gives

$$\sigma_{norm} = \int \mathrm{d}y\ \mathrm{d}x\ \mathrm{d}q_1\ \mathrm{d}q_2\ f(q_1)f(q_2)\frac{(2\pi)^4|\mathcal{M}|^2}{8|q_1||q_2|}\frac{\mathrm{d}\Phi_n(q_1,q_2;p_1,...,p_n)}{\mathrm{d}x}$$
$$\times W(y,x)\mathrm{Acc}(y)\,\eta_{trigg}(y)\,\eta_{btag}(y). \tag{C.23}$$

C.5.1 Detector Acceptance

Acc(y), in included to account for limited detector acceptance. This term is defined to be 1 for the following:

- $\Delta R(jet, lepton) > 0.5$
- $\Delta R(jet_i, jet_j) > 0.5$
- muon: $|\eta_\mu| < 2.0$
- electron: $|\eta_e| < 1.1$
- $p_T^{jet} > 20.0$ GeV/c
- $p_T^{lepton} > 20.0$ GeV/c
- $\not\!\!E_T \equiv \sqrt{(\sum_{jets,lep} p_x)^2 + (\sum_{jets,lep} p_y)^2} > 20.0$ GeV/c^2

and 0 otherwise.

The $\mathrm{d}\Phi_n$ term is now a function of 14 variables. Integration time can be drastically reduced by choosing variables of integration allowing VEGAS to concentrate function calls in areas of phase space that give the largest contribution to the matrix element. This choice of variables depends on the matrix element called, so it will be different for signal and background integrations. As was done for the signal event probability, advantage is taken of the narrow Breit-Wigner peaks in the top quark and W-boson masses. There is only a single Breit-Wigner for the background,

corresponding to the W-boson. Some results useful for either integration are given here first before deriving the equations specific to signal or background.

The simplest expression written in terms of final and initial state particles is [16]:

$$\mathrm{d}\Phi_n(q_1, q_2; p_1, \ldots, p_n) = \delta^4\left(q_1 + q_2 - \sum_{i=1}^{n} p_i\right) \prod_{i=1}^{n} \frac{\mathrm{d}^3\vec{p_i}}{(2\pi)^3 2E_i} \tag{C.24}$$

For both the signal and background normalizations, the following general result is useful for phase states defined in terms of intermediate decaying particles [16]:

$$\begin{aligned} \mathrm{d}\Phi_n(P; p_1, \ldots, p_n) &= \mathrm{d}\Phi_j(q; p_1, \ldots, p_j) \\ &\quad \times \mathrm{d}\Phi_{n-j+1}(P; q, p_{i+1}, \ldots, p_n)(2\pi)^3 \ \mathrm{d}q^2, \end{aligned} \tag{C.25}$$

where

$$q^2 = \left(\sum_{i=1}^{j} E_i\right)^2 - \left|\sum_{i=1}^{j} \vec{p}_i\right|^2. \tag{C.26}$$

The strategy is to reduce the total phase space into a phase space differential for each intermediate decay vertex. Then a relatively simple formula can be used to express the differential in terms of invariant masses and an angle of a daughter particle from each vertex. The general result for $\mathrm{d}\Phi_2$, the phase space for the decay of a body of mass M to 2 particles of mass m_1 and m_2, is shown next (all calculated in rest frame of M) [16].

$$\begin{aligned} d\Phi_2(P; p_1, p_2) &= \delta^4(P - p_1 - p_2)\frac{\mathrm{d}^3\vec{p}_1}{(2\pi)^3 2E_1}\frac{\mathrm{d}^3\vec{p}_2}{(2\pi)^3 2E_2} \\ &= \delta(E_{tot} - E_1 - E_2)\frac{1}{4(2\pi)^6}\frac{\mathrm{d}^3\vec{p}_2}{E_1 E_2}, \\ &= \delta(E_{tot} - E_1 - E_2)\frac{1}{4(2\pi)^6}\frac{|\vec{p}_2|^2 \ \mathrm{d}|\vec{p}_2| \ \mathrm{d}^2\Omega_2}{E_1 E_2}. \end{aligned} \tag{C.27}$$

Using

$$\left|\frac{\partial(E_{tot}-E_1-E_2)}{\partial|\vec{p}_2|}\right| = \left|\frac{\partial E_1}{\partial|\vec{p}_2|}+\frac{\partial E_2}{\partial|\vec{p}_2|}\right| = \frac{p}{E_1}+\frac{p}{E_2} = \frac{Mp}{E_1E_2}, \tag{C.28}$$

$$E_1 = \frac{M^2-m_2^2+m_1^2}{2M}, \tag{C.29}$$

and

$$p \equiv |\vec{p}_1| = |\vec{p}_2| = \frac{\sqrt{(M^2-(m_1-m_2)^2)(M^2-(m_1+m_2)^2)}}{2M}, \tag{C.30}$$

some algebra gives

$$d\Phi_2(P;p_1,p_2) = \frac{\phi(M,m_1,m_2)\ \mathrm{d}^2\Omega_2}{(2\pi)^6}, \tag{C.31}$$

where

$$\phi(M,m_1,m_2) \equiv \frac{\sqrt{(M^2-(m_1-m_2)^2)(M^2-(m_1+m_2)^2)}}{8M^2}. \tag{C.32}$$

The function, ϕ, depends only upon invariant masses so is itself an invariant quantity.

C.5.2 Signal Normalization

For $p\overline{p} \to t\overline{t} \to l\nu +$ jets the matrix element is calculated directly as described in Ref. [22]. It has negligible values everywhere except near the four Breit-Wigner (BW) peaks corresponding to the two top and two W pole masses. This motivates the choice of m_{thad}, m_{tlep}, m_{Whad}, and m_{Wlep} as four of the integration variables. The other 10 variables are the angles of both b-quarks, Ω^2_{bhad} and Ω^2_{blep}; the angles of the top quark which decays to the hadronically decaying W, Ω^2_{thad}; the angle of the lepton, Ω^2_{lep}; and the angle of one of the quarks from the hadronic W decay, $\Omega^2_{q_2}$.

Using Eqn. C.25 three times,

$$\begin{aligned}
\mathrm{d}\Phi_6 &= \mathrm{d}\Phi_3(q_{thad}; p_{q_1}, p_{q_2}, p_{bhad})(2\pi)^3 \ \mathrm{d}m^2_{thad} \\
&\times \mathrm{d}\Phi_3(q_{tlep}; p_{lep}, p_\nu, p_{blep})(2\pi)^3 \ \mathrm{d}m^2_{tlep} \\
&\times \mathrm{d}\Phi_2(P_{tot}; q_{thad}, q_{tlep}).
\end{aligned} \tag{C.33}$$

The two terms corresponding to the top quark decay can be expanded again in terms of the subsequent W decay using Eqns C.25 and C.31. This gives:

$$\begin{aligned}
\mathrm{d}\Phi_3(q_{thad}) &= \mathrm{d}\Phi_2(q_{Whad}; p_{q_1}, p_{q_2})\mathrm{d}\Phi_2(q_{thad}; q_{Whad}, p_{bhad}) \\
&\times (2\pi)^3 \ \mathrm{d}m^2_{Whad} \\
&= \frac{1}{(2\pi)^9}\phi(m_{Whad}, m_{q_1}, m_{q_2})\phi(m_{thad}, m_{Whad}, m_{bhad}) \\
&\times \ \mathrm{d}^2\Omega_{q_1} \ \mathrm{d}^2\Omega_{Whad} \ \mathrm{d}m^2_{Whad}. \\
\mathrm{d}\Phi_3(q_{tlep}) &= \frac{1}{(2\pi)^9}\phi(m_{Wlep}, m_{lep}, m_\nu)\phi(m_{tlep}, m_{Wlep}, m_{blep}) \\
&\times \ \mathrm{d}^2\Omega_{lep} \ \mathrm{d}^2\Omega_{Wlep} \ \mathrm{d}m^2_{Wlep}.
\end{aligned} \tag{C.34}$$

The term corresponding to the primary vertex, $\mathrm{d}\Phi_2(P_{tot})$, can be rewritten directly using Eqn. C.31. With the following definition:

$$\begin{aligned}
\phi^{sgn}_{tot} &\equiv \phi(\sqrt{s}, m_{thad}, m_{tlep})\phi(m_{Whad}, m_{q_1}, m_{q_2})\phi(m_{thad}, m_{Whad}, m_{bhad}) \\
&\times \phi(m_{Wlep}, m_{lep}, m_\nu)\phi(m_{tlep}, m_{Wlep}, m_{blep}),
\end{aligned} \tag{C.35}$$

Eqn. C.33 becomes

$$\begin{aligned} \mathrm{d}\Phi_6 = \frac{1}{(2\pi)^{18}}\phi_{tot}^{sgn}\ \mathrm{d}m_{thad}^2\ \mathrm{d}m_{tlep}^2\ \mathrm{d}m_{Whad}^2\ \mathrm{d}m_{Wlep}^2 \\ \times\ \mathrm{d}^2\Omega_{q_1}\ \mathrm{d}^2\Omega_{Whad}\ \mathrm{d}^2\Omega_{lep}\ \mathrm{d}^2\Omega_{Wlep}\ \mathrm{d}^2\Omega_{tlep}, \end{aligned}$$

Combining this result with equations C.23 and C.3 gives the full expression for the normalization of the signal probabilities:

$$\begin{aligned} \sigma_{norm}^{sgn} = \int \mathrm{d}y\ \mathrm{d}q_1\ \mathrm{d}q_2 f(q_1)f(q_2)\frac{(2\pi)^4|\mathcal{M}|^2}{8|q_1||q_2|}\mathrm{Acc}(y)\,\eta_{trigg}(y)\,\eta_{btag}(y) \\ \times \frac{1}{(2\pi)^{18}}\phi_{tot}^{sgn}\ \mathrm{d}m_{thad}^2\ \mathrm{d}m_{tlep}^2\ \mathrm{d}m_{Whad}^2\ \mathrm{d}m_{Wlep}^2 \\ \times\ \mathrm{d}^2\Omega_{q_1}\ \mathrm{d}^2\Omega_{Whad}\ \mathrm{d}^2\Omega_{lep}\ \mathrm{d}^2\Omega_{Wlep}\ \mathrm{d}^2\Omega_{tlep} \\ \times W_{lep}(1/p_{lep}^{meas}, 1/p_{lep})\frac{\delta^2(|\Omega_{lep}^{meas}| - |\Omega_{lep}|)}{|p_{lep}|^2} \\ \times \prod_{i=1}^{4}\frac{\delta^2(\Omega_{jet_i} - \Omega_{q_i})}{|\vec{p}_{jet_i}|^2}W_{jet}(p_{jet_i}, p_{q_i}). \end{aligned} \tag{C.36}$$

Some further simplification is possible– specifically, elimination of the δ-functions through integration of the $\mathrm{d}y$ variables. The differential $\mathrm{d}y$ is over the phase space of reco-level particles:

$$\mathrm{d}y = |\vec{p}_{lep}^{meas}|^2\ \mathrm{d}|\vec{p}_{lep}^{meas}|\ \mathrm{d}^2\Omega_{lep}^{meas}\prod_{i=1}^{4}|\vec{p}_{jet_i}|^2\ \mathrm{d}|\vec{p}_{jet_i}|\ \mathrm{d}^2\Omega_{jet_i}.$$

Integration over $\mathrm{d}\Omega_{lep}^{meas}$ and the jet angles ($\mathrm{d}\Omega_{jet_i}$) eliminates the δ-functions. This gives the intermediate result for σ_{norm}: (Note that $f(q_1)$ and $f(q_2)$ have been replaced by $f'(x_1)$ and $f'(x_2)$.)

$$\begin{aligned}\sigma_{norm}^{sgn} = & \int \mathrm{d}x_1 \mathrm{d}x_2 f'(x_1) f'(x_2) \mathrm{Acc}(y)\, \eta_{trigg}(y)\, \eta_{btag}(y) \frac{(2\pi)^4 |\mathcal{M}|^2}{8|\vec{q}_1||\vec{q}_2|} \frac{1}{(2\pi)^{18}} \phi_{tot}^{sgn} \\ & \times\ \mathrm{d}m_{thad}^2\ \mathrm{d}m_{tlep}^2\ \mathrm{d}m_{Whad}^2\ \mathrm{d}m_{Wlep}^2\ \mathrm{d}^2\Omega_{q_1}\ \mathrm{d}^2\Omega_{Whad}\ \mathrm{d}^2\Omega_{lep}\ \mathrm{d}^2\Omega_{Wlep}\ \mathrm{d}^2\Omega_{tlep} \\ & \times W_{lep}(1/p_{lep}^{meas}, 1/p_{lep})\ \mathrm{d}|\vec{p}_{lep}^{meas}| \prod_{i=1}^{4} W_{jet}(p_{jet_i}, p_{q_i})\ \mathrm{d}|\vec{p}_{jet_i}|. \end{aligned} \tag{C.37}$$

Importance Sampling for Signal Normalization

Each Breit-Wigner peak is transformed using Eqn. E.7. The integrations over $\vec{p}_{jet_i}$ (and lepton p_T, if applicable) are transformed using Eqn. E.2. The result is:

$$\begin{aligned}\sigma_{norm}^{sgn} = & \int \mathrm{d}x_1 \mathrm{d}x_2 f'(x_1) f'(x_2) \frac{(2\pi)^4 |\mathcal{M}|^2}{8|\vec{q}_1||\vec{q}_2|} \frac{1}{(2\pi)^{18}} \phi_{tot}^{sgn}\ \mathrm{Acc}(y)\, \eta_{trigg}(y)\, \eta_{btag}(y) \\ & \times\ \mathrm{d}^2\Omega_{q_1}\ \mathrm{d}^2\Omega_{Whad}\ \mathrm{d}^2\Omega_{lep}\ \mathrm{d}^2\Omega_{Wlep}\ \mathrm{d}^2\Omega_{tlep} \\ & \times\ \mathrm{d}r_{gaus}^{lep}(1/p_{lep}) \frac{|p_{lep}^{meas}|^2 W_{lep}(1/p_{lep}^{meas}, 1/p_{lep})}{G_{lep}(1/p_{lep}, 1/p_{lep}^{meas}, \sigma_{lep})} \\ & \times \prod_{i=1}^{4} \frac{W_{jet}(p_{jet_i}, p_{q_i})}{G(p_{q_i}, p_{jet_i}, \sigma_i)}\ \mathrm{d}r_{gaus}(p_{jet_i}) \\ & \times \frac{\mathrm{d}r(m_{thad})\ \mathrm{d}r(m_{tlep})\ \mathrm{d}r(m_{Whad})\ \mathrm{d}r(m_{Wlep})}{h(m_{thad}) h(m_{tlep}) h(m_{Whad}) h(m_{Wlep})}. \end{aligned} \tag{C.38}$$

Integration Limits for Signal Normalization

- x_1, x_2:

  The variables x_1 and x_2 are allowed to vary from 0 to 1. The upper limit ensures that the energy doesn't exceed the maximum allowed. The total energy that must be conserved in the $p\overline{p}$ collision is $\sqrt{sx_1x_2}$, where $\sqrt{s} = 1960$ GeV. The lower integration limits allow

for combinations of x_1 and x_2 which do not have sufficient energy to generate final state particles at rest, so it is necessary to impose the following condition:

$$x_1 x_2 \geq \frac{(2m_{top}^{min})^2}{s},$$

with

$$m_{top}^{min} = m_b + m_W^{min}, \tag{C.39}$$

$$m_W^{min} = 2m_f. \tag{C.40}$$

Here m_b is the mass of the b-quark, and m_f is the mass of the W-boson daughters. It is assumed that the masses of the leptons and light quarks are negligible, so m_f is set to zero.

- $\Omega_{q_1}, \Omega_{Whad}, \Omega_{lep}, \Omega_{Wlep}, \Omega_{tlep}$:

  For the integrations over angles, all values are allowed. Thus $cos\theta$ varies from 0 to 1, and ϕ varies from 0 to 2π.

- $r(m_{thad})$ (hadronic top mass):

  $r(m_{thad})$ is allowed to vary uniformly from r_{thad}^{min} to r_{thad}^{max}, where r_{thad}^{min} and r_{thad}^{max} are calculated using Eqn. E.7. m_{top}^{min} was defined in C.39. Γ_{thad} is the width of the hadronic top mass. m_{thad}^{max} as defined here ensures energy conservation and allows enough energy to generate the leptonic top quark at rest:

$$m_{thad}^{max} = \sqrt{s x_1 x_2} - m_{top}^{min}.$$

- $r(m_{tlep})$ (leptonic top mass): $m_{top}^{min} \leq m_{tlep} \leq \sqrt{s x_1 x_2} - m_{thad}$

- $r(m_{Whad})$ (hadronic W mass): $0 \leq m_{Whad} \leq m_{thad} - m_b$

- $r(m_{Wlep})$ (leptonic W mass): $0 \leq m_{Wlep} \leq m_{tlep} - m_b$

- $r_{gaus}(p_{jet_i})$:

  The lower limit of $r_{gaus}(p_{jet_i})$ is chosen so that $m_{jet_i} \geq m_{quark_i}$. The upper limit is 1. Eqn. E.4 is used to calculate p_{jet}.

- $r^{lep}_{gaus}(p^{meas}_{lep})$: 0 to 1

Calculation of Kinematic Variables for Signal Normalization

Next it is necessary to calculate the 4-momenta of all particles in order to calculate the matrix element. This is done as follows:

- p_{tophad} (hadronic top quark):

  The energy is fixed by the following:

$$E_{tophad} = \frac{1}{2\sqrt{sx_1x_2}}(sx_1x_2 - m^2_{toplep} + m^2_{tophad}).$$

  This is used with m_{tophad} and Ω_{thad} to get the 4-vector for the hadronic top quark in the lab CM frame.

- p_{toplep} (leptonic top quark):

$$E_{toplep} = \sqrt{sx_1x_2} - E_{tophad},$$
$$\vec{p}_{toplep} = -\vec{p}_{tophad}. \tag{C.41}$$

- p_{bhad}, p_{blep}, p_{q_1}, p_{q_2}, p_{lep}, and p_ν:

  Equations C.30 are used to get the energy and $|\vec{p}|$ for the W bosons and b-quarks. These are combined with Ω_{Whad} and Ω_{Wlep} to get the 4-vectors for the 4 daughter particles,

which are then converted to the $p\overline{p}$ CM frame using the 4-vectors of the parent top quarks as the boost vectors.

Next the 4-vectors of the W bosons, expressed in the $p\overline{p}$ CM frame, are used with p_{toplep}, Ω_{q_1}, m_{toplep}, and m_{Wlep} to get p_{q_1} and p_{q_2}, the 4 vectors of the quarks from the hadronic W decay. The same thing is done for the leptonic W boson to get p_{lep} and p_ν in the $p\overline{p}$ CM frame.

Finally, all 4-vectors are boosted to the lab rest frame using the proton 4-vector to get the boost vector. The energy of the proton in the lab rest frame, E_p, is $x_1\sqrt{s}/2$. The anti-proton energy is $E_{\overline{p}} = x_2\sqrt{s}/2$. The matrix element, $|\mathcal{M}|^2$, is calculated in the lab rest frame.

C.5.3 Background Normalization

To make the calculation simpler for the background normalization, the phase space is broken up into 3 parts as if there were an initial decay to 2 particles: the W boson, which subsequently decays leptonically, and a second composite particle which decays to four quarks. Here, since the four quarks are all light and come from the same vertex, they are labeled p_5,p_6,p_7,and p_8.

$$\begin{aligned} & \mathrm{d}\Phi_6(P; p_{lep}, p_\nu, p_5, p_6, p_7, p_8) && \text{(C.42)} \\ &= \mathrm{d}\Phi_2^W(q_W; p_{lep}, p_\nu)\ \mathrm{d}\Phi_5(P; q_W, p_5, p_6, p_7, p_8)(2\pi)^3\ \mathrm{d}m_W^2 \\ &= \mathrm{d}\Phi_2^W(q_W; p_{lep}, p_\nu)\mathrm{d}\Phi_2(P; q_{quarks}, q_W) \\ &\times \ \mathrm{d}\Phi_4^{quarks}(q_{quarks}; p_5, p_6, p_7, p_8) \\ &\times \ (2\pi)^6\ \mathrm{d}m_{quarks}^2\ \mathrm{d}m_W^2, && \text{(C.43)} \end{aligned}$$

where

$$m^2_{quarks} = \left(\sum_{i=5}^{8} E_i\right)^2 - \left|\sum_{i=5}^{8} \vec{p}_i\right|^2 . \tag{C.44}$$

Eqn. C.31 is used to rewrite the two $d\Phi_2$ terms, getting

$$\begin{aligned} &d\Phi_6(P; p_{lep}, p_\nu, p_5, p_6, p_7, p_8) = \\ &\quad (2\pi)^6 \; dm^2_{quarks} \; dm^2_W \; d\Phi_4^{quarks} \\ &\quad \times \frac{\phi(m_W, m_{lep}, m_\nu) \; d^2\Omega_{lep}}{(2\pi)^6} \frac{\phi(\sqrt{s}, m_{quarks}, m_W) \; d^2\Omega_W}{(2\pi)^6} \\ &\quad = \frac{1}{(2\pi)^6} \phi^{bkg}_{tot} \; dm^2_{quarks} \; dm^2_W \; d\Phi_4^{quarks} \; d^2\Omega_{lep} \; d^2\Omega_W , \end{aligned} \tag{C.45}$$

where ϕ^{bkg}_{tot} is defined similarly to ϕ^{sgn}_{tot}:

$$\phi^{bkg}_{tot} \equiv \phi(m_W, m_{lep}, m_\nu)\phi(\sqrt{s}, m_{quarks}, m_W). \tag{C.46}$$

RAMBO

The RAMBO package is used for calculation of $d\Phi_4^{quarks}$ [27]. This package was designed to generate n particles from the decay of a single particle randomly distributed in phase space. RAMBO takes as its normal input n, the number of particles; a mass for each of the n particles; and the total center-of-mass energy, m_{quarks}. It returns the particle momenta for the n randomly generated particles, and a weight for the event. This weight is proportional to the volume in phase space, which is exactly the term $d\Phi_4^{quarks}$ that is needed for the background normalization integral.

The RAMBO code was modified to take the point in phase space randomly generated by VEGAS as an input. The weight returned by VEGAS is actually $(2\pi)^{12}$ times the phase space volume, so the weight is divided by $(2\pi)^{12}$ and used as the value of $d\Phi_4^{quarks}$.

Importance Sampling for Background Normalization

As was done for the signal normalization integration, the matrix element, $|\mathcal{M}|^2$, is divided by the $h(m_W)$ defined in Eqn. E.6, and $\mathrm{d}m_W^2$ is replaced by $\mathrm{d}r(m_W)$ defined in Eqn. E.7. The integrals over $|\vec{p}_{jet_i}|$ and $|\vec{p}_{lep}|$ are also modified using Eqn. E.2.

The result is

$$\begin{aligned}\sigma_{norm}^{bkg} = & \int \mathrm{d}x_1 \mathrm{d}x_2 f'(x_1) f'(x_2) \frac{(2\pi)^4 |\mathcal{M}|^2}{8|\vec{q}_1||\vec{q}_2|} \,\mathrm{Acc}(y)\, \eta_{trigg}(y)\, \eta_{btag}(y) \\ & \times \frac{1}{(2\pi)^6} \phi_{tot}^{bkg} \,\mathrm{d}^2\Omega_{lep} \,\mathrm{d}^2\Omega_W \,\mathrm{d}\Phi_4^{quarks} \frac{\mathrm{d}(r(m_W))}{h(m_W)} \,\mathrm{d}m_{quarks}^2 \\ & \times \,\mathrm{d}r_{gaus}^{lep}(1/p_{lep}) \frac{|p_{lep}^{meas}|^2 W_{lep}(1/p_{lep}^{meas}, 1/p_{lep})}{G_{lep}(1/p_{lep}, 1/p_{lep}^{meas}, \sigma_{lep})} \\ & \times \prod_{i=1}^{4} \frac{W_{jet}(p_{jet_i}, p_{q_i})}{G(p_{q_i}, p_{jet_i}, \sigma_i)} \,\mathrm{d}r_{gaus}(p_{jet_i}) \end{aligned} \tag{C.47}$$

Integration Limits for Background Normalization

- x_1, x_2:

  Same as in C.5.2, but masses of final state particles are different:

  $$x_1 x_2 \geq \frac{(m_W^{min} + 4m_q)^2}{s},$$

  where m_q is the mass of the quark, here assumed to be massless, and m_W is the same as that defined in Eqn. C.40.

- Ω_{lep}, Ω_W:

  For the integrations over angles, all values are allowed. Thus $cos\theta$ varies from 0 to 1, and ϕ varies from 0 to 2π.

- $r(m_W)$ (W-boson mass):$0 \leq m_W^2 \leq (\sqrt{s} - \sum_{i=1}^{4} m_{q_i})^2$

- m_{quarks}^2 (mass of 4-quark system): $(\sum_{i=1}^{4} m_{q_i})^2 \leq m_{4quarks}^2 \leq (\sqrt{s} - m_W)^2$

- Φ_4^{quarks}:

  The invariant mass of the 4-quark system is passed to RAMBO, and is used to constrain the phase space of the 4 randomly-generated particle 4-momenta.

- $r_{gaus}(p_{jet_i})$: $r_{gaus}(p_{jet_i})$ has a minimum such that $p_{jet_i} \geq m_{q_i}$. The maximum value is 1. Eqn. E.2 is used to calculate r_{gaus}.

- $r_{gaus}^{lep}(p_{lep}^{meas})$: 0 to 1

Calculation of Kinematic Variables for Background Normalization

- W-boson:

  The energy of the W-boson is determined in the $p\overline{p}$ rest frame with the following:

$$E_W = \frac{1}{2\sqrt{sx_1x_2}}(sx_1x_2 - m_{quarks}^2 + m_W^2).$$

  This is used along with Ω_W and m_W^2 to calculate the 4-vector for the W-boson.

- lepton, ν

  The lepton and neutrino 4-momenta vectors are calculated in the W rest frame using m_W^2 and Ω_{lep}. They are then boosted to the lab CM frame.

- p_5,p_6,p_7,p_8:

  These are calculated by RAMBO under the constraint that the square of the invariant mass of the 4-quark system, given by Eqn. C.44, is equal the integration variable m_{quarks}^2. These 4-vectors are all in the rest frame of the 4-quark system. They are then boosted to the lab CM frame.

The matrix element, $|\mathcal{M}|^2$, is calculated in the lab CM frame, unlike the signal normalization which is calculated in the lab rest frame.

Acceptance Cuts for Background Normalization

The cuts described in Section C.4.1 for the background event probability, as well as the use of only positive W-helicity diagrams, are applied again. In order to apply the acceptance cuts, it is necessary to boost the parton 4-momenta vectors to the lab rest frame. These are boosted using the proton and anti-proton momenta to get the boost vectors:

$$\begin{aligned}(p_p)_z &= \frac{1}{2}(x_2 - x_1)\sqrt{s x_1 x_2} \\ (p_{\overline{p}})_z &= -(p_p)_z. \end{aligned} \tag{C.48}$$

The final result is:

$$\begin{aligned}\sigma_{norm}^{bkg} = \int \mathrm{d}x_1 \mathrm{d}x_2 f'(x_1) f'(x_2) &\frac{(2\pi)^4 2\mathrm{Acc}(x)|\mathcal{M}^+|^2}{8|\vec{q}_1||\vec{q}_2|}\ \mathrm{Acc}(y)\,\eta_{trigg}(y)\,\eta_{btag}(y) \\ &\times \frac{1}{(2\pi)^6}\phi_{tot}^{bkg}\ \mathrm{d}^2\Omega_{lep}\ \mathrm{d}^2\Omega_W\ \mathrm{d}\Phi_4^{quarks}\frac{\mathrm{d}r(m_W)}{h(m_W)} \\ &\times\ \mathrm{d}r_{gaus}^{lep}(1/p_{lep})\frac{|p_{lep}^{meas}|^2 W_{lep}(1/p_{lep}^{meas}, 1/p_{lep})}{G_{lep}(1/p_{lep}, 1/p_{lep}^{meas}, \sigma_{lep})} \\ &\times \prod_{i=1}^{4}\frac{W_{jet}(p_{q_i}, p_{jet_i})}{G(p_{q_i}, p_{jet_i}, \sigma_i)}\ \mathrm{d}r_{gaus}(p_{jet_i}).\end{aligned} \tag{C.49}$$

D. VEGAS

VEGAS is the external package used to perform the integrals for signal and background probabilities and normalizations [89]. Some modifications to the standard code (downloaded from Gnu Scientific Library v.1.5 [91]) were required for this analysis and are described here.

VEGAS uses importance sampling, which means that the integration is performed by sampling points in phase space based on a probability distribution, p. The probability distribution is optimized through an iterative process to minimize the error in the estimate of the integral.

The integral, I, is approximated by sampling N sample points within the phase space volume, V, evaluating the integrand, f, at each point:

$$I \equiv \int f \, \mathrm{d}V = \int \frac{f}{p} \, \mathrm{d}V \approx \left\langle \frac{f}{p} \right\rangle \pm \sqrt{\frac{\langle f^2/p^2 \rangle - \langle f/p \rangle^2}{N}}. \tag{D.1}$$

It can be shown (see Ref. [90]) that the condition for p which minimizes the error is:

$$p = \frac{|f|}{\int |f| \, \mathrm{d}V}. \tag{D.2}$$

If this condition is satisfied, the error in the estimate will be zero. Of course, $I(|f|)$ is not known exactly, so several iterations of N calls to the function f are required to improve the determination of the shape of p.

D.1 Damping constant

Calls to the function are weighted by the probability distribution by breaking up each dimension into a number of bins, M. By default, there are 50 bins per dimension. Initially, each

bin has equal width. Assuming the range of integration is 0 to 1 for each dimension, each bin has width $1/M$ for the first iteration. The probability distribution is modified by varying the widths of the M bins in each dimension. If D is the number of dimensions, $N/(MD)$ calls are made per bin. A smaller bin size means a higher density of function calls in the corresponding region of phase space.

The probability distribution for the x_{th} dimension is determined by:

$$p(x) = \frac{1}{M\Delta x_i}, x_i - \Delta x_i \leq x \leq x_i \tag{D.3}$$

where $i = 1, \cdots, M$.

After N/D function calls for a dimension, the average value of the integrand for each bin is calculated. These values, $\overline{f}_i$, are used to calculate a new bin size for the i_{th} bin:

$$m_i = K \left\{ \left(\frac{\overline{f}_i \Delta x_i}{\sum_j \overline{f}_j \Delta x_j} - 1 \right) \frac{1}{\ln\left(\frac{\overline{f}_i \Delta x_i}{\sum_j \overline{f}_j \Delta x_j} \right)} \right\}^{\alpha} \tag{D.4}$$

K is a normalization constant which gives $\sum_i^{N/D} m_i = 1$. The damping constant, α, is used to stabilize the grid reshaping from one iteration to the next. The normal value of α is between 1 and 2, but it was set to 0.5 for the matrix element integration. This is necessary for the normalization integration due to the large number of dimensions in the normalization integral, which in turn results in relatively small numbers of function calls per bin. It is also used for the event probability integral to allow fewer function calls without risking the early exclusion of important regions of phase space. A value of 0.5 for α prevents the grid from reshaping too drastically before enough iterations have taken place to provide sufficient statistics.

D.2 Error estimation

The formulae used to calculate the integral and standard deviation after a set of iterations are:

$$\begin{aligned} \overline{I} &= \sigma_{\overline{I}}^2 \sum_k \frac{I_k}{\sigma_k^2} \\ \sigma_{\overline{I}} &= \sqrt{\sum_k \frac{1}{\sigma_k^2}}. \end{aligned} \tag{D.5}$$

It is pointed out in Ref. [89] that the integral and error may be badly underestimated in the earliest iterations if the integrand has high, narrow peaks. This was found to be the case, so the VEGAS code was modified to use the following:

$$\begin{aligned} \overline{I} &= \sum_k \frac{I_k^3}{\sigma_k^2} / \sum_k \frac{I_k^2}{\sigma_k^2} \\ \sigma_{\overline{I}} &= \overline{I} \sqrt{\sum_k I_k^2/\sigma_k^2}. \end{aligned} \tag{D.6}$$

E. IMPORTANCE SAMPLING

If f can be written as a function, $f'(r)$, times a differential, $\mathrm{d}r$, such that $f'(r)$ is as flat as possible, then there will be little optimization needed by VEGAS. This is possible if $f(x) = \alpha h(x)$, where $h(x)\ \mathrm{d}x = \ \mathrm{d}r$, and $r = \int h(x)\ \mathrm{d}x$ and is analytically solvable.

Firstly, this is used for the background event probability and normalization integrations for integration over the parton momenta. Since $W_{jet}(p_{jet}, p_q)$ is a double Gaussian, dividing by a Gaussian of the appropriate width and mean, and changing the integration variable accordingly, can help save the number of iterations needed to shape the grid. This is done in the first section.

Secondly, the scattering amplitude, $|\mathcal{M}|^2$, is sharply peaked for masses in the vicinity of the resonance masses for the top quark and W boson. This peak motivates the use of the W and top quark masses as integration variables, and subsequent transformations to decrease the number of required iterations. This is done for the signal normalization and both background integrations, as described in the second section. Note that, for the signal event probability integration, the invariant squared masses are used directly as integration variables. This is because subsequent transformations do not add very much improvement, and the function calls for the $t\bar{t}$ matrix element are quick enough that extra iterations are not that costly.

E.1 Parton/jet momenta

For each value of $\vec{p}_{jet}$, W_{jet} is divided by a Gaussian with mean $p_{jet}(p_q)$ and width, $\sigma = 3.5\sqrt{p_{jet}}$. (Similarly, for integration over $1/p_T^{lep}$, W_{lep} is divided by a Gaussian with mean $1/p_{lep}^{meas}$ and mean 0.2649.)

Consider the following:

$$
\begin{aligned}
I &= \int \mathrm{d}|\vec{p}_{jet}| W_{jet}(p_q, p_{jet}) \\
&= \int \mathrm{d}|\vec{p}_{jet}| \left(\frac{W_{jet}(p_q, p_{jet})}{\frac{1}{\sigma\sqrt{2\pi}} e^{-(p_{jet}-p_q)^2/2\sigma^2}} \right) \frac{1}{\sigma\sqrt{2\pi}} e^{-(p_{jet}-p_q)^2/2\sigma^2}.
\end{aligned} \tag{E.1}
$$

With the following definitions:

$$
\begin{aligned}
r_{gaus}(p_{jet}) &\equiv \frac{1}{\sqrt{\pi}} \int^{(p_{jet}-p_q)/\sqrt{2}\sigma} e^{-t^2}\ \mathrm{d}t, \\
\mathrm{d}r_{gaus} &= \frac{1}{\sigma\sqrt{2\pi}} e^{-(p_{jet}-p_q)^2/2\sigma^2}\ \mathrm{d}p_{jet},
\end{aligned} \tag{E.2}
$$

the new integrand is close to a flat function:

$$
I = \int \mathrm{d}r_{gaus} \left(\frac{W_{jet}(p_q, p_{jet})}{G(p_q, p_{jet}, \sigma)} \right),
$$

where

$$
G(p_q, p_{jet}, \sigma) \equiv \frac{1}{\sigma\sqrt{2\pi}} e^{-(p_{jet}-p_q)^2/2\sigma^2}.
$$

For the calculation of the reco-level jet energies from the variable r_{gaus}, the FORTRAN function DGAUSN is used. This calculates the inverse of the Gaussian distribution function. If

$$
P(x) = \frac{1}{\sqrt{2\pi}} \int_{-\infty}^{X(P)} e^{-t^2/2}\ \mathrm{d}t, \tag{E.3}
$$

DGAUSN(P) returns X(P). Using Eqn. E.2,

$$\begin{aligned} r_{gaus}(p_{jet}) &= \frac{1}{\sqrt{\pi}} \int_{\infty}^{(p_{jet}-p_q)/\sqrt{2}\sigma} e^{-t^2}\ \mathrm{d}t, \\ &= \frac{1}{\sqrt{2\pi}} \int_{\infty}^{(p_{jet}-p_q)/\sigma} e^{-u^2/2}\ \mathrm{d}u, \\ \mathrm{DGAUSN}(r_{gaus}) &= \frac{p_{jet}-p_q}{\sigma} \\ p_{jet} &= p_q + \sigma \times \mathrm{DGAUSN}(r_{gaus}(p_{jet_i})). \end{aligned} \tag{E.4}$$

E.2 m_W^2 and m_t^2

As mentioned earlier, it is expected that $|\mathcal{M}|^2$ has the shape:

$$\frac{m_R\Gamma_R}{(m^2-m_R^2)^2+m_R^2\Gamma_R^2} \tag{E.5}$$

for masses in the vicinity of a resonance of mass, m_R, and width, Γ_R. If

$$h(m^2) = \frac{m_R\Gamma_R}{(m^2-m_R^2)^2+m_R^2\Gamma_R^2}, \tag{E.6}$$

then

$$\begin{aligned} r &= \int h(m^2)\ \mathrm{d}m^2 \\ &= \int \frac{m_R\Gamma_R \mathrm{d}m^2}{(m^2-m_R^2)^2+m_R^2\Gamma_R^2} \\ &= \frac{1}{m_R\Gamma_R}\tan^{-1}\left(\frac{m^2-m_R^2}{m_R\Gamma_R}\right), \end{aligned} \tag{E.7}$$

then

$$
\begin{aligned}
|\mathcal{M}|^2 \, \mathrm{d}m^2 &= \frac{|\mathcal{M}|^2}{h(m^2)} \, \mathrm{d}\left(\tan^{-1}\left(\frac{m^2 - m_R^2}{m_R \Gamma_R}\right)\right) \\
&= |\mathcal{M}|^2 \frac{\mathrm{d}r(m^2)}{h(m^2)}.
\end{aligned} \tag{E.8}
$$

F. C-HOLE SCINTILLATION COUNTER INSTALLATION

F.1 Introduction

Over the shutdown period ending in November 2003, eight additional scintillation counters were installed in the C-layer of the muon scintillation detection system (Sect. 3.2.5) to provide more complete muon trigger coverage and increase the muon acceptance in the bottom of the DØ detector. Each scintillation counter is identified by the proportional drift tube (PDT) chamber (Sect. 3.2.5) with which it is associated. There are two C-Hole counters for each of PDTs 216, 215, 235, and 236. The counters closest to the centerline are labeled with an 'N' (for Narrow), while those closest to the outside of the counters are labeled with a 'W' (for Wide). Thus, '216N' designates the narrow counter (closest to centerline) installed beneath PDT 216. Fig. F.1 shows the hole in the outer layer of the scintillation detection system in the central region that the new counters fill.

The new scintillation counters are similar in design to the other scintillation counters in the central muon system, having two 25 mm PMTs each. A complete description of the design and construction of these new counters can be found in Ref. [95]. Here a brief description is given of the testing and installation of the C-Hole scintillation counters.

F.2 Pre-Installation Testing

The nominal voltage was determined for one of the 8 counters by accurately measuring the plateau curve. The plateau curve is a plot of the muon detection efficiency vs. operating voltage for a particular photomultiplier tube (PMT). It was determined using small trigger counters

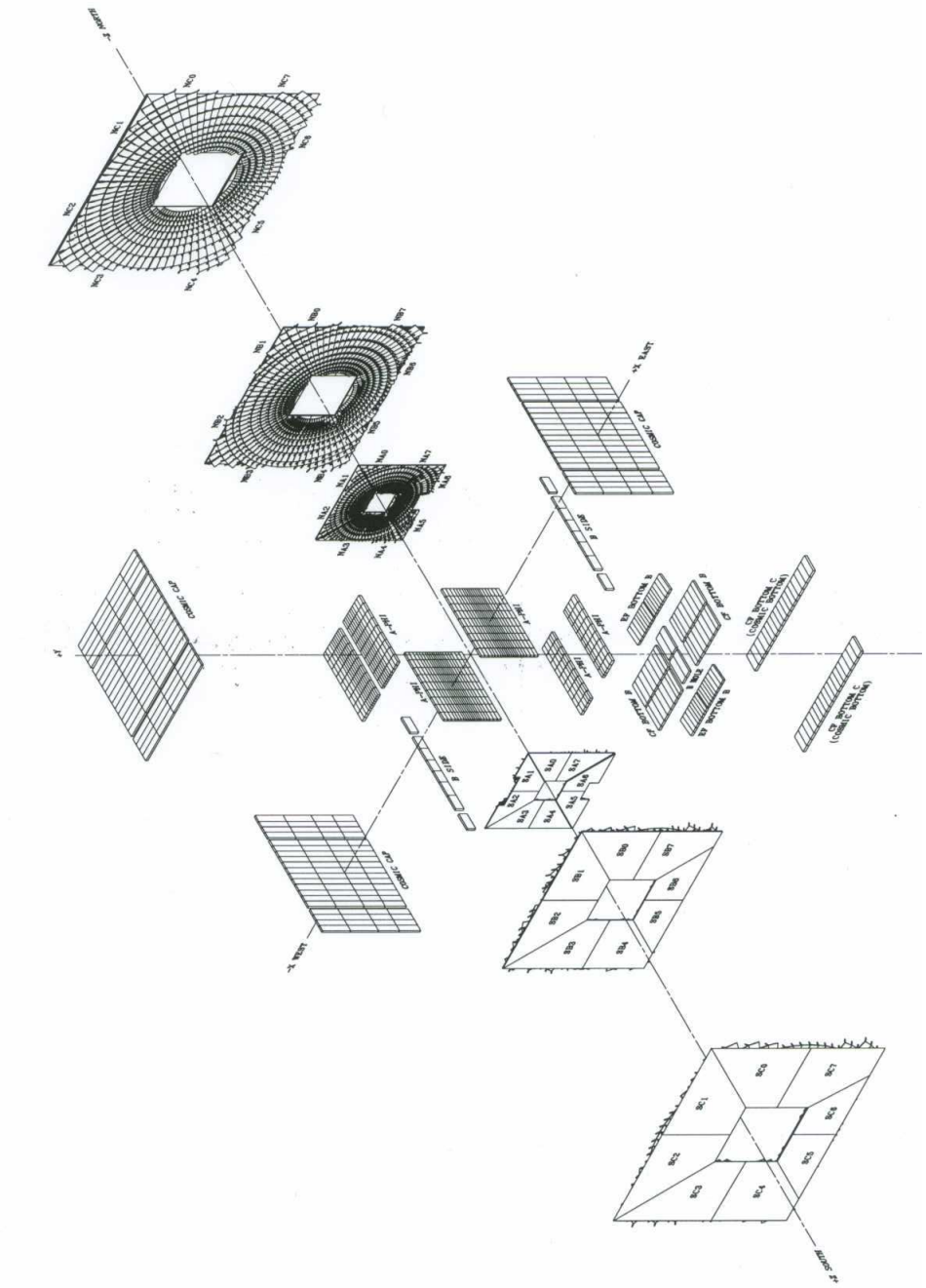

Fig. F.1. 3-dimensional layout of the muon scintillator detection system.

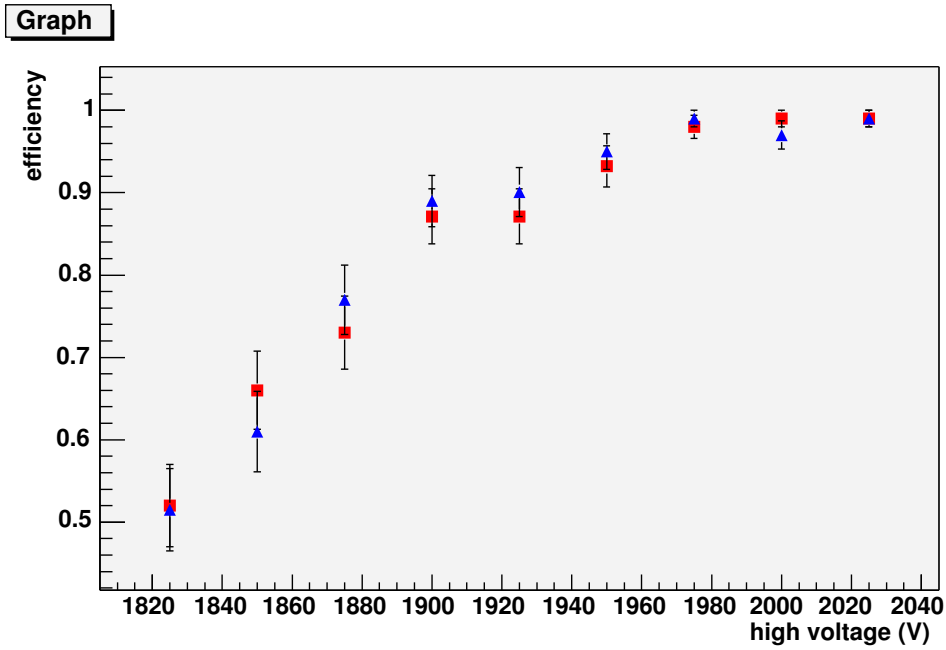

Fig. F.2. Voltage plateau curves for two PMTs of a typical C-Hole counter

placed immediately above and below the counter to be tested. Signals coincident in the two small trigger counters indicate a cosmic muon (i.e. a muon from pion decays from interactions of protons with the earth's atmosphere) passing through the three detectors. The number of hits in the counter to be tested divided by the number of hits coincident with the other two counters gives a muon detection efficiency. This was done for voltages ranging from 1875 to 2025 V in 25 V increments. A typical plateau curve is shown in Fig. F.2. The nominal voltage was taken to be the voltage beyond which the efficiency is relatively stable.

For the remaining counters, it was assumed by the group performing the testing that the nominal voltage could be determined by comparing the detector response to a 85 μCi Ra^{226} source between the counters and the fully-tested counter. The nominal voltages were raised until the response was greater than or equal to the first counter's response for each corner for each PMT. Nominal voltages were raised an additional 100 V beyond this to account for

differences in PMT and scintillation counter responses. High voltage for counters on the east and west sides of the DØ detector are provided separately by two high voltage (HV) fanout hubs located in the bottom of the DØ detector. The nominal voltage for each set of four counters was taken to be the average of the voltages for the eight PMTs in each group.

F.3 Counter Installation

Each scintillation counter in the B- and C-layers of the central muon detection system has 2 PMTs, and each PMT requires a high voltage cable and a signal cable. In addition to this, all scintillation counters have optical light fibers permanently connected to a LED pulser system [96] for periodic testing. These cables are bound together and run on the floor of the DØ detector from the scintillation counters directly to the nearest corners of the detector foundation. From there the HV cables are routed to the fanout hubs. Optical light fibers are routed to the light mixing boxes (LMBs) of the LED pulser system, which provides LED pulses through the optical fiber to the face of the PMT to simulate a signal from the scintillating material. These particular LMBs are located on the B-Hole scintillation counters (205, 245, 206, and 246), located in the vicinity. Coaxial signal cables for counters on the east side of the detector are connected to Scintillation Front-End (SFE) boards in SFE crate 56 (in the Collision Hall), while signal cables for the west-side counters are connected to SFE boards in SFE crate 55.

F.3.1 Method of installing counters

To facilitate moving the scintillation counters into their final positions, unistrut frames were constructed for pairs of counters, one pair for each of the four PDT chambers. Ropes were attached to each corner of the frames for use in pulling the counter pairs from either side of the DØ detector. Because the frames were not rigidly connected to the scintillation counters, care had to be taken to ensure that the frames and counters moved together at all times. Counters

within each pair were connected to each other with mylar tape. This was done to avoid damage to the optical fibers, since they are rigidly mounted to the surfaces of the counters.

Since the cables and ropes are fairly exposed, and pulling on either once the counters are in position can not only damage the light fibers, but also move the counters out of position, signs were placed at each corner at the bottom of the DØ detector to warn people not to disturb the ropes or cables.

F.4 Post-Installation Testing

Immediately after installation, the LED pulsing system was used to ensure proper operation of the installed counters. This test verified proper operation of PMTs and the readout of the PMT, but is not by itself a complete test of the counter. Data was therefore collected in a special run in which HV was turned on for only octants 5 and 6 (the octants in the bottom of the detector), and only triggers from octants 5 and 6 were generated. This provided a complete test of the installed counters.

G. MUON SCINTILLATION T_0 CALIBRATION

Scintillation counters (Sect. 3.2.5) give as an output for every hit a time associated with the hit. The hit times are calibrated in such a way that a muon traveling from a $p\overline{p}$ collision at the center of the detector will be coincident on the center of the counter at a time of 0 ns. Of course, detectors have some width and length, so there is a natural width to the time distribution for individual counters even without noise or background muons.

At the time of the t_0 calibration, there were two distinct types of data formats. The raw data was stored in a format containing all the information from all parts of the detector to reconstruct physics objects. The other format, commonly referred to as *TMBs* or *thumbnails*, store processed events and contain less information. The central A-layer scintillation counters were calibrated in December 2002 using TMBs. BC-layer counters have two photomultiplier tubes (PMTs) each, and the TMB files contained only averages of the times from each tube. Thus TMB files could not be used to calibrate individual PMTs in the BC-layer counters (see [97]).

For this reason, BC-layer counters in the central region were calibrated channel-by-channel (i.e. for every PMT) using a combination of processed data, stored in TMB files, and a smaller set of data stored in the raw data format.

G.1 Procedure for Determining the t_0s

The input files for the initial calibration were all from a single run taken on 4 August 2003, chosen both because it had a large number of events (270 nb^{-1}) and because the muon system was operating normally. A modified version of *MuoExamine*, a package designed to monitor online muon data collection, was used for the t_0 analysis. It was modified to allow multiple

runs, and to record hits from individual PMTs for each scintillation counter in the BC layer. For every scintillation counter, three histograms were created: one for each of the two PMTs, and a third containing the difference in times between the two PMTs. The only event selection was the requirement to pass a set of muon triggers at Level 2 and a set of jet triggers at Level 3. Only hits were used for which both PMTs fired.

Histograms were fit to Gaussian, and the central values were used to determine the average time for each PMT of every counter. A typical counter's results are shown in Fig. G.1.

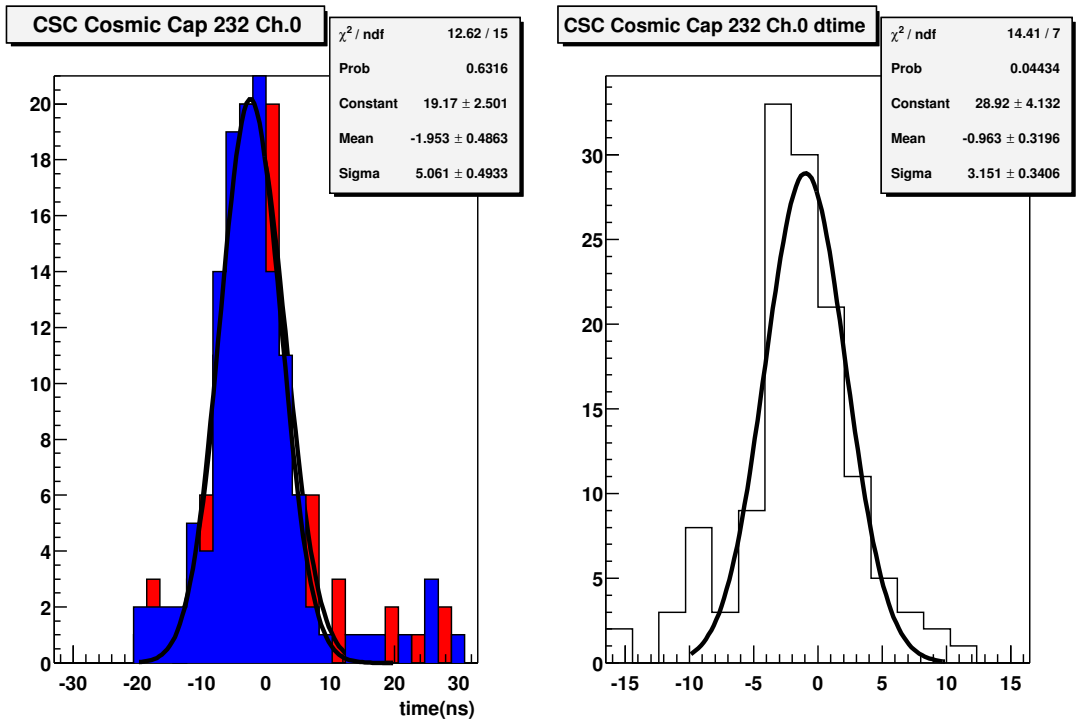

Fig. G.1. Histograms for typical counter. The two shades in the plot on the left correspond to two different PMTs for the same counter. The plot on the right shows the difference in times between the two PMTs for every muon hit. All times are in ns.

These fitted central values, along with the errors in the fits, were processed to obtain the t_0 correction. The scintillation counters are calibrated such that muons coming from physics

events from $p\overline{p}$ collisions at the center of the detector arrive at a time of 0 ns. So the fitted central values are used to correct the calibrations to give a resulting average time of 0 ns. The distributions of fit errors (Figures G.2 and G.3) show that roughly 65% of the counters had fit errors less than 1 ns. Fit values with errors less than 1 ns were used directly. For around 50 of the remaining counters, the time difference was used in combination with a single good PMT fit to determine the calibration constants. For the rest, no channel-by-channel correction was done. The bad fits are attributed to low statistics, particularly in the bottom of the detector near the detector centerline.

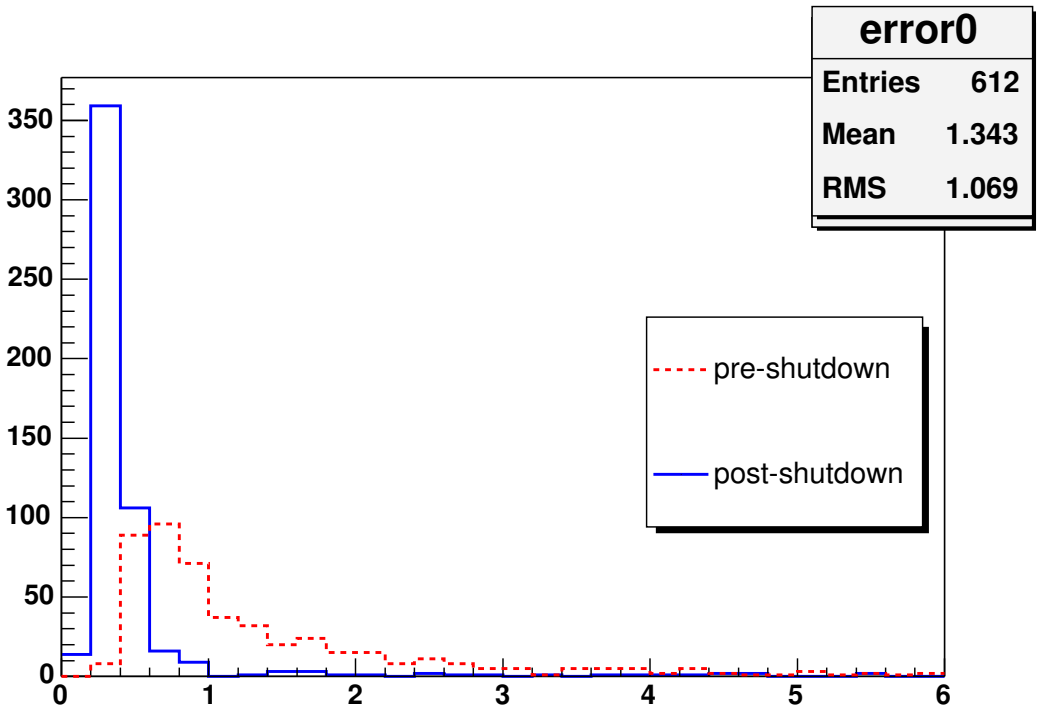

Fig. G.2. Distribution of errors in calculated means for all C-layer PMTs, before and after the calibration which occurred during the shutdown period.

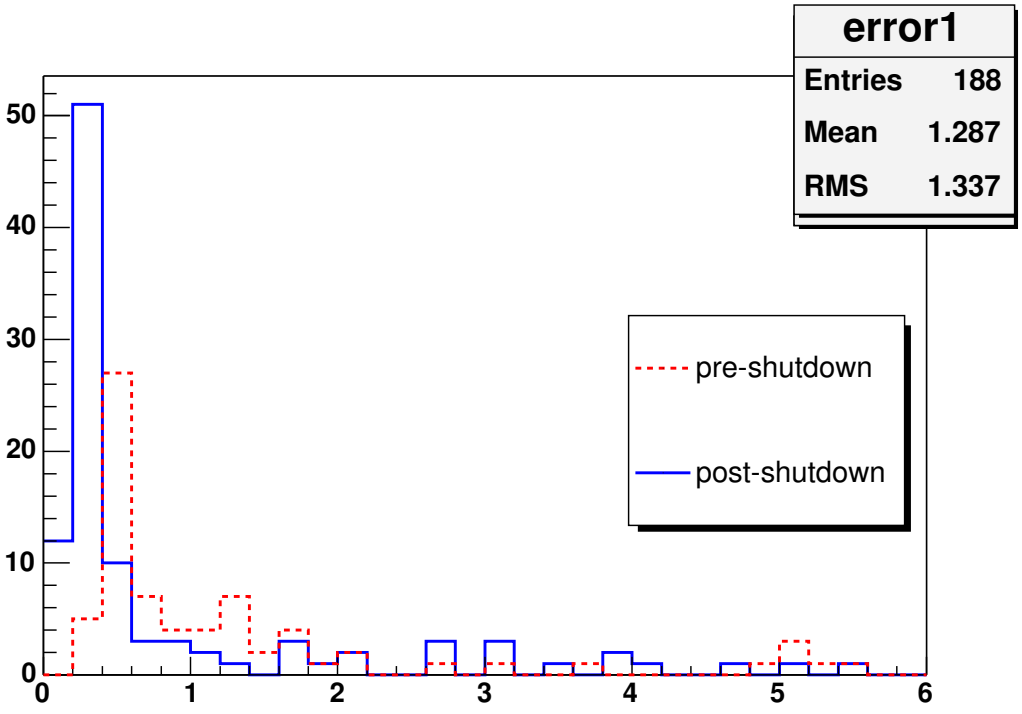

Fig. G.3. Distribution of errors in calculated means for all B-layer PMTs, before and after the calibration which occurred during the shutdown period.

G.2 Results of t_0 Calibration

Corrected t_0s were downloaded just prior to the first physics run (185462) taken on 22 November 2003. Data was analyzed using similar methods to determine the effect of the download. Several runs from the first two weeks, containing roughly 700 nb^{-1} of data, were used. The effect was measured using the average time from each pair of PMTs. Figures G.4 and G.5 show the before and after t_0 distributions for the central C- and B-layer scintillation counters, respectively. All histograms are normalized to unity to allow for proper comparison of distributions. For counters in both the B- and C-layer, the new values are clearly centered more tightly around zero.

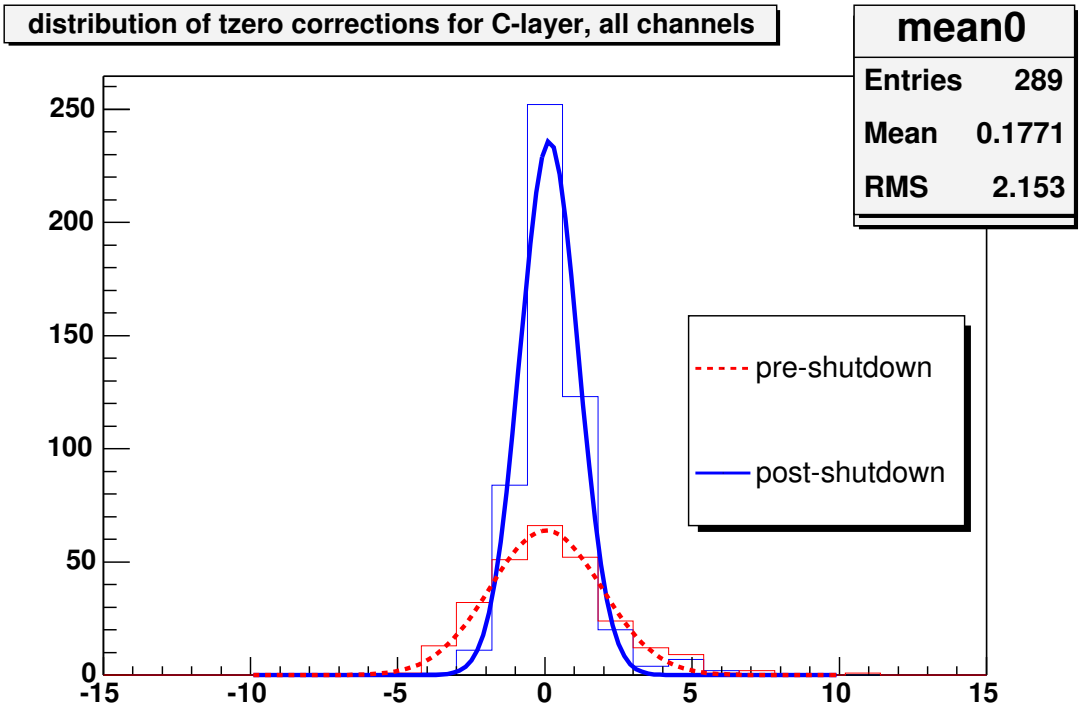

Fig. G.4. Mean values of times (in ns) for all C-layer PMTs, before and after calibration, with Gaussian fits. Dashed lines are prior to the new calibration (during the shutdown period), solid lines are after.

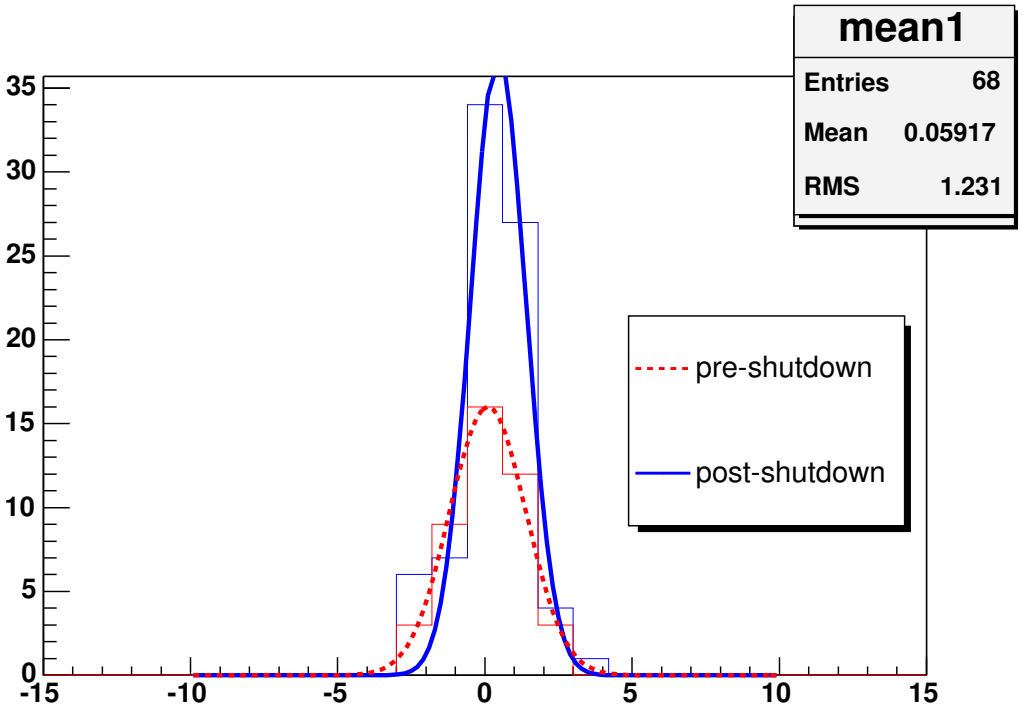

Fig. G.5. Mean values of times (in ns) for all B-layer PMTs, before and after calibration, with Gaussian fits. Dashed lines are prior to the new calibration (during the shutdown period), solid lines are after.

Fig. G.6 shows the overall improvement in the entire central muon scintillation detection system.

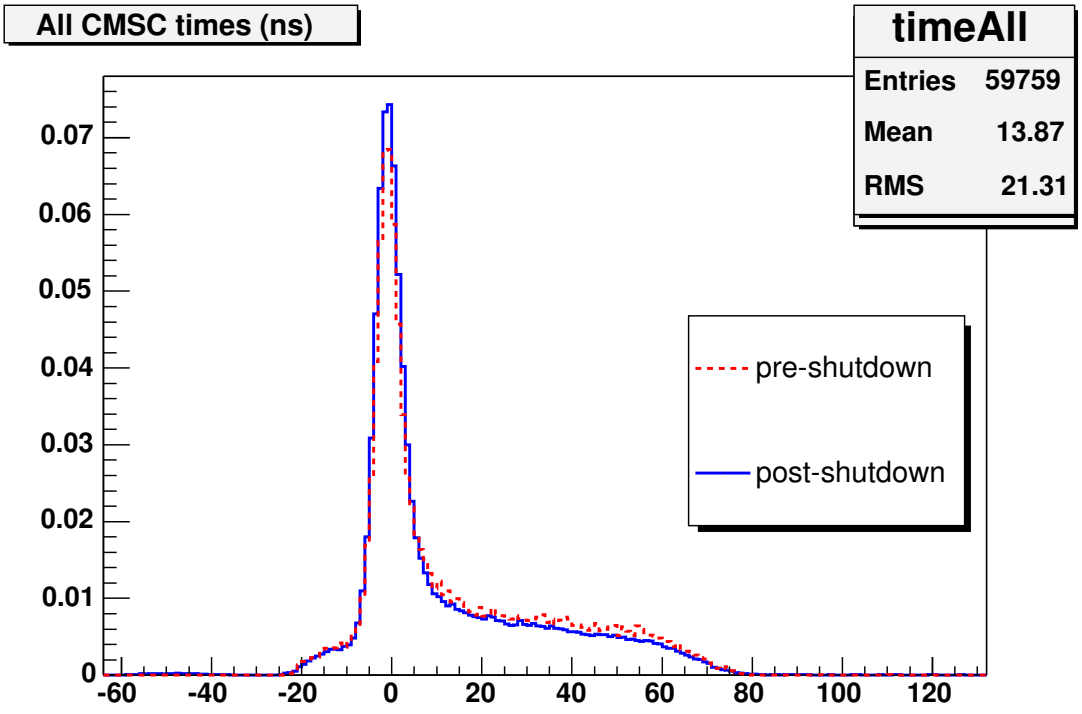

Fig. G.6. All times (in ns) for all PMTs for events passing trigger, before and after the calibration which occurred during the shutdown period.

G.3 $Z \rightarrow \mu\mu$ data

Finally, $Z \rightarrow \mu\mu$ data events were to further characterize the improvement in the t_0 calibration. $Z \rightarrow \mu\mu$ events were chosen to get a sample of events with a reasonably low level of cosmic muons. Events from thumbnails were chosen which met the following criteria:

- 2 medium muons with $p_T \geq 8$ GeV
- opposite charge

- z of DCA within 5 cm
- $70 \leq$ reconstructed Z mass ≤ 110

Four plots were created, shown in Figures G.7, G.8, G.9, and G.10. The first 2 show the changes in distributions for scintillator hits in the A-layer and BC-layer, respectively. One sees a qualitative improvement in the BC-layer time distribution for these $Z \rightarrow \mu\mu$ events. The values are centered more closely around zero.

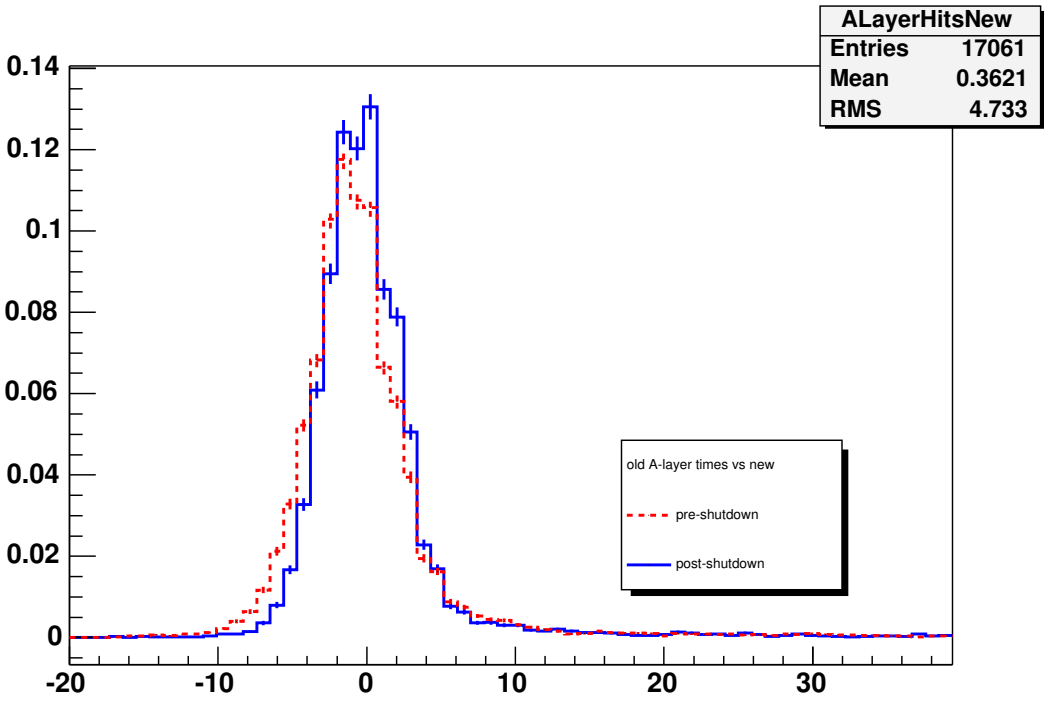

Fig. G.7. A-layer Scintillator times (in ns) for $Z \rightarrow \mu\mu$ events

The third plot shows the change to cosmic cut efficiencies before and after calibration. Clearly, the cosmic cut efficiency is strongly analysis-dependent, as further cuts to reduce cosmic background would have had a large effect on the cosmic cut efficiency. This was done just to

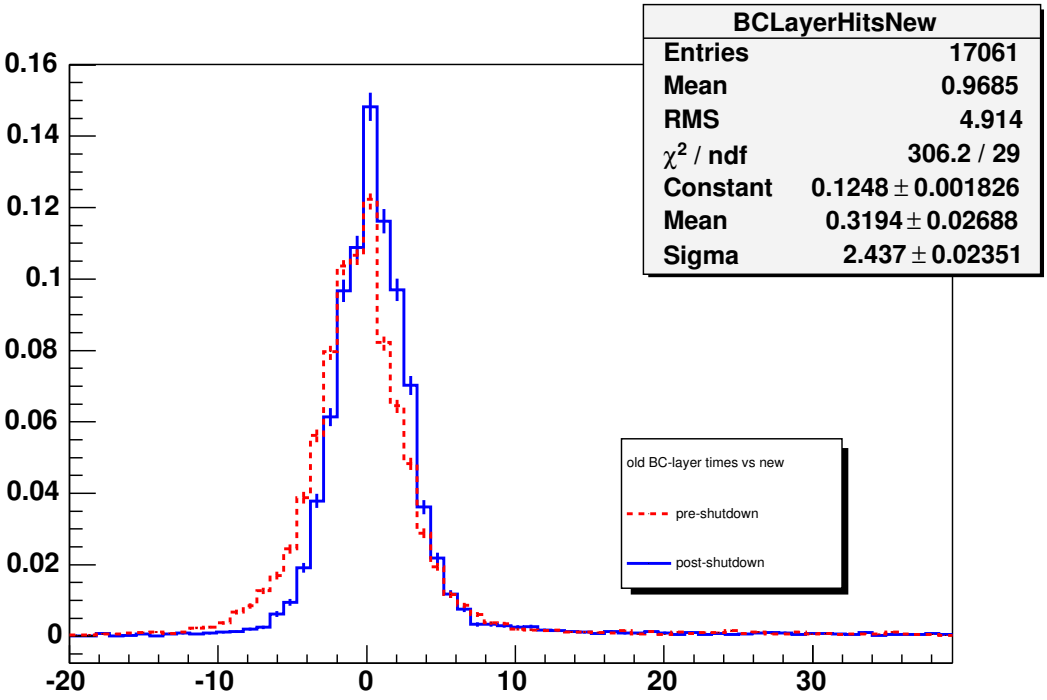

Fig. G.8. BC-layer Scintillator times (in ns) for $Z \rightarrow \mu\mu$ events

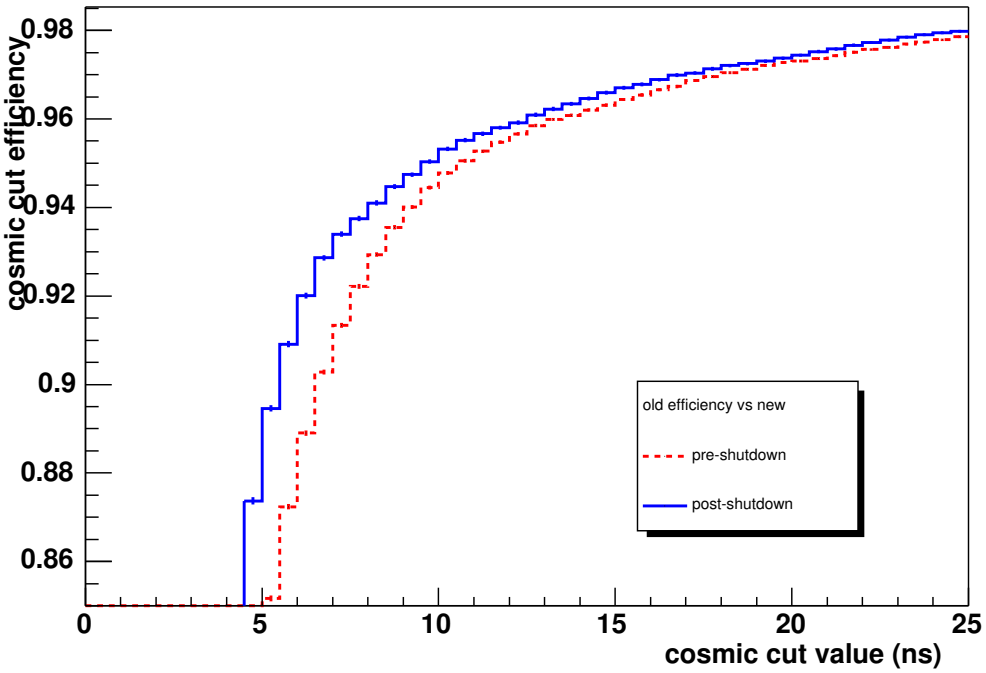

Fig. G.9. Cosmic cut efficiencies vs cosmic cut values (in ns) for $Z \rightarrow \mu\mu$ events

get a general idea of how the t_0 calibration might affect cosmic cut efficiencies for a non-specific analysis.

The cosmic cut efficiency for a particular value of the cosmic cut was calculated in the following way:

$$\text{efficiency} = \frac{N_{loose} - N_{tight}}{N_{loose}}$$

where N_{loose} is the number of events before the cosmic cut, and N_{tight} is the number of events after.

Events passed the cosmic cut if either the A-layer time or the BC-layer time is smaller in magnitude (in ns) than the cosmic cut value.

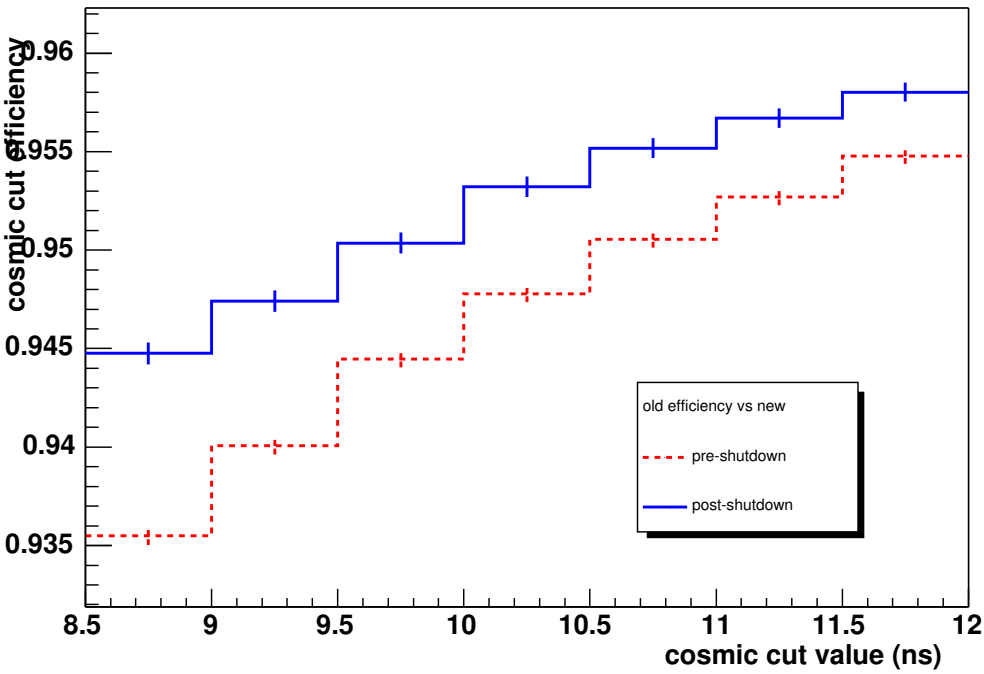

Fig. G.10. Blowup of cosmic cut efficiencies.

LIST OF REFERENCES

[1] S. L. Glashow, "Partial Symmetries Of Weak Interactions," Nucl. Phys. **22**, 579 (1961);
S. Weinberg, "A Model Of Leptons," Phys. Rev. Lett. **19**, 1264 (1967);
A. Salam, in *Proceedings of the Eighth Nobel Symposium, on Elementary Particle Theory, Relativistic Groups, and Analyticity, Stockholm, Sweden, 1968*, edited by N. Svartholm (Almqvist and Wikell, Stockholm, 1968).

[2] S. L. Glashow, J. Iliopoulos and L. Maiani, "Weak Interactions with Lepton - Hadron Symmetry," Phys. Rev. D **2**, 1285 (1970);
M. Kobayashi and T. Maskawa, "CP Violation In The Renormalizable Theory Of Weak Interaction," Prog. Theor. Phys. **49**, 652 (1973).

[3] P. H. Garbincius,"Tevatron collider operations and plans," in *Proceedings of 39th Rencontres de Moriond on Electroweak Interactions and Unified Theories, La Thuile, Aosta Valley, Italy, 2004*, edited by J. Trân Thanh Vân. arXiv:hep-ex/0406013.

[4] L. H. Ryder, "Quantum Field Theory," Cambridge Univ. Press, 2nd ed.(1996).

[5] W. N. Cottingham and D. A. Greenwood, "An Introduction to the Standard Model of Particle Physics," Cambridge Univ. Press (2003).

[6] T. P. Cheng and L. F. Li, "Gauge theory of elementary particle physics"

[7] M. Beneke *et al.*,"Top quark physics,"arXiv:hep-ph/0003033.

[8] M. J. G. Veltman, "Limit On Mass Differences In The Weinberg Model," Nucl. Phys. B **123**, 89 (1977).

[9] A. Sirlin, "Radiative Corrections In The SU(2)-L X U(1) Theory: A Simple Phys. Rev. D **22**, 971 (1980).

[10] W. J. Marciano and A. Sirlin, "Radiative Corrections To Neutrino Induced Neutral Current Phenomena In The Phys. Rev. D **22**, 2695 (1980) [Erratum-ibid. D **31**, 213 (1985)].

[11] W. F. L. Hollik, "Radiative Corrections in the Standard Model and their Role for Precision Tests of the Electroweak Theory," Fortsch. Phys. **38**, 165 (1990).

[12] t. L. E. Group [OPAL Collaboration],"A Combination of Preliminary Electroweak Measurements and Constraints on the Standard Model," [arXiv:hep-ex/0612034].

[13] M. Cacciari, S. Frixione, M. L. Mangano, P. Nason and G. Ridolfi, "The t anti-t cross-section at 1.8-TeV and 1.96-TeV: A study of the systematics due to parton densities and scale dependence," JHEP **0404**, 068 (2004) [arXiv:hep-ph/0303085].

[14] N. Kidonakis and R. Vogt, "Next-to-next-to-leading order soft-gluon corrections in top quark hadroproduction," Phys. Rev. D **68**, 114014 (2003) [arXiv:hep-ph/0308222].

[15] Z. Sullivan, "Understanding single-top-quark production and jets at hadron colliders," Phys. Rev. D **70**, 114012 (2004) [arXiv:hep-ph/0408049].

[16] W. M. Yao *et al.* [Particle Data Group], "Review of particle physics," J. Phys. G **33**, 1 (2006).

[17] D. Acosta *et al.* [CDF Collaboration], "Measurement of $B(t \to Wb)/B(t \to Wq)$ at the Collider Detector at Fermilab," Phys. Rev. Lett. **95**, 102002 (2005) [arXiv:hep-ex/0505091].

[18] V. M. Abazov *et al.* [D0 Collaboration], "Measurement of $B(t \to Wb)/B(t \to Wq)$ at s**(1/2) = 1.96-TeV," Phys. Lett. B **639**, 616 (2006) [arXiv:hep-ex/0603002].

[19] J. Swain and L. Taylor, "First determination of the quark mixing matrix element V(tb) independent of assumptions of unitarity," Phys. Rev. D **58**, 093006 (1998) [arXiv:hep-ph/9712420].

[20] R. Arnowitt and P. Nath, "Supersymmetry and supergravity: Phenomenology and grand unification," arXiv:hep-ph/9309277.

[21] N. Polonsky and S. Su, "More Corrections to the Higgs Mass in Supersymmetry," Phys. Lett. B **508**, 103 (2001) [arXiv:hep-ph/0010113].

[22] F. Fiedler *et al.*, "Measurement of the Top Quark Mass with the Matrix Element Method at DØ Run-II", DØ Note 4717 (2005).

[23] G. Garzón *et al.*, "Measurement of the $t\bar{t}$ Production Cross Section in $p\overline{p}$ Collisions at $\sqrt{s} = 1.96$ TeV using secondary vertex b-tagging", DØ Note 5113 (2006).

[24] [D0 Collaboration] "Measurement of the $t\bar{t}$ Production Cross-section at $\sqrt{s} = 1.96$ TeV in the Lepton+jets Final States using a Topological Method", DØ Note 4422 (2004).

[25] C. Clement *et al.*, "Measurement of the $t\bar{t}$ Production Cross-Section at $\sqrt{s} = 1.96$ TeV in the Electron+Jets Final State using a Topological Method", DØ Note 4662 (2004).

[26] M.Angelou, et al, *Top Trigger Efficiency Measurements and the* top_trigger *package*, DØ Note 4512 (2004).

[27] R. Kleiss, W. J. Stirling and S. D. Ellis, *A New Monte Carlo Treatment Of Multiparticle Phase Space At High-Energies*, Comput. Phys. Commun. **40**, 359 (1986).

[28] R. Harrington, "Integration of Probabilities for Matrix Element Method ($t\bar{t} \rightarrow l + jets$)", DØ Note 4957 (2005).

[29] F. Maltoni and T. Stelzer, *MadEvent: Automatic event generation with MadGraph*, JHEP **0302**, 027 (2003) [arXiv:hep-ph/0208156].

[30] V. M. Abazov *et al.* [D0 Collaboration], "A precision measurement of the mass of the top quark," Nature **429**, 638 (2004) [arXiv:hep-ex/0406031].

[31] `http://www-d0.fnal.gov/Run2Physics/top/d0_private/wg/top_analyze/Ipanema/Ipanema.html`

[32] F. Fiedler *et al.*, "Top Quark Mass Measurement with the Matrix Element Method in the Lepton+Jets Final State at DØ Run II", DØ5053 (2006).

[33] V.M.Abazov *et al.*, *The Upgraded DØDetector*, accepted by Nucl. Instrum. Meth. A, arXiv:physics/0507191(2005).

[34] S.Abachi *et al.*, Nucl. Instrum. Methods Phys. Res., Sect. A **338**, 185 (1994).

[35] T.Zhao *et al.*, IEEE Transactions on Nuclear Science 49, 1092 (2002).

[36] R. Lipton, "The DØSilicon Tracker", Nucl. Instrum. Meth. A418, 85 (1998).

[37] M.L. Mangano, M. Moretti, F. Piccinini, R. Pittau, A. Polosa, JHEP 0307:001,2003, hep-ph/0206293;
M.L. Mangano, M. Moretti, R. Pittau, Nucl.Phys.B632:343-362,2002, hep-ph/0108069;
F. Caravaglios, M.L. Mangano, M. Moretti, R. Pittau, Nucl.Phys.B539:215-232,1999, hep-ph/9807570.

[38] T. Sjöstrand, P. Edén, C. Fribert, L. Lönnblad, G. Miu, S. Mrenna and E. Norrbin, Computer Physics Commun. **135**(2001) 238.

[39] H. L. Lai *et al.*, Eur. Phys. J. C12:375-392, 2000.

[40] D. Lange, A. Ryd *et al.*, *The EvtGen Event Generator Package*, in Proceedings of CHEP (1998).

[41] S. Jadach, Z. Was, R. Decker, J. H. Kuehn, Comp.Phys.Commun. 76(1993) 361 (CERN TH-6793 preprint).

[42] J. Thompson,"Introduction To Colliding Beams At Fermilab," FERMILAB-TM-1909

[43] T. Cole *et al.*, "A Report on the Design of the Fermi National Accelerator Laboratory Superconducting Accelerator",Beams-doc-1888-v1

[44] C. W. Schmidt,"Review Of Negative Hydrogen Ion Sources," FERMILAB-LU-166 *Presented at 1990 Linear Accelerator Conf., Albuquerque, NM, Sep 10-14, 1990*

[45] D. Patterson, "The FNAL 200-MeV Linac," FERMILAB-MISC-1986-01

[46] R. J. Noble,"The Fermilab Linac Upgrade," FERMILAB-LU-172 *Presented at 1990 Linear Accelerator Conf., Albuquerque, NM, Sep 10-14, 1990*

[47] Concepts Rookie Book, `http://www-bdnew.fnal.gov/operations/rookie_books/Concepts_v3.pdf`

[48] Linac Rookie Book, `http://www-bdnew.fnal.gov/operations/rookie_books/LINAC_v2.pdf`

[49] Booster Rookie Book, `http://www-bdnew.fnal.gov/operations/rookie_books/Booster_V3_1.pdf`

[50] Main Injector Rookie Book, `http://www-bdnew.fnal.gov/operations/rookie_books/Main_Injector_v1.pdf`

[51] Antiproton Source Rookie Book, `http://www-bdnew.fnal.gov/operations/rookie_books/Pbar_V1_1.pdf`

[52] Tevatron Rookie Book, `http://www-bdnew.fnal.gov/operations/rookie_books/Tevatron_v1.pdf`

[53] S. D. Holmes,"Status of the Fermilab Main Injector and recycler,"FERMILAB-CONF-97-298 *Talk given at the 17th IEEE Particle Accelerator Conference (PAC 97), Vancouver, Canada, 12-16 May 1997*

[54] G. W. Foster, W. Chou and E. Malamud, "Proton driver study. II. (Part 1)," FERMILAB-TM-2169

[55] C-C. Miao, FERMILAB-CONF-98-395-E (1998).

[56] DØUpgrade Collaboration, "DØSilicon Tracker Technical Design Report," DØ Note 2169 (1994).

[57] D. Adams *et al.*, "The DØCentral Fiber Tracker Technical Design Report," DØ Note 4164 (1999).

[58] A. Gordeev *et al.*, "Technical Design Report of the Forward Preshower Detector for the D0 Upgrade," DØ Note 3445 (1998).

[59] M. Adams *et al.*, "Design Report of the Central Preshower Detector for the DØ Upgrade" (1996). http://d0server1.fnal.gov/users/qianj/CPS/doc/dn3104.pdf

[60] J. Brzezniak *et al.*, "Conceptual Design Of A 2-Tesla Superconducting Solenoid For The Fermilab D0 Detector Upgrade," FERMILAB-TM-1886 (1994).

[61] L. Groers, "DØ Calorimeter Upgrades for Tevatron RunII", DØ Note 4240, Proceedings for the IXth International Conference on Calorimetry in Particle Physics, Annecy, France, Oct 9-14, 2000.

[62] V. M. Abazov *et al.*, "The muon system of the Run II D0 detector," Nucl. Instrum. Meth. A **552**, 372 (2005) [arXiv:physics/0503151].

[63] B. Baldin *et al.*, "Technical Design of the Central Muon System," DØ Note 3365 (1998).

[64] H. T Diehl and A. S. Ito, "Central Muon Upgrade Cosmic Cap Side Wall Gap Conters," DØ Note 3355 (1997).

[65] Y. Hu *et al.*, "The central track trigger of the D0 experiment," IEEE Trans. Nucl. Sci. **51**, 2368 (2004).

[66] G. C. Blazey [D0 Collaboration], "The D0 run II trigger," FERMILAB-CONF-97-395-E http://www.slac.stanford.edu/spires/find/hep/www?r=fermilab-conf-97-395-e *To be published in the proceedings of 10th IEEE Real-Time Computer Applications in Nuclear, Particle and Plasma Physics (RT 97), Beaune, France, 22-26 Sep 1997*

[67] M. Adams *et al.*, "Level-2 Calorimeter Preprocessor Technical Design Report", DØ Note 3651 (1999).

[68] R. Hirosky [D0 Collaboration], "The D-Zero Level 2 Trigger for Run II Physics," *Proceedings of the 11th IEEE Real-Time Conference (RT 133), Santa Fe, NM, 14-18 June 1999*

[69] D. Baden and D. Toback, "Specification of the Level 2 Central Tracking Trigger Preprocessor Crate with inputs from the Level 2 Silicon Tracking Trigger" (1999). http://www.nhn.ou.edu/~abbott/L2Trigger/l2stt_2_l2ctt_documentation.ps

[70] A. Maciel *et al.*, "The L2-Muon Trigger Methods and Algorithms", DØ Note 4756, v1.0 (2005).

[71] K. Black, "A Precision Measurement of the Top Quark Mass", Boston University PhD Dissertation, (2005).

[72] O. Boeriu *et al.*, "CFT Light Yield Studies", DØ Note 4602 (2004).

[73] D. Adams, "Finding Tracks", DØ Note 2958-2 (1998).

[74] A. Khanov, "HTF: histogramming method for finding tracks. The algorithm description." DØ Note 3778 (2000).

[75] H. Greenlee, "The DØ Kalman Track Fit", DØ Note 4303 (2004).

[76] A. García-Bellido, *et al.*, "Primary Vertex certification in p14", DØ Note 4320 (2004).

[77] A. García-Bellido, *et al.*, "Primary Vertex certification in p14", DØ Note 4320 (2004).

[78] G. Bernardi, *et al.*, "NADA: A New Event by Event Hot Cell Killer", DØ Note 3687 (1999).

[79] G. Bernardi, *et al.*, "Improvement of the NADA Algorithm: Hot Cell Killing in DØ Run II Data", DØ Note 4057 (2002).

[80] J. -R. Vlimant, *et al.*, "Technical description of the T42 Algorithm for the calorimeter noise suppression", DØ Note 4146 (2003).

[81] J. Kozminski, *et al.*, "Electron Likelihood in p14", DØ Note 4449 (2004).

[82] J. Agram, *et al.*, "Jet Energy Scale at DØ Run II", DØ Note 4720 (2005).

[83] N. Makovec and J. -F. Grivaz, "The Relative Data-Monte Carlo Jet Energy Scale", DØ Note 4807, v.4.1 (2005).

[84] M. Angelou, *et al.* [The Top Physics Working Group of the DØ Collaboration], "DØ Top Analysis and Data Sample for the Winter Conferences 2004", DØ Note 4419 v6 (2004).

[85] C. Clémente, *et al.*, "MuonID Certification for p14", DØ Note 4350, v1.0 (2004).

[86] E. Nurse and P. Telford, "Measurement of $\sigma\times$ Branching Ratio for $Z \to \mu\mu$ in $p\overline{p}$ collisions at $\sqrt{s} = 1.96$ TeV", DØ Note 4231 (2003).

[87] L. Feligioni, *et al.*, "Update on b-quark jet identification with Secondary Vertex reconstruction using DØreco version p14", DØ Note 4414 (2004).

[88] V. Abazov, *al.* [D0 Collaboration], "Measurement of the top quark mass in the lepton + jets final state with the matrix element method," Phys. Rev. D **74**, 092005 (2006) [arXiv:hep-ex/0609053].

[89] G. P. Lepage,"A New Algorithm for Adaptive Multidimensional Integration," Journal of Computational Physics 27, 192-203 (1978)
`http://www.slac.stanford.edu/spires/find/hep/www?r=clns-80\%2F447`

[90] W. H. Press, B. P. Flannery, S. A. Teukolsky, & W. T. Vetterling, *Numerical recipes in C: the art of scientific computing.* New York: Cambridge University Press, 1988

[91] M. Galassi *et al*, *GNU Scientific Library Reference Manual (2nd Ed.)*, ISBN 0954161734
`http://www.gnu.org/software/gsl`

[92] C. Biscarat, "A package for ALPGEN Monte Carlo event generation", DØ Note 4939 (2006).

[93] E. Barberis, *et al.*, "The Matrix Method and its Error Calculation", DØ Note 4564 (2004).

[94] A. Schwartzman and C. Tully, "Effect of e/h on the Relative b-to-light Jet Energy Scale Systematics", DØ Note 4870 (2005).

[95] H.T. Diehl, DØ Note 4088, January 25, 2003.

[96] P. Hanlet *et al.*, "LED pulser system for Fermilab's D0 Muon Scintillation counters," Nucl. Instrum. Meth. A **521**, 343 (2004).

[97] C. Bailey *et al*, "Channel-by-channel Calibration of the Central Muon Scintillators", DØ Note 4291 (2002).

[98] M. G. Bowler,"E+ E- Production Of Heavy Quarks In The String Model," Z. Phys. C **11**, 169 (1981).

[99] C. Peterson, D. Schlatter, I. Schmitt and P. M. Zerwas, "Scaling Violations In Inclusive E+ E- Annihilation Spectra," Phys. Rev. D **27**, 105 (1983).

[100] E. Brubaker *et al.* [Tevatron Electroweak Working Group], "Combination of CDF and D0 results on the mass of the top quark," arXiv:hep-ex/0608032.

Robert D. Harrington

Department of Physics, Northeastern University phone: *(617)373-2955*
110 Forsyth St., 111 Dana Research Center fax: *(617)373-2943*
Boston, MA 02115 email: *harringt@fnal.gov*

Education:

PhD in Physics, Northeastern University, Boston, MA (expected) May 2007

BS in Physics, The University of Texas at Austin May 1993

Employment:

Research Assistant 7/03 - present

Northeastern University, Boston,MA

Teaching Assistant 6/02 - 7/03

Northeastern University, Boston,MA

Manufacturing Manager 6/00 - 6/02

E-Beam Review Division, KLA-Tencor, Bedford, MA

Officer 5/93 - 6/00

United States Navy

WORK AND RESEARCH EXPERIENCE

DØ Experiment, Fermilab, Batavia, IL July 2003 - present

- Top quark mass measurement in lepton+jets channel using a method which maximizes the use of kinematic information available for each event through the evaluation of signal and background matrix elements (matrix element method):
  - Performed detailed data to Monte Carlo comparisons.
  - Developed framework for evaluating QCD multijet background.

  - Improved matrix element method in the following ways:
    * Introduced heavy-flavor matrix elements using Madgraph-based code.
    * Introduced b-tagging to improve matching of jets to partons and to improve discrimination between signal and background.
- Monte Carlo studies:
  - Incorporated $t\bar{t}$ ALPGEN sample generation into general framework allowing for generation of samples that could be used by entire collaboration.
  - Performed studies of factorization scales to optimize fit of Monte Carlo to data.
- Hardware installation:
  - Tested scintillation detectors using a Ra^{226} source to optimize the photomultiplier tube (PMT) operating voltage.
  - Installed scintillation detectors on the floor of the detector to increase the muon scintillation coverage in the outer layer of the muon detector system.
- Muon scintillation system calibration:
  - Information from raw data used to calibrate for the first time the relative timing of individual PMTs for scintillation detectors containing pairs of PMTs.
  - Processed data using a tight $Z \rightarrow \mu\mu$ selection and cosmic muon rejection to perform re-calibration of all scintillation detectors in the central muon detector system.
- Operational shifts:
  - Completed over 700 hours of shifts responsible for monitoring quality of data being collected by the experiment.

KLA-Tencor Corporation, Bedford, MA June 2000 - June 2002

Managed manufacturing of thermal field emission electron sources for applications of electron microscopy to semiconductor wafer inspection, directly supervising 12 technical personnel.

U.S. Navy June 1993 - June 2000

- (1998-2000) **Engineering Instructor, Newport, RI**: Developed and implemented curriculum covering all aspects of nuclear and conventional steam plant engineering for 300 junior officer students per year.

- (1995-1998) **Surface Warfare Officer, U.S. Navy**, served aboard USS John C. Stennis. *Operational duties:* Officer of the Deck Underway, responsible for navigation, propulsion, and all other shipboard activities for 3200+ member crew. Propulsion Plant Watch Officer, responsible for operations of nuclear power plant propulsion and electrical power generation. *Administrative duties:* Reactor Auxiliaries Division Officer, 10/95-10/97, supervised 20 personnel in maintenance and operation of shipboard diesel engines. Reactor Damage Control Officer, 10/97-3/98, maintained preparedness of department of 350+ personnel in responding to shipboard emergencies.

AWARDS

Selected to attend 54th Meeting of Nobel Laureates, Lindau, Germany	June 2004
GAANN Fellowship	2002-2003
Minnie Stevens Piper Foundation Scholar award	1989-1993
National Merit Scholarship, University of Texas at Austin	1988

COMMUNITY SERVICE

GEAR UP: (8/2005-5/2006) Participated in GEAR UP (Gaining Early Awareness and Readiness for Undergraduate Programs) at the John D. O'Bryant School of Mathematics and Science, Roxbury, MA, tutoring high school students in-class and after school in physics and mathematics.

CONFERENCES AND WORKSHOPS ATTENDED

Top Quark Symposium at Michigan, The Michigan Center for Theoretical Physics, Ann Arbor, MI, April 7-8, 2005

2005 APS April Meeting, April 16-19, Tampa, FL

54th Meeting of Nobel Laureates, Lindau, Germany, June 25-July 2, 2004

TALKS

"Measurement of the Top Quark Mass in the Lepton+Jets Channel at DØ", 2005 APS April Meeting, Tampa, FL

REFERENCES

Prof. Emanuela Barberis, Northeastern University

Dr. Aurelio Juste, Fermi National Accelerator Laboratory

Dr. Michele Weber, Fermi National Accelerator Laboratory

PUBLICATIONS

Primary publications:

- V. M Abazov *et al.* [D0 Collaboration], "Measurement of the top quark mass in the lepton+jets final state with the matrix element method." accepted for publication by Phys. Rev. D [arXiv:hep-ex/0609053].

Publications as member of the D0 top group:

- V. M. Abazov *et al.* [D0 Collaboration], "Measurement of $B(t \to Wb)/B(t \to Wq)$ at $\sqrt{s}$ = 1.96-TeV," Phys. Lett. B **639**, 616 (2006) [arXiv:hep-ex/0603002].
- V. M. Abazov *et al.* [D0 Collaboration], "The upgraded D0 detector," Nucl. Instrum. Meth. A **565**, 463 (2006) [arXiv:physics/0507191].
- V. M. Abazov *et al.* [D0 Collaboration], "Measurement of the t anti-t production cross section in p anti-p collisions at s**(1/2) = 1.96-TeV in dilepton final states," Phys. Lett. B **626**, 55 (2005) [arXiv:hep-ex/0505082].
- V. M. Abazov *et al.* [D0 Collaboration], "Measurement of the W boson helicity in top quark decays," Phys. Rev. D **72**, 011104 (2005) [arXiv:hep-ex/0505031].

- V. M. Abazov *et al.* [D0 Collaboration], "Measurement of the t anti-t production cross section in p anti-p collisions at s**(1/2) = 1.96-TeV using lepton + jets events with lifetime b-tagging," Phys. Lett. B **626**, 35 (2005) [arXiv:hep-ex/0504058].
- V. M. Abazov *et al.* [D0 Collaboration], "Measurement of the t anti-t production cross section in p anti-p collisions at s**(1/2) = 1.96-TeV using kinematic characteristics of lepton + jets events," Phys. Lett. B **626**, 45 (2005) [arXiv:hep-ex/0504043].

(**46** total publications as a member of the D0 Collaboration)